UNIVERSITY OF SOUTHAMPTON

FACULTY OF ENGINEERING, SCIENCE AND MATHEMATICS

Optoelectronics Research Centre

Light-Induced Ferroelectric Domain Engineering in Lithium Niobate & Lithium Tantalate

by

Christopher E. Valdivia

Thesis for the degree of Doctor of Philosophy

June 2007

UNIVERSITY OF SOUTHAMPTON

ABSTRACT

FACULTY OF ENGINEERING, SCIENCE AND MATHEMATICS
OPTOELECTRONICS RESEARCH CENTRE

Doctor of Philosophy

Light-Induced Ferroelectric Domain Engineering in Lithium Niobate & Lithium Tantalate

by Christopher E. Valdivia

The influence of illumination on ferroelectric domain engineering in lithium niobate and lithium tantalate is investigated. The conventional method of domain inversion is electric field poling, which suffers from several limitations such as a requirement for photolithography and high-voltage equipment, the formation of inhomogeneous electric fields, and a minimum domain size of micrometres. Through the use of directed laser light, either in the presence or absence of an externally applied electric field, these limitations can be overcome and new fabrication capabilities are revealed.

Illumination of the polar faces of lithium niobate with UV pulsed light has directly formed inverted surface domains. On the −z face, unpatterned light formed randomly scattered domain dots which could be ordered by illumination with a periodic intensity pattern. On the +z face, UV illumination induced random nano-scale nucleation points which grew along the crystalline y axes in a process referred to as all-optical poling. Electro-static interaction between these 100–300-nm wide domain lines deflected their growth directions, forming self-organized three-fold symmetric patterns, exhibiting the underlying symmetry of the crystals. Periodic intensity patterning allowed ordered alignment of these features along a preferred y axis.

Light-assisted poling is the simultaneous application of an external electric field and laser illumination. Using wavelengths ranging from near-UV to near-IR, the electric field required for domain nucleation was reduced for increasing intensities. This effect was most prominent in crystals highly doped with MgO, achieving a reduction of 90% and 98% for cw and fs-pulsed light, respectively. Arbitrary domain patterns were directly written by the scanning of a focused beam. Periodically poled gratings were formed using periodic intensity patterns via a phase mask, forming domain engineered crystals suitable for quasi-phase-matched nonlinear frequency conversion.

Contents

List of Figures

List of Tables

Declaration of Authorship

I, Christopher E. Valdivia, declare that the thesis entitled *Light-Induced Ferroelectric Domain Engineering in Lithium Niobate & Lithium Tantalate* and the work presented in the thesis are both my own, and have been generated by me as the result of my own original research. I confirm that:

- this work was done wholly or mainly while in candidature for a research degree at this University;
- where any part of this thesis has previously been submitted for a degree or any other qualification at this University or any other institution, this has been clearly stated;
- where I have consulted the published work of others, this is always clearly attributed;
- where I have quoted from the work of others, the source is always given. With the exception of such quotations, this thesis is entirely my own work;
- I have acknowledged all main sources of help;
- where the thesis is based on work done by myself jointly with others, I have made clear exactly what was done by others and what I have contributed myself;
- parts of this work have been published, as listed in Appendix A.

Signed: ....

Dated: ....

Acknowledgements

As with any substantial body of work, contributions from many individuals have been made in a variety of ways. I would like to thank my supervisor, Professor R. W. Eason, for his encouragement, support, guidance, and belief in me over the last three years. The research fellows in our group, Dr. Collin Sones and Dr. Sakellaris Mailis, have been instrumental in my transition into this field of ferroelectrics, and have provided countless hours of debate and companionship in the lab. I would also like to thank Dr. Jeffrey Scott, Tleyane Sono, Iain Welllington, and Alistair Muir for many helpful discussions.

Within the ORC department, I am grateful to Professors Peter G. R. Smith and David P. Shepherd for insightful feedback during my 9- and 15-month reports. I would also like to thank Dr. Katia Gallo, Dr. Lu Ming, and Dr. Corin Gawith for many useful discussions, and to Dr. John Mills for making the FAST lab laser system simple to operate (and to fix it when it wasn't). I am also very grateful to Dr. Wei Loh for helpful professional development advice. Some of this work was also made possible by the very kind sharing of facilities by David Beckett in Engineering Sciences, and Zondy Webber in Physics. I would also like to thank the ORC department itself, which provides a warm welcome to all its students.

Much of this research was completed in collaboration with several research groups. These included: Dr. Ian P. Clark of the Lasers for Science Facility at Rutherford Appleton Laboratory, UK, for providing access and expertise on the use of a frequency doubled dye laser system; Associate Professor Venkatraman Gopalan and Dr. David A. Scrymgeour at Pennsylvania State University, USA, for access to piezoelectric force microscopy and related discussions; Professor Karsten Buse, Dr. Elisabeth Soergel, Dr. Mark C. Wengler, and Tobias Jungk at University of Bonn, Germany, for collaborations in light-assisted poling and scanning force microscopy; and Professor Vladimir Ya. Shur at Ural State University, Russia, for useful discussions on poling dynamics.

I would also like to acknowledge the donation of time for use of an FIB milling machine by Dr. Chengge Jiao and Lloyd Peto of the FEI Company, UK, the short-term loan of a spectrophotometer by Shimadzu Corporation, and the supply of two Hf:CLN samples by Dr. E. Kokanyan of the National Academy of Sciences, Armenia.

I would like to give special thanks to my family for the same continuous support and encouragement I have received throughout my life. And I am always delighted (and sometimes surprised) that, despite these brief three years, we managed to fit in our wedding. Thank you Tressa, for your loving support and constant inspiration.

Finally, a special thanks to lithium niobate for never failing to produce surprises...

List of Acronyms

AFM atomic force microscopy

AOP all-optical poling

APE annealed proton exchange

BSHG backward-propagating second harmonic generation

CLN congruent lithium niobate

CLT congruent lithium tantalate

cw continuous wave

DC-EFM dynamic-contact electrostatic force microscopy

DFG difference frequency generation

EFP electric-field poling

Er:CLN Er-doped congruent lithium niobate

Fe:CLN Fe-doped congruent lithium niobate

Fe:SLN Fe-doped stoichiometric lithium niobate

Fe:LN Fe-doped lithium niobate

FIB focused ion beam

HexLN hexagonally-poled lithium niobate

HF hydrofluoric acid

Hf:CLN Hf-doped congruent lithium niobate

Hf:LN Hf-doped lithium niobate

IR infrared

ITO indium tin oxide, $Sn:In_2O_3$

KDP potassium dihydrogen phosphate, KH_2PO_4

KTP potassium titanate phosphate, $KTiOPO_4$

LAP light-assisted poling

LIFE light-induced frustrated etching

LN lithium niobate

LT lithium tantalate

Mg:CLN Mg-doped congruent lithium niobate

Mg:CLT Mg-doped congruent lithium tantalate

Mg:LN Mg-doped lithium niobate

Mg:SLN Mg-doped stoichiometric lithium niobate

Mg:SLT Mg-doped stoichiometric lithium tantalate

Nd:CLN Nd-doped congruent lithium niobate

Nd:LN Nd-doped lithium niobate

Nd:YVO_4 Nd-doped yttrium vanadate

Nd:YAG Nd-doped yttrium aluminum garnet

NPC nonlinear photonic crystal

PC photonic crystal

PFM piezoelectric force microscopy

ppm parts per million

ODT optical damage threshold

OPA optical parametric amplifier

OPG optical parametric generation

OPO optical parametric oscillation

OPPLN optically periodically-poled lithium niobate

PPLN periodically-poled lithium niobate

PPLT periodically-poled lithium tantalate

QPM quasi-phase-matching

SAW surface acoustic wave

SEM scanning electron microscopy

SFG sum frequency generation

SFM scanning force microscopy

SHG second harmonic generation

SIMS secondary ion mass spectrometry

SLN stoichiometric lithium niobate

SLT stoichiometric lithium tantalate

TEM transmission electron microscope

UV ultraviolet

VTE vapor transport equilibration

VUV vacuum ultraviolet

Zn:CLN Zn-doped congruent lithium niobate

Zn:LN Zn-doped lithium niobate

Chapter 1

Introduction

Since the invention of the laser in 1960 [Maiman60], investigation into nonlinear optical phenomena has become possible through the use of these directional, coherent, high intensity light sources [Bloembergen65]. Almost immediately, the nonlinear generation of an optical harmonic was demonstrated in quartz [Franken61]. This observation revealed new techniques for manipulating light with a nonlinear response, which had never been achieved in the past.

Nonlinear interactions are most efficient when phase matched. In general, due to the natural dispersion of all real materials, fundamental and second harmonic waves propagate with different velocities and will develop a relative phase difference. In perfect phase matching, both waves propagate with the same velocity and hence nonlinearly-generated waves add constructively throughout the interaction region. One method of achieving this ideal occurrence is birefringent phase matching. By carefully choosing the material and the polarization direction in the crystal, a suitable operating condition may be found where the birefringence and dispersion effectively cancel to produce perfect phase matching. However, considerable drawbacks of this method are the limitation of choice of materials and propagation directions, resulting in the use of non-optimal nonlinear coefficients of the crystal. Additionally, not all nonlinear interactions are phase-matchable in this way.

An alternative method is called quasi-phase-matching (QPM). In this technique, first proposed in [Armstrong62], the sign of the second-order nonlinear susceptibility, $\chi^{(2)}$, is periodically modulated in a crystal so that the interaction between the fundamental and second harmonic waves is always constructive, although not perfectly in-phase. This eliminates the problems of birefringent phase matching, allowing the use of a desired material and polarization direction to maximize the nonlinear interaction. Additionally, the choice of interacting wavelengths can be made by the design of the period of this quasi-phase-matched grating.

Ferroelectrics are a class of materials in which $\chi^{(2)}$ can be electrically controlled. These non-centrosymmetric crystals exhibit many diverse yet related properties, including pyroelectricity and piezoelectricity. Ferroelectric crystals below a critical temperature called the Curie point, T_c, maintain an inherent spontaneous polarization, P_s, even in the absence of an external electric field. Regions of differing polarization states, called ferroelectric domains, exhibit a hysteresis loop of polarization versus electric field. Domains of anti-parallel orientation possess $\chi^{(2)}$ of opposite sign, precisely the requirement for QPM. Tailoring the domain structure of ferroelectric crystals allows the engineering of quasi-phase-matched materials and highly efficient nonlinear interactions. This internal polarization is a major source of current interest in many ferroelectric materials.

Ferroelectricity was first discovered in rochelle salt in 1921 [Valasek21]. Another 14 years passed before another ferroelectric, potassium dihydrogen phosphate, KH_2PO_4 (KDP), was discovered [Busch35], prompting the belief that this property may have been limited to a handful of materials. However, starting in the 1940s, an explosion of new ferroelectric crystals occurred [Subbarao73], including the discovery of ferroelectricity in lithium niobate, $LiNbO_3$ (LN), and lithium tantalate, $LiTaO_3$ (LT) [Matthias49].

LN and LT are artificial crystals exhibiting many useful properties, often with material responses sufficiently large for technological importance. This has driven the fabrication of large high-quality single-crystals, making LN a preferred nonlinear material for optics. Its wide range of properties allows for the potential of a nonlinear optical chip [Stegeman85], integrating optical waveguides (ex. Ti-indiffusion, proton exchange), lasing (doped with rare-earth ions), nonlinear frequency conversion (periodically poled for QPM), switching (electro-optic modulation), and beam deflection (acousto-optic gratings). A review of the photonic applications of LN is presented in [Arizmendi04].

A particular advantage of LN and LT is the capability of controlling the sign of the nonlinear coefficient, $\chi^{(2)}$, by inverting the orientation of the spontaneous polarization in a process referred to as domain inversion, or simply *poling*. Currently, domain inversion is most successfully achieved by the application of a patterned electric field, referred to as electric-field poling (EFP). Periodic poling of ferroelectrics has many applications, including second harmonic generation (SHG), sum and difference frequency generation (SFG and DFG, respectively), and optical parametric oscillation (OPO). Domain inversion can also be used to form electrically-controllable cylindrical lenses, optical switching, and beam deflection [Yamada96], piezoelectric microstructures [Sones02], and electro-optic Bragg gratings [Risk94]. Many applications would benefit from new fabrication techniques to overcome limitations of current methods. For example, most common fabrication can achieve periods no smaller than several micrometres, preventing devices from realizing short-wavelength SHG, backward-propagating SHG (BSHG), and electro-optic Bragg reflection. Several domain periods required for linear and nonlinear functions of technological significance are listed in Table 1.1. Investigations into new techniques for

TABLE 1.1: A list of several domain periods required for QPM nonlinear frequency conversion or electro-optic reflection grating in LN.

Function	Input λ [nm]	Domain Period [µm]
OPO	1064	$\sim$30
SHG	1500	17.7
SHG	1064	6.8
SHG	800	2.6
SHG	600	0.95
BSHG	1064	0.17
Bragg Reflection	1500	0.34

domain inversion also reveal a greater understanding of the domain inversion process itself, and may assist in the optimization of such devices.

The objective of this work is to explore both the fabrication and application of micron to sub-micron ferroelectric domains to allow nonlinear optical phenomena not currently possible with larger-period devices. A simpler, more flexible technique for domain engineering is sought, with special focus on LN and LT as the nonlinear medium. These investigations have focused on two key directions, both involving the influence of light on the domain inversion process. The first method, referred to as all-optical poling (AOP), is the direct formation of inverted domains by irradiation with ultraviolet (UV) ns-pulsed light. The second method, referred to as light-assisted poling (LAP), is the formation of inverted domains by simultaneous application of a uniform external electric field and spatially-patterned optical field. These new poling methods are schematically compared to regular EFP in Figure 1.1.

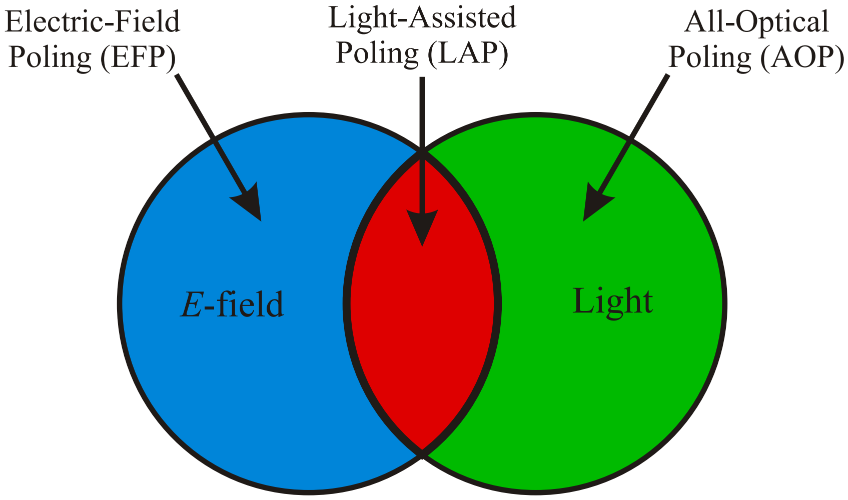

FIGURE 1.1: Relationship between the poling schemes of electric-field poling, all-optical poling, and light-assisted poling.

This thesis begins with an introduction into the background information in Chapter 2. This firstly includes an outline of second-order nonlinear frequency conversion and more specifically, SHG and QPM. Secondly, the field of ferroelectrics is introduced, with special focus on the material most extensively studied throughout this research, which was nominally-pure and doped LN crystals. Lithium tantalate is also compared, having many similar characteristics.

A review of domain engineering is presented in Chapter 3, including details of relevant previous research, current corroborating observations made during this research, and new measurements on the specific materials under test. Special attention is paid towards EFP and the kinetics of domain inversion. The influence of light on poling is very important to the remaining chapters, and therefore prior and current publications are detailed here.

The UV-light-induced surface modification of LN is presented in Chapter 4. The illumination of the $-z$ face of LN by UV ns-pulsed light with fluences under the ablation threshold has previously been observed to produce etch frustration. The nature of these etch frustration features is revealed here as tiny isolated domains. These domains could be controlled by the fluence and illumination pattern, merging over areas of high intensity. These features have been visualized and re-oriented by scanning force microscopy (SFM) under collaboration with the group of Professor K. Buse at the University of Bonn, Germany. Results from this research have been published in [Sones05a].

The AOP of LN is presented in Chapter 5. In these investigations, the $+z$ face of LN was illuminated by UV ns-pulsed light with fluences near and above the ablation threshold, forming a self-organized pattern of nano-scale domain lines. An ordered alignment of domain lines could be achieved by illumination via a phase mask. SFM imaging verified the presence of the domains prior to etching, in collaboration with the group of Associate Professor V. Gopalan at Pennsylvania State University, USA. Results from this research have been published in [Valdivia05d; Wellington07], and were the topic of an invited presentation [Valdivia05c].

The LAP of LN and LT is presented in Chapter 6. Firstly, the influence of the intensity of continuous wave (cw) visible light on the electric field required for nucleation is investigated, and compared to prior research using cw UV light. Secondly, the influence of the peak intensity of fs-pulsed near-UV to near-IR light on the electric field required for nucleation is investigated. A comparison of cw and fs-pulsed light is made, and the kinetics and mechanisms of domain growth are discussed. Finally, latent-LAP is introduced wherein illumination with fs-pulsed light was followed by a delay and subsequent application of an electric field. Results from this research have been published in [Sones05b; Valdivia06], and were presented in [Valdivia05a; Valdivia05b].

Finally, Chapter 7 summarizes the results of this thesis, and presents future research directions. The appendix includes a list of papers and presentations published to date based on this research.

Bibliography

[Arizmendi04] L. Arizmendi, *Photonic applications of lithium niobate crystals.* Phys. Status Solidi A, 201(2), 253–283 (2004).

[Armstrong62] J. A. Armstrong, N. Bloembergen, J. Ducuing, and P. S. Pershan, *Interactions between light waves in a nonlinear dielectric.* Phys. Rev., 127(6), 1918–1939 (1962).

[Bloembergen65] N. Bloembergen, Nonlinear optics: A lecture note and reprint volume. Frontiers in Physics, W. A. Benjamin Inc., New York (1965).

[Busch35] G. Busch and P. Scherrer, *A new seignettoelectric substance.* Naturwiss., 23, 737 (1935).

[Franken61] P. A. Franken, A. E. Hill, C. W. Peters, and G. Weinreich, *Generation of optical harmonics.* Phys. Rev. Lett., 7(4), 118–120 (1961).

[Maiman60] T. H. Maiman, *Stimulated optical radiation in ruby.* Nature, 187(4736), 493–494 (1960).

[Matthias49] B. T. Matthias and J. P. Remeika, *Ferroelectricity in the ilmenite structure.* Phys. Rev., 76(12), 1886–1887 (1949).

[Risk94] W. P. Risk, S. D. Lau, and M. A. McCord, *Third-order guided-wave distributed Bragg reflectors fabricated by ion-exchange in* $KTiOPO_4$. IEEE Photon. Technol. Lett., 6(3), 406–408 (1994).

[Sones02] C. Sones, S. Mailis, V. Apostolopoulos, I. E. Barry, C. Gawith, P. G. R. Smith, and R. W. Eason, *Fabrication of piezoelectric micro-cantilevers in domain-engineered* $LiNbO_3$ *single crystals.* J. Micromech. Microeng., 12(1), 53–57 (2002).

[Sones05a] C. L. Sones, C. E. Valdivia, J. G. Scott, S. Mailis, R. W. Eason, D. A. Scrymgeour, V. Gopalan, T. Jungk, and E. Soergel, *Ultraviolet laser-induced sub-micron periodic domain formation in congruent undoped lithium niobate crystals.* Appl. Phys. B, 80(3), 341–344 (2005).

[Sones05b] C. L. Sones, M. C. Wengler, C. E. Valdivia, S. Mailis, R. W. Eason, and K. Buse, *Light-induced order-of-magnitude decrease in the electric field for domain nucleation in MgO-doped lithium niobate crystals.* Appl. Phys. Lett., 86(21), 212901 (2005).

[Stegeman85] G. I. Stegeman and C. T. Seaton, *Nonlinear integrated optics.* J. Appl. Phys., 58(12), R57–R78 (1985).

[Subbarao73] E. C. Subbarao, *Ferroelectric and antiferroelectric materials.* Ferroelectrics, 5(1), 267–280 (1973).

[Valasek21] J. Valasek, *Piezo-electric and allied phenomena in rochelle salt.* Phys. Rev., 17(4), 475–481 (1921).

[Valdivia05a] C. E. Valdivia, C. L. Sones, S. Mailis, R. W. Eason, M. C. Wengler, and K. Buse, *Visible-light-induced tenfold reduction of the electric field required for ferroelectric domain nucleation in MgO-doped lithium niobate.* In Conference on Lasers and Electro-Optics, CMW4, OSA, Baltimore, USA (2005).

[Valdivia05b] C. E. Valdivia, C. L. Sones, S. Mailis, J. D. Mills, and R. W. Eason, *Ultrashort-pulse optically-assisted domain engineering in lithium niobate.* In International Symposium on Micro- and Nano-Scale Domain Structuring in Ferroelectrics (ISDS), Ekaterinburg, Russia (2005).

[Valdivia05c] C. E. Valdivia, C. L. Sones, J. G. Scott, S. Mailis, R. W. Eason, D. A. Scrymgeour, V. Gopalan, and I. Clark, *Nano-scale ultraviolet laser-induced ferroelectric surface domains in lithium niobate*. In Conference on Lasers and Electro-Optics - Europe (invited), OSA, Munich, Germany (2005).

[Valdivia05d] C. E. Valdivia, C. L. Sones, J. G. Scott, S. Mailis, R. W. Eason, D. A. Scrymgeour, V. Gopalan, T. Jungk, E. Soergel, and I. Clark, *Nanoscale surface domain formation on the* $+z$ *face of lithium niobate by pulsed ultraviolet laser illumination*. Appl. Phys. Lett., 86(2), 022906 (2005).

[Valdivia06] C. E. Valdivia, C. L. Sones, S. Mailis, J. D. Mills, and R. W. Eason, *Ultrashort-pulse optically-assisted domain engineering in lithium niobate*. Ferroelectrics, 340, 75–82 (2006).

[Wellington07] I. T. Wellington, C. E. Valdivia, T. J. Sono, C. L. Sones, S. Mailis, and R. W. Eason, *Ordered nano-scale domains in lithium niobate single crystals via phase-mask assisted all-optical poling*. Appl. Surf. Sci., 253(9), 4215–4219 (2007).

[Yamada96] M. Yamada, M. Saitoh, and H. Ooki, *Electric-field induced cylindrical lens, switching and deflection devices composed of the inverted domains in* $LiNbO_3$ *crystals*. Appl. Phys. Lett., 69(24), 3659–3661 (1996).

Chapter 2

Background

2.1 Second-Order Nonlinear Interactions

In common interactions between light and matter, the processes can often be described by a linear model of the polarizability of the material,

$$P_i^{(1)}(\omega) = \varepsilon_0 \chi_{ij}^{(1)} E_j \tag{2.1}$$

where ω is the angular frequency of the optical field E, ε_0 is the permittivity of free space, and $\chi_{ij}^{(1)}$ is the linear susceptibility which describes the linear response of the material with refractive index n and absorption α. With high magnitude optical fields, a nonlinear material response must be accounted for. The nonlinear polarizability can be expressed as the power series [Boyd03],

$$P_i(\omega) = \varepsilon_0 \left[\chi_{ij}^{(1)} E_j + \chi_{ijk}^{(2)} E_j E_k + \chi_{ijkl}^{(3)} E_j E_k E_l + \cdots \right] \tag{2.2}$$

$$P = P^{(1)} + P^{(2)} + P^{(3)} + \cdots \tag{2.3}$$

where $\chi_{ijk}^{(2)}$ and $\chi_{ijkl}^{(3)}$ are the second- and third-order susceptibilities, respectively, and $P^{(m)}$ is the m-order polarizability. Even-ordered susceptibilities, $\chi^{(2m)}$ ($m \in \mathbb{Z}^+$), are non-zero only in non-centrosymmetric materials (i.e. materials that do not have a center of inversion symmetry). In most materials and applications, the nonlinear coefficients of significance are $\chi^{(2)}$ and $\chi^{(3)}$ due to the rapid decrease in magnitudes of each successive nonlinear polarizability coefficient.

A tensor of nonlinear optical coefficients, d_{ijk}, is typically used in place of the second-order nonlinear susceptibility, $\chi^{(2)}$, according to the relation [Boyd03],

$$d_{ijk} = \frac{1}{2}\chi_{ijk}^{(2)} \tag{2.4}$$

The d tensor can be described by a contracted notation, where d_{ijk} is expressed using two indices d_{il}, with l defined as follows:

$$\begin{array}{rcccccc} jk: & 11 & 22 & 33 & 23,32 & 31,13 & 12,21 \\ l: & 1 & 2 & 3 & 4 & 5 & 6 \end{array} \tag{2.5}$$

permitting the convenient rearrangement of the third-order tensor into a 3×6 two-dimensional matrix.

Second-order nonlinear interactions form several related processes involving three-wave mixing. One such example is the linear electro-optic effect, also known as the Pockels effect, where a DC or low frequency E-field alters the refractive index in the optical regime. The nonlinear tensor can be related to the electro-optic coefficients, r_{ijk}, by the relation [Kirkby02b],

$$d_{ijk} = -\frac{1}{4}(n_i n_j)^2 r_{kji} \tag{2.6}$$

where n_i and n_j are the refractive indices at the optical frequency along the appropriate crystal directions. Other effects include optical rectification (generation of a DC E-field), second harmonic generation (SHG), difference frequency generation (DFG), sum frequency generation (SFG), and optical parametric generation (OPG). For example, in SHG, the polarizability of a material is described by the following relation [Boyd03],

$$\begin{bmatrix} P_x(2\omega) \\ P_y(2\omega) \\ P_z(2\omega) \end{bmatrix} = 2\varepsilon_0 \begin{bmatrix} d_{11} & d_{12} & d_{13} & d_{14} & d_{15} & d_{16} \\ d_{21} & d_{22} & d_{23} & d_{24} & d_{25} & d_{26} \\ d_{31} & d_{32} & d_{33} & d_{34} & d_{35} & d_{36} \end{bmatrix} \begin{bmatrix} E_x^2(\omega) \\ E_y^2(\omega) \\ E_z^2(\omega) \\ 2E_y(\omega)E_z(\omega) \\ 2E_x(\omega)E_z(\omega) \\ 2E_x(\omega)E_y(\omega) \end{bmatrix} \tag{2.7}$$

using the contracted notation. A second-harmonic wave is generated due to the accelerated charges forming the polarization. All of the above effects involve frequency conversion as a result of the time-varying nonlinear polarization.

2.1.1 Frequency Conversion

The second-order nonlinear polarization results in parametric processes between three waves within a nonlinear material, leading to an optical response with additional frequency components. These can be divided into three types of interactions: SFG, DFG, and OPG. Therefore, an oscillating wave can generate waves at harmonics of the fundamental angular frequency ω, and the interaction of two optical waves, $\omega_1 > \omega_2$, can generate the sum and difference frequencies, $(\omega_1 + \omega_2)$ and $(\omega_1 - \omega_2)$, respectively. Each interaction is constrained by the requirement for conservation of both energy and momentum.

SFG is the process whereby two input optical waves, ω_1 and ω_2, generate a third optical wave at the sum frequency. By energy conservation,

$$\hbar\omega_1 + \hbar\omega_2 = \hbar\omega_3 \tag{2.8}$$

$$\omega_1 + \omega_2 = \omega_3 \tag{2.9}$$

where ω_1 and ω_2 are the angular frequencies of the input optical waves, ω_3 is the angular frequency of the output optical wave, $\hbar = h/2\pi$, and h is Planck's constant. Therefore, the generated wave oscillates at the sum of the input frequencies. A special case of SFG is SHG, in which the input waves are degenerate; i.e. both oscillate with the same frequency $\omega = \omega_1 = \omega_2$. Then by the same argument,

$$\omega + \omega = 2\omega \tag{2.10}$$

generating an optical wave at the second-harmonic of the fundamental input wave. The input need not be strictly two separate beams, but can be a single wave from which two photons are mixed to form another at twice the frequency.

Similarly, DFG involves the input of two optical waves to generate a third, but in this case at a lower frequency. Following the same energy conservation equation as SFG (2.8), the frequencies involved are related by,

$$\omega_3 - \omega_2 = \omega_1 \tag{2.11}$$

where ω_3 and ω_2 are input waves generating ω_1.

In contrast, OPG involves the input of a single wave, often referred to as the pump ($\omega_p = \omega_3$), generating two lower frequency waves, the signal ($\omega_s = \omega_1$) and idler waves ($\omega_i = \omega_2$),

$$\omega_p = \omega_s + \omega_i \tag{2.12}$$

This process is utilized in the optical parametric amplifier (OPA) of the femtosecond laser system used extensively in Chapter 6.

As mentioned above, nonlinear interactions must also obey conservation of momentum. Considering the case of SFG in particular, the processes are further constrained by,

$$\hbar k_1 + \hbar k_2 = \hbar k_3 \tag{2.13}$$

$$\Delta k = k_3 - k_2 - k_1 = 0 \tag{2.14}$$

which relate the propagation constants, $k_j = 2\pi n_j/\lambda_j = n_j\omega_j/c$, of the input and output waves. In non-dispersive media, this places the same constraint on the waves as the requirements of energy conservation. However, in real materials with dispersion, (2.14) becomes,

$$\Delta k = \frac{2\pi n_3}{\lambda_3} - \frac{2\pi n_2}{\lambda_2} - \frac{2\pi n_1}{\lambda_1} = 0 \tag{2.15}$$

$$\Delta k = \frac{n_3 \omega_3}{c} - \frac{n_2 \omega_2}{c} - \frac{n_1 \omega_1}{c} = 0 \tag{2.16}$$

where n_j is the refractive index at ω_j, and Δk is referred to as the *phase mismatch*, or more accurately as the *wave vector mismatch*.

Equations 2.15 and 2.16 describe a condition of *perfect phase matching* ($\Delta k = 0$) which would occur in non-dispersive media or in the rare coincidence where refractive indices happen to follow this relation.

In general however, $\Delta k \neq 0$, resulting in a phase mismatch between the input and output waves and a *non-phase-matched* interaction. The distance over which a relative π phase shift is experienced between the input and output waves is called the *coherence length* ℓ_c [Fejer92],

$$\Delta k = \frac{2\pi n_3}{\lambda_3} - \frac{2\pi n_2}{\lambda_2} - \frac{2\pi n_1}{\lambda_1} = \frac{\pi}{\ell_c} \tag{2.17}$$

$$\frac{n_3}{\lambda_3} - \frac{n_2}{\lambda_2} - \frac{n_1}{\lambda_1} = \frac{1}{2\ell_c} \tag{2.18}$$

From energy conservation considerations of (2.8),

$$\frac{1}{\lambda_3} = \frac{1}{\lambda_2} + \frac{1}{\lambda_1} \tag{2.19}$$

Putting this relation into (2.18) and solving for the coherence length in terms of the input waves,

$$\ell_c = \frac{1}{2} \frac{\lambda_1 \lambda_2}{(n_3 - n_2)\lambda_1 + (n_3 - n_1)\lambda_2} \tag{2.20}$$

In the case of SHG, the fundamental wavelength $\lambda_f = \lambda_1 = \lambda_2$ propagates with a refractive index $n_f = n_1 = n_2$, and the second-harmonic wave at $\lambda_s = \lambda_3$ propagates with $n_s = n_3$, and therefore the equation governing the coherence length reduces to,

$$\ell_c = \frac{\lambda_f}{4(n_s - n_f)} \tag{2.21}$$

From these relations, a medium with greater dispersion exhibits a shorter coherence length. The dispersion curves are well known for many materials and therefore the coherence length can be calculated via the appropriate Sellmeier equations.

The efficiency of frequency conversion relies on the overlap of high intensity waves over a long interaction length. Therefore an optimum focusing condition exists in a crystal, and is closely approximated by confocal focusing where twice the Rayleigh range is set equal to crystal length, and the beam waist is positioned in the centre of the crystal [Boyd68]. Assuming no pump depletion, the SHG conversion efficiency follows the relation [Miller98],

$$\eta_{\mathrm{SHG}} = \frac{P_{2\omega}}{P_\omega} = 16\pi^2 \frac{d_{\mathrm{eff}}^2 Z_0}{n_\omega n_{2\omega} \lambda_f^3} L P_\omega \mathrm{sinc}^2(\Delta k L/2) \tag{2.22}$$

where P_ω and $P_{2\omega}$ are the powers at frequency ω and 2ω, respectively, d_{eff} is the effective nonlinear coefficient, n_ω and $n_{2\omega}$ are the refractive indices, λ_f is the wavelength of the fundamental wave, Δk is the wavevector mismatch, $k = \omega n_\omega / c = 2\pi n_\omega / \lambda$ is the magnitude of the wavevector, L is the interaction length, $Z_0 = \sqrt{\mu_0/\varepsilon_0}$ is the impedance of free space, and μ_0 and ε_0 are the permeability and permitivity of free space, respectively. The efficiency of a device is often quoted as %/W, calculated by dividing both sides of (2.22) by P_ω, eliminating it from the right side of the equation.

2.1.2 Birefringent Phase Matching

As introduced above, phase matching is necessary to achieve significant and controllable nonlinear interactions. However, all real materials suffer from the problem of dispersion, and therefore special care must be taken to satisfy this parameter.

Birefringent phase matching is an instance of perfect phase matching whereby the dispersion is compensated completely by the birefringence by choosing specific polarization vectors in the crystal. Birefringent phase matching is only successful in certain crystals where the birefringence is large enough to offset the dispersion, and then only within a range of wavelengths. Byer reported that out of 22000 crystals studied, birefringence sufficient for phase-matching was present in less than 100 [Byer97].

The use of birefringence, by definition, requires that one of the three waves propagate with an orthogonal polarization vector, assuming colinear waves. Type I birefringent phase-matching refers to the case where both input waves have parallel polarization vectors, while Type II birefringent phase-matching refers to the case where the input waves have orthogonal polarization vectors. Typically the polarization vectors do not provide access to the largest nonlinear coefficients, as cross-terms of the $\chi^{(2)}$ tensor are in general not as large as the diagonal terms. This forces the use of other coefficients which can be significantly smaller than the maximum value available in the crystal. Crystals must also be specially cut and polished to enable optimum access to the polarization vectors required in the material. However, temperature-tuning of the phase-matched wavelengths is still possible over a limited range determined by the temperature-dependent refractive indices of the material.

Birefringent phase matching utilizes one wave with ordinary polarization ($n_1 = n_o$) and the second polarized perpendicularly (n_2). To achieve phase-matching [i.e. $n_2(2\omega) = n_1(\omega)$], the propagation angle θ between the k-vector and the optical axis must be controlled according to the relation [Boyd03],

$$\frac{1}{n_2^2(\theta)} = \frac{\sin^2\theta}{n_e^2} + \frac{\cos^2\theta}{n_o^2} \tag{2.23}$$

where n_o and n_e are the ordinary and extraordinary refractive indices, respectively. The birefringent phase matching angle for SHG becomes,

$$\sin^2\theta = \frac{\left(\dfrac{1}{n_o^2(\omega)} - \dfrac{1}{n_o^2(2\omega)}\right)}{\left(\dfrac{1}{n_e^2(2\omega)} - \dfrac{1}{n_o^2(2\omega)}\right)} \tag{2.24}$$

although in general there is not a guaranteed solution for θ, and requires birefringence sufficient to compensate the dispersion. Where a solution exists, the nonlinear interaction experiences an effective nonlinearity, d_{eff}, due to the walk-off angle [Dmitriev99],

$$\rho(\theta) = \arctan[(n_o/n_e)^2 \tan\theta] - \theta \tag{2.25}$$

for a negative uniaxial crystal. The resulting d_{eff} for a negative uniaxial 3m crystal is [Boyd03],

$$\text{Type I: } d_{\text{eff}} = d_{31}\sin\theta - d_{22}\cos\theta\sin(3\phi) \tag{2.26}$$

$$\text{Type II: } d_{\text{eff}} = d_{22}\cos^2\theta\cos(3\phi) \tag{2.27}$$

where ϕ is the azimuthal angle between the propagation direction and xz plane.

2.1.3 Quasi-Phase Matching

Quasi-phase-matching (QPM) is an alternative technique to phase-match nonlinear interactions [Armstrong62]. The advantage of this method is that it does not rely on birefringence, thus freeing the design of a device to use the maximum nonlinear coefficient whilst extending the range of phase-matchable wavelengths to include the entire transparent region. Instead of birefringence, this technique requires that the material can be engineered to invert the sign of the nonlinear coefficient, $\chi^{(2)}$. An overview of quasi-phase-matching (QPM) is provided in [Byer97].

Since birefringence is not a pre-requisite of QPM, the phase-mismatch $\Delta k \neq 0$ of (2.14) must be nullified by other means. Without phase-matching, energy flows from the input waves into the output waves until they experience a relative π phase shift between them at a distance of one coherence length ℓ_c (2.17). After this distance, the energy flows back from the output waves to the input waves over the next ℓ_c. This process repeats along the length of the nonlinear material, preventing a significant magnitude of the generated waves from ever accumulating. If, however, the sign of the nonlinear coefficient, $\chi^{(2)}$, could be alternated every coherence length, then the phase-mismatch

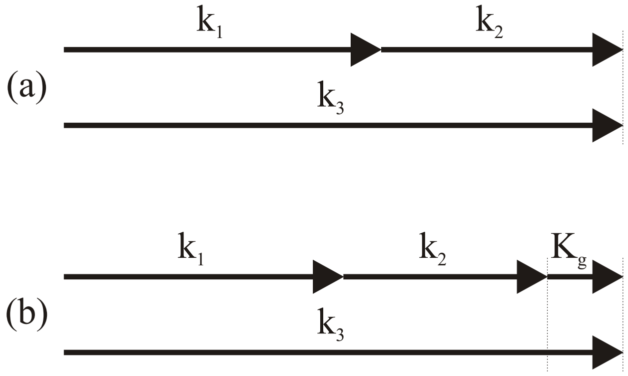

Figure 2.1: Phase matching vector diagram, showing the conditions of (a) perfect phase matching (as in birefringent phase matching) and (b) quasi-phase-matching.

could be periodically reset, allowing the build-up of the magnitude of the generated wave. Because the phases of the waves are not perfectly matched throughout the material, this technique is referred to as *quasi*-phase-matching.

The alternating sign of $\chi^{(2)}$ for QPM introduces into the material a grating vector $K_g = 2\pi m/\Lambda_g$, where $\Lambda_g = 2\ell_c$ is the fundamental period and m is the grating order. Therefore, the phase-matching condition becomes,

$$k_3 = k_2 + k_1 + K_g \tag{2.28}$$

$$\Delta k = k_3 - k_2 - k_1 - \frac{2\pi m}{\Lambda_g} = 0 \tag{2.29}$$

This condition is described graphically in Figure 2.1.

As implied by the above definition of K_g, higher order gratings ($m > 1$) are also effective in QPM. Higher order gratings are desirable where small periods are technically difficult to fabricate. The trade-off for this benefit is that QPM is inherently less efficient than perfect phase matching by the factor,

$$\frac{\eta_{\text{QPM}}}{\eta_{\text{PPM}}} = \frac{1}{m^2}\frac{4}{\pi^2} \tag{2.30}$$

where m is the order of QPM, and η_{QPM} and η_{PPM} are efficiencies of QPM and perfect phase matching, respectively. Therefore, higher order QPM is less efficient, diminishing as $1/m^2$. A comparison to non-phase matched and perfectly phase matched interactions is shown in Figure 2.2, where the intensity of the generated wave is plotted versus length of the nonlinear interaction. First-order QPM builds-up the intensity of the generated wave monotonically, inverting the sign of $\chi^{(2)}$ at every coherence length. Higher-order QPM, instead, allows the intensity to oscillate across m coherence lengths before permanently increasing.

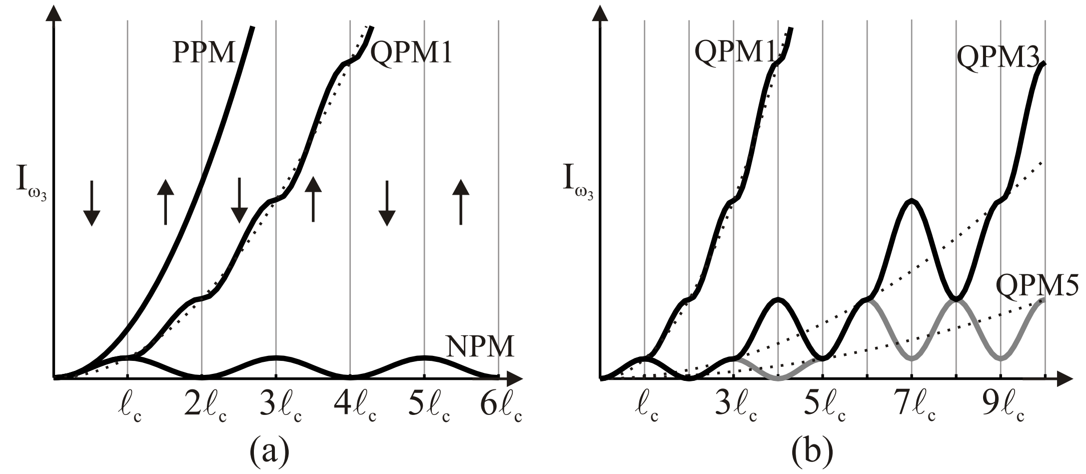

FIGURE 2.2: Comparison of relative phase-matching efficiencies for no phase-matching (NPM), perfect phase-matching (PPM), and 1st order (QPM1), 3rd order (QPM3), and 5th order (QPM5) quasi-phase-matching. The arrows indicate the direction of the spontaneous polarization, or the sign of $\chi^{(2)}$. The dotted lines represent a factor of $(2/m\pi)^2$ reduction in efficiency from perfect phase matching for each order, m. The plot in (a) is after [Byer97].

However, this reduction in efficiency is compensated by the freedom to use the maximum nonlinear coefficient of the crystal, which can often provide a far greater nonlinear interaction than birefringent phase-matching. For example, Webjörn *et al.* estimated that first-order QPM was $(d_{33}/d_{31})^2(2/\pi)^2 \simeq 20$ times more efficient than birefringent phase-matching in lithium niobate [Webjörn89]. QPM also allows the engineering of the crystal for operation at the design wavelength, which in principle is limited only by the absorption of the material. In practice, the design of suitable QPM gratings may also be limited by the size scales over which the material must be engineered, which is reduced in highly dispersive media.

Figure 2.2 also implies that the size of each region of inverted $\chi^{(2)}$ is very important in determining the efficiency of nonlinear interactions. This is quantitatively clear from Fourier analysis of the periodically modulated material, where the second-order nonlinear coefficient can be described by [Byer97],

$$d(x) = d_{\text{eff}} \sum_{m=-\infty}^{\infty} \tfrac{2}{m\pi} \sin(m\pi D) e^{(-iK_m x)} \tag{2.31}$$

where d_{eff} is the effective nonlinear coefficient for the propagating wave, $K_m = 2\pi m/\Lambda_g$ is the magnitude of the grating vector for the mth Fourier component, $D = l/\Lambda_g$ is the duty cycle with a domain inverted region of the length l, and x is the distance parallel to the grating vector. From this relation, the effective nonlinear coefficient for the mth Fourier component is,

$$d_m = (2/m\pi)\sin(m\pi D) d_{\text{eff}} \tag{2.32}$$

which attains a maximum magnitude for $D = (2a+1)/(2m) < 1$ for $a \in \mathbb{Z}^*$. For QPM of odd-order ($m = 1, 3, 5, \ldots$), an optimum duty cycle is $D = 1/2$. For QPM of even-order ($m = 2, 4, 6, \ldots$), an optimum duty cycle is $D = 1/2m$, which is 1/4 for $m = 2$. Therefore, the efficiency of a QPM device can be calculated similarly to (2.22), and is given by [Miller98],

$$\eta_{\mathrm{QPM}} = \frac{P_{2\omega}}{P_\omega} = 16\pi^2 \frac{d_m^2 Z_0}{n_\omega n_{2\omega} \lambda_f^3} L P_\omega \mathrm{sinc}^2(\Delta k_Q L/2) \tag{2.33}$$

where $\Delta k_Q = \Delta k - K_m$ is the QPM phase-mismatch.

Materials can be engineered to provide QPM gratings in both one- and two-dimensions, often referred to as periodically poled crystals and nonlinear photonic crystals, respectively.

2.1.3.1 1D QPM: Periodically Poled Crystal

When Armstrong *et al.* first proposed the idea of introducing a relative π phase correction to the interacting waves every coherence length (i.e. QPM), several one-dimensional methods to obtain this were also suggested [Armstrong62]. A first method was to reflect the waves after traveling a coherence length, where they will undergo a relative π phase shift. This has since been modified to include *modal phase matching*, where the structure of a waveguide has been constructed such that material dispersion is compensated by waveguide modal dispersion [Anderson71], conceptually similar to the idea of multiple reflections. Secondly, resonant cavities, such as Fabry-Pérot interferometers, could be used to bring the waves back into phase while increasing the effective interaction length. The third method was to pass the waves through a dispersive linear medium, compensating for the phase-mismatch of the nonlinear medium. The final, more efficient modification of the previous method would be to pass the waves through a second nonlinear medium where the orientation of the nonlinearity had been inverted, and then repeat this for each coherence length.

The most commonly used method of forming one-dimensional QPM nonlinear interactions is a further modification of this latter proposed method, where separate crystals are not brought together, but rather the nonlinear coefficient of a single crystal is periodically inverted. This can be either done during crystal growth [Feng80] or after crystal growth, by twinning of GaAs [Gordon93; Wu98] or quartz [Yamada06], for example. Other methods of forming QPM gratings in nonlinear ferroelectric crystals after growth are discussed in Section 3.2. Two instances of such materials are periodically-poled lithium niobate (PPLN) and periodically-poled lithium tantalate (PPLT) which are commercially and technologically important examples of one-dimensional periodically poled crystals, discussed in greater detail in Section 3.3.1. PPLN and PPLT have demonstrated a great versatility in the range of wavelengths that can be quasi-phase-matched, including UV [Meyn01], visible [Yamada93], near- to mid-infrared [Yi06], and THz-waves [LHuillier07a; LHuillier07b].

2.1.3.2 2D QPM: Nonlinear Photonic Crystal

Nonlinear photonic crystals (NPC) are the generalization of the periodically poled crystal into two dimensions, first proposed in [Berger98]. This is analogous to the extension of the quarter-wave stack [one-dimensional *linear* photonic crystal (PC)] to the two-dimensional planar PC.

Whereas a one-dimensional QPM structure is composed of laminar plates of materials with $\chi^{(2)}$ of opposite sign, a two-dimensional QPM structure is composed of a periodic lattice in a plane. In general, the lattice could be composed of arbitrary shapes located centrally on a periodic grid. Analysis of this structure reveals that the grating vector K_g of the one-dimensional case is replaced by a two-dimensional reciprocal lattice vector G. Intuitively, different propagation vectors will experience different crystal periods and nonlinear generation will not necessarily be colinear with the input waves.

The fabrication of NPC has been demonstrated in LN, forming hexagons on a hexagonal grid, creating so-called hexagonally-poled lithium niobate (HexLN) [Broderick00]. In this material, 2nd-, 3rd-, and 4th-harmonic generation from an input wave of $\lambda = 1536$ nm was demonstrated [Broderick02]. Finally a quasi-crystal of hexagons in a two-dimensional NPC was also demonstrated in LN [Bratfalean05].

2.2 Ferroelectrics

Ferroelectricity is a relatively newly-discovered phenomenon [Valasek21], in use in a variety of applications that exploit their wide range of physical properties. Of the 32 point group crystal classes, 21 are non-centrosymmetric which means that the behavior of these crystals depend upon the *orientation* of an applied field. All but one of these crystal classes are piezoelectric, producing an electric field when stressed, and producing stress when in the presence of an electric field. Ten of these classes are pyroelectric, which display a temperature-dependent spontaneous polarization, P_s, along a unique polar axis in the absence of an external electric field. Ferroelectric crystals are a subgroup of the pyroelectric crystals which possess multiple states of orientation which can be switched between when subjected to an electric field. The study of ferroelectrics is reviewed in [Mitsui76] and [Lines77].

A crystal is in its *ferroelectric phase* when $T < T_c$, known as the Curie temperature. As the temperature is raised toward this point, P_s decreases until it vanishes at $T = T_c$.

Above this temperature, the crystal is in its *paraelectric phase* where it has randomly oriented electric dipoles which can align with an external electric field, but no longer exhibits a spontaneous polarization.

2.2.1 Lithium Niobate

Lithium niobate, $LiNbO_3$ (LN), is an artificial negative uniaxial, non-centrosymmetric, ferroelectric crystal exhibiting a three-fold rotational symmetry about its z axis, which is both the polar axis and optic axis. With two stable anti-parallel ferroelectric states, the built-in spontaneous polarization, $P_s = {\sim}75$ µC/cm^2, can be reversed by the external application of an electric field above the coercive field, E_c. This material is widely studied for its broad range of properties and applications. Its structure and basic properties have been summarized by Weis and Gaylord [Weis85], and more recently a collection of reviews has been edited by Wong [Wong02].

The Czochralski growth method was first applied to the fabrication of LN in [Ballman65; Nassau66a]. This technique, commonly used to grow materials such as silicon and gallium arsenide, begins with a seed crystal attached to a rotating rod. The seed is dipped into a platinum crucible containing a melt of high-purity compounds, Li_2O and Nb_2O_5, held just above the melting temperature of the target material. The seed initiates new crystal growth as it is withdrawn from the melt, and slowly cools by heat conduction through the rod. Using an electric field during growth forces mono-domain crystal formation [Nassau66b]. Presently, the Czochralski method is the preferred technique for the fabrication of bulk single crystal LN. All discussion of LN herein refers to single-crystal optical-grade material, unless otherwise stated.

Important parameters of LN include its stoichiometry, crystal structure, defects, and optical and electrical properties, discussed in further detail below. An overview of general properties of LN and its isomorph, lithium tantalate, $LiTaO_3$ (LT), for both congruent and stoichiometric compositions is presented in Table 2.1.

2.2.1.1 Stoichiometry

Lithium niobate can be grown in a range of compositions. The composition exactly matching its chemical compound symbol, $LiNbO_3$, having a ratio of [Li]:[Nb]:[O] of 1:1:3, is referred to as *stoichiometric* lithium niobate (SLN). However, a Li deficiency incorporates into the crystal even in melts with greater than 50% Li_2O, making growth of the stoichiometric composition technically challenging. More common and technically simpler to grow is the *congruently melting* composition, hereafter referred to simply as *congruent* lithium niobate (CLN). The advantage of this composition is that both the

TABLE 2.1: Comparison of the physical, electrical, and optical properties of congruent and stoichiometric lithium niobate and lithium tantalate.

Material:	CLN	SLN	CLT	SLT
Li [mol%] [b]	48.5	49.9	48.5	49.95
Melting Point [°C] [a]	1253	-	1650	-
Curie Point, T_c [°C] [b]	1145	1200	600	690
Density [kg/m^3] [a]	4647	-	7465	-
Transparency [nm] [b]	325–5500	305–5500	290–5500	270–5500
ODT (cw) [kW/cm^2]	$\sim$10 [a]	1000 [b]	$\sim$10 [b]	1000 [b]
E_c [kV/mm] [b]	22	4	22	1.7
Lattice Constant [Å] [b]				
a	5.150	5.148	5.154	5.151
c	13.864	13.857	13.781	13.773
Piezoelectric Coefficients [pC/N] [c]				
$d_{p(15)}$	68	-	26	-
$d_{p(22)}$	21	-	7	-
$d_{p(31)}$	-1	-	-2	-
$d_{p(33)}$	6.2	-	8	-
Dielectric Constant [a]				
$\epsilon_{11}^{\mathrm{T}}$	85.2	-	53.6	-
$\epsilon_{33}^{\mathrm{T}}$	28.7	-	43.4	-
Refractive Index (λ = 633 nm) [b]				
n_o	2.2868	2.2865	2.1768	2.1770
n_e	2.2028	2.1898	2.1821	2.1745
Electro-Optic Coefficients (λ = 632.8 nm) [pm/V] [a,b]				
r_{13}	10	10.4	8	8.1
r_{22}	6.8	-	-	-
r_{33}	31.5	38.3	32.2	35.5
Nonlinear Optical Coefficients (λ = 1064 nm) [pm/V] [b]				
d_{31}	6.1	6.3	2.3	2.5
d_{22}	2.5	-	1.7	-
d_{33}	34.1	44.3	26.2	30.4

[a] Data from Yamaju Ceramics Ltd. (http://www.yamajuceramics.co.jp)

[b] Data from Oxide Corporation (http://www.opt-oxide.com)

[c] [Yue03]

solid and liquid phase co-exist at this ratio [Abrahams02],

$$\frac{[\mathrm{Li}]}{[\mathrm{Li}]+[\mathrm{Nb}]} = 0.4845 \qquad \text{or} \qquad 1 > \frac{[\mathrm{Li}]}{[\mathrm{Nb}]} = 0.942 \tag{2.34}$$

The majority of commercially available LN is of congruent composition, and has been most widely studied.

Due to several undesirable properties of CLN, such as the inherent high defect concentration caused by its Li deficiency, stoichiometric compositions have also been investigated and grown by several modified techniques. One important method is the double-crucible Czochralski method [Kitamura97] where the melt is divided into two chambers. The inner crucible, from which the seed is pulled, is maintained Li-rich. The outer crucible, which feeds the inner crucible, is maintained at a stoichiometric composition by continually supplying powder at a rate that compensates for the crystal growth rate. Another method of obtaining stoichiometric compositions is vapor transport equilibration (VTE) [Jundt90; Katz04] where a CLN crystal is heated in a closed crucible with a Li-rich powder, Li_3NbO_4. Vapor transport and diffusion increases the composition of the crystal to the phase boundary of ~49.9-mol% Li_2O. The Curie temperature can be measured to determine the Li content of a crystal, as it reliably increases from $T_c = 1410$ K to 1470 K as the Li content increases from congruent to stoichiometric compositions. However, precisely stoichiometric material has not yet been achieved, so all these materials are more accurately classified as "near-stoichiometric" which must be understood whenever a "stoichiometric" material is referred to herein and in the literature.

Nonetheless, these materials do approach the stoichiometric limit in many of the desirable material properties. One such material parameter that changes with composition is the coercive field (electric field required for domain inversion, discussed further in Section 3.2), which decreases from ~22 kV/mm in congruent material to ~3 kV mm^{-1} in near-stoichiometric material [Bermúdez00]. An increasing Li content decreases the ultraviolet (UV) absorption edge [Furukawa98], increases the photoconductivity and reduces the saturated space charge field [Jazbinšek02], reducing photorefractive damage [Katz04].

2.2.1.2 Structure and Defects

LN is a uniaxial crystal of the trigonal crystal system and 3m point group. It belongs to the *perovskite* structural family, so-called for the mineral of the same name, $CaTiO_3$. The ideal structure of the perovskite is an XYZ_3 composition that can be viewed as a cubic closed packed arrangement of Z atom layers [Bhalla00]. However, unlike the perfect perovskite structure, Li^+ and Nb^{5+} have similar ionic radii and hence result in a *distorted perovskite* [Schirmer91]. The regular and distorted perovskite structures are compared in Figure 2.3, after [Niizeki67].

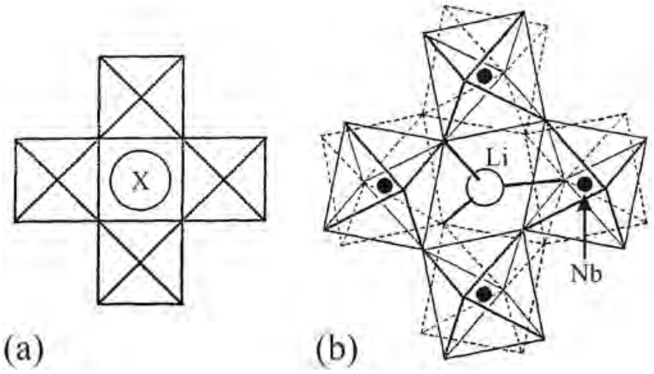

Figure 2.3: Comparison of the (a) regular perovskite structure to the (b) distorted perovskite structure of LN, after [Niizeki67].

The structure of LN can be divided into either hexagonal unit cells containing six formula units per cell, or a rhombohedral unit cell containing two formula units per cell. This structure can be visualized as a hexagonal close-packed configuration forming oxygen octahedra. In the ideal stoichiometric composition, the centres of these octahedra are filled one-third by each of lithium ions, niobium ions, and vacancies (V). However, the Li^+—O^{2-} bond is weaker than the Nb^{5+}—O^{2-} bond [Schirmer91], and hence demonstrates a growth away from stoichiometry, and a tendency towards the congruent composition of (2.34).

Above its Curie point, LN is in its paraelectric phase. In this phase, the Nb atoms are centered between oxygen planes, whereas the Li atoms lie either slightly above or slightly below an oxygen layer, with the average position being planar with the oxygen. This configuration results in the non-polar paraelectric phase of the crystal.

Below its Curie point, LN is in its ferroelectric phase. The crystal maintains the same structure of oxygen atoms, but the positions of both the Nb and Li are different. Looking along the +z direction of the crystal, the oxygen octahedral interstices are filled in the order of {Nb, V, Li, Nb, V, Li, ...}. Both the Nb and Li atoms are displaced slightly from their paraelectric positions along the +z direction, shown in Figure 2.4. The spontaneous polarization, P_s, inherent in this ferroelectric phase is a result of the charge separation from this repositioning of ions.

Due to the Li deficiency inherent in the congruent composition of LN, a high level of intrinsic defects is present, commonly referred to as *non-stoichiometric defects.* There is some disagreement in the literature as to the precise nature of this defect structure. For example, Kim *et al.* analyze a chemical formula of $[\mathrm{Li}_{0.95}\mathrm{V}_{0.04}\mathrm{Nb}_{0.01}]_{\mathrm{Li}}\mathrm{NbO}_3$ in which Nb occupies some of the Li sites ($\mathrm{Nb}_{\mathrm{Li}}$), and is surrounded by vacancies (V) on Li sites (V_{Li}) required for charge neutrality, forming a defect dipole [Kim01]. On the other hand, Abrahams and Marsh infer a chemical formula of $[\mathrm{Li}_{1-5x}\mathrm{Nb}_{5x}]_{\mathrm{Li}}[\mathrm{Nb}_{1-4x}\mathrm{V}_{4x}]_{\mathrm{Nb}}\mathrm{O}_3$ with $x \simeq 0.0118$, in which Nb occupies some of the Li sites, and some of the Nb sites are vacant

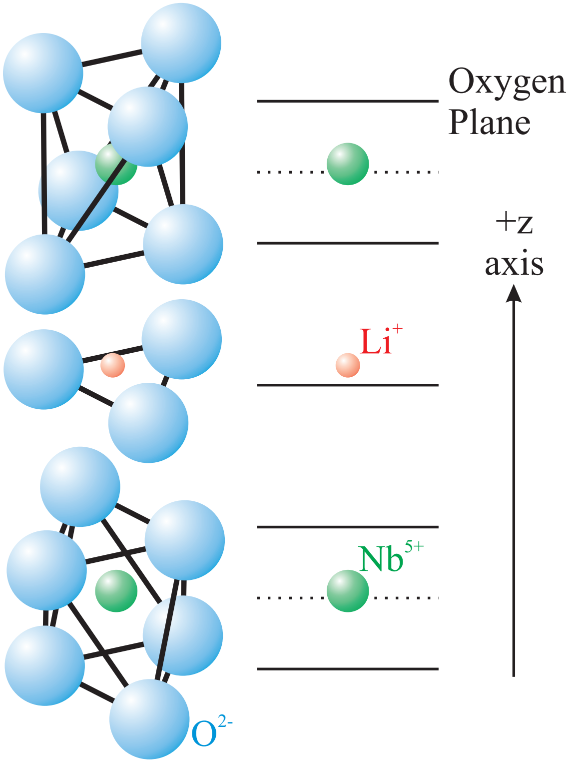

FIGURE 2.4: Schematic of the structure of lithium niobate in the ferroelectric phase ($T < T_c$), after [Weis85]. In the paraelectric phase, Li moves down to the oxygen plane (on average) and Nb is centered between oxygen planes (dotted lines).

(V_{Nb}) [Abrahams86]. A comparison of Curie temperatures relating to defect models with either Li- or Nb-vacancies suggested that the Li-vacancy model best described the defect structure qualitatively and quantitatively [Masaif03]. Other defect models have also been proposed, such as both Li- and Nb-vacancies simultaneously [Abdi06]. Despite these differing models, it is commonly accepted that the anti-site defect, Nb on a lithium site, $\mathrm{Nb}_{\mathrm{Li}}^{4+}$, plays an important role in non-stoichiometric defects [Schirmer91].

2.2.1.3 Optical and Electrical Properties

Lithium niobate is host to a variety of properties that make it a highly studied material for many application areas. The most basic optical property is the refractive index which, due to its uniaxial character, can be described by n_o and n_e, the refractive indices for a polarization vector along the ordinary (x,y) and extraordinary (z) crystalline directions. The dispersion curve is well-established in LN, and is specified by its Sellmeier equations, fitting the refractive index across its transparency window for a range of temperatures and several Li concentrations. In undoped CLN, the Sellmeier equation of [Kirkby02a] is

$$n^2(\lambda, T) = a_1 + \frac{a_2 + b_1 f(T)}{\lambda^2 - (a_3 + b_2 f(T))^2} + b_3 F(T) + a_4 \lambda^2 \tag{2.35}$$

TABLE 2.2: Sellmeier coefficients a_i and b_i for both ordinary, n_o, and extraordinary, n_e, refractive indices in undoped CLN, from [Kirkby02a].

Coef.	n_o	n_e
a_1	4.9048	4.5820
a_2	1.1775×10^5	0.9921×10^5
a_3	2.1802×10^2	2.1090×10^2
a_4	-2.7153×10^{-8}	-2.1940×10^{-8}
b_1	2.2314×10^{-2}	5.2716×10^{-2}
b_2	-2.9671×10^{-5}	-4.9143×10^{-5}
b_3	2.1429×10^{-8}	2.2971×10^{-8}

$$f(T) = (T - 24.5)(T + 570.5) \tag{2.36}$$

where T is the temperature (°C), λ is the free-space wavelength (nm), and a_i and b_i are the Sellmeier coefficients, listed in Table 2.2.

The temperature-dependent refractive indices of undoped CLN can be determined for wavelengths down to 400 nm using the Sellmeier equations of [Kirkby02a], with refractive indices also specified for selected wavelengths down to 124 nm. Room temperature refractive indices of 5-mol% Mg-doped lithium niobate (Mg:LN) for 400–5000 nm are also presented [Jundt02], with temperature dependence across −50–250°C introduced for a wavelength range of 400–1200 nm in [Schlarb94]. The ordinary and extraordinary refractive indices across the transparency region at room temperature are plotted in Figure 2.5. Also shown here is the SHG coherence length plotted against the fundamental wavelength, calculated via (2.21). Due to the temperature-dependent dispersion of undoped LN, the coherence length curve shifts downwards with increasing temperature.

A generally important property of a material is its transmission spectrum, plotted for undoped CLN and SLN in Figure 2.6. The transmission spectra of undoped CLN from two suppliers are compared, showing all the same features and an identical absorption band-edge at $\lambda = 322$ nm. The transmission spectrum of SLN from a third supplier showed very similar features to CLN, as well as the expected UV-shifted absorption edge at $\lambda = 312$ nm. Incorporation of dopants alter this transmission spectrum, introducing new absorption bands, shifting the UV absorption edge and an OH-absorption peak. All these properties detailed in the transmission spectra will be compared with all other dopant types investigated below in Section 2.2.2. All the transmission spectra data presented herein was measured using a Shimadzu UV-3600 UV-Vis-NIR Spectrophotometer on loan from Shimadzu Corporation. Previous measurements by Mamedov have detailed the reflectance and absorption of LN in the vacuum ultraviolet (VUV) wavelength region [Mamedov84].

Ferroelectric crystals such as LN also exhibit many other more exotic properties which are either optical or electrical in nature. These properties include the pyroelectric, piezoelectric, photoelastic, photovoltaic, electro-optic, and photorefractive effects [Weis85], as

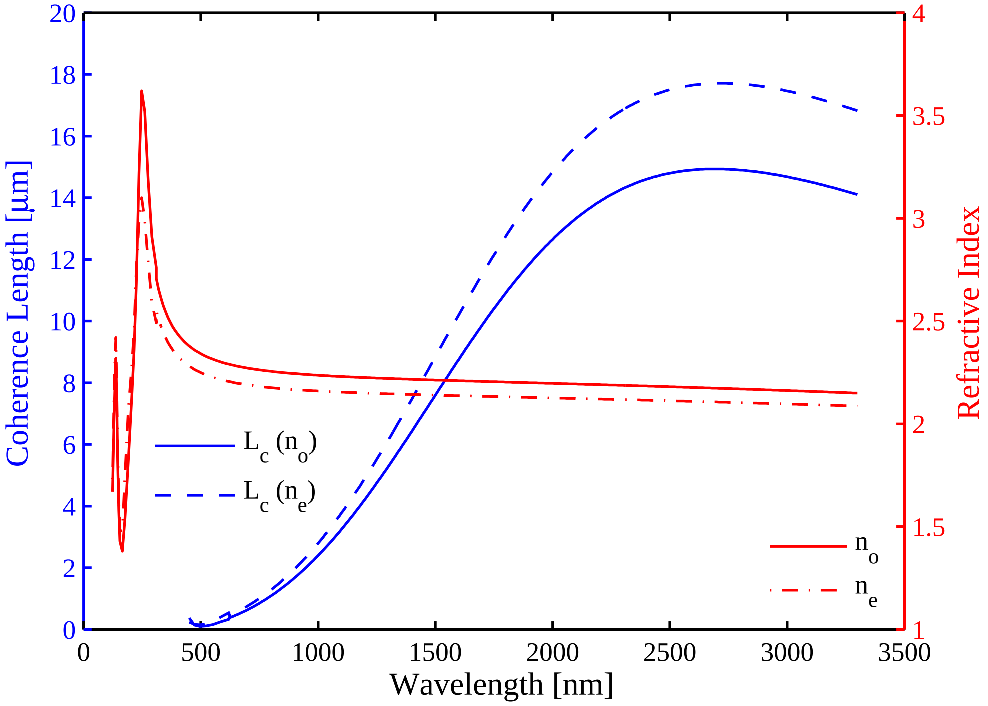

Figure 2.5: Refractive index and SHG coherence length as a function of fundamental wavelength for both ordinary and extraordinary polarized light in undoped CLN at room temperature.

well as optical nonlinearity. Many of these properties are coupled and can coexist in a single process. For example, the photorefractive effect is a result of the combination of the photovoltaic and electro-optic effects, discussed further in Section 2.2.2.1. An important reason that LN is highly valued in optics research is due to its large electro-optic and nonlinear coefficients, r_{ijk} and d_{ijk}, respectively.

LN displays a pyroelectric effect along the polar axis only, meaning that the pyroelectric first-order tensor has a single non-zero coefficient. This is caused by the rearrangement of the Li and Nb ions relative to the oxygen octahedra wherein an increasing temperature reduces both the ion displacement and the resultant spontaneous polarization [Weis85]. This change in polarization can be detected by the flow of charge to and from the surface.

The optical nonlinearity third-rank tensor, d_{ijk}, contains 27 coefficients. In the cases where $\chi^{(2)}$ dispersion can be ignored, valid only when far from material resonances and thus in a “lossless” regime, the Kleinman symmetry condition [Kleinman62] asserts that d is independent of the permutation of the indices i, j, k, such that $d_{122} = d_{212} = d_{221}$, for example. Therefore, the 27 coefficients of the d tensor can be reduced to 10 independent elements. In the 3m crystal class, symmetries further reduce the coefficients

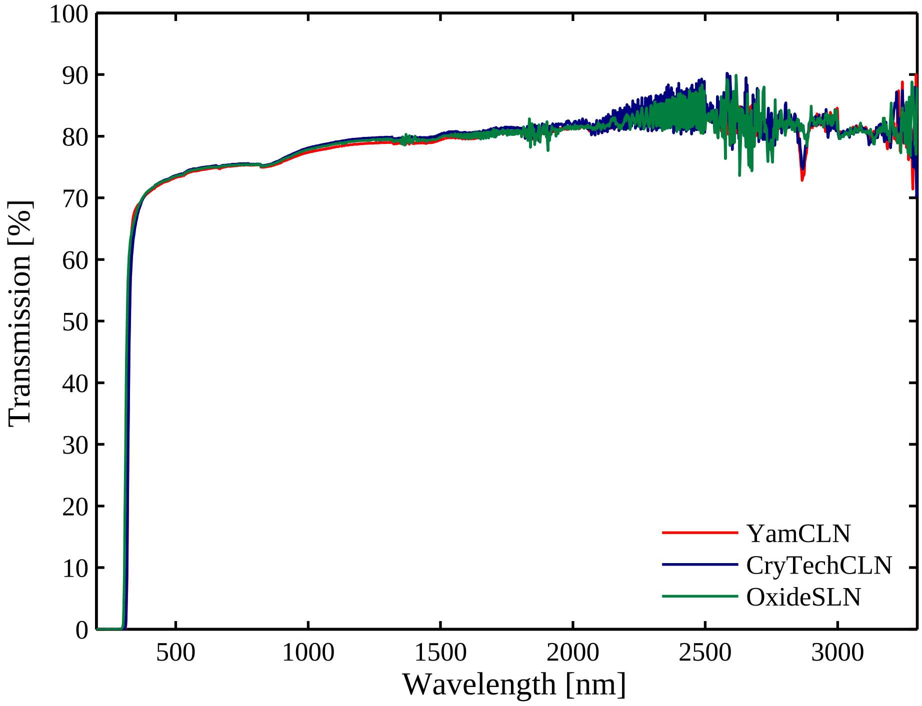

FIGURE 2.6: Transmission spectra of undoped CLN and SLN. YamCLN, CryTechCLN, and OxideSLN were supplied by Yamaju Ceramics Ltd., Crystal Technology Ltd., and Oxide Corporation, respectively. All samples were 0.5-mm thick. The signal variability measured for $\lambda \gtrsim 1500$ nm is due to detector noise, measured using a Shimadzu UV-3600 UV-Vis-NIR Spectrophotometer on loan from Shimadzu Corporation. Typical accuracies were within ±1 nm.

to 3 independent non-zero values, described by the relation [Butcher65],

$$d_{3\mathrm{m}} = \begin{bmatrix} 0 & 0 & 0 & 0 & d_{31} & -d_{22} \\ -d_{22} & d_{22} & 0 & d_{31} & 0 & 0 \\ d_{31} & d_{31} & d_{33} & 0 & 0 & 0 \end{bmatrix} \tag{2.37}$$

using contracted notation.

Finally, LN is an electrical insulator with a bandgap of $E_g \simeq 3.75$–4 eV [Redfield74]. At room temperature, LN has a very low electrical conductivity of $\sigma = \sim 10^{-13}$ $(\Omega\ \mathrm{m})^{-1}$, increasing with temperature [Kovacs02].

2.2.2 Dopants in Lithium Niobate

An important advantage of lithium niobate is the ability of its crystal structure to accommodate large levels of dopants due to its structural flexibility [Schirmer91]. In turn, the introduction of dopant materials are able to tune the existing properties or to create new properties entirely, opening up the LN family of crystals to a wider range of applications with improved performance.

One property of broad interest is photorefraction. This optically-induced inhomogeneity in both LN and LT, first reported by [Ashkin66], was viewed both as optical damage detrimental to device performance and as a possibility for new types of devices based on optical data storage and holography [Chen68]. This new application drove researchers to investigate adding dopants to *increase* the photorefractive properties. These photorefractive dopants are discussed in Section 2.2.2.1. Other applications, using second-order nonlinear interactions for example, required a *reduction* in the susceptibility to this optical damage. These so-called photoresistant dopants are discussed in Section 2.2.2.2.

Many applications of integrated optical circuits benefit from the use of an optically active gain medium. For example, this has allowed the integration of laser medium and harmonic generation onto a single crystal [Fujimura00a]. The incorporation of optically active rare-earth dopants in LN is one method of achieving this, discussed in Section 2.2.2.3.

2.2.2.1 Photorefractive Dopants

Photorefraction is a result of the interaction of several processes in photorefractive materials. Illumination, particularly of high intensity I, causes excitation of charge carriers into the conduction or valence bands for electrons or holes, respectively. Charge carriers are photo-excited from donor trap sites and drift until they are re-captured in an acceptor trap site [Chen69]. The dark conductivity (σ_d) and the photoconductivity (σ_{ph}) allow the separation of photo-induced charges. Spatially inhomogeneous intensity causes charge carrier migration to and accumulation in the darker regions due to less excitation and smaller conductivity, setting up space charge fields, E_{sc}. The space charge fields alter the local ordinary and extraordinary refractive indices, n_o and n_e, respectively, via the electro-optic effect,

$$\Delta n = -\tfrac{1}{2} r n^3 E \tag{2.38}$$

where r is the appropriate electro-optic coefficient, n is the refractive index, and E is the applied electric field. The photorefractive index change resulting from the space charge field is defined as [Furukawa98],

$$\delta \Delta n_{ph} = \Delta n_o - \Delta n_e = \frac{n_e^3}{2} \left[\frac{r J_{ph}}{(\sigma_d + \sigma_{ph})} \right] \tag{2.39}$$

where $\sigma = \sigma_d + \sigma_{ph}$ is the conductivity. In LN, $\sigma_d \ll \sigma_{ph}$ and therefore can often be neglected. However, the measured change in birefringence also has a large component due to heating of the crystal by two photon absorption, which can be separated from the photorefractive effect by measuring the transient and steady-state values [Razzari05].

The bulk photogalvanic current is $J_{ph} = G\alpha I$, where G is the Glass constant, and α is the absorption coefficient. This can be written in tensor form, $J_i = G_{ijk} E_j E_k^*$, where G_{ijk} is the photovoltaic tensor, and * represents complex conjugation [Weis85].

In undoped nominally-pure LN, several types of impurities remain in parts per million (ppm) concentrations. This includes Fe, which is found in LN in two valence states, Fe^{2+} and Fe^{3+}. These impurity defects act as electron donor and acceptor sites, respectively, with energy levels within the bandgap of LN. Visible light, particularly near $\lambda \simeq 500$ nm, can excite electrons from this defect state to the conduction band. The movement of these photo-induced charges is governed by drift due to Coulomb forces and pyroelectric fields, the bulk photogalvanic current (also known as the photovoltaic current), and diffusion caused by non-uniform illumination forming spatially-varying concentrations of charge carriers. The processes of charge excitation and transport in photorefractive crystals are reviewed in [Buse97a; Buse97b].

This property of Fe impurities allows for the intentional doping of LN with high concentrations of Fe to enhance photorefraction [Glass74]. The bulk photogalvanic current density,

$$J_{ph} \propto [\mathrm{Fe}^{2+}] \tag{2.40}$$

is proportional to the concentration of Fe^{2+} valence state ions, $[\mathrm{Fe}^{2+}]$. However the conductivity,

$$\sigma \propto [\mathrm{Fe}^{2+}]/[\mathrm{Fe}^{3+}] \tag{2.41}$$

is proportional to the ratio of $[\mathrm{Fe}^{2+}]$ to $[\mathrm{Fe}^{3+}]$. Therefore, a higher $[\mathrm{Fe}^{3+}]$ provides a larger saturation photorefractive index change,

$$\Delta n_{sat} \propto E_{sc,sat} = J_{ph}/\sigma \propto [\mathrm{Fe}^{3+}] \tag{2.42}$$

which can be realized by the introduction of a higher dopant concentration of Fe. The photoconductivity has been shown to increase in Fe-, Cu-, and Rh-doped LN, as well as undoped LN having undergone reduction [Ohmori75]. Therefore, this same discussion applies equally for other photorefractive dopants [McMillen98], such as Cu, which can be found in the valence states of Cu^{+} and Cu^{2+}.

The transmission spectra of Fe-doped congruent lithium niobate (Fe:CLN) is shown in Figure 2.7. A pronounced broad absorption band is clearly present in the visible region near $\lambda \simeq 500$ nm due to the addition of the Fe^{2+} photo-excitable impurity defects. The OH-absorption band in the infrared region is unchanged from undoped CLN.

2.2.2.2 Photoresistant Dopants

In many applications, photorefraction is detrimental to device performance. Photorefraction introduces uncontrolled phase shifts, reduces the efficiency of phase matching

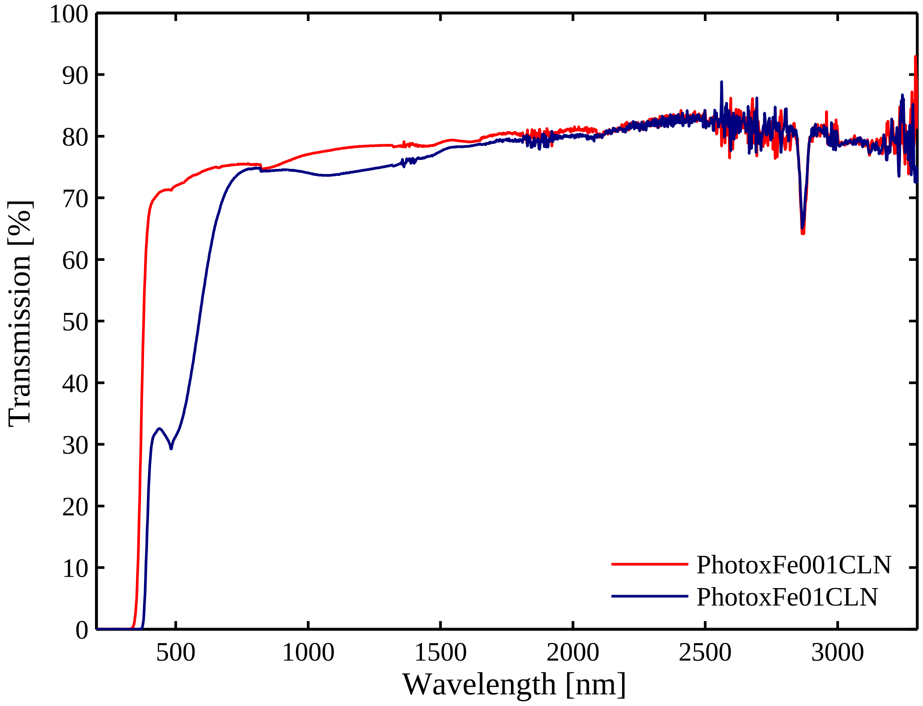

Figure 2.7: Transmission spectra of CLN with 0.01-mol% (PhotoxFe001CLN) and 0.1-mol% (PhotoxFe01CLN) Fe-doping, supplied by Photox Optical Systems Ltd. Both crystals were 1-mm thick. Measured using a Shimadzu UV-3600 UV-Vis-NIR Spectrophotometer on loan from Shimadzu Corporation. Typical accuracies were within ±1 nm.

in nonlinear interactions, and causes optical distortion [Prokhorov90]. Therefore, limits are placed on the operational range of intensities usable in many devices to avoid these effects. For these reasons, the phenomenon is often referred to as *photorefractive damage*, or simply *optical damage*.

Methods of counteracting photorefractive damage are desirable to extend the applications and performance of devices. One method proposed for removing this problem of photorefractive damage was to apply an external field to cancel the internal field within the material [Ohmori75]. However, this method would not successfully counteract charge migration in all directions, as inhomogeneous illumination causes charge carriers to drift and diffuse in a spatially-inhomogeneous direction. An alternative method of limiting photorefractive damage is by operating devices at high temperatures $\geq$170°C [Ashkin66], where increased dark conductivity [Gerson86; Battle00] prevents the build-up of space charge fields due to the conduction of thermally-excited charge [Chen69]. Large area uniform illumination can also subsequently “erase” the effect [Ashkin66] via increased conductivity due to the photoconductivity. Finally, limiting device operation to infrared (IR) wavelengths also eliminates photorefractive damage.

However, many applications would benefit from room temperature continuous operation with visible and even near-UV wavelengths. This can be accomplished by doping LN with so-called photoresistant dopants, also called non-photorefractive dopants, such as Mg, Zn, Hf, In, and Sc.

The most common dopant used for reducing the effects of photorefraction is Mg via the introduction of up to 9-mol% MgO into the melt, forming Mg:LN. The improved resistance to optical damage is a result of an increase in the photoconductivity with an unchanged photogalvanic current [Bryan84]. Therefore, following (2.42), a reduced photorefractive index change is observed in Mg-doped material.

The photoconductivity of Mg-doped congruent lithium niobate (Mg:CLN) experiences a rapid change as the MgO concentration approaches ∼4.6-mol%, referred to as the optical damage threshold (ODT), above which the photoconductivity levels off. At doping levels above the ODT, a 100-fold increase in the resistance to optical damage was observed [Zhong80].

The threshold effect is a result of how Mg incorporates into the LN structure. At dopant concentrations below the ODT, experiments have verified that Mg replaces the $\mathrm{Nb_{Li}}$ anti-site defects [Schirmer91; Volk94]. Above threshold doping concentrations, Mg begins to replace both Li and Nb sites. Therefore, the crystal threshold is reached when the $\mathrm{Nb_{Li}}$ defects have been minimized in the crystal.

For doping concentrations above the ODT, the optical absorption reduces due to fewer intrinsic defects, the UV absorption edge shifts towards a higher photon energy, and the OH-absorption band increases in frequency. The change in OH-absorption is believed to be a result of a change in the hydrogen bond in the oxygen triangle above the $\mathrm{Nb_{Nb}}$ due to the incorporation of Mg on some of these sites [Iyi95]. This shift in the OH-absorption band is a convenient indication that the threshold doping level has been achieved, as the 2870-nm peak observed in undoped CLN and lightly-doped Mg:CLN shifts to 2830 nm in Mg:CLN doped above the ODT [Bryan84]. These altered properties can be viewed in the transmission spectra of 5-mol% doped Mg:CLN provided by Crystal Technology Ltd. and Photox Optical Systems Ltd. (Figure 2.8).

The concentration of Mg-doping required to reach the ODT of a LN material is dependent upon its stoichiometry [Furukawa00]. Materials which are Li-rich require a lower concentration of Mg-doping. Near-stoichiometric LN has fewer $\mathrm{Nb_{Li}}$ defects and thus less Mg is required to replace them [Sweeney84]. Therefore, 1-mol% Mg-doped stoichiometric lithium niobate (Mg:SLN) provided by Deltronic Crystal Industries was doped above the ODT, as shown in Figure 2.8. An added benefit of Mg:SLN is that both the photoconductivity increases and the photogalvanic current decreases each by 1–2 orders of magnitude, together combining to increase the resistance to photorefractive damage by at least four orders of magnitude [Furukawa98; Furukawa00].

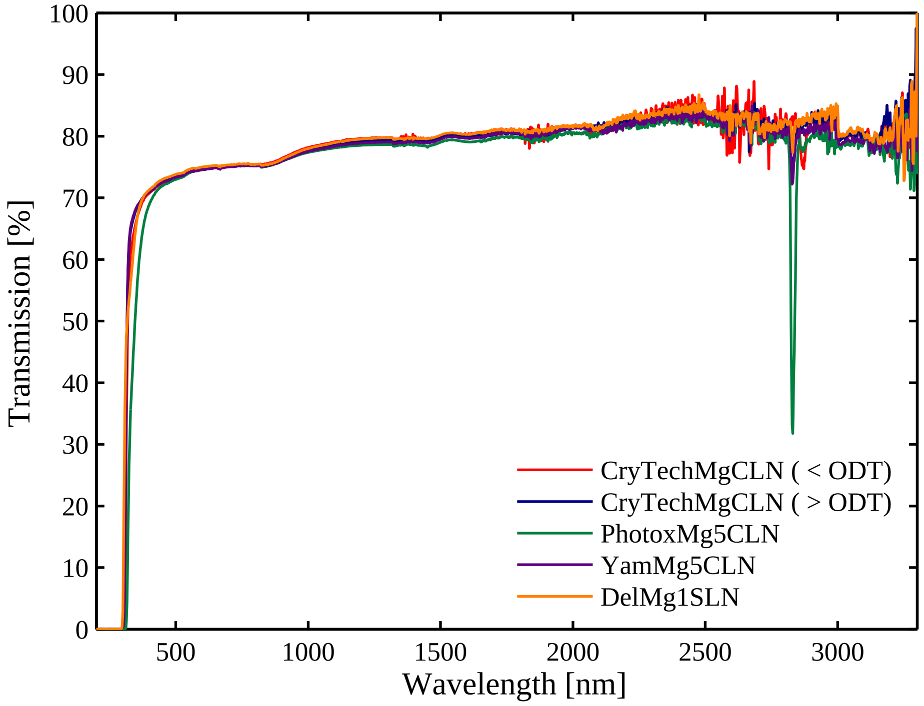

FIGURE 2.8: Transmission spectra of CLN supplied by Crystal Technology Ltd. with Mg-doping above and below the optical damage threshold (ODT) (CryTechMgCLN), 5-mol% Mg-doping supplied by Photox Optical Systems Ltd. (PhotoxMg5CLN) and Yamaju Ceramics Ltd. (YamMg5CLN), and SLN with 1-mol% Mg-doping, supplied by Deltronic Crystal Industries (DelMg1SLN). All crystals were 0.5-mm thick, except PhotoxMg5CLN which was 5-mm thick. Measured using a Shimadzu UV-3600 UV-Vis-NIR Spectrophotometer on loan from Shimadzu Corporation. Typical accuracies were within ±1 nm.

There is some disagreement in the literature on the impact of stoichiometry to the sensitivity to photorefractive damage of a material. Furukawa *et al.* observed a *greater* sensitivity to photorefractive damage in SLN than in CLN using continuous wave (cw) $\lambda = 1064$ nm light [Furukawa00]. On the contrary, with the addition of Mg-doping, the *same* reduction in sensitivity was observed in both CLN and SLN materials. However, as noted above, SLN material reached this threshold at a much lower doping concentration than for CLN. On the other hand, measurements by Katz *et al.* showed a *reduced* sensitivity to photorefractive damage in SLN even without Mg-doping [Katz04]. Therefore, it is likely that the photorefractive response of Li-rich material is strongly dependent upon the fabrication conditions. This is quite reasonable considering that defects are expected to strongly impact photorefraction. The majority of studies have found a reduction in photorefraction in compositions approaching stoichiometry.

Mg:LN has become the preferred material for most frequency conversion applications. In addition to the above mentioned improvement in photorefractive resistance, this status is only possible because the introduction of the Mg dopant maintains the second-order

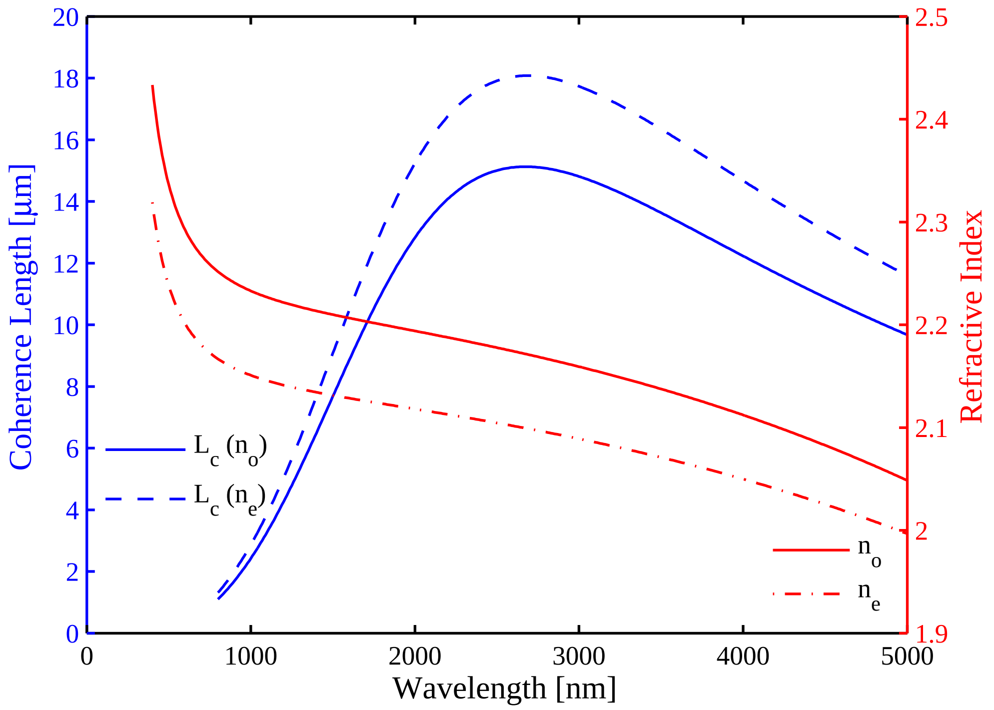

FIGURE 2.9: Refractive index and SHG coherence length as a function of fundamental wavelength for both ordinary and extraordinary polarized light in 5-mol% Mg:LN at room temperature.

optical nonlinear coefficients, d_{33} and d_{31}, with values at least as high as those of undoped CLN [Shoji97]. The refractive indices and SHG coherence lengths are similar to those of undoped CLN, and are plotted in Figure 2.9 using the Sellmeier equations of [Jundt02].

The incorporation of Zn into the melt via the compound ZnO, forming Zn-doped lithium niobate (Zn:LN), was expected to have similar effects as Mg dopant due to their identical charge state (Zn^{2+}, Mg^{2+}), similar ionic radius, and very good distribution throughout the crystal [Volk90]. Indeed, the same optical damage resistance of above-threshold Mg-doping was achieved by Zn-doping above its ODT of ∼6-mol% [Zhang01]. However, unlike Mg-doping where the photorefractive index change drops quickly at threshold, increasing concentrations of Zn smoothly and slowly decreases the photorefractive index change up to threshold, which was reported in this earlier work to be ∼7-mol% [Volk94].

This gradual threshold, perhaps the reason for the disagreement in the Zn-doping levels stated above, is also manifested in the OH-absorption peak [Volk94]. As expected for low concentrations, the peak was located at 2874 nm in 5.4-mol% Zn-doping. At 7.2-mol%, however, a new primary peak centered at 2833 nm emerged, while a residual 2874-nm peak remained. Additionally, a smaller secondary peak at 2852 nm appeared. Increasing the concentration to 9-mol%, the residual peak had vanished completely, while the new primary and secondary peaks gained prominence.

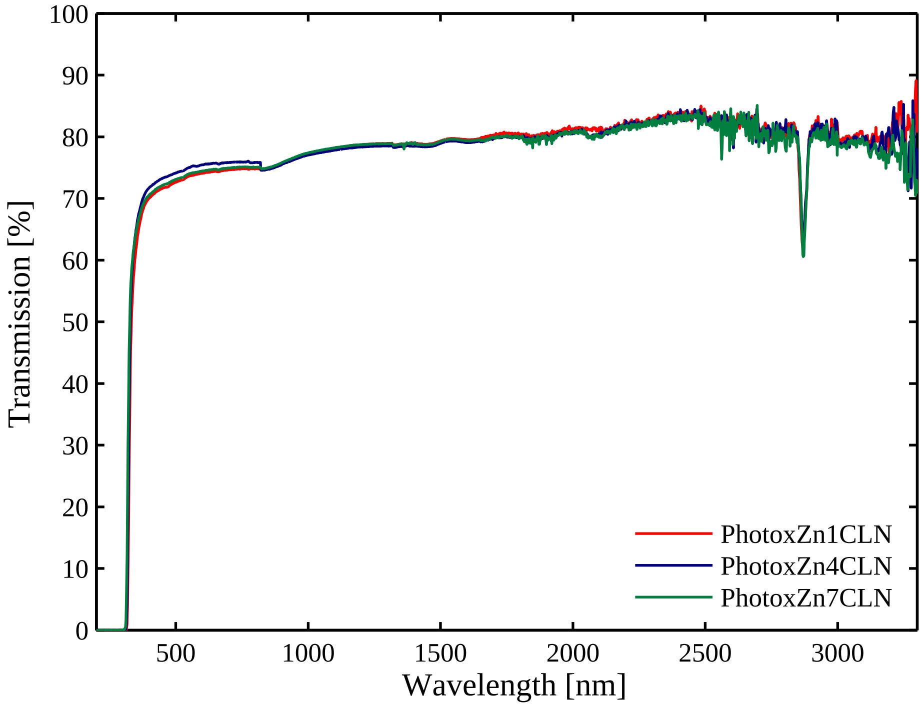

Figure 2.10: Transmission spectra of CLN with 1-mol% (PhotoxZn1CLN), 4-mol% (PhotoxZn4CLN), and 7-mol% (PhotoxZn7CLN) Zn-doping, supplied by Photox Optical Systems Ltd. All samples were 1-mm thick. Measured using a Shimadzu UV-3600 UV-Vis-NIR Spectrophotometer on loan from Shimadzu Corporation. Typical accuracies were within ±1 nm.

The cause of this gradual change in properties as compared to Mg-doping may be a result of how the Zn incorporates into the crystal [Volk94]. It is believed that Zn may incorporate into both Li and Nb sites for concentrations below threshold, which effectively increases the concentration required to minimize Nb_{Li} defects, making threshold effects less prominent.

The transmission spectra through CLN crystals doped with 1-, 4-, and 7-mol% ZnO (Photox Optical Systems Ltd.) is shown in Figure 2.10. Even the highest doping level does not show a shift in the OH-absorption peak, indicating that the ODT doping concentration has not yet been reached. It also shows very little change in the UV absorption edge.

The introduction of Hf^{4+} into the crystal via the HfO_2 compound, forming Hf-doped lithium niobate (Hf:LN), has also been demonstrated to improve the resistance to photorefraction by increasing the dark- and photo-conductivities [Kokanyan04]. With an ODT of only 4-mol%, Hf-doped congruent lithium niobate (Hf:CLN) provides a reduction in photorefraction at least as great as 6-mol% Mg:CLN [Razzari05]. An additional advantage of this material is that it has been periodically poled during growth, forming domain widths of 4–50 μm [Kokanyan02]. However, as with Zn-doping, the fabrication of these materials is not as mature as for undoped or Mg-doped CLN.

Photorefraction can also be decreased by oxidation at high temperatures in air, converting Fe^{2+} electron donors to Fe^{3+} electron traps. An improved method of high temperature processing with an applied voltage of 1000 V can achieve a higher degree of oxidation throughout the crystal, reducing the visible light absorption and resulting photorefraction [Falk05].

2.2.2.3 Rare-Earth Dopants

The introduction of rare-earth dopants into LN provides the possibility of lasing and frequency conversion in a single medium. The Nd^{3+} ion incorporates onto a Li site within the oxygen octahedron, shifted slightly towards the nearest vacancy [Prieto99]. Lasing in Nd-doped lithium niobate (Nd:LN) was first demonstrated in [Evlanova67]. Lasing was extended to other rare-earth dopants by Johnson and Ballman, also demonstrating birefringently phase-matched self-frequency-doubling of the laser emission in Tm^{3+}-doped LN [Johnson69]. Self-frequency-doubling was extended to Nd:LN [Dmitriev79], and later demonstrated in Nd:LN co-doped with Mg to reduce photorefractive damage [Fan86]. Recently, lasing at $\lambda = 1085$ nm was demonstrated from a Ti-indiffused waveguide in a Nd-diffused layer on z-cut Mg:LN by pumping at the absorption band of $\lambda = 809$ nm [Fujimura00b]. QPM SHG of the lasing wavelength was also demonstrated in an annealed proton exchange (APE) waveguide in an Nd-diffused layer [Fujimura00a]. Simultaneous generation of multi-frequency (red, green, and blue) cw light was achieved in bulk Nd:LN which had been aperiodically-poled during crystal growth [Capmany00; Capmany01]. An important demonstration of using electric-field poling (Section 3.3) to form periodically-poled Nd:LN was demonstrated in [Grisard01].

Different rare-earth dopants provide different lasing wavelengths, pump wavelengths, optical performance, and doping characteristics in the crystal. Therefore, there has also been research into periodic poling of LN doped with Er^{3+} [Bermúdez98] and Yb^{3+} [Capmany99] for use in self-frequency-doubled lasing [Montoya99].

2.2.2.4 Dopant Comparison

The types of dopants used in LN were classified above in three categories: photorefractive (multivalent transition metals), photoresistant (monovalent ions), and optically active (rare-earth ions). Dopants typically occupy either Li or Nb sites, as the vacant oxygen octahedra acts as a buffer region between the repelling cations. This substitutional position is determined by how the dopant—O bond length and dopant oxidation state impact the crystal stability due to the distortion introduced into the oxygen octahedron

Table 2.3: Comparison of the 1/e UV band-edge and OH absorption peaks of lithium niobate and lithium tantalate for different compositions and dopants, measured using a Shimadzu UV-3600 UV-Vis-NIR Spectrophotometer on loan from Shimadzu Corporation. Typical accuracies were within ±1 nm.

Material	Band Edge (nm)	OH Peak (nm)	Peak Shift (nm) [n]
CLN [a]	322	2868	-
CLN [b]	322	2866	-
SLN [c]	312	2884	+17
Mg:CLN (< ODT) [a,l]	315	2872	+5
Mg:CLN (> ODT) [a,m]	313	2830	−37
5-mol% Mg:CLN [e,m]	331	2830	−37
5-mol% Mg:CLN [b,m]	313	2828	−39
1-mol% Mg:SLN [d,m]	308	2830	−37
1-mol% Zn:CLN [e]	327	2870	+3
4-mol% Zn:CLN [e]	324	2870	+3
7-mol% Zn:CLN [e]	322	2870	+3
5-mol% Hf:CLN [g]	322	2862	−5
0.01-mol% Fe:CLN [e]	372	2868	+1
0.1-mol% Fe:CLN [e]	539	2866	−1
CLT [b]	277	2866	−1
1-mol% Mg:CLT [b]	279	2872	+5
7-mol% Mg:CLT [b]	273	2870	+3

[a] Material from Crystal Technology Ltd.
[b] Material from Yamaju Ceramics Ltd.
[c] Material from Oxide Corporation
[d] Material from Deltronic Crystal Industries
[e] Material from Photox Optical Systems Ltd.
[g] Material from E. Kokanyan, National Academy of Sciences, Armenia
[l] MgO-doping less than the optical damage threshold (ODT)
[m] MgO-doping greater than the ODT
[n] Shift in OH absorption peak relative to the undoped CLN peak

[Xue06]. That study showed that photoresistant and rare-earth dopants occupy the Li sites, while the photorefractive dopants prefer to occupy the Nb site. This latter case is strongly affected by non-stoichiometric defects and co-dopants. In high concentrations, substitution occurs on both Li and Nb sites in a ratio that maintains charge neutrality.

Transmission spectra were taken for materials ranging in composition and dopants. The observed OH absorption peaks and UV band-edges are shown in Table 2.3. The band-edge is calculated as the wavelength of $1/e$ transmission, without correction for either reflection losses or for the variation in thicknesses of the samples. Samples of LT (Section 2.2.3) are also included in this table for comparison. OH peak shifts of ≤ 5 nm are not significant to the investigated properties of these materials.

2.2.3 Lithium Tantalate

Lithium tantalate, $LiTaO_3$ (LT), is an isomorph of LN where the Ta^{5+} ion replaces the Nb^{5+} ion. LT is grown similarly to LN, forming a congruent material (CLT) using the regular Czochralski method with a spontaneous polarization $P_s = \sim 50\ \mu C/cm^2$. Unlike LN, the melting temperature is a larger 1650°C, but the Curie temperature is a much reduced 600°C. This reduction can have an important impact on the processing of domain-engineered devices, as processes such as indiffusion for the formation of waveguides, for example, may raise the crystal above its Curie temperature, destroying the domain structure. As in LN, there is also similar interest in developing stoichiometric lithium tantalate (SLT) materials.

Due to the similar structure, many of the properties of LN are qualitatively the same in LT. In fact, many of the values are even quantitatively similar [Sturman92]. Therefore, many of the discussions above apply equally well to both materials. The transmission spectrum of the material is very similar to LN, as shown in Figure 2.11. The same OH-absorption band is present, and the absorption edge is shifted ~50 nm towards the UV. Additionally, LT has similar optical nonlinear coefficients and photorefractive ODT (Table 2.1). As with LN, LT also shows an increased photoconductivity and resulting reduced saturation photorefractive index change with an increase in Li content [Holtmann04]. Periodically poled SLT has been fabricated to produce blue SHG, showing no photorefractive damage with > 1 W input power while operating at room temperature [Kurimura06].

Many of the similarities and differences between LN and LT are discussed further in relation to the properties of ferroelectric domain inversion in Chapter 3.

2.2.4 Other Nonlinear Crystals

There are many other crystals exhibiting nonlinear optical responses. Several ferroelectric crystals are reviewed in [Kuz'minov90], including potassium niobate ($KNbO_3$), potassium tantalate niobate ($KTa_{0.65}Nb_{0.35}O_3$), lead zinc niobate ($Pb_3ZnNb_2O_9$), lead magnesium niobate ($Pb_3MgNb_2O_9$), strontium barium niobate ($Sr_{1-x}Ba_xNb_2O_6$, SBN), barium metaborate (BaB_2O_4, BBO), and potassium titanate phosphate ($KTiOPO_4$, KTP). The properties of each material make them particularly suited to a specific application, such as electro-optic devices (ex. SBN) or birefringent phase-matching (ex. BBO).

The nonlinear optical coefficients of many materials show large discrepancies across the literature, varying by as much as a factor of 2. In an attempt to clarify these values, absolute and relative measurements of phase-matched SHG nonlinear coefficients were reported for potassium dihydrogen phosphate (KH_2PO_4, KDP), BBO, LIO, KTP,

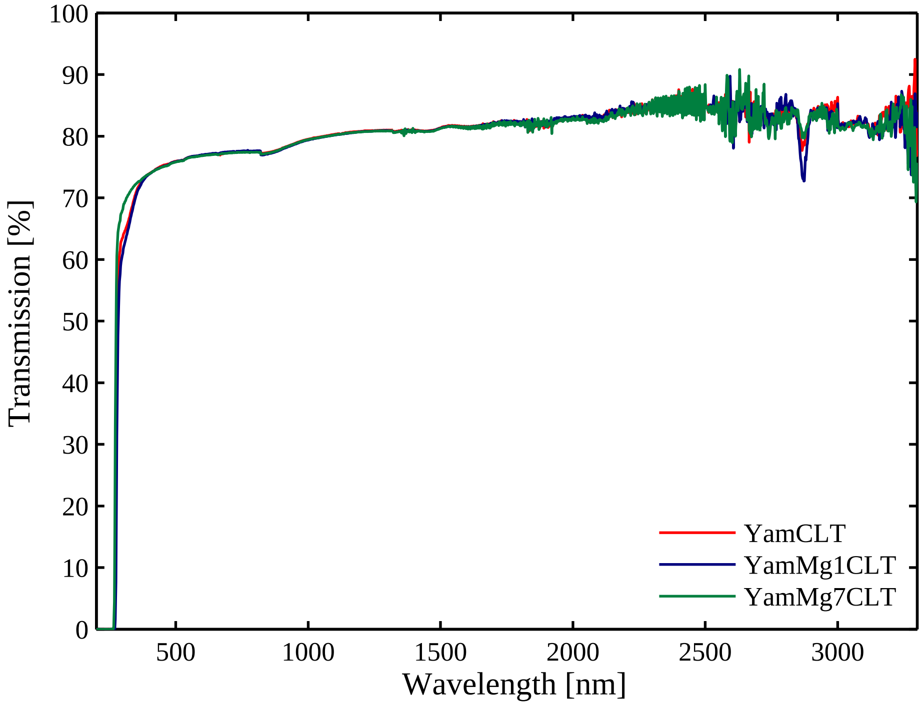

FIGURE 2.11: Transmission spectra of undoped CLT (YamCLT), and CLT with 1-mol% (YamMg1CLT) and 7-mol% (YamMg7CLT) Mg-doping, supplied by Yamaju Cermics Ltd. The YamCLT and YamMg7CLT crystals were 0.5-mm thick, and the YamMg1CLT crystal was 1-mm thick. Measured using a Shimadzu UV-3600 UV-Vis-NIR Spectrophotometer on loan from Shimadzu Corporation. Typical accuracies were within ±1 nm.

and Mg:LN [Eckardt90]. Further, these investigations using several measurement techniques, absolute measurements of the *d* coefficients were made of many materials including quartz, and various ferroelectric (LN, LT, Mg:LN, KTP, KDP) and semiconductor (GaAs, GaP, ZnS, CdS, ZnSe, CdTe) materials [Shoji97].

KTP is also used in periodically-poled QPM devices that exploit its large nonlinear coefficients, transparency down to UV wavelengths, and lack of photorefraction. Several methods of electric field periodic poling of KTP are reviewed in [Canalias06].

Bibliography

[Abdi06] F. Abdi, M. D. Fontana, M. Aillerie, and P. Bourson, *Coexistence of Li and Nb vacancies in the defect structure of pure LiNbO*$_3$ *and its relationship to optical properties.* Appl. Phys. A, 83(3), 427–434 (2006).

[Abrahams86] S. C. Abrahams and P. Marsh, *Defect structure dependence on composition in lithium niobate.* Acta Cryst. B, 42(1), 61–68 (1986).

[Abrahams02] S. C. Abrahams and C. Florea, *Stoichiometry, defect structure and composition of $LiNbO_3$*. In K. K. Wong (editor), Properties of Lithium Niobate, EMIS Datareviews Series, 3–7, INSPEC, London (2002).

[Anderson71] D. B. Anderson and J. T. Boyd, *Wideband CO_2 laser second harmonic generation phase matched in GaAs thin-film waveguides.* Appl. Phys. Lett., 19(8), 266–268 (1971).

[Armstrong62] J. A. Armstrong, N. Bloembergen, J. Ducuing, and P. S. Pershan, *Interactions between light waves in a nonlinear dielectric.* Phys. Rev., 127(6), 1918–1939 (1962).

[Ashkin66] A. Ashkin, G. D. Boyd, J. M. Dziedzic, R. G. Smith, A. A. Ballman, J. J. Levinstein, and K. Nassau, *Optically-induced refractive index inhomogeneities in $LiNbO_3$ and $LiTaO_3$.* Appl. Phys. Lett., 9(1), 72–74 (1966).

[Ballman65] A. A. Ballman, *Growth of piezoelectric and ferroelectric materials by the CzochraIski technique.* J. Am. Cer. Soc., 48(2), 112–113 (1965).

[Battle00] C. C. Battle, S. Kim, V. Gopalan, K. Barkocy, M. C. Gupta, Q. X. Jia, and T. E. Mitchell, *Ferroelectric domain reversal in congruent $LiTaO_3$ crystals at elevated temperatures.* Appl. Phys. Lett., 76(17), 2436–2438 (2000).

[Berger98] V. Berger, *Nonlinear photonic crystals.* Phys. Rev. Lett., 81(19), 4136–4139 (1998).

[Bermúdez98] V. Bermúdez, J. Capmany, J. G. Sole, and E. Dieguez, *Growth and second harmonic generation characterization of Er^{3+} doped bulk periodically poled $LiNbO_3$.* Appl. Phys. Lett., 73(5), 593–595 (1998).

[Bermúdez00] V. Bermúdez, L. Huang, D. Hui, S. Field, and E. Diguez, *Role of stoichiometric point defect in electric-field-poling lithium niobate.* Appl. Phys. A, 70(5), 591–594 (2000).

[Bhalla00] A. S. Bhalla, R. Guo, and R. Roy, *The perovskite structure - a review of its role in ceramic science and technology.* Mat. Res. Innovat., 4(1), 3–26 (2000).

[Boyd68] G. D. Boyd and D. A. Kleinman, *Parametric interaction of focused gaussian light beams.* J. Appl. Phys., 39(8), 3597–3639 (1968).

[Boyd03] R. W. Boyd, Nonlinear optics. Academic Press, Inc., 2 edition (2003).

[Bratfalean05] R. T. Bratfalean, A. C. Peacock, N. G. R. Broderick, K. Gallo, and R. Lewen, *Harmonic generation in a two-dimensional nonlinear quasi-crystal.* Opt. Lett., 30(4), 424–426 (2005).

[Broderick00] N. G. R. Broderick, G. Ross, H. L. Offerhaus, D. J. Richardson, and D. C. Hanna, *Hexagonally poled lithium niobate: A two-dimensional nonlinear photonic crystal.* Phys. Rev. Lett., 84(19), 4345–4348 (2000).

[Broderick02] N. G. R. Broderick, R. T. Bratfalean, T. M. Monro, D. J. Richardson, and C. M. de Sterke, *Temperature and wavelength tuning of second-, third-, and fourth-harmonic generation in a two-dimensional hexagonally poled nonlinear crystal.* J. Opt. Soc. Am. B, 19(9), 2263–2272 (2002).

[Bryan84] D. A. Bryan, R. Gerson, and H. E. Tomaschke, *Increased optical damage resistance in lithium niobate.* Appl. Phys. Lett., 44(9), 847–849 (1984).

[Buse97a] K. Buse, *Light-induced charge transport processes in photorefractive crystals I: Models and experimental methods.* Appl. Phys. B, 64(3), 273–291 (1997).

[Buse97b] K. Buse, *Light-induced charge transport processes in photorefractive crystals II: Materials.* Appl. Phys. B, 64(4), 391–407 (1997).

[Butcher65] P. N. Butcher, Nonlinear optical phenomena. Engineering Experiment Station, Ohio State University, Bulletin 200, Engineering Experiment Station, Ohio State University, Columbus, Ohio (1965).

[Byer97] R. L. Byer, *Quasi-phasematched nonlinear interactions and devices.* J. Nonlinear Opt. Phys. & Mater., 6(4), 549–592 (1997).

[Canalias06] C. Canalias, V. Pasiskevicius, and F. Laurell, *Periodic poling of $KTiOPO_4$: From micrometer to sub-micrometer domain gratings.* Ferroelectrics, 340(1), 27–47 (2006).

[Capmany99] J. Capmany, V. Bermudez, and E. Dieguez, *Bulk periodically poled lithium niobate doped with Yb^{3+} ions: Growth and characterization.* Appl. Phys. Lett., 74(11), 1534–1536 (1999).

[Capmany00] J. Capmany, V. Bermudez, D. Callejo, J. G. Sole, and E. Dieguez, *Continuous wave simultaneous multi-self-frequency conversion in Nd^{3+}-doped aperiodically poled bulk lithium niobate.* Appl. Phys. Lett., 76(10), 1225–1227 (2000).

[Capmany01] J. Capmany, *Simultaneous generation of red, green, and blue continuous-wave laser radiation in Nd^{3+}-doped aperiodically poled lithium niobate.* Appl. Phys. Lett., 78(2), 144–146 (2001).

[Chen68] F. S. Chen, J. T. LaMacchia, and D. B. Fraser, *Holographic storage in lithium niobate.* Appl. Phys. Lett., 13(7), 223–225 (1968).

[Chen69] F. S. Chen, *Optically induced change of refractive indices in $LiNbO_3$ and $LiTaO_3$.* J. Appl. Phys., 40(8), 3389–3396 (1969).

[Dmitriev79] V. G. Dmitriev, E. V. Raevskii, N. M. Rubina, L. N. Rashkovich, . O. Silichev, and A. A. Fomichev, *Simultaneous emission at the fundamental frequency and the second harmonic in an active nonlinear medium: neodymium-doped lithium metaniobate.* Sov. Tech. Phys. Lett., 4, 590 (1979).

[Dmitriev99] V. G. Dmitriev, G. G. Gurzadyan, and D. N. Nikogosyan, Handbook of nonlinear optical crystals, volume 64 of *Springer Series in Optical Sciences*. Springer, Berlin (1999).

[Eckardt90] R. C. Eckardt, H. Masuda, Y. X. Fan, and R. L. Byer, *Absolute and relative nonlinear optical coefficients of KDP, KD*P, BaB_2O_4, $LiIO_3$, MgO:$LiNbO_3$, and KTP measured by phase-matched second-harmonic generation.* IEEE J. Quantum Electron., 26(5), 922–933 (1990).

[Evlanova67] N. F. Evlanova, A. S. Kovalev, V. A. Koptski, L. S. Kornienko, A. M. Prokhorov, and L. N. Rashkovich, *Stimulated emission of $LiNbO_3$ crystals with neodymium impurity.* JETP Lett., 5, 291 (1967).

[Falk05] M. Falk and K. Buse, *Thermo-electric method for nearly complete oxidization of highly iron-doped lithium niobate crystals.* Appl. Phys. B, 81(6), 853–855 (2005).

[Fan86] T. Y. Fan, A. Cordova-Plaza, M. J. F. Digonnet, R. L. Byer, and H. J. Shaw, *Nd:MgO:$LiNbO_3$ spectroscopy and laser devices.* J. Opt. Soc. Am. B, 3(1), 140–148 (1986).

[Fejer92] M. M. Fejer, G. A. Magel, D. H. Jundt, and R. L. Byer, *Quasi-phase-matched second harmonic generation: Tuning and tolerances.* IEEE J. Quant. Electron., 28(11), 2631–2654 (1992).

[Feng80] D. Feng, N.-B. Ming, J.-F. Hong, Y.-S. Yang, J.-S. Zhu, Z. Yang, and Y.-N. Wang, *Enhancement of second-harmonic generation in* $LiNbO_3$ *crystals with periodic laminar ferroelectric domains*. Appl. Phys. Lett., 37(7), 607 (1980).

[Fujimura00a] M. Fujimura, T. Kodama, T. Suhara, and H. Nishihara, *Quasi-phase-matched self-frequency-doubling waveguide laser in Nd:*$LiNbO_3$. IEEE Photonics Technol. Lett., 12(11), 1513–1515 (2000).

[Fujimura00b] M. Fujimura, Y. K. Shin, and H. Nishihara, *CW laser oscillation in Z-cut Nd-diffused Ti:MgO:*$LiNbO_3$ *waveguides*. Jap. J. Appl. Phys., Part 2, 39(4A), 288–290 (2000).

[Furukawa98] Y. Furukawa, K. Kitamura, S. Takekawa, K. Niwa, and H. Hatano, *Stoichiometric Mg:*$LiNbO_3$ *as an effective material for nonlinear optics*. Opt. Lett., 23(24), 1892–1894 (1998).

[Furukawa00] Y. Furukawa, K. Kitamura, S. Takekawa, A. Miyamoto, M. Terao, and N. Suda, *Photorefraction in* $LiNbO_3$ *as a function of [Li]/[Nb] and MgO concentrations*. Appl. Phys. Lett., 77(16), 2494–2496 (2000).

[Gerson86] R. Gerson, J. F. Kirchhoff, L. E. Halliburton, and D. A. Bryan, *Photoconductivity parameters in lithium niobate*. J. Appl. Phys., 60(10), 3553–3557 (1986).

[Glass74] A. M. Glass, D. von der Linde, and T. J. Negran, *High-voltage bulk photovoltaic effect and the photorefractive process in* $LiNbO_3$. Appl. Phys. Lett., 25(4), 233–235 (1974).

[Gordon93] L. Gordon, G. L. Woods, R. C. Eckardt, R. R. Route, R. S. Feigelson, M. M. Fejer, and R. Byer, *Diffusion-bonded stacked GaAs for quasiphase-matched second-harmonic generation of a carbon dioxide laser*. Electron. Lett., 29(22), 1942–1944 (1993).

[Grisard01] A. Grisard, L. Barraco, E. Lallier, and J. P. Pocholle, *Periodically poled neodymium-doped lithium niobate*. In Conference on Lasers and Electro-Optics, 291–292, OSA, Baltimore, USA (2001).

[Holtmann04] F. Holtmann, J. Imbrock, C. Baumer, H. Hesse, E. Kratzig, and D. Kip, *Photorefractive properties of undoped lithium tantalate crystals for various composition*. J. Appl. Phys., 96(12), 7455–7459 (2004).

[Iyi95] N. Iyi, K. Kitamura, Y. Yajima, S. Kimura, Y. Furukawa, and M. Sato, *Defect structure model of MgO-doped* $LiNbO_3$. J. Solid State Chem., 118(1), 148–152 (1995).

[Jazbinšek02] M. Jazbinšek, M. Zgonik, S. Takekawa, M. Nakamura, K. Kitamura, and H. Hatano, *Reduced space-charge fields in near-stoichiometric* $LiTaO_3$ *for blue, violet, and near-ultraviolet light beams*. Appl. Phys. B, 75(8), 891–894 (2002).

[Johnson69] L. F. Johnson and A. A. Ballman, *Coherent emission from rare earth ions in electro-optic crystals*. J. Appl. Phys., 40(1), 297–302 (1969).

[Jundt90] D. H. Jundt, M. M. Fejer, and R. L. Byer, *Optical properties of lithium-rich lithium niobate fabricated by vapor transport equilibration*. IEEE J. Quant. Electron., 26(1), 135–138 (1990).

[Jundt02] D. H. Jundt, *Dispersion effects in undoped and MgO-doped* $LiNbO_3$. In K. K. Wong (editor), Properties of Lithium Niobate, EMIS Datareviews Series, 115–118, INSPEC, London (2002).

[Katz04] M. Katz, R. K. Route, D. S. Hum, K. R. Parameswaran, G. D. Miller, and M. M. Fejer, *Vapor-transport equilibrated near-stoichiometric lithium tantalate for frequency-conversion applications.* Opt. Lett., 29(15), 1775–1777 (2004).

[Kim01] S. Kim, V. Gopalan, K. Kitamura, and Y. Furukawa, *Domain reversal and nonstoichiometry in lithium tantalate.* J. Appl. Phys., 90(6), 2949–2963 (2001).

[Kirkby02a] C. J. G. Kirkby and C. Florea, *Dispersion properties of* $LiNbO_3$ *and tables.* In K. K. Wong (editor), Properties of Lithium Niobate, EMIS Datareviews Series, 119–128, INSPEC, London (2002).

[Kirkby02b] C. J. G. Kirkby and C. Florea, *Electro-optic coefficients of* $LiNbO_3$. In K. K. Wong (editor), Properties of Lithium Niobate, EMIS Datareviews Series, 131–140, INSPEC, London (2002).

[Kitamura97] K. Kitamura, Y. Furukawa, and N. Iyi, *Progress in single crystal growth of* $LiNbO_3$ *using double crucible Czochralski method.* Ferroelectrics, 202(1), 21–28 (1997).

[Kleinman62] D. A. Kleinman, *Nonlinear dielectric polarization in optical media.* Phys. Rev., 126(6), 1977–1979 (1962).

[Kokanyan02] E. P. Kokanyan, V. G. Babajanyan, G. G. Demirkhanyan, J. B. Gruber, and S. Erdei, *Periodically poled structures in doped lithium niobate crystals.* J. Appl. Phys., 92(3), 1544–1547 (2002).

[Kokanyan04] E. P. Kokanyan, L. Razzari, I. Cristiani, V. Degiorgio, and J. B. Gruber, *Reduced photorefraction in hafnium-doped single-domain and periodically poled lithium niobate crystals.* Appl. Phys. Lett., 84(11), 1880–1882 (2004).

[Kovacs02] L. Kovacs, K. Polgar, and C. Florea, *Electrical properties of* $LiNbO_3$. In K. K. Wong (editor), Properties of Lithium Niobate, EMIS Datareviews Series, 91–96, INSPEC, London (2002).

[Kurimura06] S. Kurimura, S. V. Tovstonog, R. Watanabe, and K. Kitamura, *Periodically poled stoichiometric lithium tantalate for pure blue light generation.* In Conference on Lasers and Electro-Optics, CML3, OSA, Long Beach, USA (2006).

[Kuz'minov90] Y. S. Kuz'minov and A. M. Prokhorov, Ferroelectric crystals for laser radiation control. Adam Hilger Series on Optics and Optoelectronics, IOP Publishing Ltd., Bristol (1990).

[LHuillier07a] J. A. LHuillier, G. Torosyan, M. Theuer, Y. Avetisyan, and R. Beigang, *Generation of THz radiation using bulk, periodically and aperiodically poled lithium niobate Part 1: Theory.* Appl. Phys. B, 86(2), 185–196 (2007).

[LHuillier07b] J. A. LHuillier, G. Torosyan, M. Theuer, C. Rau, Y. Avetisyan, and R. Beigang, *Generation of THz radiation using bulk, periodically and aperiodically poled lithium niobate Part 2: Experiments.* Appl. Phys. B, 86(2), 197–208 (2007).

[Lines77] M. E. Lines and A. M. Glass, Principles and applications of ferroelectrics and related materials. International Series of Monographs on Physics, Oxford University Press, Oxford (1977).

[Mamedov84] A. M. Mamedov, *Optical properties (VUV region) of* $LiNbO_3$. Opt. Spectrosc., 56(6), 645–649 (1984).

[Masaif03] N. Masaif, S. Jebbari, F. Bennani, M. Hafid, and A. Jennane, *Experimental and analytical study of defect structures in nonstoichiometric lithium tantalate and lithium niobate.* Phys. Stat. Sol. B, 240(3), 640–648 (2003).

[McMillen98] D. McMillen, T. Hudson, J. Wagner, and J. Singleton, *Holographic recording in specially doped lithium niobate crystals.* Opt. Express, 2(12), 491–502 (1998).

[Meyn01] J. P. Meyn, C. Laue, R. Knappe, R. Wallenstein, and M. M. Fejer, *Fabrication of periodically poled lithium tantalate for UV generation with diode lasers.* Appl. Phys. B, 73(2), 111–114 (2001).

[Miller98] G. D. Miller, Periodically poled lithium niobate: Modeling, fabrication, and nonlinear-optical performance. Ph.D. thesis, Stanford University (1998).

[Mitsui76] T. Mitsui, I. Tatsuzaki, and E. Nakamura, An introduction to the physics of ferroelectrics. Ferroelectricity and related phenomena, Gordon and Breach, New York (1976).

[Montoya99] E. Montoya, J. Capmany, L. E. Bausa, T. Kellner, A. Diening, and G. Huber, *Infrared and self-frequency doubled laser action in* Yb^{3+}*-doped* $LiNbO_3$*:MgO.* Appl. Phys. Lett., 74(21), 3113–3115 (1999).

[Nassau66a] K. Nassau, H. J. Levinstein, and G. M. Loiacono, *Ferroelectric lithium niobate: 1. Growth, domain structure, dislocations and etching.* J. Phys. Chem. Solids, 27(6-7), 983–988 (1966).

[Nassau66b] K. Nassau, H. J. Levinstein, and G. M. Loiacono, *Ferroelectric lithium niobate: 2. Preparation of single domain crystals.* J. Phys. Chem. Solids, 27(6-7), 989–996 (1966).

[Niizeki67] N. Niizeki, T. Yamada, and H. Toyoda, *Growth ridges, etched hillocks, and crystal structure of lithium niobate.* Jap. J. Appl. Phys., 6(3), 318–326 (1967).

[Ohmori75] Y. Ohmori, Y. Yasojima, and Y. Inuishi, *Photoconduction, thermally stimulated luminescence, and optical damage in single crystal of* $LiNbO_3$. Jpn. J. Appl. Phys., 14(9), 1291–1300 (1975).

[Prieto99] C. Prieto, *Influence of lithium niobate stoichiometry on the lattice position of* Nd^{3+} *in* Nd:$LiNbO_3$. Opt. Mater., 12(1), 135–142 (1999).

[Prokhorov90] A. M. Prokhorov and Y. S. Kuz'minov, Physics and chemistry of crystalline lithium niobate. Adam Hilger Series on Optics and Optoelectronics, IOP Publishing Ltd., Bristol (1990).

[Razzari05] L. Razzari, P. Minzioni, I. Cristiani, V. Degiorgio, and E. P. Kokanyan, *Photorefractivity of hafnium-doped congruent lithium-niobate crystals.* Appl. Phys. Lett., 86(13), 131914 (2005).

[Redfield74] D. Redfield and W. J. Burke, *Optical absorption edge of* $LiNbO_3$. J. Appl. Phys., 45(10), 4566–4571 (1974).

[Schirmer91] O. F. Schirmer, O. Thiemann, and M. Wohlecke, *Defects in* $LiNbO_3$ *— I. Experimental aspects.* J. Phys. Chem. Solids, 52(1), 185–200 (1991).

[Schlarb94] U. Schlarb and K. Betzler, *Influence of the defect structure on the refractive indices of undoped and Mg-doped lithium niobate.* Phys. Rev. B, 50(2), 751–757 (1994).

[Shoji97] I. Shoji, T. Kondo, A. Kitamoto, M. Shirane, and R. Ito, *Absolute scale of second-order nonlinear-optical coefficients.* J. Opt. Soc. Am. B, 14(9), 2268–2294 (1997).

[Sturman92] B. I. Sturman and V. M. Fridkin, The Photovoltaic and Photorefractive Effects in Noncentrosymmetric Materials. Ferroelectricity and Related Phenomena, Gordon and Breach Science Publishers (1992).

[Sweeney84] K. L. Sweeney, L. E. Halliburton, D. A. Bryan, R. R. Rice, R. Gerson, and H. E. Tomaschke, *Threshold effect in Mg-doped lithium-niobate.* Appl. Phys. Lett., 45(7), 805–807 (1984).

[Valasek21] J. Valasek, *Piezo-electric and allied phenomena in rochelle salt.* Phys. Rev., 17(4), 475–481 (1921).

[Volk90] T. R. Volk, V. I. Pryalkin, and N. M. Rubinina, *Optical-damage-resistant* $LiNbO_3$*:Zn crystal.* Opt. Lett., 15(18), 996–998 (1990).

[Volk94] T. Volk, N. Rubinina, and M. Wöhlecke, *Optical-damage-resistant impurities in lithium niobate.* J. Opt. Soc. Am. B, 11(9), 1681–1687 (1994).

[Webjörn89] J. Webjörn, F. Laurell, and G. Arvidsson, *Fabrication of periodically domain-inverted channel waveguides in lithium niobate for second harmonic generation.* J. Lightwave Technol., 7(10), 1597–1600 (1989).

[Weis85] R. S. Weis and T. K. Gaylord, *Lithium niobate: summary of physical properties and crystal structure.* Appl. Phys. A, 37, 191–203 (1985).

[Wong02] K. K. Wong (editor), Properties of Lithium Niobate. EMIS Datareviews Series, INSPEC, Exeter (2002).

[Wu98] Y. S. Wu, R. S. Feigelson, R. K. Route, D. Zheng, L. A. Gordon, M. M. Fejer, and R. L. Byer, *Improved GaAs bonding process for quasi-phase-matched second harmonic generation.* J. Electrochem. Soc., 145(1), 366–371 (1998).

[Xue06] D. Xue and X. He, *Dopant occupancy and structural stability of doped lithium niobate crystals.* Phys. Rev. B, 73(6), 064113 (2006).

[Yamada93] M. Yamada, N. Nada, M. Saitoh, and K. Watanabe, *First-order quasi-phase matched* $LiNbO_3$ *waveguide periodically poled by applying an external field for efficient blue second-harmonic generation.* Appl. Phys. Lett., 62(5), 435–436 (1993).

[Yamada06] T. Yamada, S. Kurimura, K.-i. Hayashi, and K. Kitamura, *Second harmonic generation in blue region by 1st-order QPM in quartz.* In Conference on Lasers and Electro-Optics, CMB7, OSA, Long Beach, USA (2006).

[Yi06] J. Yi, H. Ishizuki, I. Shoji, T. Taira, and S. Kurimura, *Generation of 6* μm *radiation by optical parametric oscillator and difference frequency generation in periodically poled* $LiNbO_3$. Jap. J. Appl. Phys., 45(1 A), 111–115 (2006).

[Yue03] W. Yue and J. Yi-jian, *Crystal orientation dependence of piezoelectric properties in* $LiNbO_3$ *and* $LiTaO_3$. Opt. Mater., 23(1-2), 403–408 (2003).

[Zhang01] Y. Zhang, Y. H. Xu, M. H. Li, and Y. Q. Zhao, *Growth and properties of Zn doped lithium niobate crystal.* J. Crystal Growth, 233(3), 537–540 (2001).

[Zhong80] G.-G. Zhong, J. Jian, and Z.-K. Wu, *Measurements of optically induced refractive-index damage of lithium niobate doped with different concentrations of MgO.* In Proceedings of the 11th International Quantum Electronics Conference, 631, OSA, New York, USA (1980).

Chapter 3

Domain Engineering

Many applications utilize the second-order nonlinear response of a material. These applications benefit from or require the inversion of the sign of the $\chi^{(2)}$ nonlinear coefficient, or equivalently the spontaneous polarization, P_s. Connected regions of identical sign of $\chi^{(2)}$ are referred to as *domains*. Domain engineering is the process of controlling the sign of $\chi^{(2)}$ throughout a crystal, introducing new or enhanced functionality by the pattern of domains. The precise control necessary for domain engineering requires knowledge of the microscopic process of inversion and how this can be achieved, described in detail in the following sections. This discussion is primarily devoted to the consideration of LN and LT which are the materials investigated in the remaining chapters, and therefore has been limited to the consideration of 180° domains; i.e. *anti-parallel* domains in which the spontaneous polarization can be described by either $+P_s$ or $-P_s$ only.

3.1 Visualization of Domains

Domain engineering requires the ability to distinguish between anti-parallel domains formed of material with a different sign of $\chi^{(2)}$. Many techniques have been proposed and demonstrated to visualize the domain structure of materials, most of which provide either two-dimensional information at a surface or an averaged effect over the thickness of the crystal. A few such techniques were reviewed for periodic domain structures in [Bermúdez00], whereas a more comprehensive list for many materials and domain configurations has been compiled in [Soergel05], highlighting many advantages and disadvantages of each technique. The visualization methods that were used in the experimentation of Chapters 4, 5, 6, are explained further below.

Visualization of structures using these techniques does not guarantee that the structure is composed of opposite domains. Each method below may have several other explanations for the observed image. Therefore, several visualization methods must be used to corroborate the domain-nature of the structure when this is in doubt.

3.1.1 Optical Techniques

In a perfect crystal, domains of opposite orientation alter the sign of the $\chi^{(2)}$ coefficient only. Thus, $\chi^{(1)}$ is unaffected and as a result no refractive index difference exists between ideal domains. Therefore simple microscopy is incapable of distinguishing domains of opposite orientation. Nonetheless, several optical methods of detecting domains have been demonstrated and are in common use.

In real domain engineered materials, the inversion of the domain symmetry between adjacent regions of the crystal forces a stress-induced birefringence at the domain walls due to the photoelastic effect. Viewing these structures under crossed polarizers in an optical microscope allows the visualization of these domain walls [Gopalan96b], although this contrast can be eliminated by subsequent annealing CLN [Kim05].

Due to the inverted axis of the crystal between adjacent domains, all material parameters that depend upon a non-centrosymmetric structure also invert, including the electro-optic effect. Therefore by applying a uniform voltage across a multi-domain structure, refractive index contrast is realized and domains become visible under normal optical microscopy [Gopalan99a]. However, the applicable voltage range is limited by domain re-inversion and spreading, as discussed in Section 3.3. Using CLN or CLT, this is not a barrier to visualization. However, SLN and SLT materials are more sensitive to low voltages, placing a much lower limit on the maximum applicable voltage and thus reducing the observable electro-optic refractive index contrast.

Visualization by coherent light from an Ar^+ laser is possible by applying an electric field across the crystal [Müller03b]. Here, the near-field profile imaged the domains directly, and the far-field provided the Fourier transform of the domain profile, providing averaged information about spatial orientations of the domain boundaries. Visualization was also possible during growth of these domains, capturing information during inversion [Müller04]. In periodic domain patterns, the far-field profile can provide information on the period, duty cycle, and homogeneity of the domain structure across the illuminated region [Müller05].

3.1.2 Hydrofluoric Acid Etch

Perhaps the currently preferred technique for high-resolution visualization of domain structures is chemical etching. The benefit of this technique is that it replaces the problem of imaging domain structures with the more conventional problem of imaging topographical features. Following etching, scanning electron microscopy (SEM), atomic force microscopy (AFM), or other surface-profiling methods can be applied for very reliable imaging.

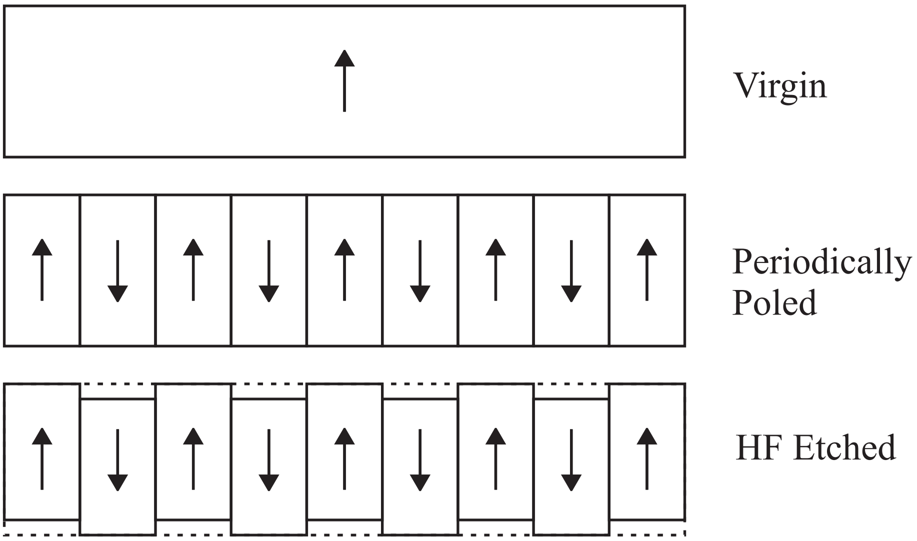

Figure 3.1: Schematic of HF etching of LN along the z direction, viewed in cross-section. The arrows indicate the direction of the z axis within each domain. The dotted lines represent the crystal surface prior to chemical etch.

Table 3.1: Etch rates of LN in pure HF acid at room temperature.

	Etch rate [μm/hr]		
Axis	− face	+ face	Ref.
z	0.8	nil	[Sones02]
y	0.08–0.11	0.04–0.05	(this study)

Chemical etching of LN is possible with either pure hydrofluoric acid (HF) acid or a mixture of HF/HNO_3 acids. These acids preferentially etch the −z face while leaving the +z face virtually untouched even after 600 hours, achieving the lowest surface roughness by etching in pure HF [Sones02]. This preferential etching of the −z face may be due to weaker bond strengths in both the LiO_6 and NbO_6 octahedra [Xue02] and wider oxygen triangle [Zhang05] on the −z side. The etch characteristics along the z direction of LN are shown schematically in Figure 3.1, viewed in cross-sectional profile.

The y faces also exhibit a similar etch characteristic, with the −y face etching much faster than the +y face in HF acid [Niizeki67]. The cross-sectional profile of periodic domain structures, such as PPLN (Section 3.3.1), is often visualized by y-face etching of a cut and polished crystal. The x face, on the other hand, shows no preferential etching after cutting and polishing domain-structured LN, as expected, due to the symmetry along this axis. The etch characteristics along the y direction of LN are shown schematically in Figure 3.2, viewed from the z face. A comparison of room-temperature etch rates along the y and z directions is shown in Table 3.1.

Despite its widespread use, there are several drawbacks of the chemical etching method for visualizing domains. Firstly, chemically etching the surface is a destructive process

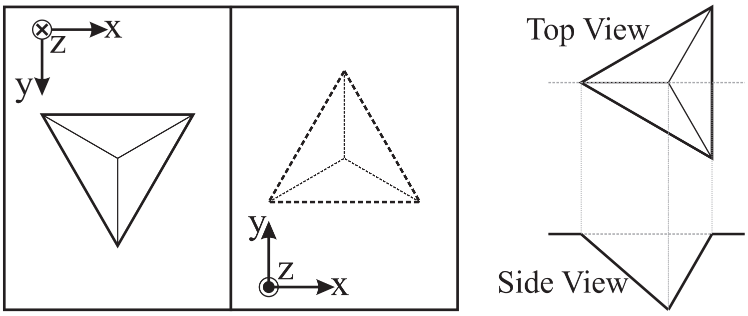

FIGURE 3.2: Schematic of HF etching of LN along the y direction, viewed from the z face. The solid triangle represents an etched region on the top z face, with the interior lines depicting the interior topography caused by preferential etching along the three y axes. The dashed triangle represents an etched region on the bottom z face. The triangle viewed from the top appears as an asymmetric triangular trench in a side-view cross-section through the center, after [Niizeki67].

which may limit the usefulness of the material for further application. Secondly, the surface structure resulting from chemical etching is not necessarily wholly determined by the domain orientation alone. For example, frustrated etching has been observed due to visible [Barry99] and UV [Mailis02] illumination. There is even some evidence that etching itself might impact the domain structure [Shur05b].

For research presented in this manuscript, all chemical etching was completed using 48% HF acid solution at room temperature without agitation, unless otherwise stated. A typical etch duration was 20 minutes, but depending on the purpose could range from just a few minutes up to a day. Where not explicitly stated, 20–30 minutes can be assumed.

3.1.3 Scanning Force Microscopy

An alternative method for imaging domain structures is the use of scanning force microscopy (SFM), a modification of atomic force microscopy (AFM) [Binnig86]. This non-destructive scanned imaging technique provides a high lateral resolution that is confined to a near-surface volume. Under controlled conditions, SFM is becoming an established technique for both visualizing and inverting ferroelectric domains [Kolosov95; Eng98; Hu02; Kalinin02; Xue03].

The SFM technique was first applied to visualize ferroelectric domains by oscillating the tip on a piezoelectric sample and detecting the resulting electrostatic forces via a lock-in amplifier [Saurenbach90]. By instead applying an oscillating voltage to a metalized AFM tip in contact mode, the small piezoelectric deflections of the crystal were detected by a lock-in amplifier [Kolosov95]. In this technique later referred to as piezoelectric force microscopy (PFM), the voltage applied to the piezoelectric material changed its thickness via the converse piezoelectric effect.

The change in the thickness of a piezoelectric material under an applied electric field follows [Jungk07],

$$\frac{\Delta t}{t} = E d_p \tag{3.1}$$

$$\Delta t = E t d_p = V d_p \tag{3.2}$$

where Δt is the change in the thickness t, $E = V/t$ is the applied electric field, V is the applied voltage, and d_p is the relevant piezoelectric coefficient. From this first order approximation, the change in the thickness of the sample is dependent upon the voltage and *not* the electric field at the tip. This is true even for an inhomogeneous E-field because $V = \int_0^t E(s)\mathrm{d}s$.

Quantitative data can be obtained by measuring the deflection of the tip when scanning over a large-area electrode on the crystal. Electrical contact between the SFM tip and the electrode presents a uniform voltage across a large area of the crystal. Without this electrode, the tip affects a small volume of the crystal only and results in a clamped mechanical deflection, diminishing the apparent piezoelectric response [Jungk07]. This clamped response is one reason the reported piezoelectric deflections vary considerably as compared to those measured by other techniques.

A PFM can generate many types of measurement signals. Regular AFM signals include the internal signal (change in cantilever vertical position, related to the derivative of topography), topography (calculated from the internal signal), and lateral force (measuring in-plane forces, such as friction). The primary PFM signals, due to the applied oscillating voltage and detected by a lock-in amplifier, are the amplitude, A (magnitude of cantilever deflection), and phase, ϕ (phase of cantilever deflection) responses. These PFM signals are commonly combined to form the X-signal, $X = A\ \cos(\phi)$, and the Y-signal, $Y = A\ \sin(\phi)$.

Due to the inversion of the piezoelectric response in domains of opposite orientation, the piezoelectric deflection of opposite domains should have identical amplitudes (A) but 180° relative phase shift (ϕ) between them. However until recently PFM measurements have been fraught with an unexplained frequency dependence, different amplitudes and a non-180° phase shift between anti-parallel domains, resulting in inconsistent data in the literature. Typical frequencies used are in the range 1–100 kHz, well below mechanical resonances of LN [Ogi02] or the cantilever. Nonetheless, a frequency-dependent background response of the system has been observed and strongly influences measurements.

The reason this background is so important is that it contains both an amplitude, A, and phase, ϕ, thus typically reducing both the amplitude and phase contrast of an unprocessed signal. From the measured signals of the +z ($\mathbf{P}$) and −z ($\mathbf{N}$) faces, the background system response, $\mathbf{B}$, at each angular frequency ω, is determined according to the relation,

$$\mathbf{B} = \frac{1}{2}(\mathbf{P} + \mathbf{N}) \tag{3.3}$$

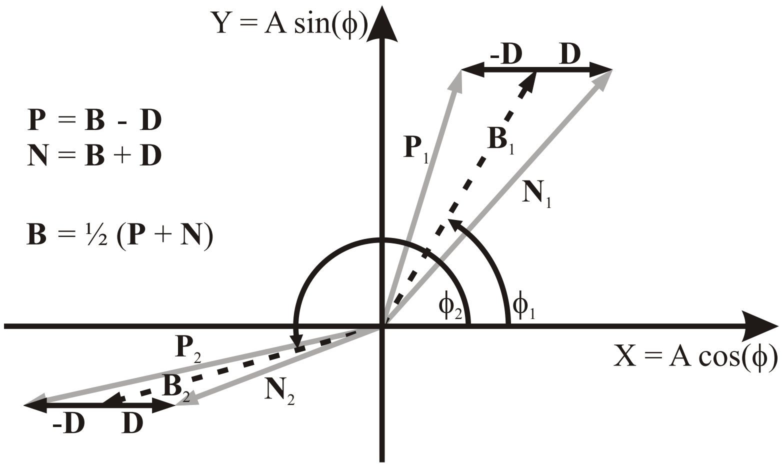

FIGURE 3.3: Background-correction technique for quantitative PFM scans. Two different background signals, $\mathbf{B}_1$ and $\mathbf{B}_2$, are shown for two angular frequencies, ω_1 and ω_2, respectively, after [Jungk06].

as graphically depicted in Figure 3.3. To determine the corrected domain response, **D**, this background must be subtracted (for example, $\mathbf{D} = \mathbf{N} - \mathbf{B}$) [Jungk06]. With the background-corrected signal, the amplitude and phase can be completely recovered, and can reliably determine not only which regions are anti-parallel, but also their absolute orientation. This same background signal was observed on glass and metal samples, and therefore is independent of the sample type and must be a property of the PFM setup.

An alternative mode of operation is referred to as dynamic-contact electrostatic force microscopy (DC-EFM) in which an AC or DC voltage is applied to a tip in contact or non-contact with the surface [Hong98]. The tip is deflected by surface charge and therefore has been proposed to image ferroelectric domains via the surface compensation charges which are of opposite polarity on the −z and +z faces. However, this mode of operation is very similar to PFM and there is considerable disagreement in the literature whether electro-static or piezoelectric forces are measured. Many recent publications, however, have attributed the images to the piezoelectric response. In this thesis, the term DC-EFM has been used only when DC voltages have been applied to the sample under test.

3.1.4 Other Visualization Methods

In addition to the above visualization methods, there are many techniques that have been used to image domain structures. One such example is the SHG microscope, which has been used to show contrast on the x, y, and z faces of LN, as well as for buried structures [Kurimura97]. The SHG interference microscope modified this design for three-dimensional imaging using multiple interference images, providing up to 2 μm spatial resolution and 3 μm depth resolution [Uesu04]. Electron emission from ferroelectrics has also been shown to permit video imaging of the domain reversal process [Rosenman00]. In LN, for example, heating causes electron emission from the +z face, while cooling causes emission from the −z face. Scanning confocal luminescence is possible in LN lightly doped with Er^{3+}, where rearrangement of the defect complex between as-grown and inverted domains alters the emission spectrum [Dierolf03; Dierolf04b].

3.2 Ferroelectric Domain Inversion

Ferroelectric domain inversion is the process of reversing the direction of the spontaneous polarization of a ferroelectric material, thus inverting the sign of the $\chi^{(2)}$ nonlinear coefficient and many other properties of the material. The LN and LT family of crystals, under consideration in the following chapters, contain only 180° domains. Other ferroelectric crystals can have other orientations of P_s, such as $BaTiO_3$ [Forsbergh49] or $KNbO_3$ [Hirohashi05] which exhibit 90° domains.

The preparation of a ferroelectric crystal into a single-domain state is referred to as *poling.* At a later time, a crystal can be "re-poled" to invert the direction of spontaneous polarization globally or locally, creating a domain structure containing both "up" and "down" anti-parallel domain orientations. Throughout this thesis, the term "poling" will be used to specify any process that achieves domain inversion within a ferroelectric crystal.

In LN, inversion of the direction of spontaneous polarization is achieved when the Nb and Li atoms have been repositioned within the oxygen lattice. In the original orientation looking along the +z direction of the crystal, the oxygen octahedral interstices are filled in the order of {Nb, V, Li, Nb, V, Li, ...}, as shown in Figure 2.4. During domain inversion, Nb atoms move to the equivalent position about the center line between two oxygen planes, while Li atoms must be forced through an oxygen layer to a equivalent displacement on the opposite side. Viewed along the same direction as prior to inversion, these movements result in the octahedral interstices being filled in the order of {Nb, Li, V, Nb, Li, V, ...}, which is the reverse of the order seen above. As both these states are equivalent, the crystal exhibits two stable states and a hysteresis in moving between each state.

To analyze the effect of domain inversion, a slice through a crystal is shown schematically and viewed from the +z face in Figure 3.4. The schematic shows the positions of anions on two adjacent oxygen layers and all cations in between, where the lattice distortions have been ignored for simplicity [Abrahams66; Ohgaki92]. Each ion between the lower (blue) and upper (purple) oxygen layers is located at a different height along the z axis (pointing out of the page), with Li^+ near the bottom layer, V in the center, and Nb^{5+} nearer the top layer. The hexagonal axes, a_h, are shown with a projection of the

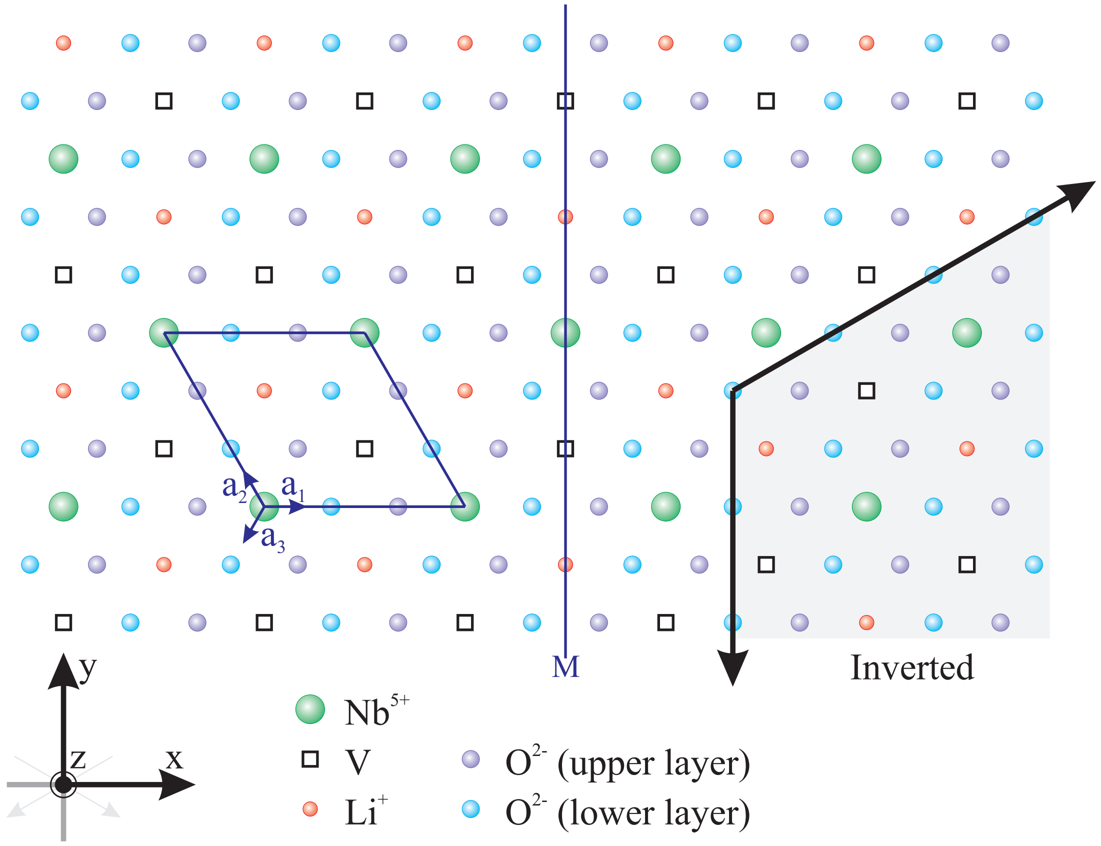

FIGURE 3.4: Crystal lattice on the +z face of defect-free LN, showing the hexagonal axes (a_h), orthohexagonal (Cartesian) axes (x,y,z), and mirror plane (M). Each ion is located at a different height along the z axis in the following order (bottom to top): O^{2-} (blue), Li^+, V, Nb^{5+}, O^{2-} (purple). The shaded region to the right of the black lines shows a hexagonal inverted domain.

hexagonal unit cell onto the z face. The orthohexagonal (Cartesian) axis, x, is defined as parallel to one of the hexagonal axes and perpendicular to a plane of mirror symmetry, M. The y axis is perpendicular to both x and z.

A domain-inverted region is shown to the right of the two black lines in Figure 3.4. Comparing the y axes of the two domain regions reveals that in addition to the inversion of the z axis, the y axis also undergoes an inversion. This can be more clearly seen in the x-face cross-sectional profile shown in Figure 3.5. This schematic clearly demonstrates the reversal of the cation order along the z axis, as mentioned above. However it also highlights a similar reversal along the y axis. In the virgin domain orientation, the cation order between adjacent oxygen layers, as viewed along the +y direction, is {Nb, Li, V, Nb, Li, V, ...}. In the inverted region, looking along the same direction, this order has changed to {Nb, V, Li, Nb, V, Li, ...}, again a reverse of the previous order.

From the above observations, domain inversion in LN and LT occurs via a rotation of the crystal axes about the x axis, thus inverting not only the z axis but the y axis as well. This is the origin of the y-face preferential etching observed in the cross-section

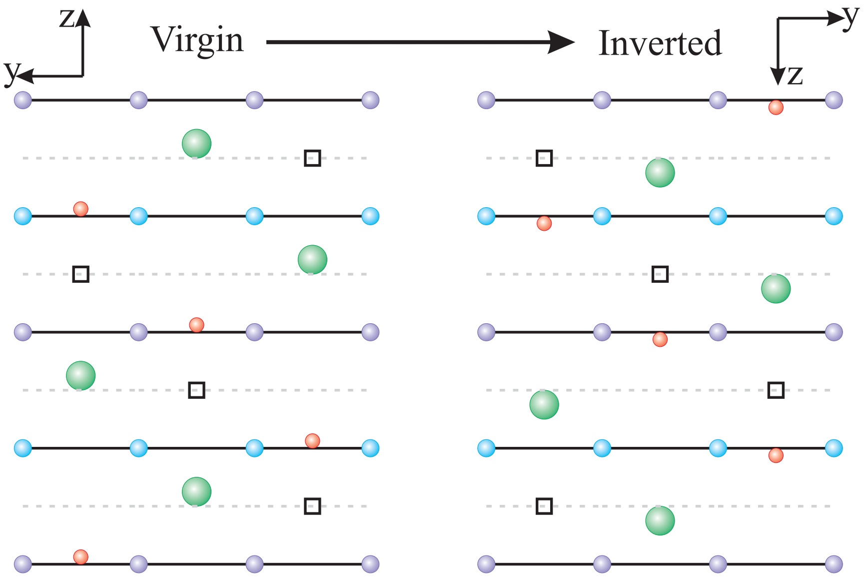

FIGURE 3.5: Crystal lattice on the x face of defect-free LN, showing a virgin (as-grown) orientation on the left and an inverted orientation on the right. During poling, the movement of the Li^+ across the oxygen layer (solid black lines) and the repositioning of the Nb^{5+} relative to the center of two oxygen layers (dashed grey line) inverts the orientation of both the z and y axes.

of PPLN devices previously mentioned in Section 3.1.2. Inversion of the y direction has also been verified experimentally via reflection SHG measurements of as-grown and poled materials [Sono06].

3.2.1 Domain Inversion Techniques

The above discussion of ferroelectric domain inversion described the microscopic behavior during inversion, but said nothing of how this inversion is achieved. Fortunately there are a multitude of techniques available in which to realize domain inversion, each with different requirements, advantages, and disadvantages.

The domain structure can be controlled during growth of a crystal. Periodically inverted domains in LN have been formed during Czochralski growth via rotation-induced growth striations [Nai-Ben82] or using a growth technique of laser-heated pedestal growth [Magel90]. However, the ability to form a user-defined periodicity of the domain structure after fabrication of the material is highly desirable. Therefore the remaining techniques will focus on post-fabrication methods.

Many fabrication techniques require the use of high temperatures, sometimes approaching the Curie point ($T_c \simeq 1140°C$). Domain inversion has been demonstrated via Ti-indiffusion in LN [Miyazawa79; Qin97], where the high temperatures have a secondary effect of out-diffusing Li^+. However, domain inversion also occurs upon heating alone, likely caused by pyroelectric fields and Li^+ out-diffusion [Nakamura87], resulting in space-charge fields caused by concentration gradients of defects and their free electrons [Huang94]. Periodic patterning has been achieved by using patterned Ti-indiffusion [Webjörn89b] or silica deposition [Webjörn89a], both of which prevent Li^+ out-diffusion selectively, generating blue [Webjörn89a] and green [Fujimura91] light by QPM SHG.

Ion beam bombardment has also produced domain inversion in LN. Haycock and Townsend proposed that electron beam bombardment could cause a widening of the gap in the oxygen layer, allowing Li^+ to pass through with an applied E-field at high temperature [Haycock86]. By masking the large-area electron beam with a lithographically-defined Au pattern, periodic domains were formed [Keys90]. Scanning an electron beam over the −z face without an applied voltage formed directly-written domains in a vacuum and at room temperature [Yamada91], allowing the generation of blue light by SHG [Ito91]. Domain inversion of thin films has also been demonstrated by a focused ion beam (FIB) using Ga^{2+} ions, enabling domain engineering across topographically-structured devices such as ridge waveguides [Li06]. Direct-write methods of forming domain engineered materials, however, suffer from slow writing speeds, which is of particular importance for periodic patterns.

Newer methods of defining domain structures involve the use of SFM and similar apparatus. By applying suitably large voltages (of order 100 V) to the metal-coated tip of an SFM (typically ≤ 50 nm radius of curvature), the highly inhomogeneous electric fields can form inverted domains on both the −z and +z faces [Xue03; Rosenman03]. The high-resolution of the SFM technique allowed the recording of data within the domain orientation of a LT thin film with a spacing of 25.6 nm between “domain bits”, producing an information density of nearly 1 Tbit/inch^2 [Tanaka06]. A simpler method of using a tungsten pen with applied voltage of 800–1800 V has also been shown to form domains of straight lines or curves in LN [Mohageg05]. As with ion beam bombardment, the direct-write nature of these processes make them prohibitive for large-area periodic patterning due to the slow speed and introduction of stitching errors.

Currently, the most technologically important and versatile method of domain inversion in many types of ferroelectric crystals is that of electric-field poling (EFP), described in detail below in Section 3.3. The methods of domain formation used extensively throughout the following chapters are EFP, all-optical poling (AOP, Chapter 5), and light-assisted E-field poling (LAP, Chapter 6).

3.3 Electric-Field Poling

Until recently, LN was believed to be a frozen ferroelectric, meaning that domain inversion was not possible at room temperature because Li^+ could not move through the oxygen layer. However Yamada *et al.* changed this view with the first demonstration of domain inversion by an applied electric field at room temperature [Yamada93]. This

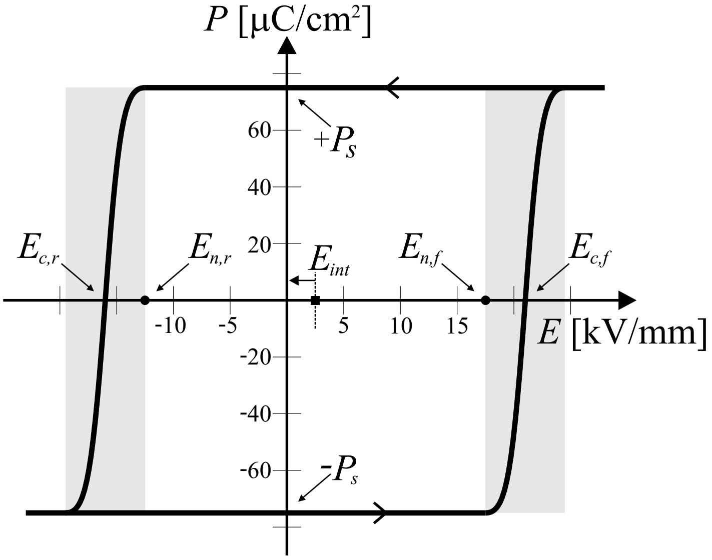

FIGURE 3.6: Schematic representation of the ferroelectric hysteresis loop of polarization versus applied electric field for LN. The greyed areas represent the poling intervals over which the poling current flows, centered about $E_{c,f}$ and $E_{c,r}$, the coercive fields in the forward and reverse directions, respectively. The magnitude of the internal field, E_{int}, is viewed graphically as the center point of the horizontally shifted hysteresis loop.

was likely made possible by improvements in the fabrication quality of large crystals of LN, reducing the concentration of defects and reducing the electric field necessary to force domain inversion. Presently, electric-field poling (EFP) has become the most widely used and reliable method of domain engineering, particularly in the LN and LT family of crystals.

Ferroelectrics exhibit a hysteresis loop of polarization, P, versus externally applied electric field, E, which can be measured via the current as the voltage across the crystal is changed. P is the macroscopic polarization averaged over the entire crystal area under measurement. Initially, $P = -P_s$, where P_s is the spontaneous polarization of the crystal. Increasing $E > 0$ makes little or no change to P until it nears a material-dependent parameter called the coercive field, E_c. As E is ramped above E_c, the P changes quickly from $-P_s$ to $+P_s$ and remains at $P = +P_s$ for further ramping $E > E_c$. Reducing E to zero does not change P back to its original value, as both $\pm P_s$ are stable domain states in LN. Similarly, ramping $E < 0$ only changes P when near and above E_c, upon which P returns to the original state of $-P_s$. This is depicted schematically in Figure 3.6.

The coercive field, E_c, described above is a very important parameter, and depends upon many characteristics of the material. E_c is often loosely defined as the electric field for which domain inversion occurs. However, as evident in the grey regions of Figure 3.6, the macroscopic polarization of the material changes over a range of electric fields. Furthermore, this range depends upon the rate of change of the electric field. More accurately, one can define E_c as either the E-field at which the maximum poling current is reached [Chao95] or, more commonly, the E-field for which 50% of the domain area has reversed (i.e. $P = 0$) [Tian04], which are not necessarily equivalent. Others have also used an arbitrarily-chosen current threshold to define the coercive field [Wengler04]. The value of E_c depends strongly upon the composition, where near-stoichiometric and VTE materials showed 10- and 100-fold reductions, respectively, from congruent LN [Tian04]. Additionally, E_c decreases with increasing temperature [Ishizuki03], as expected from the increased mobility of ions. In general, the coercive field can be viewed as a macroscopic quantity concerning the inversion of large-area domains.

The coercive field value is different for domain inversion in the forward ($-P_s$ to $+P_s$) and reverse ($+P_s$ to $-P_s$) directions, and are called $E_{c,f}$ and $E_{c,r}$, respectively. This can be seen in Figure 3.6 as a horizontal shift in the hysteresis curve due to the presence of an *internal field*, E_{int}. With the internal field parallel to the direction of spontaneous polarization in the virgin state, the magnitude of the internal field is defined as,

$$E_{int} = \tfrac{1}{2}(E_{c,f} - E_{c,r}) \tag{3.4}$$

and its percentage of the coercive field is calculated as,

$$E_{int}(\%) = \frac{E_{c,f} - E_{c,r}}{E_{c,f} + E_{c,r}} \times 100 \tag{3.5}$$

following the definitions of [Tian04]. The cause of this asymmetry is the presence of intrinsic defect dipoles related to the non-stoichiometric defects, $\mathrm{Nb_{Li}}$ and $\mathrm{V_{Li}}$. A difference between the virgin domain orientation and the opposite domain orientation results because the defect dipoles are frozen in their as-grown state. This has been referred to as a “frustrated state” which persists for months or longer [Gopalan01]. However, annealing at temperatures > 100°C can quickly reorient the internal field with the new polarization direction [Gopalan96a]. Poling LT at a temperature of 250°C reduced the coercive field to one quarter of its room temperature value and eliminated the internal field [Battle00]. The magnitude of the internal field also vanishes as the composition approaches stoichiometry [Gopalan01]. While the spontaneous polarization of LN is independent of the Mg concentration, $E_{c,f}$ and E_{int} are reduced with increased Mg concentration [Hu03].

It is important to distinguish the difference between bulk poling on the macroscopic level and poling on the microscopic level. The latter case is dominated by *nucleation*, the first appearance of new 180° inverted domain seeds and growth at their boundaries. In view of the polarization hysteresis loop, nucleation first occurs when the macroscopic polarization of the material begins to change at the start of the grey areas of Figure 3.6. The electric field required for the nucleation of domains, here referred to as the *nucleation field*, E_n, has a smaller magnitude than the coercive field and corresponds to the appearance of the first domain seeds. The widths of the grey regions have been exaggerated in this schematic for illustration purposes only, and hence the magnitude of the nucleation field is typically much closer to the coercive field, although the exact difference depends upon the material and its poling kinetics (Section 3.4). The nucleation field is the same parameter named by Tian *et al.* as the *starting coercive field* in [Tian05b].

As with the coercive field, the nucleation field is different in the forward and reverse poling directions, $E_{n,f}$ and $E_{n,r}$, respectively. These values can be used similarly to estimate the internal field,

$$E_{int} = \tfrac{1}{2}(E_{n,f} - E_{n,r}) \tag{3.6}$$

$$E_{int}(\%) = \frac{E_{n,f} - E_{n,r}}{E_{n,f} + E_{n,r}} \times 100 \tag{3.7}$$

A comparison of measured nucleation fields and internal fields for various compositions and dopants of LN and LT is presented in Table 3.2.

As previously mentioned, the application of an external electric field produces a *poling current*. Because ferroelectrics are insulators, this manifests as a displacement current and very little, if any, current flows through the crystal at room temperature. The poling current redistributes the surface charge from one crystal face to the other. This charge is present on the crystal as a charge compensation mechanism for the ends of the dipoles at the surface. The surface charge density is therefore equivalent to the spontaneous polarization of the material, $\sigma_c = \mp P_s$, where the minus sign indicates a negative charge compensation on the +z face and the plus sign indicates a positive charge compensation on the −z face. For stable domain inversion, this surface charge is redistributed such that twice the charge on the domain-inverted area must flow through the external circuit,

$$Q = 2P_s A \cdot EF = \int I_p \mathrm{d}t \tag{3.8}$$

where I_p is the poling current, A is the area of domain inversion, and EF is an empirical factor which is usually chosen to be within the range $1 < EF < 2$.

From (3.8) it is obvious that the poling current first begins to flow as the first regions are inverted, or as A is increased from zero. This corresponds to the first domain nucleation appearing when the applied E-field reaches the nucleation field. Further increases in the applied E-field must then increase the poled area, further increasing the poling charge, Q, until the surface charge has been re-compensated, the macroscopic polarization P equals the spontaneous polarization P_s of the opposite domain state, and the entire region under the electric field has inverted.

3.3.1 Periodically Poled Lithium Niobate

EFP enables the patterning the domain inverted region through the use of a patterned electrode, commonly defined by photolithography. This technique has led to the birth

Table 3.2: Comparison of the nucleation field of lithium niobate and lithium tantalate for different compositions and dopants, determined by microscopic optical imaging during ramping of the applied E-field in the fused silica holder used in Figure 6.1.

	Nucleation Field [kV/mm]		Internal Field	
Material	Forward	Reverse	[kV/mm]	Percentage
Undoped CLN [a,b]	20.81	15.77	2.52	13.8
Undoped SLN [c]	5.75	4.70	0.52	10.0
Mg:CLN (< ODT) [a,l]	5.30	3.79	0.75	16.6
Mg:CLN (> ODT) [a,m]	6.01	5.61	0.20	3.4
5-mol% Mg:CLN [b,m]	6.34	5.78	0.28	4.6
1-mol% Mg:SLN [d,m]	2.65	2.54	0.06	2.3
1-mol% Zn:CLN [e]	19.28	14.62	2.33	13.8
4-mol% Zn:CLN [e]	10.62	9.47	0.58	5.7
7-mol% Zn:CLN [e]	7.81	5.49	1.16	17.5
0.01-mol% Fe:CLN [e]	19.08	15.57	1.76	10.1
0.1-mol% Fe:CLN [e]	21.35	16.24	2.56	13.6
1-mol% Nd:CLN [f]	16.98	11.84	2.57	17.8
5-mol% Hf:CLN [g]	10.98	5.17	2.91	36.0
Ti-CLN	19.13	14.30	2.42	14.5
Undoped CLT [b]	20.41	12.04	4.18	25.8
1-mol% Mg:CLT [b]	18.37	*	-	-
7-mol% Mg:CLT [b]	3.09	1.72	0.69	28.5
0.5-mol% Mg:SLT [c]	0.55	0.49	0.03	5.7

[a] Material from Crystal Technology Ltd.
[b] Material from Yamaju Ceramics Ltd.
[c] Material from Oxide Corporation
[d] Material from Deltronic Crystal Industries
[e] Material from Photox Optical Systems Ltd.
[f] Material from MolTech GmbH
[g] Material from E. Kokanyan, National Academy of Sciences, Armenia
[l] MgO-doping less than the ODT
[m] MgO-doping greater than the ODT
* Crystal breakdown

and wide-spread adoption of periodically-poled lithium niobate (PPLN) as a domain-engineered material ideally suited for QPM nonlinear interactions in the infrared to visible wavelength regimes, including SHG [Houe95a] and optical parametric oscillation (OPO) [Myers95].

The fabrication of PPLN is usually accomplished using one of two EFP poling techniques, both requiring the use of photolithography. In the first instance, shown in Figure 3.7(a), the pattern is transfered to a metal layer which acts as a patterned electrode [Yamada93]. This electrode is usually insulated by a covering of photoresist or silica. On the opposite face, a uniform electrode is used. A high voltage signal exceeding the coercive field of the material (∼22 kV/mm for CLN) is applied across the crystal,

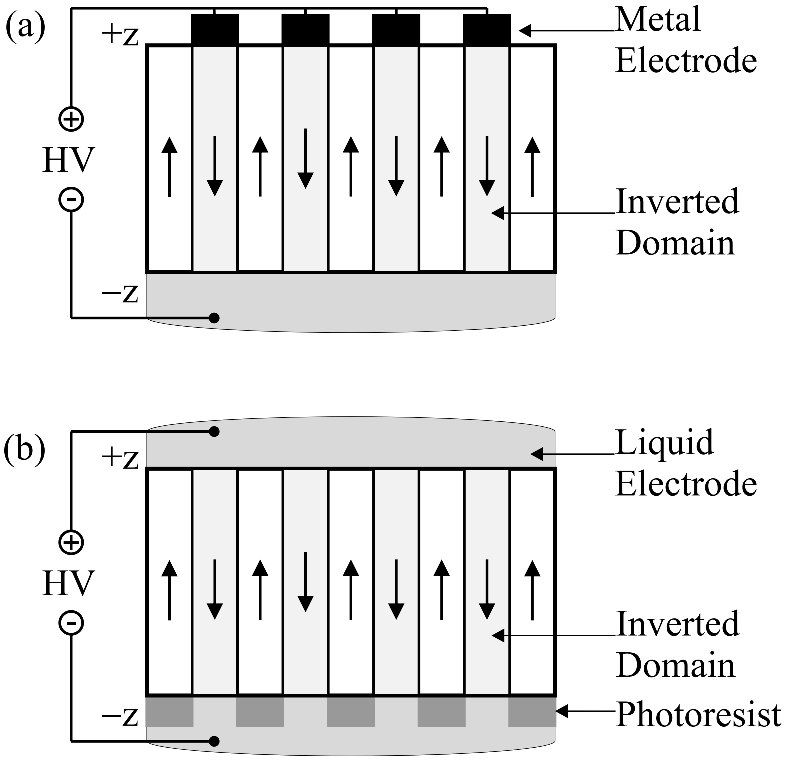

FIGURE 3.7: Electric-field periodic poling setup using (a) metal and (b) photoresist patterning of the electrodes on the +z and −z face, respectively, forming bulk PPLN.

domain-reversing the regions under the electrodes. In a second approach to periodic poling, shown in Figure 3.7(b), photoresist is used as a patterned insulating layer with uniform liquid electrodes on both faces [Webjörn94]. By exceeding the coercive field, domain reversal is possible where the liquid is in contact with the crystal in the areas without photoresist.

In both instances of EFP, a positive voltage is applied to the +z face and the −z face is typically grounded. Optimal poling and initial nucleation were observed when the metal or photoresist layers were patterned on the +z or −z faces, respectively [Miller98]. However, the −z face is more suitable for waveguiding applications because it is not altered by high-temperature processing unlike the +z face which can domain-invert by Li^+ out-diffusion. Metal electrodes have also been observed to reduce the measured bulk polarization of the crystal after several poling cycles, called *ferroelectric fatigue* or *ageing.* Using tap water, an ionic conductor, has shown no change in the polarization over many poling cycles [Tian05a]. The cause of the fatigue may result from the formation of a dielectric surface layer, suppression of domain inversion by surface or volume defects, and/or domain wall pinning. Furthermore, SFM-poling showed that nucleation on the −z face was easier and more stable than on the +z face [Xue03]. Therefore photoresist patterning, which also requires fewer fabrication steps, appears to have an advantage over metal electrode patterns.

In periodic poling using either metal or photoresist patterns, optimal domain patterns are achieved when the grating vector is parallel to the x axis of the crystal. This is due to anisotropic domain broadening, where domains grow faster in the y direction than in the x direction [Sheng06]. Therefore to achieve domain patterns as close to the electrode pattern as possible, these hexagonal domains oriented with their walls along the y axes are preferred. This is understandable due to the tendency for inverted domains to form hexagonal structures in LN, following the underlying 3-fold crystalline symmetry.

EFP has been used over the last 14 years to form high-quality PPLN, applying a single long voltage pulse (typically at least hundreds of milliseconds) until the desired area has inverted. An Al electrode pattern formed a 1st-order domain grating producing SHG of blue light [Yamada93]. Blue light was also generated from a photoresist-pattern PPLN using LiCl electrodes [Webjörn94]. KTP was also periodically patterned using metal [Chen94] and photoresist [Chen95] patterns, generating SHG blue light. In LN, the power of SHG blue light was increased to 450 mW by operating the crystal at elevated temperatures (150°C) to avoid photorefractive effects [Ross98].

An adaptation of the above technique is referred to as *pulsed* EFP, where multiple short-duration voltage pulses (typically of order 1 ms) are applied to the crystal to improve the uniformity of the poled structures. Initial voltage pulses nucleate domains on the z faces, whereas subsequent pulses were observed to provide faster growth along the z axis as compared to the lateral dimensions, thus enabling high-aspect ratios [Yamada98]. This pulsed-voltage technique was later used in Mg:LN using a Ta metal electrode covered with a silica layer on the +z face, and poled at a temperature of 100°C [Mizuuchi04]. Grating periods as small as 1.4 µm penetrated the crystal up to a 200-µm depth, and produced SHG at a wavelength of 342 nm. Periodic inversion as deep as 3 mm was possible by poling at 250°C where the coercive field of Mg:LN is reduced to 25% of its room temperature value [Ishizuki03].

In periodically-patterned EFP, nucleation occurs at the edges of the electrode where the electric field is the largest [Nakamura02]. The domain then spreads both underneath and outside the electrode, where the outward growth of the domain is self-terminating [Nakamura02] due to the exponential dependence of wall-velocity on the electric field [Gopalan98a], which reduces away from the electrode. One method of counteracting this preferential nucleation at the electrode edges is to self-assemble polystyrene spheres in the openings of the patterned photoresist. By effectively adding edges to the electrode throughout the region to be poled, nucleation is promoted across the inversion region, potentially improving the achievable aspect-ratios [Peng06].

Advantages of these EFP techniques are the ability for domain inversion at room temperature, the use of lithographically-defined patterns for fast parallel processing intrinsically compatible with microelectronics fabrication, and the ability to reliably define regular rectangular domains with high aspect-ratios aligned along a y axis.

3.3.2 Backswitch Poling

In both LN and LT, an external electric field must be applied for a minimum duration, called the stabilization time t_{stab}, to invert a stable domain. If the E-field is applied for $t < t_{stab}$, wall motion will reverse either completely or partially, re-inverting the newly-formed domains. In LT, the stabilization times are of order 1 s and 0.1 s for forward and reverse poling, respectively [Gopalan01]. In LN, the stabilization time was 30 ms and 5 ms for forward and reverse poling, respectively [Gopalan01]. The large asymmetry in the poling directions is due to the presence of the internal field due to the non-stoichiometric defects, $\mathrm{Nb_{Li}}$ and $\mathrm{V_{Li}}$. Kim *et al.* propose that applying the external E-field longer than t_{stab} overcomes the $\mathrm{Nb_{Li}}$ defect by pushing the Nb through the oxygen layer [Kim01]. Due to the negligible Li mobility at room temperature, however, the $\mathrm{V_{Li}}$ defect does not change and remains in the form of the internal field. The difference in t_{stab} between LN and LT may be due to a difference in the non-stoichiometric defect complexes associated with the internal field, or simply a difference in the defect density.

While the existence of a minimum stabilization time limits the process of EFP, it has also been applied to successfully control periodic domain structures in a process called *backswitch poling*. In this three-step process, a poling field is applied for a short duration near the stabilization time ("high field"), rapidly lowered towards zero ("low field"), then ramped back up to an intermediate E-field ("stabilization field"). Patterned domain inversion occurs during the "high field" stage, backswitching occurs in the "low field" stage. The precise timings and E-fields chosen determine the width of the domains and the duty cycle of a periodic structure by controlling and limiting the reverse domain wall motion [Batchko99]. Multiplication of the pattern frequency can also occur by maintaining nucleation at the electrode edges only, halving the period of the domain structure [Shur00].

3.3.3 Surface Poling

Regular bulk poling produces bulk domains extending throughout the entire thickness of a sample [Figure 3.7(a-b)]. However for applications using integrated optical circuits, only waveguide depths (several microns) are necessary, permitting a technique called *surface poling*. Surface poling is a modification of regular EFP where the empirical factor, *EF*, of (3.8) is increased to deliver an over-abundance of charge. This results in a condition called *over-poling*, where the poled region extends outside the boundaries of the electroded region. This is usually an undesirable effect because the duty cycle no longer matches the electrode pattern and the domains begin to merge below the surface. In surface poling, the domains in the bulk are *intentionally* merged, poling the entire volume of the crystal except small regions below the patterned insulator on the $-$z face, shown in Figure 3.8. The non-inverted regions remain in their original orientation due to trapped charge beneath the patterned insulator.

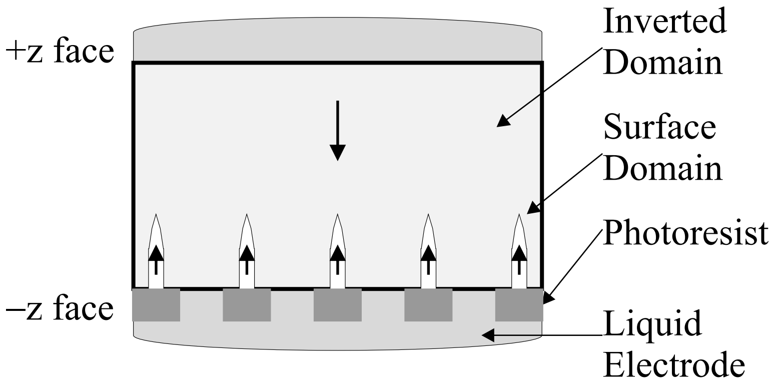

FIGURE 3.8: Surface periodic poling setup using photoresist patterning of the electrodes on the −z face.

By patterning the photoresist insulating layer on the −z face and applying an $EF = 8$ through liquid or conducting gel electrodes, domain depths of up to ∼10 µm and periods down to ∼1 µm were realized [Busacca02]. Similar domain gratings were later used for first-order QPM SHG, producing blue light in a Ti-indiffused waveguide, but the 90% duty cycle severely limited the efficiency of the device [Busacca04]. Surface poling has also been demonstrated in a proton-exchanged waveguide in LN with a period of 16.8 µm [Busacca06a], and in undoped CLT with a 1.5-µm period and at least 10-µm depth, but poor uniformity [Busacca06b]. The use of a silica insulating layer on LN improved the surface poling quality and reproducibility for periods of 3 µm, preventing poling defects which tended to occur using photoresist [Busacca05].

Due to the lateral spreading inherent in the over-poling used to fabricate surface domains, the duty cycle of the photoresist insulating pattern is not faithfully transfered to the domain pattern. Therefore, smaller openings in the photoresist layer (duty cycle <50%) are required to counteract the necessary lateral spreading and allow a domain duty cycle to approach the ideal 50%. New experiments attempted to address this concern of the non-ideal duty cycle. A combination of mask duty cycle, empirical factor ($EF > 2$), and photolithography exposure and development times must be optimized for the ideal QPM domain structures to result. For periods of 2–3 µm and mask patterns with openings ∼20%, this requires photolithographic features of ∼400–600 nm. With conventional photolithography, features on this scale are very difficult, especially over the large areas required for many-period structures of millimetres or centimetres. For instance, residual photoresist within the mask openings results in under-poling, with poor quality structures constructed of segmented domains.

To overcome the limits of conventional photolithography, two-dimensional interference lithography was used to define a photoresist pattern for surface poling in LN, with very small periods of ∼0.5 µm on the −z face, though no optical measurements have been made [Grilli05]. However, this technique does not provide a simple way of controlling the duty cycle of the photoresist, and would therefore likely be limited to low-efficiency devices.

Currently, surface poling is a useful fabrication method of forming surface domain gratings for waveguiding geometries, but applications are constrained by the limited control over domain duty-cycle.

3.4 Kinetics of Domain Inversion

The kinetics of ferroelectric domain inversion in LN and LT are reviewed in [Gopalan01] and [Shur05a]. For precision domain engineering, the control over domain evolution must be understood and implemented. Several aspects of domain growth and nucleation are important to the domain engineering of subsequent chapters and are discussed in the following sections.

3.4.1 Domain Wall Growth

Ferroelectric domain inversion, both creation and spreading of domains, occurs through the process of nucleation. Domain reversal begins with nucleation at the electrode edges and surface defects. Upon further application of the E-field, nucleation seeds extend through the crystal towards the opposite face. Lateral growth merges the domain nuclei and eventually spreads outside the boundary of the electrodes. There are three distinct types of nucleation [Shur05a], as depicted in Figure 3.9. 1D and 2D nucleations are growth along and growth outward from an existing domain wall, respectively. 3D nucleation, on the other hand, is inversion of a new solitary domain.

Growth of an existing domain is best explained by a nucleation mechanism wherein the growth rate is controlled by 1D and 2D nucleation steps of needle-like domains along the domain wall [Miller60]. The domain wall growth continues by micron-scale domain steps, sequentially propagating along the wall in the y direction [Shur02]. However, the growth of these nucleations is constrained not only to the domain wall but also to specifically the −y direction only, never in the +y direction. This asymmetry along the y directions means that a hexagonal domain will grow outward from only three of its six corners, as shown in Figure 3.10(a). Firstly, a nucleation will occur at the corner along the −y direction, then promote additional nucleation along the domain wall in the other two −y directions until the +y corner is reached. These domain steps are visible under crossed polarizers only when viewed at a very high video frame rate or when the applied voltage is low compared to the coercive field, since the wall velocity is exponentially dependent upon the applied electric field [Miller60]. However, Figure 3.10(b) shows an image of the HF-etched +z face of Mg:CLN which has captured a hexagonal domain "frozen" during growth. Because the y axis also inverts during domain reversal it is

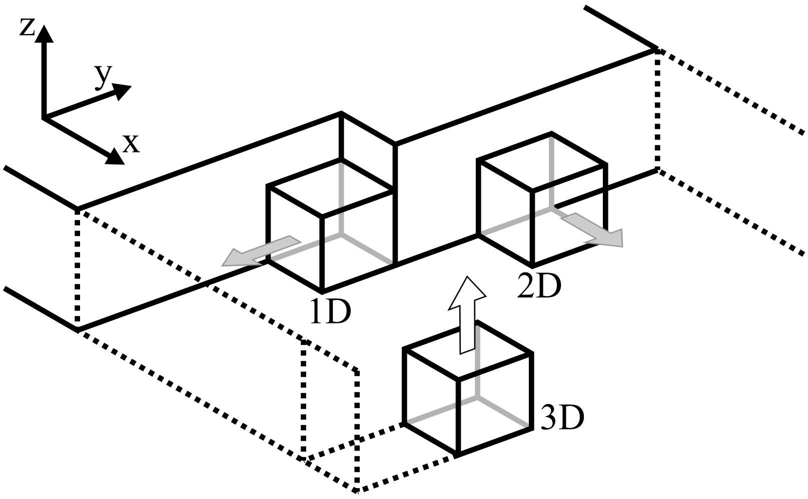

FIGURE 3.9: Schematic depicting 1D, 2D, and 3D nucleation types, after [Shur05a]. The solid lines represent the boundaries of the inverted domain amongst the unpoled surrounding material defined by the dashed lines. The grey arrows indicate the direction of domain wall growth by 1D and 2D nucleations. The white arrow indicates domain growth along the polar axis.

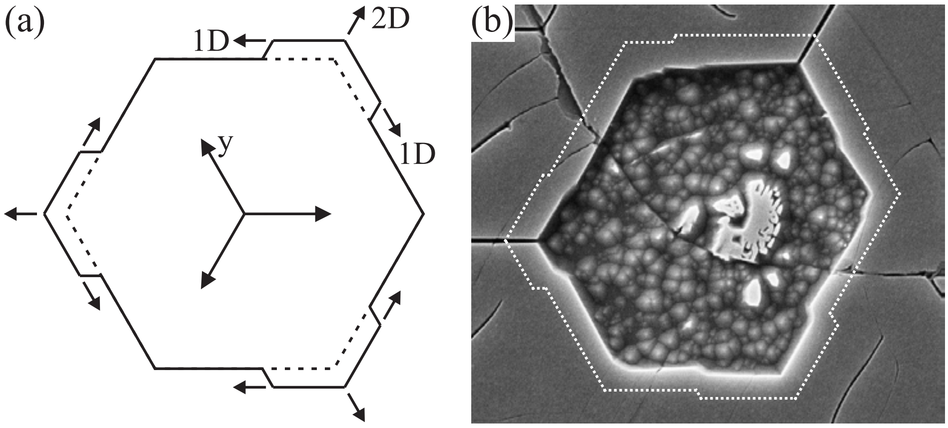

FIGURE 3.10: (a) Schematic of hexagonal domain growth by nucleation along the −y directions only. The y axes are specified for the virgin orientation of the crystal. (b) SEM micrograph of hexagonal domain growth in the Mg:CLN material used in the experiments of Chapter 5, after HF etching. The dotted lines highlight the exterior shape of the inverted domain.

necessary to specify that the directional labels of Figure 3.10 describe the y axes in the *original* (virgin) domain orientation of the crystal.

3.4.2 Domain Pinning and Internal Field

The poling current in LN is characterized by many sharp spikes over the poling interval, referred to as Barkhausen pulses or Barkhausen noise [Chynoweth58]. The jerky domain wall movement causing these current spikes implies that a domain wall may remain static for a prolonged duration. Upon subsequent movement, an “imprint” of its previous position is visible due to a strain field related to the non-stoichiometry of the crystal. The imprint fades in < 1 s due to the disappearance of the strain fields [Gopalan99a]. One cause of such jerky motion is the rapid merging of adjacent domains [Shur02].

Jerky wall motion is also a result of domain pinning centres, particularly dominant with low E-fields. A pinning centre is a crystal defect site which presents an energy barrier to a domain wall, preventing its motion. Domain pinning is strongly dependent upon the stoichiometry of the crystal, with near-stoichiometric materials having a lower defect density and hence less pinning. Therefore, non-stoichiometric defects have been proposed as the cause of domain pinning [Kim01]. The high coercive field in congruent materials may be largely influenced by the high concentration of these defect dipoles and their pinning strengths. In CLT, pinning of a domain wall was directly observed, and an applied E-field one-tenth of the coercive field caused bowing of the domain wall between pinning centres [Yang99]. The poling current in LT appears as a single smooth peak and may be a result of a higher density of pinning centres as compared to LN.

While successful EFP at room temperature overcomes the pinning centres and reorients the $\mathrm{Nb_{Li}}$ anti-site defect after the E-field has been applied for longer than the stabilization time, the $\mathrm{V_{Li}}$ defects do not reconfigure and remain in the form of the internal field [Tian04]. The internal field can be reoriented parallel to the new polarization direction by annealing at temperatures > 100°C [Gopalan96a]. The internal field is reduced by annealing at lower temperatures, but reorientation is incomplete after a month at room temperature [Gopalan96b]. Because the internal field depends upon non-stoichiometric defects, the internal field decreases with increasing Li content from congruent to stoichiometric compositions [Gopalan98b] to as low as 8 V/mm in VTE-SLT [Tian04].

3.4.3 Non-Equilibrium Poling

Regular EFP achieves an equilibrium domain structure by use of a switching time, t_s, sufficient to stabilize inverted domains. However, backswitch poling (Section 3.3.2) is an instance in which a short t_s forced non-equilibrium conditions that affect the final domain structure. Poling under non-equilibrium conditions displays several properties not observed under regular EFP and requires an analysis of time-dependent electric fields within the ferroelectric crystal.

The local electric field, E_{loc}, within a ferroelectric is spatially inhomogeneous and depends upon the summation of several fields [Shur96; Shur05a],

$$E_{loc} = E_{ext} + E_{dep} + E_{es} + E_{bs} \tag{3.9}$$

The external field, E_{ext}, is introduced through the externally applied voltage and is dependent upon electrode geometry and proximity to the electrodes. The depolarization field, E_{dep}, is produced by bound charge at the polar surfaces and at charged domain walls (head-to-head or tail-to-tail boundaries). The external screening field, E_{es}, is caused by the redistribution of charge at the sample surfaces by the poling current, in accordance with (3.8). The bulk screening field, E_{bs}, which occurs over a longer time than external screening, is a result of the redistribution of bulk charges, reorientation of defect dipoles, and injection of carriers across the so-called *dielectric surface layer.* The dielectric surface layer is a thin "imperfect layer" with a reduced spontaneous polarization on both polar faces of the crystal [Ohmori75]. A final electric field, the residual depolarization field, is defined as,

$$E_{rd} = E_{dep} - E_{es} = \frac{2L}{d} \frac{P_s}{\varepsilon_L \varepsilon_0} \tag{3.10}$$

where d is the thickness of the crystal along the polar direction, and L and ε_L are the thickness and dielectric constant of the dielectric surface layer, respectively. E_{rd} must be overcome by E_{bs} to attain a stable domain structure.

During domain inversion, these fields are altered in a sequence shown in Figure 3.11, where the solitary + and − signs represent surface charge compensation, and the coupled + and − signs enclosed within an oval represent dipoles forming the spontaneous polarization. In equilibrium prior to poling (a), the spontaneous polarization and screening fields are directed towards the +z face, and E_{dep} opposes the spontaneous polarization. In a ferroelectric capacitor (b), where electrodes cover both polar faces, E_{ext} is applied anti-parallel to P_s. The nucleation of domains occurs by external screening when the poling current, I, delivers the opposite charge to the polar surface (c). The domain is later stabilized when bulk screening compensates for the residual depolarization field (d). If E_{bs} is not sufficient to compensate for E_{rd}, backswitching occurs.

The domain growth kinetics are determined by a parameter R, defined as [Shur05a],

$$R = \frac{\tau_{scr}}{t_s} \tag{3.11}$$

where $(1/\tau_{scr})$ and $(1/t_s)$ are the screening and switching rates, respectively. Complete screening occurs when $R \ll 1$, forming hexagonal domain shapes with walls aligned to the y axes, as in typical bulk EFP of LN. Incomplete screening occurs when $R > 1$ and may result in backswitching. The residual depolarization field suppresses nucleation along a wall (1D nucleation), and can form triangular domain shapes with walls aligned to the x axes in both CLN and CLT. Ineffective screening occurs when $R \gg 1$, further suppressing 1D nucleation and allowing 2D nucleation to dominate. The resultant domains tend toward star-shapes with three vertices at the −y corners. The typical appearance of hexagons in CLN and triangles in CLT [Gopalan99b] therefore imply a greater screening time in CLT and hence a much greater domain stabilization time, as is observed in CLT. These three domain growth conditions are experimentally demonstrated in Figure 3.12.

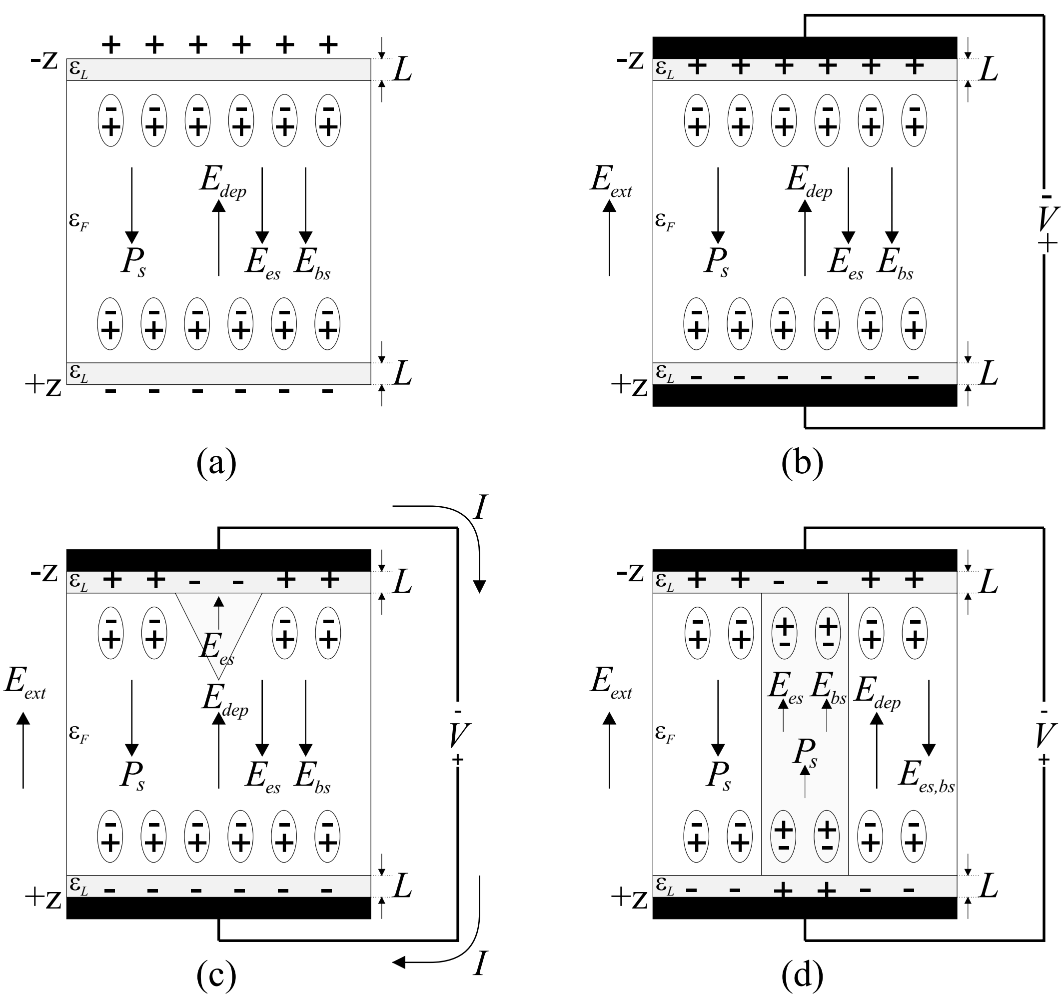

FIGURE 3.11: Schematic depicting the local electric fields within a ferroelectric crystal, showing (a) equilibrium (stable or meta-stable state), (b) ferroelectric capacitor (application of external E-field), (c) domain nucleation (effective external screening), and (d) domain stabilization (effective bulk screening).

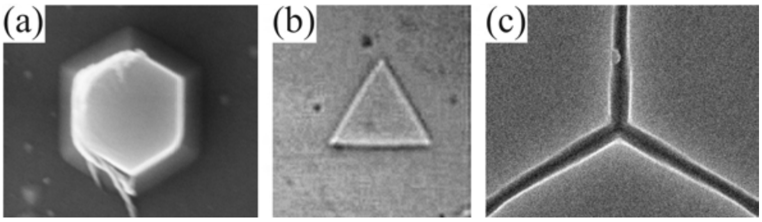

FIGURE 3.12: Domain shape using (a) complete screening, $R \ll 1$, in CLN (HF-etched), (b) incomplete screening, $R > 1$, in CLT (in-situ optical image), (c) ineffective screening, $R \gg 1$, in CLN (HF-etched). The y axis points vertically in all three images. The domains in (a) and (b) were formed via EFP, while the domain in (c) was a result of AOP (Chapter 5).

In the regime of ineffective screening, a phenomenon referred to as *correlated nucleation* and self-organization can occur [Shur05a]. The local electric field outside the inverted domain is influenced by the uncompensated depolarization field on the inside of the domain wall. The resultant local field shows a maximum value at a distance away from the domain wall that is of similar value to the dielectric surface layer thickness, and hence promotes 3D nucleation there rather than 1D or 2D nucleation at the domain wall. A repetition of this procedure creates a chain or array of nucleations in a self-organized structure following the crystalline symmetries. *Branching* occurs only under certain conditions, where new domain lines grow out from an existing line without affecting its original growth direction [Shur06].

3.5 Influence of Light on Poling

Illumination with visible and UV wavelengths has been used to influence poling and affect the domain structure of LN and LT. In the majority of such experiments thus far, incident light has produced a temporary local change in the coercive field, thereby requiring a large electric field to initiate domain nucleation and sustain domain wall movement. These reported techniques are instances of a process here referred to as *light-assisted* electric-field poling (LAP), for which new investigations are detailed in Chapter 6.

Kovalevich *et al.* were the first to explore the effects of light on ferroelectric domain inversion, noting a change in the poling current of Fe-doped lithium niobate (Fe:LN) by illumination with a He-Cd laser ($\lambda = 440$ nm), and attributing this to the photorefractive space charge field [Kovalevich78].

An early attempt at controlled domain inversion using light involved the deposition of a Cu layer on the $-$z face of LN. The Cu acted as an absorbing layer for the $\lambda = 532$ nm pulsed irradiation, increasing the temperature of the crystal below and inducing domain inversion via *thermal poling* in a small externally-applied E-field [Houe95b]. In contrast, the following experiments did not require an absorbing medium, and light directly interacted with the crystals.

Initial experiments concentrated on LT, where a light-induced transient change in the coercive field was observed. Following regular E-field poling, subsequent re-inversion could be achieving by a reduced E-field. The value of this E-field was time-dependent and recovered to its normal steady-state value after ~1000 s [Chao95]. The rate of recovery to this steady-state value was increased by illumination from a tungsten lamp or the visible lines of an Ar^+ laser due to photo-generated charges excited from impurity defects within the bandgap [Chao96]. Interferometric patterning via y face illumination caused frustrated inversion in the regions of high intensity, forming a periodic pattern of domains over a small area [Ross97; Brown99]. A model is proposed based on the screening of the depolarization field by a light-induced space-charge field [Poghosyan03]. In LN, however, no such increase in the coercive field recovery rate was observed by visible or UV light [Wengler03].

Illumination of LN, on the other hand, directly displays a *coercive field reduction* with or without any prior domain reversals. By simultaneous illumination with patterned light and application of a uniform electric-field in LN, Fujimura *et al.* produced 15-µm domain periods using a mercury lamp in the first demonstration of a LAP process [Fujimura03]. While the reduction in the coercive field was reported to be 10%, analysis of the poling current appears to indicate that initial nucleation occured for an E-field that was only 50% of the coercive field. Müller *et al.* formed an 8-µm period of segmented inversion points using UV lines of an Ar^+ laser [Müller03a]. It was also noted that on subsequent poling cycles up to an hour after illumination, the decrease in the coercive field of previously poled areas remained. However, no impact in the coercive field was observed if the illumination was before or after poling. A direct-write approach to the formation of domains in undoped and Er-doped LN has produced 2-µm domain features using a confocal microscope with $\lambda = 488$ nm light from an Ar^+ laser [Dierolf04a].

Similar LAP experiments demonstrated that the light-induced coercive field decreased with increasing intensity of illumination by cw UV light from an Ar^+ laser [Wengler04; Wengler05]. Under these conditions, the minimum light-induced coercive field decreased with increasing Mg concentration in LN, and achieved the minimum value when doped above the ODT.

Periodic domain patterning has also been demonstrated in the process of electrical fixing of photorefractive gratings in LN [Eggert04; Eggert06]. In these experiments, VTE-SLN, with its low coercive field $E_c = 2.5$ kV/mm, was Fe-doped to increase its sensitivity to photorefraction. Holographic illumination using $\lambda = 488$ nm and $I = 120$ mW/cm^2 formed a photorefractive grating vector parallel to the z axis under an external E-field near the coercive field. The light-induced space charge field was believed to be sufficient to create head-to-head domains, with the charge compensation provided by the light-induced space-charges.

Recently, light has been proposed to form micro-domains directly in photorefractive ferroelectrics without an externally applied electric field. Morozovska *et al.* [Morozovska03a; Morozovska03b] proposed that illumination with visible light along the x axis of Fe-doped lithium niobate produces a photovoltaic current leading to an accumulation of surface charge in nano-clusters at the *boundary* of the light spot, seeding the growth of micro-domains. Experiments have shown evidence of defects appearing only when there is an intensity gradient along the polar axis, resulting in the formation of these defects at the illumination boundaries. These scattering centers are proposed to be photo-induced micro-domains. However, no further clarification of the nature of these defects has been made, nor have they yet been induced in any useful pattern.

TABLE 3.3: Comparison of publications showing the influence of cw light on the poling properties of LN and LT.

Publication	Wavelength [nm]	Material	Face	Method	Result
[Kovalevich78]	440	Fe:LN	⊥ z	Focused	Induced additional Barkhausen pulses
[Houe95b]	532	LN	-z	Cu absorbing layer	Light-induced thermal poling
[Chao95] [Chao96]	Tungsten lamp Multi-line Ar$^+$	LT	z	Unfocused	Increase recovery rate of E_c
[Ross97] [Brown99]	351–364	CLT	y	Interference	Increase recovery rate of E_c
[Fujimura03]	UV lamp	Mg:CLN	z	Amplitude mask	E_c reduced by $\sim$ 10%
[Müller03a]	334, 351	CLN	z	Diffraction pattern	E_c reduced by $\sim$ 4%
[Dierolf04a]	488	CLN, Er:CLN	z	Direct-write	E_c reduced by $\sim$ 30%
[Wengler04] [Wengler05]	305, 334	CLN, Mg:CLN, Mg:SLN	z	Uniform & interference	E_c reduced by $\sim$ 50%
[Eggert04] [Eggert06]	488	Fe:SLN	⊥ z	Interference	Head-to-head domains by E_{sc}
[Morozovska03a] [Morozovska03b]	440	Fe:LN	x	Unfocused	Micro-domains at beam edge

A comparison of the previous work investigating the influence of light on the poling of LN and LT is summarized in Table 3.3.

3.6 Summary

Domain engineering in LN and LT has been studied extensively using electric-field poling. EFP has become a reliable and effective method of forming domain-inverted structures. However, this technique still exhibits several drawbacks: (1) reliance upon photolithography, adding complexity and cost; (2) limitation to periodic structures typically on the order of several micrometres; (3) a highly inhomogeneous E-field at the electrode edges and an unstructured E-field far from the surface; and (4) the requirement for very high voltages for domain inversion.

In recent years the impact of light on poling characteristics has gained considerable interest. However, optimal exposure conditions and processes for obtaining the desired domain structures has not been determined, nor have the kinetics of the growth under illumination been explored. The following chapters further investigate the interaction of light with the surface and poling properties of LN and LT in an effort to reduce or eliminate the disadvantages of EFP, and to open new opportunities for precision domain engineering.

Bibliography

[Abrahams66] S. C. Abrahams, J. M. Reddy, and J. L. Bernstein, *Ferroelectric lithium niobate: 3. Single crystal X-ray diffraction study at 24° C.* J. Phys. Chem. Solids, 27(6-7), 997–1012 (1966).

[Barry99] I. E. Barry, R. W. Eason, and G. Cook, *Light-induced frustration of etching in Fe-doped* $LiNbO_3$. Appl. Surf. Sci., 143(1-4), 328–331 (1999).

[Batchko99] R. G. Batchko, V. Y. Shur, M. M. Fejer, and R. L. Byer, *Backswitch poling in lithium niobate for high-fidelity domain patterning and efficient blue light generation.* Appl. Phys. Lett., 75(12), 1673–1675 (1999).

[Battle00] C. C. Battle, S. Kim, V. Gopalan, K. Barkocy, M. C. Gupta, Q. X. Jia, and T. E. Mitchell, *Ferroelectric domain reversal in congruent* $LiTaO_3$ *crystals at elevated temperatures.* Appl. Phys. Lett., 76(17), 2436–2438 (2000).

[Bermúdez00] V. Bermúdez, A. Gil, L. Arizmendi, J. Cochero, A. M. Baro, and E. Dieguez, *Techniques of observation and characterization of the domain structure in periodically poled lithium niobate.* J. Mater. Res., 15(12), 2814–21 (2000).

[Binnig86] G. Binnig, C. F. Quate, and C. Gerber, *Atomic force microscope.* Phys. Rev. Lett., 56(9), 930–933 (1986).

[Brown99] P. T. Brown, G. W. Ross, R. W. Eason, and A. R. Pogosyan, *Control of domain structures in lithium tantalate using interferometric optical patterning.* Optics Comm., 163(4-6), 310–316 (1999).

[Busacca02] A. C. Busacca, C. L. Sones, V. Apostolopoulos, R. W. Eason, and S. Mailis, *Surface domain engineering in congruent lithium niobate single crystals: A route to submicron periodic poling.* Appl. Phys. Lett., 81(26), 4946–4948 (2002).

[Busacca04] A. C. Busacca, C. L. Sones, R. W. Eason, and S. Mailis, *First-order quasi-phase-matched blue light generation in surface-poled Ti:indiffused lithium niobate waveguides.* Appl. Phys. Lett., 84(22), 4430–4432 (2004).

[Busacca05] A. C. Busacca, A. C. Cino, S. Riva-Sanseverino, M. Ravaro, and G. Assanto, *Silica masks for improved surface poling of lithium niobate.* Electron. Lett., 41(2), 92–93 (2005).

[Busacca06a] A. C. Busacca, M. Cherchi, S. R. Sanseverino, A. C. Cino, A. Parisi, S. Stivala, L. Colace, and G. Assanto, *Proton exchange channel waveguides compatible with surface domain engineering in lithium niobate crystals.* In Conference on Lasers and Electro-Optics, CMB4, OSA, Long Beach, USA (2006).

[Busacca06b] A. C. Busacca, C. Santini, S. R. Sanseverino, A. C. Cino, A. Parisi, and G. Assanto, *Surface periodic domain engineering in congruent lithium tantalate crystals.* In Conference on Lasers and Electro-Optics, CML2, OSA, Long Beach, USA (2006).

[Chao95] S. Chao, W. Davis, D. D. Tuschel, R. Nichols, M. Gupta, and H. C. Cheng, *Time dependence of ferroelectric coercive field after domain inversion for lithium-tantalate crystal.* Appl. Phys. Lett., 67(8), 1066–1068 (1995).

[Chao96] S. Chao and C.-C. Hung, *Large photoinduced ferroelectric coercive field increase and photodefined domain pattern in lithium-tantalate crystal.* Appl. Phys. Lett., 69(25), 3803–3805 (1996).

[Chen94] Q. Chen and W. P. Risk, *Periodic poling of $KTiOPO_4$ using an applied electric field.* Electron. Lett., 30(18), 1516–1517 (1994).

[Chen95] Q. Chen and W. P. Risk, *High-efficiency quasi-phase-matched waveguide device fabricated in $KTiOPO_4$ by electric-field poling.* In Conference on Lasers and Electro-Optics, CFA2, OSA, Baltimore, USA (1995).

[Chynoweth58] A. G. Chynoweth, *Barkhausen pulses in barium titanate.* Phys. Rev., 110(6), 1316–1332 (1958).

[Dierolf03] V. Dierolf, C. Sandmann, S. Kim, V. Gopalan, and K. Polgar, *Ferroelectric domain imaging by defect-luminescence microscopy.* J. Appl. Phys., 93(4), 2295–2297 (2003).

[Dierolf04a] V. Dierolf and C. Sandmann, *Direct-write method for domain inversion patterns in $LiNbO_3$.* Appl. Phys. Lett., 84(20), 3987–3989 (2004).

[Dierolf04b] V. Dierolf and C. Sandmann, *Inspection of periodically poled waveguide devices by confocal luminescence microscopy.* Appl. Phys. B, 78(3), 363–366 (2004).

[Eggert04] H. A. Eggert, B. Hecking, and K. Buse, *Electrical fixing in near-stoichiometric lithium niobate crystals.* Opt. Lett., 29(21), 2476–2478 (2004).

[Eggert06] H. A. Eggert, F. Kalkum, M. C. Wengler, U. Heinemeyer, and K. Buse, *Light-assisted generation of tailored ferroelectric domain structures.* Ferroelectrics, 340(1), 63–67 (2006).

[Eng98] L. M. Eng, H.-J. Guntherodt, G. Rosenman, A. Skliar, M. Oron, M. Katz, and D. Eger, *Nondestructive imaging and characterization of ferroelectric domains in periodically poled crystals.* J. Appl. Phys., 83(11), 5973–5977 (1998).

[Forsbergh49] P. W. Forsbergh, *Domain structures and phase transitions in barium titanate.* Phys. Rev., 76(8), 1187–1201 (1949).

[Fujimura91] M. Fujimura, T. Suhara, and H. Nishihara, *Ferroelectric-domain inversion induced by SiO_2 cladding for $LiNbO_3$ waveguide SHG.* Electron. Lett., 27(13), 1207–1209 (1991).

[Fujimura03] M. Fujimura, T. Sohmura, and T. Suhara, *Fabrication of domain-inverted gratings in MgO:$LiNbO_3$ by applying voltage under ultraviolet irradiation through photomask at room temperature.* Electron. Lett., 39(9), 719–721 (2003).

[Gopalan96a] V. Gopalan and M. C. Gupta, *Observation of internal field in $LiTaO_3$ single crystals: Its origin and time-temperature dependence.* Appl. Phys. Lett., 68(7), 888–890 (1996).

[Gopalan96b] V. Gopalan and M. C. Gupta, *Origin of internal field and visualization of 180° domains in congruent $LiTaO_3$ crystals.* J. Appl. Phys., 80(11), 6099–6106 (1996).

[Gopalan98a] V. Gopalan and T. E. Mitchell, *Wall velocities, switching times, and the stabilization mechanism of 180° domains in congruent $LiTaO_3$ crystals.* J. Appl. Phys., 83(2), 941–954 (1998).

[Gopalan98b] V. Gopalan, T. E. Mitchell, Y. Furukawa, and K. Kitamura, *The role of nonstoichiometry in 180° domain switching of $LiNbO_3$ crystals.* Appl. Phys. Lett., 72(16), 1981–1983 (1998).

[Gopalan99a] V. Gopalan and T. E. Mitchell, *In situ video observation of 180° C domain switching in $LiTaO_3$ by electro-optic imaging microscopy.* J. Appl. Phys., 85(4), 2304–2311 (1999).

[Gopalan99b] V. Gopalan, T. E. Mitchell, and K. E. Sicakfus, *Switching kinetics of 180° domains in congruent $LiNbO_3$ and $LiTaO_3$ crystals*. Solid State Comm., 109(2), 111–117 (1999).

[Gopalan01] V. Gopalan, N. A. Sanford, J. A. Aust, K. Kitamura, and Y. Furukawa, *Crystal growth, characterization, and domain studies in lithium niobate and lithium tantalate ferroelectrics*. In H. S. Nalwa (editor), Ferroelectrics and Dielectrics, volume 4 of *Handbook of Advanced Electronic and Photonic Materials and Devices*, 57–114, Academic Press, San Diego, USA (2001).

[Grilli05] S. Grilli, P. Ferraro, P. De Natale, B. Tiribilli, and M. Vassalli, *Surface nanoscale periodic structures in congruent lithium niobate by domain reversal patterning and differential etching*. Appl. Phys. Lett., 87(23), 233106 (2005).

[Haycock86] P. W. Haycock and P. D. Townsend, *A method of poling $LiNbO_3$ and $LiTaO_3$ below T_c*. Appl. Phys. Lett., 48(11), 698–700 (1986).

[Hirohashi05] J. Hirohashi and V. Pasiskevicius, *Quasi-phase-matched frequency conversion in $KNbO_3$ structures consisting of 90° ferroelectric domains*. Appl. Phys. B, 81(6), 761–763 (2005).

[Hong98] J. W. Hong, K. H. Noh, S.-i. Park, S. I. Kwun, and Z. G. Khim, *Surface charge density and evolution of domain structure in triglycine sulfate determined by electrostatic-force microscopy*. Phys. Rev. B, 58(8), 5078–5084 (1998).

[Houe95a] M. Houe and P. Townsend, *An introduction to methods of periodic poling for second-harmonic generation*. J. Phys. D, 28(9), 1747–1763 (1995).

[Houe95b] M. Houe and P. D. Townsend, *Thermal polarization reversal of lithium niobate*. Appl. Phys. Lett., 66(20), 2667–2669 (1995).

[Hu02] G. Hu, T. Tang, and J. Xu, *Tip effects of piezoelectric-mode atomic force microscope for local piezoelectric measurements of an $SrBi_2Ta_2O_9$ thin film*. Jpn. J. Appl. Phys., 41(1, 11B), 6793–6796 (2002).

[Hu03] M.-L. Hu, L.-J. Hu, and J.-Y. Chang, *Polarization switching of pure and MgO-doped lithium niobate crystals*. Jpn. J. Appl. Phys., 42, Part 1(12), 7414–7417 (2003).

[Huang94] L. Huang and N. A. F. Jaeger, *Discussion of domain inversion in $LiNbO_3$*. Appl. Phys. Lett., 65(14), 1763 (1994).

[Ishizuki03] H. Ishizuki, I. Shoji, and T. Taira, *Periodical poling characteristics of congruent MgO:$LiNbO_3$ crystals at elevated temperature*. Appl. Phys. Lett., 82(23), 4062–4064 (2003).

[Ito91] H. Ito, C. Takyu, and H. Inaba, *Fabrication of periodic domain grating in $LiNbO_3$ by electron beam writing for application of nonlinear optical processes*. Electron. Lett., 27(14), 1221–1222 (1991).

[Jungk06] T. Jungk, A. Hoffmann, and E. Soergel, *Quantitative analysis of ferroelectric domain imaging with piezoresponse force microscopy*. Appl. Phys. Lett., 89(16), 163507 (2006).

[Jungk07] T. Jungk, H. , and E. Soergel, *Influence of the inhomogeneous field at the tip on quantitative piezoresponse force microscopy*. Appl. Phys. A, 86(3), 353–355 (2007).

[Kalinin02] S. V. Kalinin and D. A. Bonnell, *Imaging mechanism of piezoresponse force microscopy of ferroelectric surfaces*. Phys. Rev. B, 65(12), 125408 (2002).

[Keys90] R. Keys, A. Loni, R. de la Rue, C. Ironside, J. Marsh, B. Luff, and P. Townsend, *Fabrication of domain reversed gratings for SHG in LiNbO$_3$ by electron beam bombardment.* Electron. Lett., 26(3), 188–190 (1990).

[Kim01] S. Kim, V. Gopalan, K. Kitamura, and Y. Furukawa, *Domain reversal and nonstoichiometry in lithium tantalate.* J. Appl. Phys., 90(6), 2949–2963 (2001).

[Kim05] S. Kim and V. Gopalan, *Optical index profile at an antiparallel ferroelectric domain wall in lithium niobate.* Mater. Sci. Eng. B, 120, 91–94 (2005).

[Kolosov95] O. Kolosov, A. Gruverman, J. Hatano, K. Takahashi, and H. Tokumoto, *Nanoscale visualization and control of ferroelectric domains by atomic force microscopy.* Phys. Rev. Lett., 74(21), 4309–4312 (1995).

[Kovalevich78] V. I. Kovalevich, L. A. Shuvalov, and T. R. Volk, *Spontaneous polarization reversal and photorefractive effect in single-domain iron-doped lithium niobate crystals.* Phys. Stat. Sol. A, 45(1), 249–252 (1978).

[Kurimura97] S. Kurimura and Y. Uesu, *Application of the second harmonic generation microscope to nondestructive observation of periodically poled ferroelectric domains in quasi-phase-matched wavelength converters.* J. Appl. Phys., 81(1), 369–375 (1997).

[Li06] X. Li, K. Terabe, H. Hatano, H. Zeng, and K. Kitamura, *Domain patterning thin crystalline ferroelectric film with focused ion beam for nonlinear photonic integrated circuits.* J. Appl. Phys., 100(10), 106103 (2006).

[Magel90] G. A. Magel, M. M. Fejer, and R. L. Byer, *Quasi-phase-matched second-harmonic generation of blue light in periodically poled LiNbO$_3$*. Appl. Phys. Lett., 56(2), 108–110 (1990).

[Mailis02] S. Mailis, P. T. Brown, C. L. Sones, I. Zergioti, and R. W. Eason, *Etch frustration in congruent lithium niobate single crystals induced by femtosecond ultraviolet laser irradiation.* Appl. Phys. A, 74(2), 135–137 (2002).

[Miller60] R. C. Miller and G. Weinreich, *Mechanism for the sidewise motion of 180° domain walls in barium titanate.* Phys. Rev., 117(6), 1460–1466 (1960).

[Miller98] G. D. Miller, Periodically poled lithium niobate: Modeling, fabrication, and nonlinear-optical performance. Ph.D. thesis, Stanford University (1998).

[Miyazawa79] S. Miyazawa, *Ferroelectric domain inversion in Ti-diffused LiNbO$_3$ optical waveguides.* J. Appl. Phys., 50(7), 4599–4603 (1979).

[Mizuuchi04] K. Mizuuchi, A. Morikawa, T. Sugita, and K. Yamamoto, *Electric-field poling in Mg-doped LiNbO$_3$*. J. Appl. Phys., 96(11), 6585–6590 (2004).

[Mohageg05] M. Mohageg, D. V. Strekalov, A. A. Savchenkov, A. B. Matsko, V. S. Ilchenko, and L. Maleki, *Calligraphic poling of lithium niobate.* Opt. Express, 13(9), 3408–3419 (2005).

[Morozovska03a] A. N. Morozovska, E. A. Eliseev, and V. V. Obukhovsky, *Light induced micro-domains in ferroelectrics.* Ferroelectrics, 288, 265–275 (2003).

[Morozovska03b] A. N. Morozovska, E. A. Eliseev, V. V. Obukhovsky, and V. V. Lemeshko, *Photo-microdomains in ferroelectrics: formation and light scattering caused by them.* Semiconductor Physics, Quantum Electronics & Optoelectronics, 6(3), 324–332 (2003).

[Müller03a] M. Müller, E. Soergel, and K. Buse, *Influence of ultraviolet illumination on the poling characteristics of lithium niobate crystals*. Appl. Phys. Lett., 83(9), 1824–6 (2003).

[Müller03b] M. Müller, E. Soergel, and K. Buse, *Visualization of ferroelectric domains with coherent light*. Opt. Lett., 28(24), 2515–2517 (2003).

[Müller04] M. Müller, E. Soergel, M. C. Wengler, and K. Buse, *Light deflection from ferroelectric domain boundaries*. Appl. Phys. B, 78, 367–370 (2004).

[Müller05] M. Müller, E. Soergel, K. Buse, C. Langrock, and M. M. Fejer, *Investigation of periodically poled lithium niobate crystals by light diffraction*. J. Appl. Phys., 97(4), 044102 (2005).

[Myers95] L. E. Myers, R. C. Eckardt, M. M. Fejer, R. L. Byer, W. R. Bosenberg, and J. W. Pierce, *Quasi-phase-matched optical parametric oscillators in bulk periodically poled* $LiNbO_3$. J. Opt. Soc. Am. B, 12(11), 2102–2116 (1995).

[Nai-Ben82] M. Nai-Ben, H. Jing-Fen, and F. Duan, *The growth striations and ferroelectric domain structures in Czochralski-grown* $LiNbO_3$ *single crystals*. J. Mater. Sci., 17(6), 1663–1670 (1982).

[Nakamura87] K. Nakamura, H. Ando, and H. Shimizu, *Ferroelectric domain inversion caused in* $LiNbO_3$ *plates by heat treatment*. Appl. Phys. Lett., 50(20), 1413–1414 (1987).

[Nakamura02] K. Nakamura, J. Kurz, K. Parameswaran, and M. M. Fejer, *Periodic poling of magnesium-oxide-doped lithium niobate*. J. Appl. Phys., 91(7), 4528–4534 (2002).

[Niizeki67] N. Niizeki, T. Yamada, and H. Toyoda, *Growth ridges, etched hillocks, and crystal structure of lithium niobate*. Jap. J. Appl. Phys., 6(3), 318–326 (1967).

[Ogi02] H. Ogi, Y. Kawasaki, M. Hirao, and H. Ledbetter, *Acoustic spectroscopy of lithium niobate: Elastic and piezoelectric coefficients*. J. Appl. Phys., 92(5), 2451–2456 (2002).

[Ohgaki92] M. Ohgaki, K. Tanaka, and F. Marumo, *Structure refinement of lithium (I) niobium (V) trioxide,* $LiNbO_3$*, with anharmonic thermal vibration model*. Mineralogical J., 16(3), 150–160 (1992).

[Ohmori75] Y. Ohmori, Y. Yasojima, and Y. Inuishi, *Photoconduction, thermally stimulated luminescence, and optical damage in single crystal of* $LiNbO_3$. Jpn. J. Appl. Phys., 14(9), 1291–1300 (1975).

[Peng06] L. H. Peng, Y. H. Chen, C. D. Lin, L. F. Lin, and A. H. Kung, *Sub-micrometer domain engineering on periodically poled lithium niobate*. J. Cryst. Growth, 292(2), 328–331 (2006).

[Poghosyan03] A. R. Poghosyan, *Optical control of domain structures in lithium tantalate crystals*. J. Optoelectron. Adv. Mater., 5(3), 735–740 (2003).

[Qin97] Y.-q. Qin, Y.-y. Zhu, S.-n. Zhu, H. Shu, and N.-b. Ming, *Electron probe microanalysis of periodic domain inversion in* $LiNbO_3$ *by Ti diffusion*. Mater. Lett., 30(2-3), 231–234 (1997).

[Rosenman00] G. Rosenman, D. Shur, Y. E. Krasik, and A. Dunaevsky, *Electron emission from ferroelectrics*. J. Appl. Phys., 88(11), 6109–6161 (2000).

[Rosenman03] G. Rosenman, P. Urenski, A. Agronin, Y. Rosenwaks, and M. Molotskii, *Submicron ferroelectric domain structures tailored by high-voltage scanning probe microscopy.* Appl. Phys. Lett., 82(1), 103–105 (2003).

[Ross97] G. W. Ross, P. G. R. Smith, and R. W. Eason, *Optical control of electric field poling in* $LiTaO_3$. Appl. Phys. Lett., 71(3), 309–311 (1997).

[Ross98] G. W. Ross, M. Pollnau, P. G. R. Smith, W. A. Clarkson, P. E. Britton, and D. C. Hanna, *Generation of high-power blue light in periodically poled* $LiNbO_3$. Opt. Lett., 23(3), 171–173 (1998).

[Saurenbach90] F. Saurenbach and B. D. Terris, *Imaging of ferroelectric domain walls by force microscopy.* Appl. Phys. Lett., 56(17), 1703–1705 (1990).

[Sheng06] Y. Sheng, T. Wang, B. Ma, E. Qu, B. Cheng, and D. Zhang, *Anisotropy of domain broadening in periodically poled lithium niobate crystals.* Appl. Phys. Lett., 88(4), 041121 (2006).

[Shur96] V. Y. Shur, *Fast polarization reversal process: Evolution of ferroelectric domain structure in thin films.* In C. A. P. d. Araujo, J. F. Scott, and G. W. Taylor (editors), Ferroelectric thin films: Synthesis and basic properties, Ferroelectricity and related phenomena, 153–192, Gordon & Breach Science Publishers (1996).

[Shur00] V. Y. Shur, E. L. Rumyantsev, E. V. Nikolaeva, E. I. Shishkin, D. V. Fursov, R. G. Batchko, L. A. Eyres, M. M. Fejer, and R. L. Byer, *Nanoscale backswitched domain patterning in lithium niobate.* Appl. Phys. Lett., 76(2), 143–145 (2000).

[Shur02] V. Y. Shur, E. L. Rumyantsev, E. V. Nikolaeva, E. I. Shishkin, R. B. Batchko, M. M. Fejer, R. L. Byer, and I. Mnushkina, *Domain kinetics in congruent and stoichiometric lithium niobate.* Ferroelectrics, 269, 189–194 (2002).

[Shur05a] V. Y. Shur, *Correlated nucleation and self-organized kinetics of ferroelectric domains.* In J. W. P. Schmelzer (editor), Nucleation theory and applications, 178–214, Wiley (2005).

[Shur05b] V. Y. Shur, A. I. Lobov, A. G. Shur, S. Kurimura, Y. Nomura, K. Terabe, X. Y. Liu, and K. Kitamura, *Rearrangement of ferroelectric domain structure induced by chemical etching.* Appl. Phys. Lett., 87(2), 022905 (2005).

[Shur06] V. Y. Shur, D. K. Kuznetsov, A. I. Lobov, E. V. Nikolaeva, M. A. Dolbilov, A. N. Orlov, and V. V. Osipov, *Formation of self-similar surface nano-domain structures in lithium niobate under highly nonequilibrium conditions.* Ferroelectrics, 341(1), 85–93 (2006).

[Soergel05] E. Soergel, *Visualization of ferroelectric domains in bulk single crystals.* Appl. Phys. B, 81(6), 729–751 (2005).

[Sones02] C. L. Sones, S. Mailis, W. S. Brocklesby, R. W. Eason, and J. R. Owen, *Differential etch rates in z-cut* $LiNbO_3$ *for variable* HF/HNO_3 *concentrations.* J. Mater. Chem., 12(2), 295–298 (2002).

[Sono06] T. J. Sono, J. G. Scott, C. L. Sones, C. E. Valdivia, S. Mailis, R. W. Eason, J. G. Frey, and L. Danos, *Reflection second harmonic generation on a z-cut congruent lithium niobate crystal.* Phys. Rev. B, 74(20), 205424 (2006).

[Tanaka06] K. Tanaka, Y. Hiranaga, and Y. Cho, *Real information storage using ferroelectrics with a density of 1 Tbit/inch*^{2}. Ferroelectrics, 340(1), 99–105 (2006).

[Tian04] L. Tian, V. Gopalan, and L. Galambos, *Domain reversal in stoichiometric* $LiTaO_3$ *prepared by vapor transport equilibration*. Appl. Phys. Lett., 85(19), 4445–4447 (2004).

[Tian05a] L. Tian and V. Gopalan, *Comparison of domain reversal and electro-optic properties of congruent and stoichiometric lithium tantalate*. In Integrated Optics: Devices, Materials, and Technologies IX, volume 5728, 278–282, SPIE, San Jose, CA, USA (2005).

[Tian05b] L. Tian, D. A. Scrymgeour, and V. Gopalan, *Real-time study of domain dynamics in ferroelectric* $Sr_{0.61}Ba_{0.39}Nb_2O_6$. J. Appl. Phys., 97(11), 114111 (2005).

[Uesu04] Y. Uesu, H. Shibata, S. Suzuki, and S. Shimada, *3D images of inverted domain structure in* $LiNbO_3$ *using SHG interference microscope*. Ferroelectrics, 304, 99–103 (2004).

[Webjörn89a] J. Webjörn, F. Laurell, and G. Arvidsson, *Blue light generated by frequency doubling of laser diode light in a lithium niobate channel waveguide*. Photon. Technol. Lett., 1(10), 316–318 (1989).

[Webjörn89b] J. Webjörn, F. Laurell, and G. Arvidsson, *Fabrication of periodically domain-inverted channel waveguides in lithium niobate for second harmonic generation*. J. Lightwave Technol., 7(10), 1597–1600 (1989).

[Webjörn94] J. Webjörn, V. Pruneri, P. S. Russell, J. R. M. Barr, and D. C. Hanna, *Quasi-phase-matched blue-light generation in bulk lithium niobate, electrically poled via periodic liquid electrodes*. Electron. Lett., 30(11), 894–895 (1994).

[Wengler03] M. C. Wengler, M. Müller, E. Soergel, and K. Buse, *Poling dynamics of lithium niobate crystals*. Appl. Phys. B, 76(4), 393–396 (2003).

[Wengler04] M. C. Wengler, B. Fassbender, E. Soergel, and K. Buse, *Impact of ultraviolet light on coercive field, poling dynamics and poling quality of various lithium niobate crystals from different sources*. J. Appl. Phys., 96(5), 2816–2820 (2004).

[Wengler05] M. C. Wengler, U. Heinemeyer, E. Soergel, and K. Buse, *Ultraviolet light-assisted domain inversion in magnesium-doped lithium niobate crystals*. J. Appl. Phys., 98(6), 064104 (2005).

[Xue02] D. Xue and K. Kitamura, *Origin of differential etching rates of the* $+z$ *and* $-z$ *faces of lithium niobate crystal*. Ferroelectr. Lett., 29(5-6), 89 (2002).

[Xue03] D. Xue, S. Wu, Y. Zhu, K. Terabe, K. Kitamura, and J. Wang, *Nanoscale domain switching at crystal surfaces of lithium niobate*. Chem. Phys. Lett., 377(3-4), 475 (2003).

[Yamada91] M. Yamada and K. Kishima, *Fabrication of periodically reversed domain structure for SHG in* $LiNbO_3$ *by direct electron beam lithography at room temperature*. Electron. Lett., 27(10), 828–829 (1991).

[Yamada93] M. Yamada, N. Nada, M. Saitoh, and K. Watanabe, *First-order quasi-phase matched* $LiNbO_3$ *waveguide periodically poled by applying an external field for efficient blue second-harmonic generation*. Appl. Phys. Lett., 62(5), 435–436 (1993).

[Yamada98] M. Yamada and M. Saitoh, *Fabrication of a periodically poled laminar domain structure with a pitch of a few micrometers by applying an external electric field*. J. Appl. Phys., 84(4), 2199–2206 (1998).

[Yang99] T. J. Yang, V. Gopalan, P. J. Swart, and U. Mohideen, *Direct observation of pinning and bowing of a single ferroelectric domain wall.* Phys. Rev. Lett., 82(20), 4106–4109 (1999).

[Zhang05] X. Zhang, D. Xue, and K. Kitamura, *Domain characteristics and chemical bonds of lithium niobate.* Mater. Sci. Eng. B, 120, 21–26 (2005).

Chapter 4

Ultraviolet-Light-Induced Surface Modification

With the ultraviolet (UV) absorption band-edge of congruent lithium niobate (CLN) typically near $\lambda = 320$ nm, UV light with wavelengths below this cut-off are expected to interact with the material with a fundamentally different behavior than weakly absorbed wavelengths above the band-edge. The penetration depth rapidly decreases with decreasing wavelength, diminishing to ~50 nm for $\lambda = 200$ nm [Mamedov84]. Due to these short penetration depths, UV light strongly interacts with the surface of LN. Accordingly, very different results have been observed upon UV illumination of the +z and −z faces. Therefore, the results of +z face illumination have been separated into Chapter 5, while the investigations of −z face illumination are discussed below.

Several prior experiments have investigated the interaction of UV light with CLN. The interference of $\lambda = 248$ nm ns-pulsed light (producing only minor damage), followed by short-duration HF etching, revealed surface relief gratings on both x and z faces [Mailis00]. On the x face, irradiated regions experienced a faster etch rate and the maximum etch depth was found to depend upon the penetration depth of the wavelength used [Brown02]. On the −z face, however, the regions irradiated by ~100 mJ/cm^2 showed a reduced etch rate of ~0.15 µm/hr as compared to unmodified regions with an etch rate of ~0.55 µm/hr [Brown02]. Etch frustration was also demonstrated using $\lambda = 248$ nm sub-ps pulsed light [Mailis02] and $\lambda = 244$ nm cw light [Mailis03] with fluences below their respective ablation thresholds. Recently, diffraction and interference of 248 nm ns-pulsed light has produced sub-micron etch frustration patterns [Mailis05b].

Etch frustrated features have also been demonstrated when using cw visible illumination of Fe:LN in an HF acid environment, forming a self-organized arrangement of surface features on the −z face in a process referred to as light-induced frustrated etching (LIFE) [Scott04].

The experiments included herein sought to form domain inversion via illumination without an applied electric field, and investigated the nature of the etch frustrated sub-micron features across an important range of exposure conditions on the $-$z face of undoped CLN. Some of the results presented below have been reported in [Mailis05c; Sones05].

4.1 Experimental Setup

The experimental procedure involved the illumination of the $-$z face of undoped LN to investigate the effects of UV light on the surface. The exposed crystals were 500-µm thick z-cut optically-polished CLN wafers purchased from Crystal Technology Ltd.

The $-$z face was illuminated by one of two laser systems. The first was a KrF excimer laser (Lambda Physik LPX 200) operating at a wavelength of $\lambda = 248$ nm with a pulse duration of $\sim$20 ns. The second was a frequency-doubled Q-switched Nd:YAG laser (Continuum Powerlite 8000) which was used to pump a frequency-doubled dye laser (Sirah PrecisionScan). This system output millijoule pulses of wavelengths ranging from 298–329 nm with pulse durations of $\sim$7 ns.

Both of these laser systems suffered from poor spatial uniformity. To minimize this effect, a rectangular aperture was used to select the central region of each beam where the intensity uniformity was improved. However, the results of these experiments were still affected by the remaining non-uniformity of the beam, as will be discussed in Section 4.2. The beam fluence was calculated as the energy per pulse divided by the area of the rectangular spot on the target, representing an averaged value.

The $-$z face of CLN was exposed to fluences both above and below the ablation threshold. The beam was either imaged directly onto the crystal or illuminated a phase mask. The phase masks were held above the crystal face at a distance of 125 µm using optical fibres as accurate spacers for repeatable results. The phase masks were optimized for 248- and 298-nm wavelengths and had a grating period of $\Lambda = 726$ nm. The number of pulses incident on the crystal was varied from 1–200.

After illumination, the crystals were etched in HF at room temperature for durations ranging from several minutes up to an hour. The resulting surface topography was examined by SEM, surface profilometer, and SFM.

4.2 Results

The results of UV exposure of the $-$z face of LN was strongly dependent upon the fluence. These results can be divided into two broad categories by the use of fluences

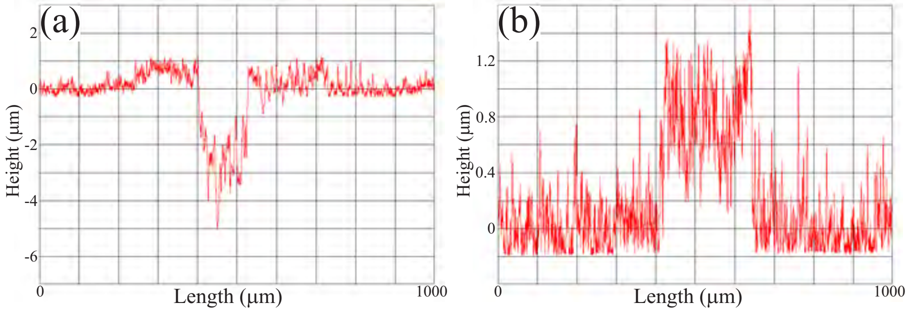

Figure 4.1: Surface profiles of UV illumination (a) above and (b) below the ablation threshold of undoped CLN using $\lambda = 321$ nm light. The samples have been HF-etched for 30 minutes.

on either side of the ablation threshold. Representative profilometer scans across illuminated areas with an HF etch of 30 minutes are displayed in Figure 4.1, showing the effect of UV illumination with fluences (a) above and (b) below the ablation threshold.

In the case of fluence above the ablation threshold, simple ablation occurred, as expected, and was not further studied on the $-z$ crystal face. However for fluences *below* the ablation threshold, the crystal became hydrophilic and displayed an effect referred to as *etch frustration*, both discussed further in the following sections.

4.2.1 UV-Induced Hydrophilicity

CLN is naturally hydrophobic. Upon UV illumination by low fluences, however, the surface can become hydrophilic. The likely reason for this change to hydrophilicity is the photo- and thermal-generation of charge caused by the strong absorption of UV light at the surface. This UV-induced hydrophilic effect has been rigorously explored in [Muir07], where the effect has been attributed to the formation of hydrophilic hydroxyl groups on the surface.

The UV-induced hydrophilic effect can be used for selective nanoparticle deposition due to electro-static interaction with the irradiated regions, investigated via a collaboration with Patrick Hole and Collin Sones (University of Southampton). A droplet of latex-bead suspension was placed on the surface of a UV-irradiated CLN crystal. Evaporation allowed preferential deposition of the latex beads (diameter of 1–3 µm) onto the illuminated regions of the CLN samples. Deposition was particularly concentrated at the edges of the illuminated regions where the intensity gradient was largest and photo-generated charges accumulated, as shown in Figure 4.2. Gold nanoparticles also showed similar deposition patterns.

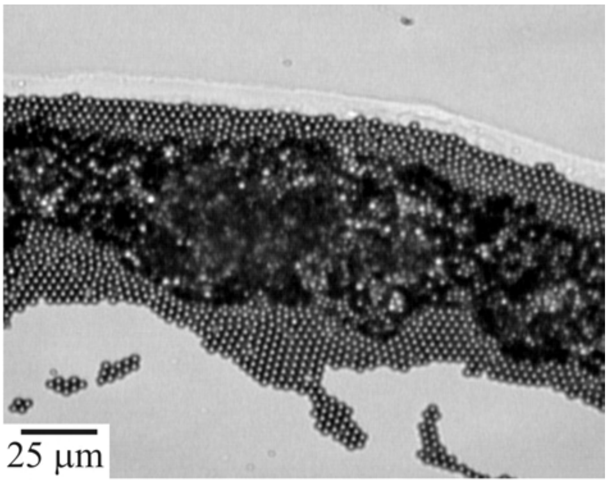

Figure 4.2: Latex nanoparticles selectively deposited onto the UV-exposed regions of CLN, concentrating along the edges of the region illuminated by 25 pulses of $\lambda = 248$ nm with a fluence of 40 mJ/cm^2.

In a similar recent technique, the charged surfaces of ferroelectric domains in LN have been exploited to allow the visualization of the crystal domain structure. Electrostatically-driven preferential deposition of charged polystyrene nanoparticles achieved patterned decoration of PPLN visible under an optical microscope [Ke07]. The difference in the UV-induced hydrophilic deposition technique is the flexibility and simplicity inherent in the patterning of the UV illumination region for controlled deposition of materials.

4.2.2 Etch Frustration

UV-induced etch frustration is a process whereby the illumination of the $-$z face of CLN caused a reduction in the subsequent HF-etch rate. This effect has been clearly demonstrated using cw, ns-pulsed, and sub-ps-pulsed light of $\lambda = 244$–248 nm in several prior publications [Brown02; Mailis02; Mailis03; Mailis05b]. Some of these results have been reproduced using 248 nm ns-pulsed light from a KrF laser and the exposure range expanded to investigate the nature of the etch frustrated features.

Unpatterned illumination of the $-$z face of undoped CLN by low fluence ($\sim$35 mJ/cm^2) was insufficient to cause ablation or any visible surface modification, verified by optical microscopy and surface profiling. However, as noted in Section 4.2.1, the illuminated areas exhibited hydrophilicity. This effect allowed the visualization of the exposed regions by passing humid air over the surface (for example, blowing on the sample), with the water vapor preferentially spreading over the irradiated areas. After HF etching, the UV-exposed regions were clearly visible to the naked eye as frosted patches. When visualized under SEM, this effect exhibited roughness across the illuminated spot, as shown in Figure 4.3(a). Under higher magnification, Figure 4.3(b) shows that this roughness was composed of randomly-positioned tiny, roundish dots. The bright white spot in the

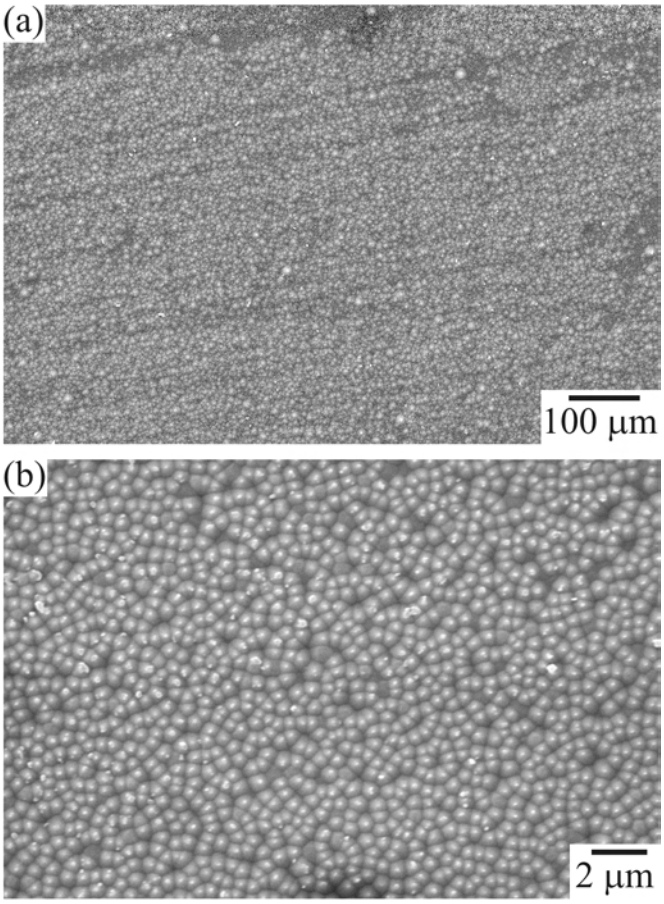

Figure 4.3: Etch frustration of the −z face of undoped CLN produced by unpatterned $\lambda = 248$ nm UV exposure of 20 pulses with ∼35 mJ/cm^2/pulse, viewed by SEM over (a) large area and (b) small area of the beam.

center of these dots in the SEM image indicate an edge where charge accumulated, such as a sharp peak.

At the edge of illumination, the etch dots disappear and the surface is much smoother, as shown in Figure 4.4, where the illuminated region appears on the right side of the image. However, tiny isolated dots remained visible away from the illuminated regions. These dots were present even on unilluminated crystals in the normal process of HF etching, appearing on the −z face only. Occasionally an entire crystal face appeared frosted due to the large number of these etch dots, although never in the high density induced within the illuminated regions.

A single etch dot is shown under high magnification in the inset of Figure 4.4. This inset clearly shows that these etch dots are in fact three-face pyramidal structures. Accordingly, a sharp peak appears in the center, as expected from previous images. Interestingly, this exact shape is expected from the etch profile of an inverted domain on the −z face due to the preferential lateral etching along the three y axes, as demonstrated in [Mailis05a].

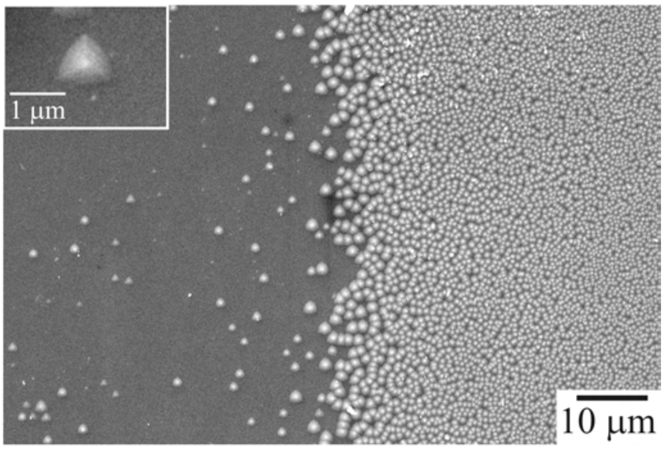

FIGURE 4.4: SEM micrograph of the edge of an etch frustration region on the −z face of undoped CLN produced by unpatterned $\lambda = 248$ nm UV exposure of 20 pulses with ~35 mJ/cm^2/pulse. The inset shows the triangular shape of the typical etch features outside of the irradiated region.

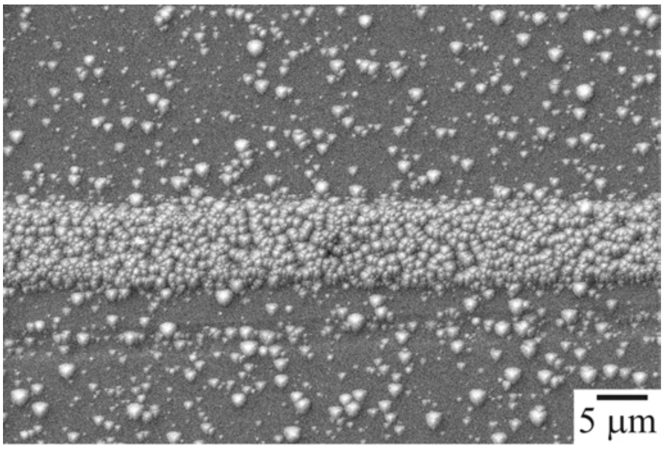

FIGURE 4.5: SEM micrograph of etch frustration resulting from cw UV scanned exposure using 50 mW of $\lambda = 244$ nm focused to a spot size of ~6 μm and scanned at a rate of 50 mm/minute.

Similar structures were also observed using frequency-doubled light from an Ar$^+$ laser ($\lambda = 244$ nm). Scanning the beam in a straight line, Sakellaris Mailis and Iain Wellington (University of Southampton) produced a similar exposure region with a high density of etch dots, shown in Figure 4.5, indicating that the higher peak intensities of pulsed light are not a requirement for the appearance of etch frustration.

All of the above examples of UV-modified surface etching exhibited a reduction in the etch rate as compared to the surrounding unilluminated regions, and is therefore referred to as “frustrated etching”. However another process has been observed, particularly near the edges of an illuminated region, where “enhanced etching” has occurred, etching at a rate faster than the unilluminated region. This effect also results in a smoother etch profile, free of the etch dots. While this effect could be very useful in the fabrication

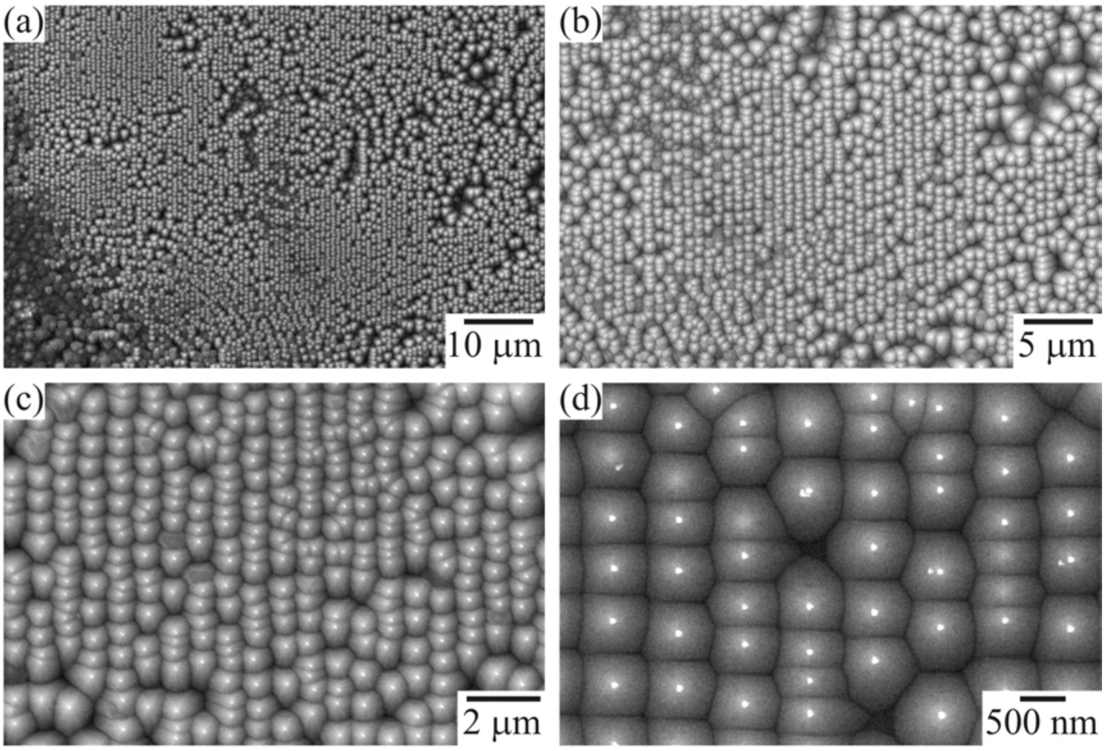

Figure 4.6: SEM micrographs of typical results of $\lambda = 248$ nm pulsed UV exposure through a phase mask of $\Lambda = 726$ nm onto the −z face of undoped CLN. The regions were exposed to several pulses with a fluence of ∼200 mJ/cm^2.

of surface structures, particularly those created by etched domain structures such as in [Sones02], obtaining this effect reliably from crystal to crystal was difficult, indicating that this effect may be highly dependent upon the surface properties. Additionally, as this effect has primarily been observed near the edges of the beam, it may rely upon a gradient of fluence rather than upon a specific value of fluence. Up to the present, no consistent results have been achieved showing enhanced etching.

4.2.3 Periodically-Patterned Etch Features

Periodic patterning of the etch-frustrated features was investigated via illumination through a $+1/-1$ order phase mask with a period of $\Lambda = 726$ nm and designed for a wavelength of $\lambda = 246$ nm, as detailed above in Section 4.1. Periodic illumination with fluences below the ablation threshold produced etch dots similar to the case of unpatterned illumination, however it provided control over the size, spacing, and alignment of these etch dots, as shown under several magnifications in Figure 4.6. Variations in the periodic pattern shows that the formation of these features are highly sensitive to the local illumination conditions and material properties.

The images of Figure 4.6 show that the frustrated etch features reproduce the phase mask pattern along the axis of periodicity. However using a phase mask of this type, an intensity pattern with half the period of the phase mask (363 nm) was expected. The consistent appearance of features on a scale equal to the period of the phase mask indicate that the diffracted 0-order beam could not be neglected. This may be due to the combination of the non-optimal wavelength (248 nm), a small angle away from normal incidence, and low quality of the phase mask. Nonetheless, regions exhibiting a period of 363 nm have also been observed [Mailis05b], although this occurred much less frequently.

Perpendicular to the phase mask grating vector, the etched feature sizes were not directly controlled in a periodic manner. Nonetheless the lengths of these features were similar to their widths. It is likely that through two-dimensional periodic patterning (such as through the use of a two-dimensionally periodic phase mask), the size of these features may be controlled in both spatial directions.

The effect of etch frustration is highly sensitive to incident fluence, as seen in Figure 4.6(a), where variations across the illumination region caused imperfections in the periodic pattern. Surprisingly, increasing the fluence towards the ablation threshold caused the surface to become *smoother*, as depicted in Figure 4.7. With a fluence of $\sim$340 mJ/cm^2, the etched dots began to merge along the periodic intensity lines (a). A fluence of $\sim$370 mJ/cm^2 began to show merging of the peaks of these etch dots (b). Increasing the fluence further allowed a greater merger between adjacent etch dots (c–e) until merging occurred between adjacent lines (f). Counter-intuitively, illumination by fluences approaching the ablation threshold caused the merger of dots, forming a smooth surface after etching.

A similar trend has recently been observed by Sakellaris Mailis and Alistair Muir (University of Southampton) in unpublished work investigating the interaction of scanned cw UV light of $\lambda = 244$ nm from a frequency-doubled Ar$^+$ laser. Increasing the intensity or dwell-time of the beam altered the scanned region from a rounded line [as in Figure 4.7(a)] to a straight line with a smooth, fully-connected top surface [as in Figure 4.7(c–d)].

A possible explanation for the above trend is *UV-induced domain inversion.* If domain inversion had occurred, a +z domain face would be presented, resisting etching and hence providing the smooth surface observed. The validity of this proposal is evaluated in the following sections.

4.2.4 Scanning Force Microscopy

Scanning force microscopy (SFM) has become a powerful tool for non-destructive visualization and manipulation of domain engineered materials. Therefore, this technique was applied to the crystals having either unpatterned or periodically-patterned illumination

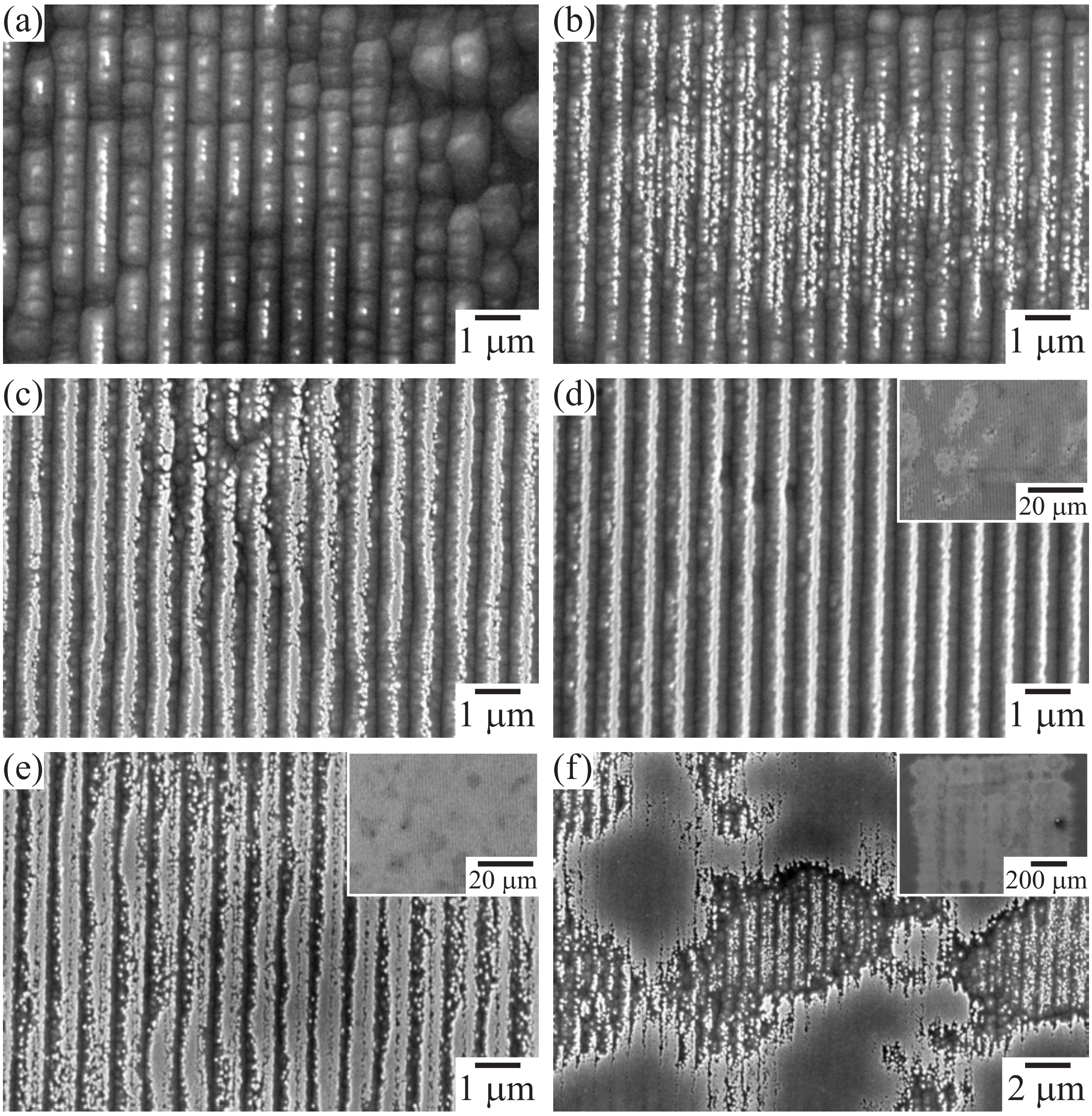

Figure 4.7: SEM micrographs showing progressively more merging of UV-induced features formed via 10-pulse illumination with $\lambda = 248$ nm light through a phase mask of $\Lambda = 726$ nm, by increasing the fluence of each spot: (a) 340, (b) 370, (c) 400, (d) 430, (e) 460, (f) 490 mJ/cm^2. The insets show the same illumination conditions at lower magnification.

with fluences below the ablation threshold. These crystals were *not* HF-etched after illumination as this process may destroy the features intended for further visualization.

Access to SFM facilities and expertise was made available by collaboration with Professor Karsten Buse's group at the University of Bonn, Germany, and Associate Professor Venkatraman Gopalan's group at Pennsylvania State University, USA. At each of these locations, a custom-modified AFM was fitted with an electrically-conductive tip through which oscillating voltages applied large electric fields locally over the surface of a sample under test. A lock-in amplifier supplied the voltage, typically $V_{\text{applied}} = 10$ V peak-to-peak and $f \simeq 35$ kHz, and detected the resulting oscillation of the AFM cantilever. Stiff

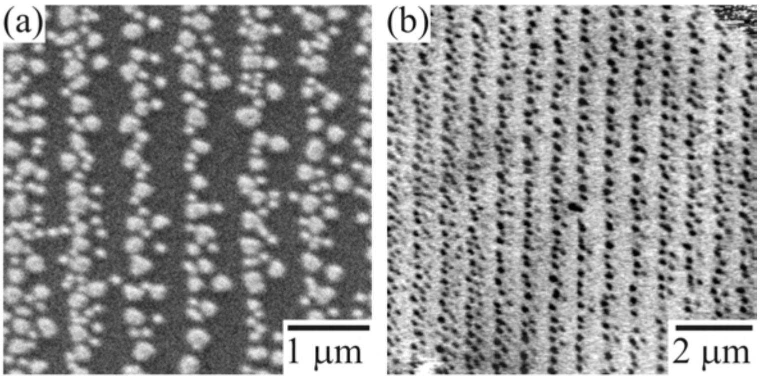

FIGURE 4.8: The −z face of undoped CLN exposed to 25 pulses of 248 nm UV light via a phase mask of period 726 nm with a fluence ∼70 mJ/cm^2, viewed by (a) SEM after HF etching, and (b) SFM amplitude scan without etching.

cantilevers with large spring constants (∼14 N/m) were used to limit the interference from surface electrostatic effects [Hu02].

4.2.4.1 SFM of UV-induced Features

The −z face of undoped CLN was illuminated by 25 pulses of $\lambda = 248$ nm light with a fluence of ∼70 mJ/cm^2, and patterned by a phase mask with $\Lambda = 726$ nm. After HF etching, etch dots formed along the periodic intensity lines with feature sizes down to 100–200 nm, as shown in Figure 4.8(a). A similarly exposed, unetched sample was investigated by SFM imaging, shown in Figure 4.8(b). These images show a clear one-to-one correspondence between etch features and PFM amplitude response.

In addition to imaging, the SFM is also capable of applying large electric fields suitable for inverting ferroelectric domains. A large voltage of ∼100 V DC was applied by the group at the University of Bonn to UV-exposed crystals. Figure 4.9 shows the SFM image both (a) before and (b) after the high-voltage DC-EFM scan across a portion of the irradiated region, delineated by the dashed lines. Within this high-voltage scan area, the contrast induced by the periodic UV light had been erased. These results imply that the contrast observed by SFM imaging may be the result of ferroelectric domains which have been re-poled through the application of higher tip voltages.

Recently, the cw UV scanned-beam experiments of Sakellaris Mailis and Alistair Muir (University of Southampton), introduced in Section 4.2.3, have also been investigated by PFM by Elizabeth Soergel (University of Bonn). In this instance, clear *domain contrast* has been observed for lines formed in the regime of high-exposure, indicating shallow surface domain formation.

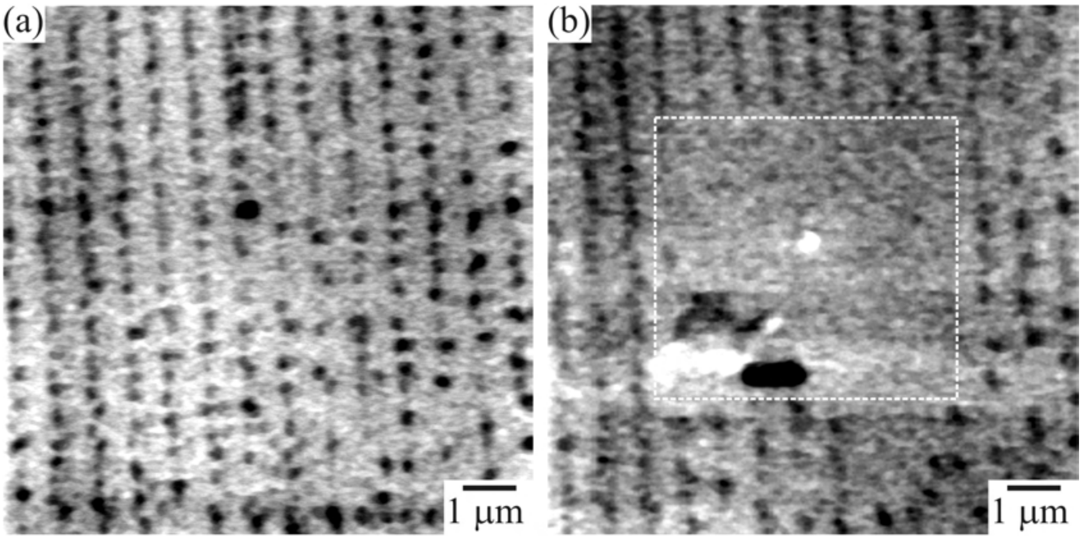

Figure 4.9: SFM scans showing the same region of undoped CLN exposed to UV illumination via a phase mask (a) before and (b) after erasure in the central region enclosed within the box by applying 100 V DC to the tip. The large bright and dark regions within the scan were believed to result from tip degradation which occurs on the application of high voltages.

4.2.4.2 SFM at the Surface

SFM scans of UV-induced features have produced contrast in amplitude-response only. To date, very little contrast has been observed in any of the phase-response scans. To understand this lack of contrast, the depth of these features must be considered.

For bulk domains, SFM is capable of clearly showing 180° contrast between up and down domains, as evidenced from both the literature and SFM scans completed at the facilities of Pennsylvania State University. In this case, the piezoelectric signal of one domain is in phase with the applied electric field, while the signal from the opposite domain is precisely 180° out of phase with the applied electric field. For non-bulk domains, where the crystal can be viewed as a composite material of two opposite domains stacked one on top of the other [Johnston03], one must recall that the electric field emanating from the SFM tip diminishes with increasing distance, yielding an effective penetration depth into the crystal. There are two main cases to consider for these surface domains.

For deep surface domains where the effective penetration depth of the electric field is comparable to or less than the surface domain depth, the material response is dominated by the surface domain. Therefore, the piezoelectric AC signal from the surface domain has a large amplitude, A, and a phase shift, ϕ, while the signal from the domain below (i.e. the bulk) has a smaller amplitude, a, and a phase shift, $(\phi + \pi)$. Therefore, the sum of these contributions to the measured signal is,

$$d_p^{\text{deep}} = A\sin(\phi) + a\sin(\phi + \pi) = A\sin(\phi) - a\sin(\phi) = (A - a)\sin(\phi) \tag{4.1}$$

resulting in a signal with the same phase as that of the surface domain, but a diminished amplitude. For such a deep surface domain, contrast in both amplitude and phase can be measured relative to the surrounding virgin crystal.

In the second case, for shallow surface domains where the effective penetration depth of the electric field from the SFM tip is much greater than the surface domain depth, the material response is dominated by the bulk below the surface domain. In this case, the piezoelectric AC signal from the surface domain has a small amplitude, b, and a phase shift, ϕ, while the signal from the bulk has a larger amplitude, B, and a phase shift, $(\phi + \pi)$. Therefore, the sum of these contributions to the measured signal is,

$$d_p^{\text{shallow}} = b\sin(\phi)+B\sin(\phi+\pi) = -b\sin(\phi+\pi)+B\sin(\phi+\pi) = (B-b)\sin(\phi+\pi) \quad (4.2)$$

resulting in a signal 180° out of phase with the surface domain and a diminished amplitude. For such a shallow surface domain, contrast is observed only in the amplitude signal because the total phase is the same as that for the surrounding virgin crystal.

In reality the field is of course three-dimensional, thus requiring consideration of both lateral dimensions as well, meaning measurements of surface domains small in lateral extent will have even more interference from the crystal environment than in the simple one-dimensional discussion above. Nonetheless, this model is capable of explaining why the SFM scans of the UV-induced surface features display contrast in the amplitude signal only, falling into the case of the shallow surface domains.

4.3 Discussion

Previous investigations of the UV illumination of the −z face of LN have shown the formation of etch frustration. Etch resistant dots on micron and sub-micron scales have been formed randomly and periodically in a single dimension. However, no previous investigations have indicated the nature of these etch resistant features, and have suggested that they result from local photo-induced charging [Mailis05b]. The results presented above, however, strongly suggest UV-induced domain inversion.

4.3.1 Nature of Etch Resistant Features

The etch resistant features were shown to be pyramidal structures in the inset of Figure 4.4. This structure is precisely the expected shape for long-duration etching of bulk domains. While the inverted domain presents a +z face on the surface (which is effectively unetched by HF), the domain can be etched from the sides as the surrounding material is etched away. LN undergoes preferential etching along the y axis, with the −y face etching at a faster rate than the +y face (Table 3.1), and therefore a triangular shape appears in cross-section. For a bulk domain to display a pyramidal structure, the etch duration must be great enough such that the sideways etching successfully removes the entire top surface of the domain. Therefore, the amount of time necessary to achieve a pyramidal etch structure is directly proportional to the lateral dimension of that domain. For sub-micron or nano-scale domains, this time is clearly on the order of minutes.

As shown in Figure 4.7, increasing the fluence of ns-pulsed UV light creates larger connected areas resistant to HF etching. Under the correct conditions, continuous periodic unetched lines formed. Furthermore, cw UV light also showed a similar trend when scanned to form a line. At low fluences, rounded lines formed and the surface appeared to have been completely removed by etching. As the fluence was increased, the flat regions in the centres of these lines also increased, indicating a greater lateral spreading and merging of the domain nucleations. This continued until large areas of the crystal were unetched, revealing a large domain-inverted region. The reason these areas do not appear as pyramidal structures is the relative large size of the merged domains in relation to the short etch times of less than 30 minutes.

The rounded shape of the structures formed by low fluences provides evidence of the shallowness of the UV-induced domains. With a relatively short etch time, the small size of individual dots are etched away by sideways etching not only at the surface, but also throughout its shallow depth. After removing this small domain-inverted cap, the underlying $-$z face was revealed, allowing the illuminated and non-illuminated regions alike to undergo regular etching along the z direction. Furthermore, as the etch depth surpassed the domain depth, under-cut etching of the domain occurred due to the inversion of the y axis compared to the material below. This increased the rate of complete removal of the top inverted-domain cap by etching of the $-$z face from its exposed underside.

To further clarify the nature of the features produced by UV illumination, SFM was used prior to etching. The measurement of an amplitude signal using the PFM technique indicated an inversion in the domain orientation. However, the lack of contrast seen in the phase signal at first suggested that the amplitude signal may have been a result of surface charge interaction. Upon further consideration of the effect of finite-depth domains, no phase contrast would be expected for shallow domains that were smaller than the penetration depth of the E-field from the tip. The further ability to erase the amplitude signal of these features by applying a large DC voltage to the tip indicated the re-poling of inverted domains.

One of the problems encountered using SFM on crystals irradiated by high fluences was the potential for cross-talk between the topography and PFM amplitude signals. Multiple pulses can cause surface structuring well-below the single-pulse ablation threshold on size scales easily detectable by SFM. However, with recent improvements in understanding of the PFM signals [Jungk06], future imaging is likely to display much improved resolution, certainty, and reliability.

The majority of the results presented above concerned the illumination with $\lambda = 248$ nm. However, other UV wavelengths were also explored from the frequency-doubled dye laser. Whereas no systematic study has as yet been made, etch frustration was also possible with longer wavelengths, as indicated in Figure 4.1 where a wavelength of $\lambda = 321$ nm was used. Longer wavelengths have the advantage of higher penetration depth and ablation threshold, and therefore may present an opportunity to form deeper domain inversion, although this has not yet been explored.

4.3.2 Mechanisms of UV-Induced Domain Inversion

There are several possible mechanisms of domain inversion by UV illumination. Firstly, local heating of the crystal takes place due to the strong absorption and short penetration depth of the UV light. Heating reduces the magnitude of the spontaneous polarization and the coercive field. Secondly, $\lambda = 248$ nm light has a photon energy above the band-gap energy and therefore can excite electron-hole pairs directly. Photo-generated charge can drift in the photovoltaic field and become trapped in near-surface defects, forming E-fields that may be sufficient for domain inversion in the thin heated zone. Thirdly, pyroelectric charge, which can induce an E-field on the order of the coercive field at the surface [Avakian76], may also play a role in establishing the poling field. These mechanisms are considered in greater detail in Chapter 5.

4.4 Summary

The UV illumination of the $-$z face of undoped CLN has produced hydrophilic and etch-frustrated regions dominated by micron and sub-micron etch dots. The nature of these dots strongly suggests very shallow inverted domains which can grow and merge with fluences increasing towards the ablation threshold. Sub-micron periodic surface structures have been formed using the simple fabrication technique of illumination via a phase mask, in principle permitting the precise control of the domain structure. The formation of these structures is highly sensitive to fluence, and therefore the quality and reproducibility of periodic structures has been limited by poor beam uniformity. Illumination with fluences above the ablation threshold produced surface ablation only, without indications of domain inversion.

Bibliography

[Avakian76] E. M. Avakian, K. G. Belabaev, A. A. Kaminskii, and V. K. Sarkisov, *Observation of the spontaneous electric breakdown in pyroelectric $LiNbO_3$ and $LiTaO_3$ crystals*. Phys. Stat. Sol. (a), 36(1), K25–K27 (1976).

[Brown02] P. T. Brown, S. Mailis, I. Zergioti, and R. W. Eason, *Microstructuring of lithium niobate single crystals using pulsed UV laser modification of etching characteristics*. Opt. Mater., 20(2), 125–134 (2002).

[Hu02] G. Hu, T. Tang, and J. Xu, *Tip effects of piezoelectric-mode atomic force microscope for local piezoelectric measurements of an $SrBi_2Ta_2O_9$ thin film*. Jpn. J. Appl. Phys., 41(1, 11B), 6793–6796 (2002).

[Johnston03] P. Johnston, *Free response of piezoelectric crystals in series and in parallel*. In Review of Progress in Quantitative Nondestructive Evaluation, volume 700 of *AIP Conf. Proc. (USA)*, 729–736, Green Bay, WI, USA (2003).

[Jungk06] T. Jungk, A. Hoffmann, and E. Soergel, *Quantitative analysis of ferroelectric domain imaging with piezoresponse force microscopy*. Appl. Phys. Lett., 89(16), 163507 (2006).

[Ke07] C. Ke, X. Wang, X. P. Hu, S. N. Zhu, and M. Qi, *Nanoparticle decoration of ferroelectric domain patterns in $LiNbO_3$ crystal*. J. Appl. Phys., 101(6), 064107 (2007).

[Mailis00] S. Mailis, G. W. Ross, L. Reekie, J. A. Abernethy, and R. W. Eason, *Fabrication of surface relief gratings on lithium niobate by combined UV laser and wet etching*. Electron. Lett., 36(21), 1801–1803 (2000).

[Mailis02] S. Mailis, P. T. Brown, C. L. Sones, I. Zergioti, and R. W. Eason, *Etch frustration in congruent lithium niobate single crystals induced by femtosecond ultraviolet laser irradiation*. Appl. Phys. A, 74(2), 135–137 (2002).

[Mailis03] S. Mailis, C. Riziotis, P. G. R. Smith, J. G. Scott, and R. W. Eason, *Continuous wave ultraviolet radiation induced frustration of etching in lithium niobate single crystals*. Appl. Surf. Sci., 206(1-4), 46–52 (2003).

[Mailis05a] S. Mailis, P. G. Lagoudakis, M. Paturzo, J. D. Mills, J. Feldmann, and R. W. Eason, *Second harmonic generation enhancement in lithium niobate micro-tips*. In Conference on Lasers and Electro-Optics, CMN4, OSA, Baltimore, USA (2005).

[Mailis05b] S. Mailis, C. L. Sones, J. G. Scott, and R. W. Eason, *UV laser-induced ordered surface nanostructures in congruent lithium niobate single crystals*. Appl. Surf. Sci., 247(1-4), 497–503 (2005).

[Mailis05c] S. Mailis, C. L. Sones, C. E. Valdivia, I. T. Wellington, A. C. Muir, J. G. Scott, and R. W. Eason, *UV radiation-induced surface wetting changes in lithium niobate single crystals*. In Conference on Lasers and Electro-Optics - Europe, OSA, Munich, Germany (2005).

[Mamedov84] A. M. Mamedov, *Optical properties (VUV region) of $LiNbO_3$*. Opt. Spectrosc., 56(6), 645–649 (1984).

[Muir07] A. C. Muir, S. Mailis, and R. W. Eason, *Ultraviolet laser-induced submicron spatially resolved super-hydrophilicity on single crystal lithium niobate surfaces*. J. Appl. Phys. (in press) (2007).

[Scott04] J. G. Scott, A. J. Boyland, S. Mailis, C. Grivas, O. Wagner, S. Lagoutte, and R. W. Eason, *Self-ordered sub-micron structures in Fe-doped $LiNbO_3$ formed by light-induced frustration of etching*. Appl. Surf. Sci., 230(1-4), 138–150 (2004).

[Sones02] C. Sones, S. Mailis, V. Apostolopoulos, I. E. Barry, C. Gawith, P. G. R. Smith, and R. W. Eason, *Fabrication of piezoelectric micro-cantilevers in domain-engineered $LiNbO_3$ single crystals*. J. Micromech. Microeng., 12(1), 53–57 (2002).

[Sones05] C. L. Sones, C. E. Valdivia, J. G. Scott, S. Mailis, R. W. Eason, D. A. Scrymgeour, V. Gopalan, T. Jungk, and E. Soergel, *Ultraviolet laser-induced sub-micron periodic domain formation in congruent undoped lithium niobate crystals*. Appl. Phys. B, 80(3), 341–344 (2005).

Chapter 5

All-Optical Poling

All-optical poling (AOP) describes a process whereby a ferroelectric crystal undergoes domain inversion induced by illumination only, without any externally applied electric fields. The UV-induced surface modification of Chapter 4 may be an instance of this process. Throughout this thesis, however, AOP is used to refer to UV illumination concentrated on the +z faced of LN crystals.

This direct optical poling technique could provide several potential advantages over regular EFP. Firstly, it is able to induce surface domain inversion in a single fabrication step, avoiding the expense and complexity of photolithographic processing. Secondly, it removes the requirement for high-voltage equipment and the issues of inhomogeneity of the E-field caused by the small period of the electrode pattern. Thirdly, it provides a technique for fabricating nano-scale domains of widths 100–300 nm, which are beyond the capability of conventional EFP.

Few prior investigations have been made into the possibility of optical poling. Photo-induced micro-domain inversion was theorized due to charge accumulation at the boundary of a light spot upon x-axis illumination of Fe:LN [Morozovska03a; Morozovska03b], although the change in the crystal was only observed indirectly by light scattering. Surface micro-structuring has also been observed during light-induced frustrated etching (LIFE), in which visible light formed self-organized structures on the surface of Fe:LN when illuminated in an HF acid environment [Scott04]. These self-organized features display very similar patterns to those of AOP detailed below.

This chapter will detail and analyze the results accomplished to date in all-optical poling using UV light of wavelengths spanning the absorption edge of LN. Some of these results have been reported in [Valdivia05a; Valdivia05b; Wellington07].

5.1 Experimental Setup

The experimental setup used for AOP was the same as that used for etch frustration of Chapter 4. One important difference was the illumination of the +z face of CLN, which this chapter exclusively details. The exposed crystals were 500-µm thick z-cut optically-polished samples of undoped CLN and Mg:CLN, each sourced from both Crystal Technology Ltd. and Yamaju Ceramics Ltd.

Illumination was conducted under two different wavelength regimes. The strong absorption (short penetration depth) regime was investigated using two sources. The first source was a KrF excimer laser (Lambda Physik LPX 200) producing a wavelength of $\lambda = 248$ nm and pulses of duration ~20 ns with millijoule energies. The second source was a frequency-quadrupled Nd-doped yttrium vanadate (Nd:YVO_4) laser (Thomson-CSF DIVA) producing a wavelength of $\lambda = 266$ nm and pulses of duration ~10 ns with up to millijoule energies and a Gaussian-like beam profile. The low absorption (longer penetration depth) regime was investigated using several wavelengths from a tunable laser. This source was a frequency-doubled Q-switched Nd-doped yttrium aluminum garnet (Nd:YAG) laser (Continuum Powerlite 8000) pumping a tunable frequency-doubled dye laser (Sirah PrecisionScan) at the Rutherford-Appleton Laboratory (RAL), producing wavelengths spanning the absorption band-edge of LN at 298–329 nm and pulses of duration ~7 ns with millijoule energies. This range of wavelengths was chosen to exploit the rapidly changing absorption depths for which different surface effects were expected, including the possibility of inducing surface domains of varying depths.

Both the KrF and dye laser systems suffered from poor spatial uniformity, and therefore a rectangular aperture was used to select a central region of the beam containing the best spatial uniformity. The fluence was calculated as the energy per pulse divided by the area of the rectangular spot on the target, representing an averaged value across the remaining non-uniformity of the beam.

Unpatterned and periodically patterned illumination was investigated using fluences ranging from ~0.1–10 J/cm^2, extending both above and below the ablation threshold. Periodic patterning was achieved by use of phase masks optimized for wavelengths of 248, 266, and 298 nm, each with a grating period of $\Lambda = 726$ nm. Each phase mask was held 125 µm above the crystal using stripped optical fibres as spacers. The number of pulses was varied from 1–200.

Following exposure, the irradiated samples were ultrasonically cleaned with solvents and viewed under an optical microscope. The samples were then chemically etched in HF acid at room temperature for 20–60 minutes. The resulting surface structuring was investigated by SEM and SFM.

5.2 Results

The UV illumination of LN was used to determine the ablation threshold, for the formation of UV-induced surface features by unpatterned and periodic illumination, and for post-poling of illuminated samples, discussed in the following sections.

5.2.1 Ablation of Lithium Niobate

The illumination of the +z face of LN by UV light immediately indicated that the fluences of most interest were of similar magnitude to those producing surface ablation. Therefore it was necessary to establish a practical value for the single-pulse ablation threshold, as reported values vary considerably from ~0.1–1 J/cm^2 for $\lambda = 248$ nm [Brown02; Florea02; Chong02].

To measure the approximate ablation threshold, a beam of $\lambda = 248$ nm light illuminated the crystal. The ablation depth, measured for various fluences, is plotted in Figure 5.1. Extrapolating this data to the x-intercept (no ablation) provides an estimate of the ablation threshold of ~0.5 mJ/cm^2. Typically, ablation depth follows the Beer's Law relation, $D_\mathrm{a} = D_0 \ln(F/F_\mathrm{th})$. However, for the data presented in Figure 5.1, linear extrapolation appears much more suitable, although this is likely the result of small range of fluences tested. The spatial non-uniformity of the beam caused uncertainty in the precise values of the ablation depth for each fluence, and therefore a more precise value for the threshold cannot be extracted from this data. Nevertheless, it provided a sufficient estimation for this investigation, and appeared to agree with the results presented in Figure 4.7, where a fluence of ~0.49 J/cm^2 did not produce ablation.

As expected from incubation effects, however, multiple pulses were capable of producing ablation at fluences below this single-pulse threshold. Furthermore, this threshold is valid only for $\lambda = 248$ nm. The longer wavelengths investigated were expect to have higher ablation thresholds because of weaker absorption and longer penetration depths, resulting in a larger light-affected volume. Indeed, as expected, ablation dropped off rapidly as the wavelength was increased above 310 nm.

5.2.2 Self-Organized Surface Features

Unpatterned illumination of the +z face of undoped CLN by UV ns-pulsed light with fluences *below* the ablation threshold had little or no noticeable effect on the crystal surface. No frustrated etch effect was observed, in part because the +z face is resistant to HF etching.

Unpatterned illumination with fluences *above* the ablation threshold, however, presented a different regime of interaction with the crystal. Post illumination, the irradiated zone

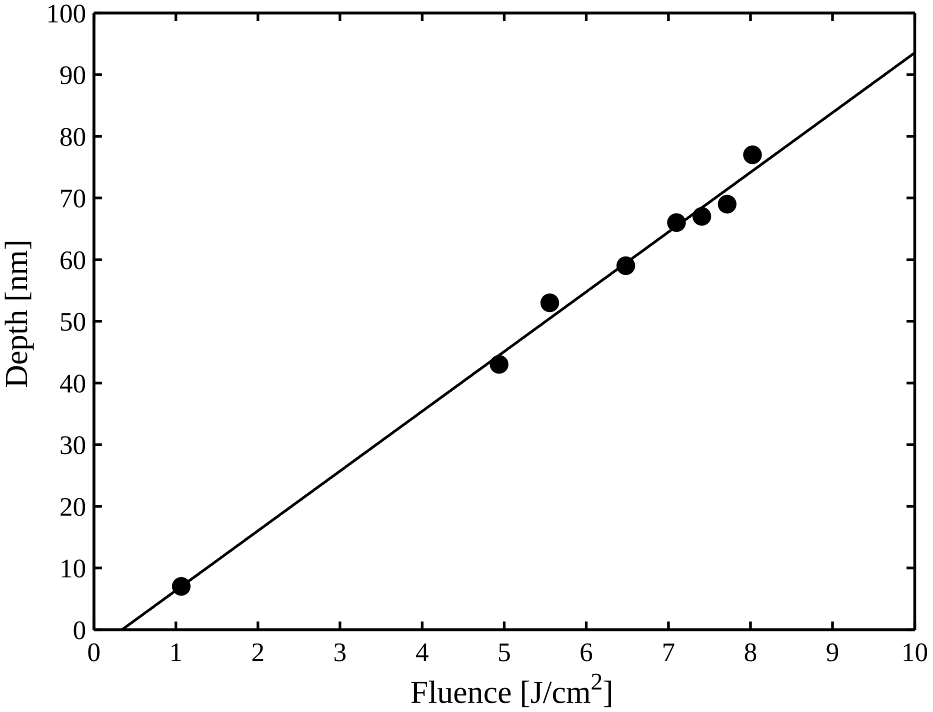

FIGURE 5.1: Single-pulse ablation depth as a function of fluence of 248-nm excimer laser light. Extrapolation of the linear trend to a depth of zero yields an estimate of the ablation threshold to be ~0.5 J/cm^2.

appeared to have been machined by regular ablation, without any clear signs of any other material changes via inspection by optical microscopy or SEM. However, techniques for the visualization of inverted ferroelectric domains showed evidence of all-optical poling, as discussed in the following sections.

5.2.2.1 UV-Induced Etch Features

After illumination, the crystal was cleaned thoroughly with solvents in an ultrasonic cleaner to remove ablation debris and other contamination. The crystal was then chemically etched with HF acid in room temperature for 20–60 minutes without agitation. This process is well-known to reveal the domain structure at the surface (Section 3.1.2).

In regions of ablation, chemical etching revealed self-organized patterns of lines aligned parallel to each of the three crystalline y axes, shown in Figure 5.2 for illumination by $\lambda = 298$ nm light. These patterns fill the ablated area and stop at the ablation edges, as shown in (a). A magnified view of the area enclosed by the dashed lines is presented in (b), showing the triangular patterns in greater detail. A 2D Fourier transform of this image is displayed in the inset, highlighting the strict 3-fold symmetry of the pattern. These patterns were *not* visible prior to etching.

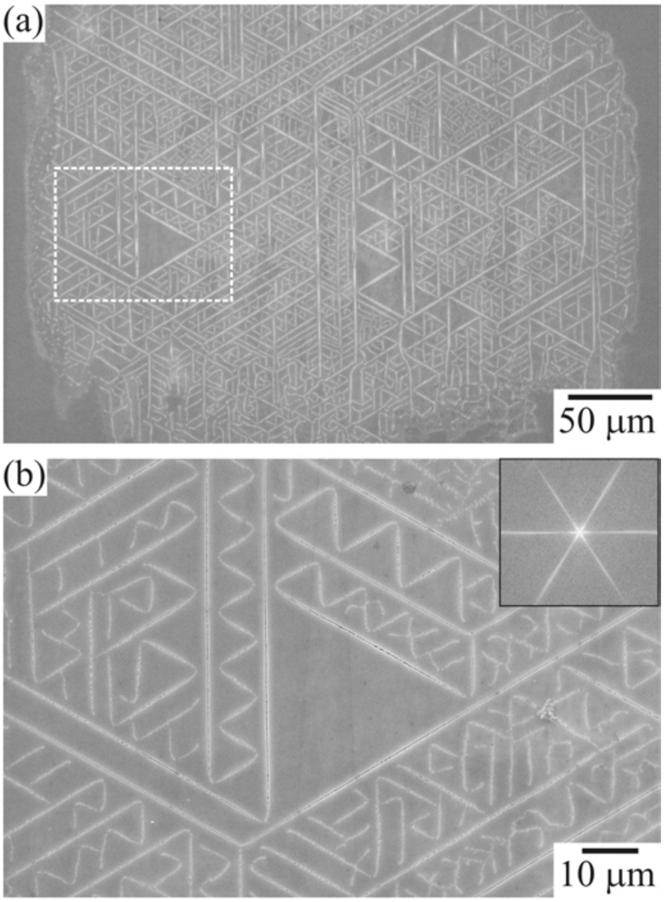

FIGURE 5.2: SEM micrographs of the +z face of undoped CLN, showing self-organized patterns revealed by HF etching following irradiation by $\lambda = 298$ nm with fluences exceeding the ablation threshold. The micrograph (a) shows that the UV-induced lines are confined to the irradiated region, with the boxed area shown in greater detail in (b). The inset of (b) shows a 2D Fourier transform of the image, demonstrating its 3-fold symmetry.

Similar self-organized line patterns resulted from unpatterned illumination using wavelengths of 248, 266, and 298–306 nm. An example of $\lambda = 266$ nm is shown in Figure 5.3, displaying the same 3-fold symmetric self-organized pattern across the ablated region. Above $\lambda = 306$ nm, instead of clean ablation, surface damage was observed due to the longer absorption depth at these wavelengths and increased ablation threshold. It may be possible to induce similar effects at these longer wavelengths operating at sufficiently high pulse fluences (> 7 J/cm^2), but this regime was not explored in this study.

To investigate the properties of these UV-induced features further, Mg:CLN crystals from Crystal Technology Ltd. were exposed by the KrF excimer laser under similar illumination conditions and subsequently etched in HF acid for 20 minutes. A typical result for a rectangular illumination pattern is shown in Figure 5.4(a), with greater detail highlighted in (b). Upon initial inspection, these features appear identical to those produced in undoped CLN.

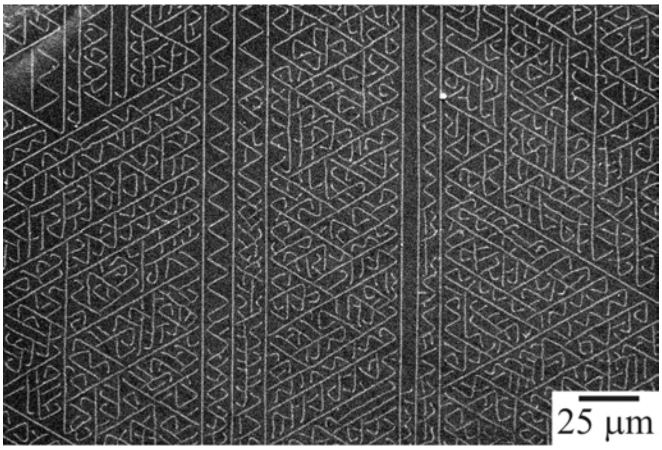

Figure 5.3: SEM micrographs of the +z face of undoped CLN, showing self-organized patterns revealed by HF etching following irradiation by $\lambda = 266$ nm with fluences exceeding the ablation threshold.

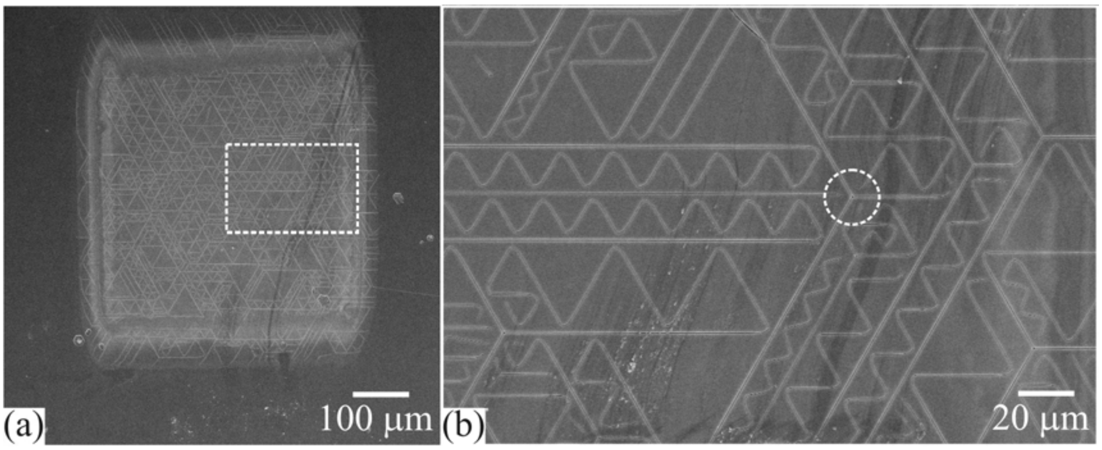

Figure 5.4: SEM micrographs of the +z face of Mg:CLN from Crystal Technology Ltd., showing self-organized patterns revealed by HF etching following irradiation by $\lambda = 248$ nm. The self-organized lines can extend beyond the edges of ablation (a), with the boxed area shown in greater detail in (b).

The lateral extent of these UV-induced features could be controlled by the patterning of the beam incident on the crystal. Figure 5.4(a) shows the effect of $\lambda = 248$ nm excimer illumination of Mg:CLN through a rectangular aperture, limiting the growth of the self-organized patterns to within the ablation region defined by the mask. However, in this example, the aperture was not precisely imaged onto the crystal and therefore low intensity light extended beyond the boundaries of the mask pattern on the crystal, promoting the growth of these lines outside of the ablated region. This demonstrated two properties of these features. Firstly, these lines were sufficiently deep to extend continuously from the bottom of the ablation region to the higher original surface outside the ablation region. Secondly, ablation is not a necessary condition for the propagation of these lines, and also may not be a requirement for the creation of additional lines.

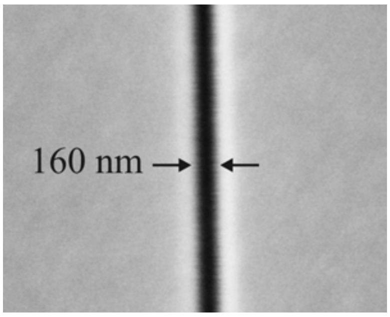

Figure 5.5: SEM micrograph of a self-organized line on the +z face induced by $\lambda = 298$ nm with fluences exceeding the ablation threshold, showing a typical width after a 30 minute HF etch.

This may provide a desirable processing window for the fabrication of devices with fluences near to, but below the ablation threshold, thereby limiting surface roughness and improving reliability.

Characteristic features of all the patterns produced by UV illumination of these CLN crystals are the 3-fold symmetry following the crystallographic axes, bending of the lines to fill the available space between adjacent features, and lack of any crossings. These features are similar to those seen in the LIFE experiments where cw visible light illuminated Fe:LN while in an HF acid environment [Scott04]. Here, the Fe-doping was postulated to induce a charge-mediated effect resulting in the modified etch characteristics.

5.2.2.2 Self-Organized Line Profiles

The sizes of UV-induced lines making up the self-organized patterns of Section 5.2.2.1 were measured using SEM imaging after HF etch times of 20–60 minutes for a range of exposure conditions. The measured widths of these lines were independent of both fluence and wavelength. In undoped CLN using the dye laser at $\lambda = 298$ nm, the line width was 0.18 ± 0.03 μm. In Mg:CLN using the KrF laser at $\lambda = 248$ nm, the line width was 0.207 ± 0.014 μm. The specified uncertainties are the standard deviations of the sets of measured values, which ranged from 100–300 nm. A typical feature is shown in Figure 5.5, depicting an etched channel of ∼160-nm width.

The depths of these UV-induced features were investigated by first etching a sample in HF for 18 hours. This ensured that the maximum etch depth would be reached for the suspected size of a few microns. However, this duration also induced considerable lateral etching, resulting in enlarged feature widths. To view the y-face cross-sectional profiles of these channels, a focused ion beam (FIB), courtesy of FEI Company (Bristol, UK), was used to mill a deep trench across two UV-induced channels, as shown in Figure 5.6(a). Viewing into the trench at a 45° angle [boxed region in (a)] allowed measurement of the channel depth, as shown in (b). Extending approximately 2 μm below the surface, these

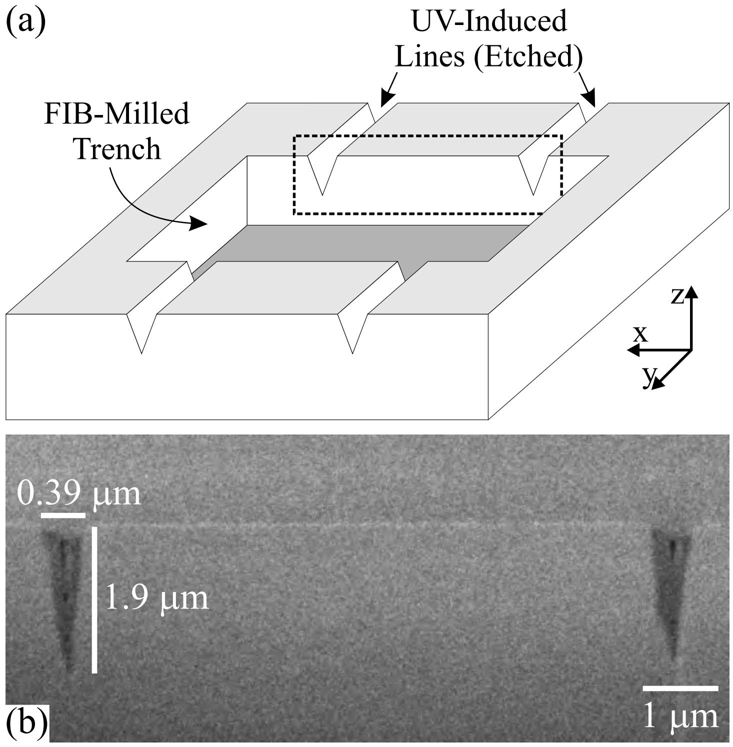

Figure 5.6: (a) Schematic of an FIB-milled trench crossing two parallel self-organized lines. (b) FIB micrograph, viewed at 45°, shows the y-face cross-section of the lines formed by $\lambda = 298$ nm with fluences exceeding the ablation threshold and revealed by an 18 hour HF etch.

depths are on the size scale required for waveguiding devices. The triangular shape of the features appeared very similar to electric-field poled surface domains, such as those fabricated by surface poling [Sones03].

5.2.2.3 Growth from Bulk Domains

Further examination of the features induced in Mg:CLN from Crystal Technology Ltd. provided information regarding the interaction of these UV-induced lines with regular bulk domains. All Mg-doped crystals received from Crystal Technology Ltd. had a small number of hexagonal domains of opposite orientation to the surrounding material scattered throughout the crystal, as revealed by HF etching. These domains could be eliminated by forward and reverse poling the desired area of the crystal, resulting in a single-domain substrate. However this step was not done for these experiments, providing a target substrate with a few randomly scattered bulk and surface domains. Following illumination by a KrF excimer laser ($\lambda = 248$ nm), UV-induced self-organized surface features merged with these bulk domains, as shown in Figure 5.7(a) after etching in HF acid. Viewing many of these features in greater detail, as in (b), shows that these bulk domains act as seeds for the UV-induced surface features which grow out

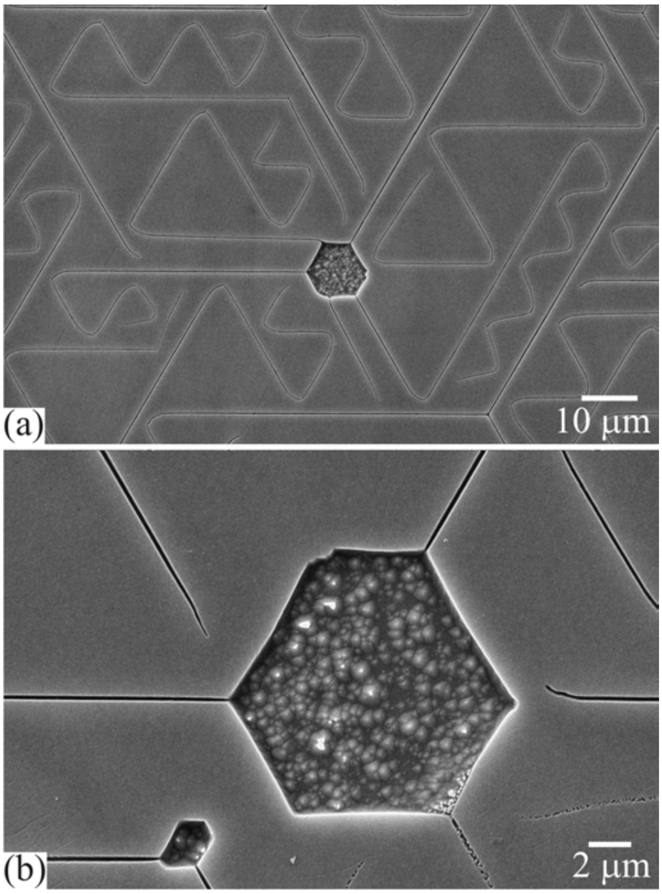

Figure 5.7: SEM micrographs of AOP features in Mg:CLN, showing (a) self-organized lines merging with bulk domains and (b) deflecting away, even when approaching a hexagonal domain at one of its corners.

preferentially from the corners of the hexagonal bulk domains and spread along the three crystalline y axes. Because these surface lines were observed to merge with hexagonal domains precisely at three of the corners only, these surface lines are proposed to grow outward from the bulk domain, acting as a nucleation point. Additionally, UV-induced surface lines that do not approach a hexagonal bulk domain precisely at one of these three corners are deflected away along another y direction. This indicates a similar interaction as observed between two UV-induced lines.

A higher magnification SEM image of another similar merger with a pre-existing hexagonal domain is shown in Figure 5.8. Importantly, however, on the bottom of this hexagonal hole different crystalline planes are revealed by preferential HF etching, allowing the determination of the directions and orientations of the three y axes in the crystal. The triangle on the bottom of the etched hole was caused by an increased etch rate along the −y directions as compared to the +y directions, forming the points of the triangle. Considering first the horizontal y axis, the etchant encountered a −y face when etching from right to left. This implies that the y axis pointed to the left within the inverted domain. However, upon domain inversion the y axis also inverts (Section 3.2),

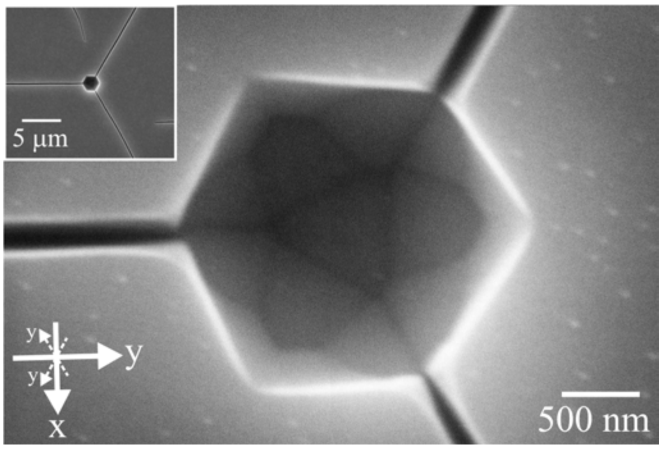

Figure 5.8: SEM micrograph of AOP features in Mg:CLN growing out from a pre-existing domain along the −y directions only, as revealed by the HF preferential etching within the hexagonal domain.

and thus the y axis is oriented to the right in the surrounding material of the virgin domain orientation (+z face). This process can be repeated for the other two equivalent y axes. The y axes are therefore specified in Figure 5.8 for the virgin orientation of the crystal. These y-axes directions were confirmed by the labeling of the wafer cuts by the manufacturer.

Figure 5.8 also shows that the UV-induced surface lines extend from the corners of the hexagonal domain along the −y directions of the virgin orientation only. The growth of these lines along the −y directions is identical to the growth observed during conventional EFP in which domains expand by nucleation growing out from and along the walls in the −y directions only (Section 3.4.1).

In comparison to the self-organized patterns seen in undoped CLN and Mg:CLN from Crystal Technology Ltd., very different results were obtained when illuminating Mg:CLN crystals from Yamaju Ceramics Ltd. Rather than the 100–1000-μm lengths of the self-organized UV-induced features, short lines reaching only tens of micrometres were observed in these crystals. With few, isolated nucleation starting points, these short lines did not have the opportunity to interact, but rather formed the three-pointed star shapes shown in Figure 5.9(a). Initially, these lines followed the three y axes, but diverged towards an x axis nearer to the end of each line. No such behavior has been observed in the self-organized patterns, as evidenced by 2D Fourier transforms.

While the behavior of the UV-induced lines may be different in Mg:CLN crystals from Yamaju Ceramics Ltd., the lines still preferentially grew out from pre-existing hexagonal domains, as shown in Figure 5.9(b–c). However, the central nucleation point in (d) exhibits a concave domain shape which could have resulted from the merger of three hexagonal domains prior to illumination [Lobov06]. Alternatively, this shape could also have formed by 1D nucleation along the lines during illumination.

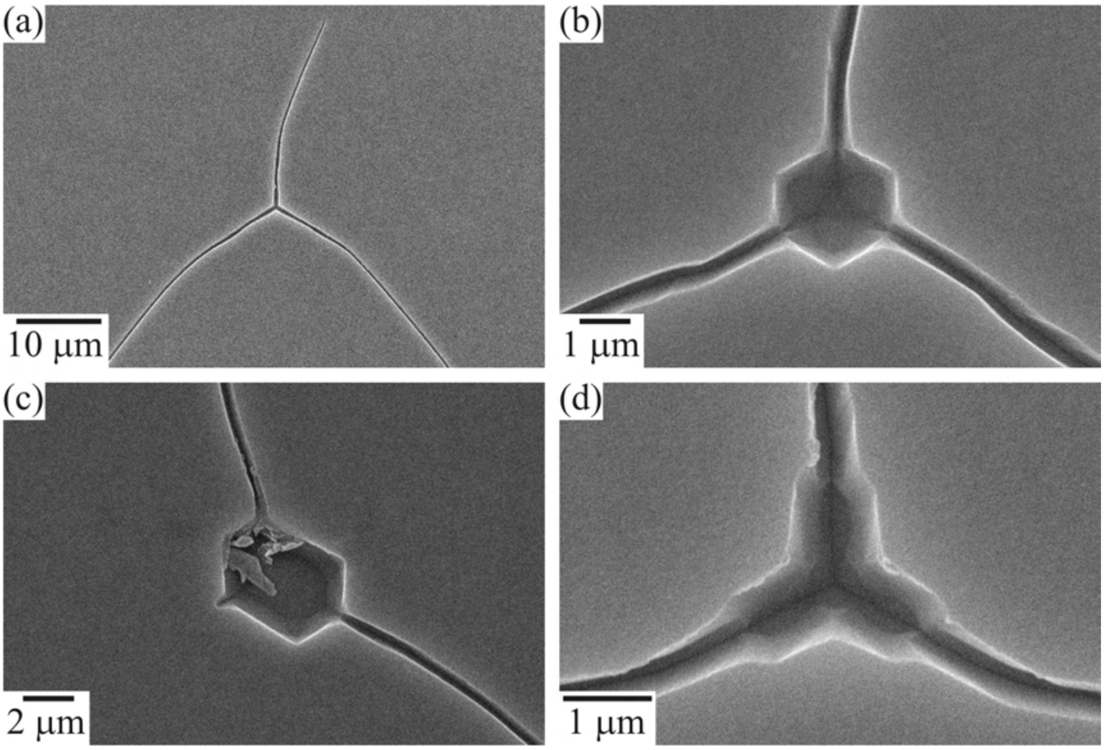

Figure 5.9: SEM micrographs of the +z face of Mg:CLN from Yamaju Ceramics Ltd., showing star-patterns and mergers with hexagonal domains, revealed by HF etching after irradiation by $\lambda = 248$ nm.

5.2.2.4 Scanning Force Microscopy

To elucidate the nature of these UV-induced features on the +z face, the SFM at Pennsylvania State University was utilized. Using 10–20 V peak-to-peak with a frequency of ~30 kHz applied to the tip, bulk poled LN was first imaged to verify the ability to distinguish between opposite domain orientations. In quasi-periodically bulk-poled crystal, provided by Lu Ming (University of Southampton), clear domain contrast was measured by PFM, with the phase-response shown in Figure 5.10(a). In addition, no corresponding topographical features were detected, as shown in (b). A surface-poled CLN crystal with a design period of $\Lambda = 2.47$ μm was also scanned, showing contrast in both phase- and amplitude-response. However, the phase-contrast was relatively weak, and therefore the amplitude-response is presented in Figure 5.10(c). Again, no topographical features were related to the PFM contrast, as shown in (d).

The same conditions were used for the imaging of UV-induced features after ultrasonic cleaning but prior to etching. A large-area amplitude-response scan clearly demonstrated contrast in the piezoelectric response of the self-ordered features, as shown in Figure 5.11(a). The region enclosed within the dashed box is presented with greater detail in (b). The line widths measured by the SFM are closely matched to the widths

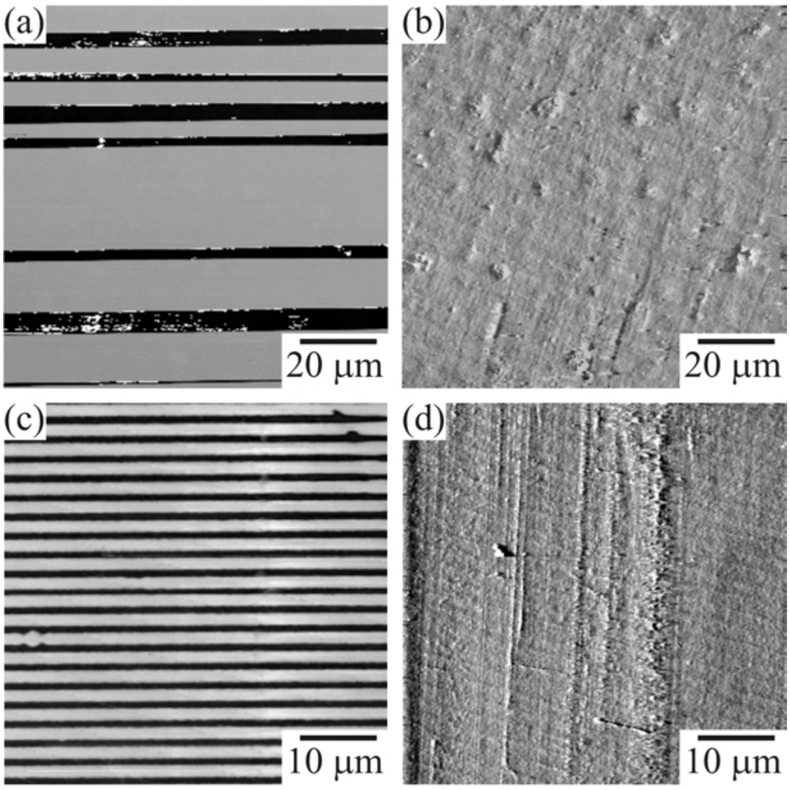

Figure 5.10: (a) PFM phase-response of a bulk quasi-PPLN sample (provided by Lu Ming, University of Southampton) and (c) PFM amplitude-response of a surface-poled PPLN having a measured period of $\Lambda \simeq 2.47$ μm. The SFM internal signal scans of the same areas [(b) and (d), respectively] indicate that there are no topographical features corresponding to the contrast in the piezo-response images.

measured after HF etching. Comparison of the PFM amplitude-response (c) and internal signal (d) scans of the same area reveal some minor correlation which is likely due to cross-talk between the signals. Finally, the amplitude-response (e) was much greater than the phase-response (f) of the same area, and achieving contrast in the phase-response was often not possible under the conditions tested. This observation agrees with the analysis concerning shallow domains from Section 4.2.4.2.

Large dark regions are also observed in Figure 5.11 which are currently unexplained. The dark regions could possibly result from the remaining debris on the surface which is not removed by ultrasonic cleaning, although the surface topography scans do not support this. It is possible that the dark regions represent large area domain inversions, although this is not supported by the HF etch profiles which do not show similar features. A remaining possibility is a material modification that alters the piezo-response or electrostatic interaction with the tip, but does not affect the etch characteristics. These dark areas do not appear on all scans, and it is entirely possible that they could simply be an artifact of scanning, although interference in the system typically appears as the random noise seen scattered throughout these images.

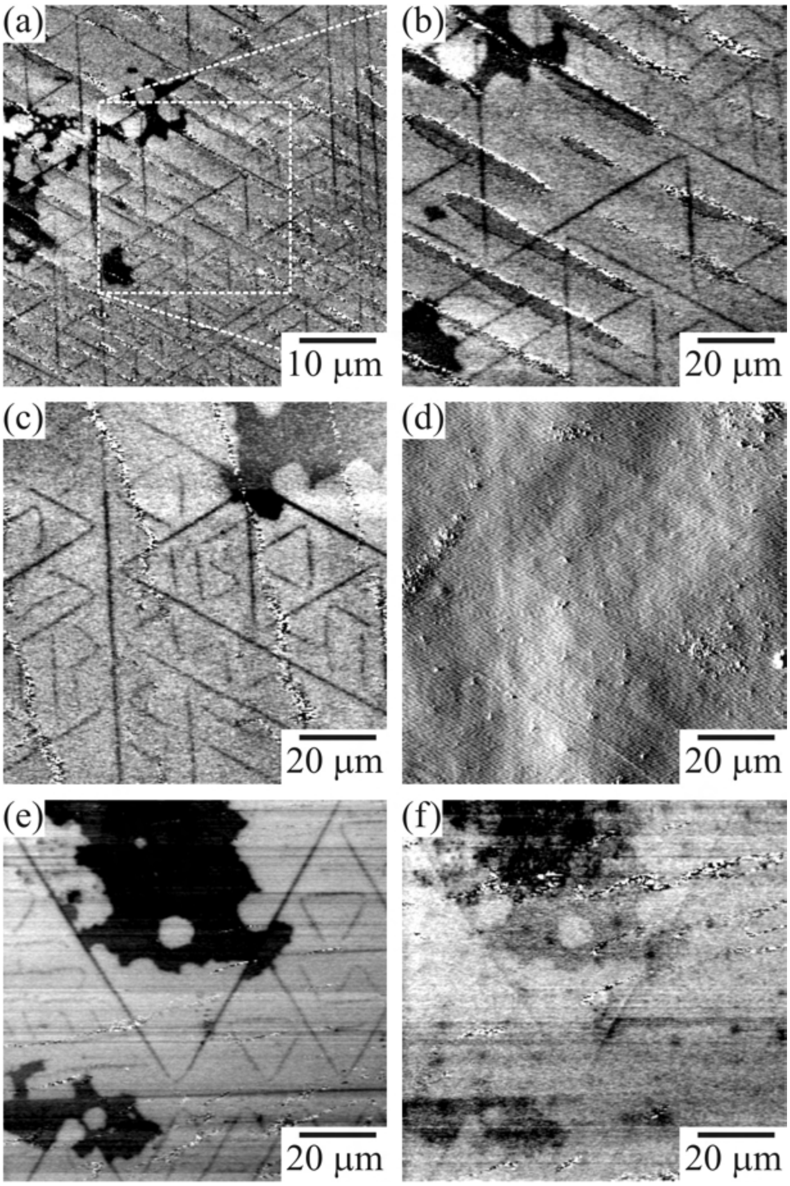

FIGURE 5.11: PFM scans of undoped CLN exposed by $\lambda = 298$ nm, showing AOP domains on the +z face (a,b). The scans show clear domain lines in amplitude-response (c), with only minor correlation in the internal signal (d). Another typical spot shows high contrast in amplitude-response (e), but poor contrast in phase-response (f).

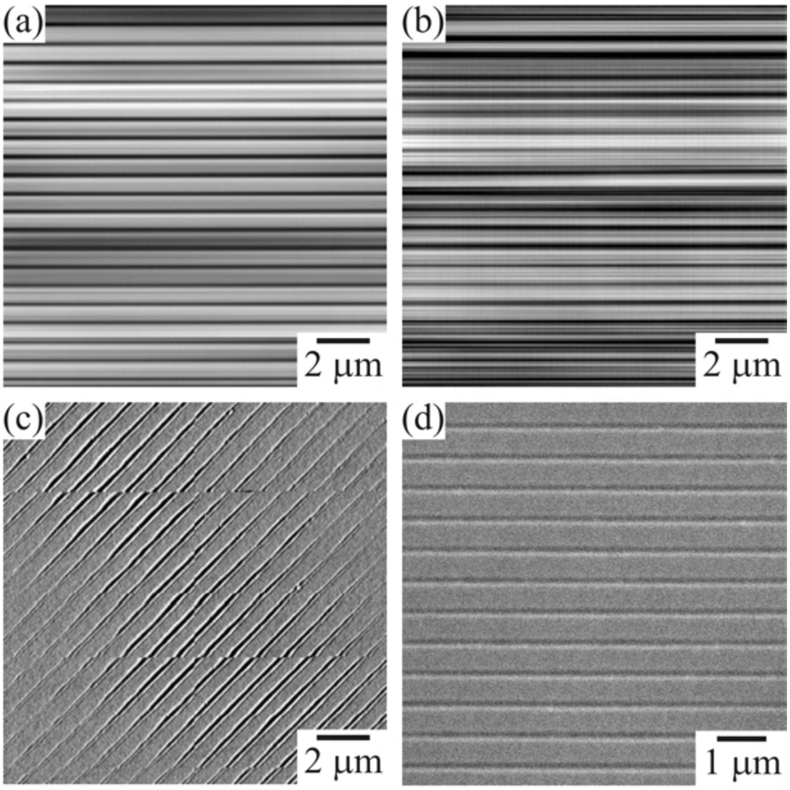

FIGURE 5.12: PFM scans of undoped CLN exposed by $\lambda = 248$ nm, showing contrast in both (a) amplitude- and (b) phase-response. Horizontal scans do not show topography, but when rotated by 45°, the internal signal shows a clear topographical grating (c). When viewed by SEM, these ablated features are clearly visible in a similarly-exposed sample (d). The two horizontal lines visible in (c) are scanning errors caused by the SFM.

SFM scans have also been made of regions exposed by $\lambda = 248$ nm light through a phase mask with $\Lambda = 726$ nm, as shown in Figure 5.12. Although contrast was observed in both the (a) amplitude- and (b) phase-response of these regions, topography was also clearly visible when rotated by 45° (c). Similar exposures of another crystal showed a matching ablation pattern without HF etching, as imaged by SEM (d). This indicates that cross-talk does exist between the PFM and topography signals, and that the appearance of contrast does not necessarily indicate a piezoelectric response from the crystal. This fact has created an inability to reliably image UV-induced features formed by illumination via a phase mask.

It is important to note that the scans completed throughout these investigations have *not* been corrected for the background response of the SFM system. The reason for this is that the importance of the background response has only recently been discovered by our collaborators at the University of Bonn [Jungk06]. Therefore, these scans suffered from all of the problems mentioned in Section 3.1.3, including inconsistent contrast from sample to sample, a reduced amplitude contrast, and a phase contrast much less than 180°. These problems also existed for the SFM scans of bulk and surface poled crystals.

However, for the UV-induced surface lines these problems often overwhelmed the PFM signal due to the shallow depth and nano-scale lateral extent of these features.

5.2.3 Ordered Alignment by Phase Mask

Further investigations of the illumination of the +z face through a phase mask were completed in collaboration with Iain Wellington and Collin Sones (University of Southampton). Phase masks with $\Lambda = 726$ nm were used with 248-, 266-, and 298-nm wavelengths from a KrF, Nd:YVO_4, and dye laser, respectively.

Unpatterned illumination by 20 pulses of $\lambda = 306$ nm light with a fluence near the ablation threshold formed a random array of etch pits and short line segments, as shown in Figure 5.13(a). These pits had a triangular shape with vertices oriented along the y axes, and were the inverse of the etch frustration pyramidal structures resulting from UV illumination on the opposite −z face. Illumination through a phase mask using several pulses of $\lambda = 298$ nm light with a fluence near the ablation threshold produced similar etch pits, but instead were strictly aligned along the periodic lines of high-intensity, as shown in Figure 5.13(b). Close inspection of (b) shows that in fact all the etch pits aligned not in the center of the high intensity, but at a very precise distance to the left side toward the low intensity region. Several etch pits also aligned at the precise symmetric point on the right side (circled), indicating that either a specific intensity or intensity-gradient is ideal for their formation.

Increasing the fluence above the ablation threshold produced quasi-periodic UV-induced lines strictly aligned along the phase mask intensity patterns, as shown in Figure 5.14(a). The non-uniformity of the beam prevented alignment throughout the beam, resulting in lines aligning along the other y axes of the crystal. Nevertheless, preferential alignment along a single y axis was achieved over much of the beam.

On closer inspection of the irradiated crystal, shown in Figure 5.14(b), two very important characteristics were revealed. Firstly, each UV-induced line was composed of a chain of etch pits and line segments that was reminiscent of domain lines formed by correlated nucleation [Shur05a]. Secondly, the *quasi*-periodicity of the structure became clear. An ablation grating corresponding to the intensity profile from the phase mask appeared across the entire beam. However the UV-induced lines did not form in every period, but instead at some multiple of the phase mask period only. The separation between adjacent lines typically ranged from 3–8 multiples of the phase mask period.

This separation between UV-induced lines is further supported by Figure 5.15. Lines forming along adjacent periods or within two periods terminated when they approached within ∼1–2 micron. However, a three-period separation was allowed over long distances, as shown in Figure 5.14(b).

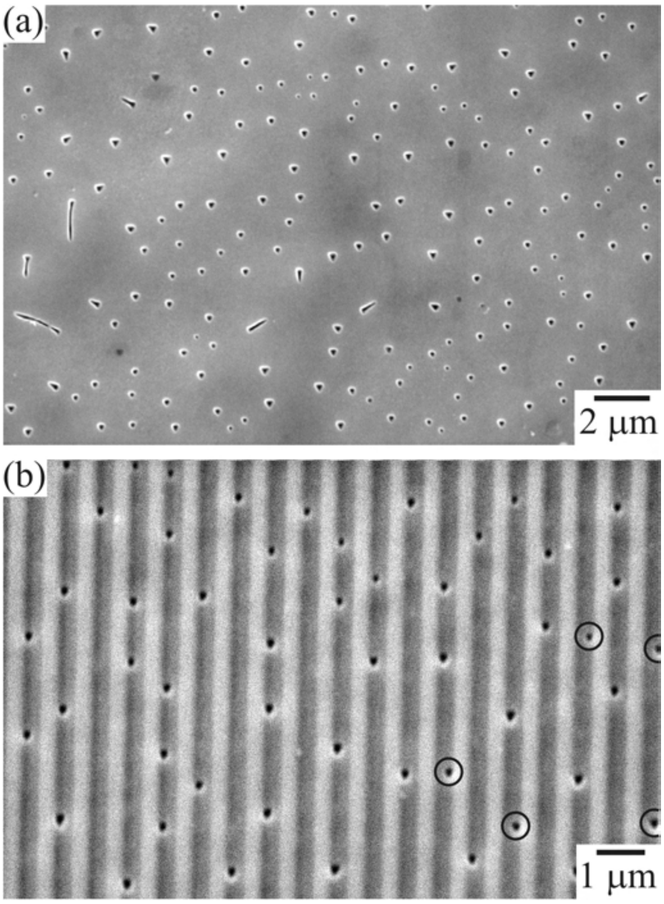

Figure 5.13: Nucleated AOP domains formed via low fluence exposures of (a) unpatterned illumination using 20 pulses of λ = 306 nm, and (b) illumination through a phase mask (Λ = 726 nm) using several pulses of λ = 298 nm.

UV-induced lines formed strictly along the high-intensity peaks, and when a segment deviated from this path, the line quickly reasserted alignment along the nearest peak. Even under conditions where the UV-induced lines did not align *along* the high-intensity peaks, each segment of the lines *did* form precisely at one of these peaks, as shown in Figure 5.16(a). Here, each line is aligned along any one of the three y axes, but the line segments still formed only in the presence of the high intensity. However, this alignment of the intensity grating with the UV-induced lines was strongly dependent upon the accurate alignment of the intensity grating with a y axis of the crystal. When the phase mask was rotated 20° away from a y axis, alignment of the UV-induced lines remained primarily along each of the three y axes without preference, as shown in Figure 5.16(b). Some dotted lines also formed along the high-intensity peaks, although the segments were typically very small, indicating that the individual segments would not grow along this arbitrary angle.

All UV-induced lines discussed above have been formed using fluences significantly above the ablation threshold, simultaneously causing the deep ablation grating. However, UV-induced lines were also formed where the fluence was sufficiently low to cause very

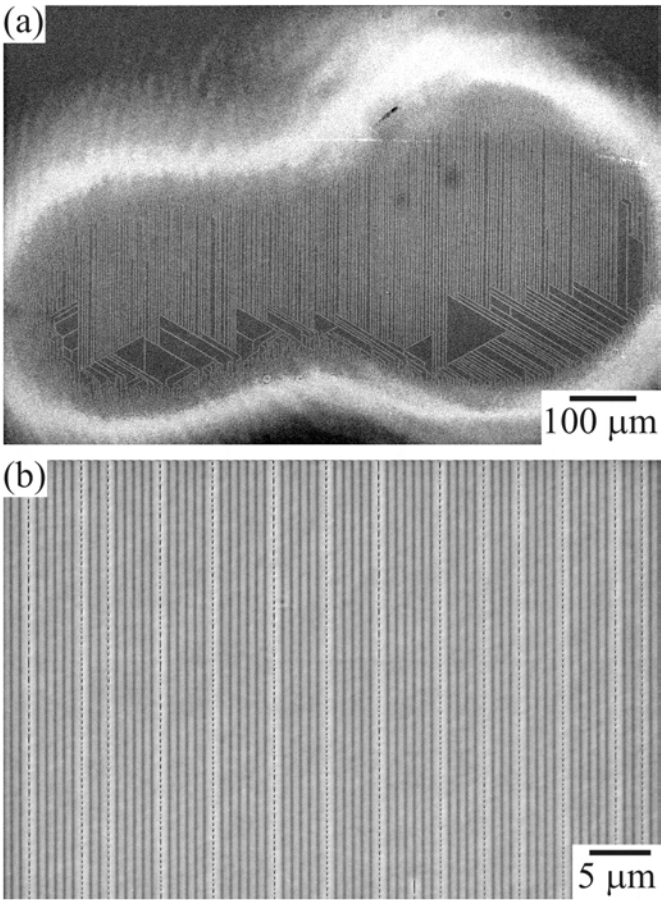

Figure 5.14: AOP domain lines aligned by $\lambda = 266$ nm illumination through a phase mask, showing (a) alignment across the majority of the laser spot, and (b) formation of domain chains running along some of the lines of illumination only, typically 3–8 phase mask periods apart.

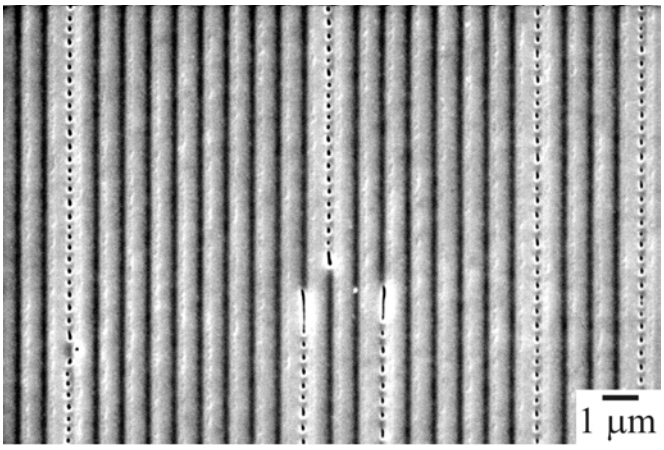

Figure 5.15: Interaction between adjacent AOP domain lines formed via illumination through a phase mask ($\Lambda = 726$ nm), limiting the minimum spacing to three phase mask periods. Domain lines were prevented from propagating when they came into closer contact.

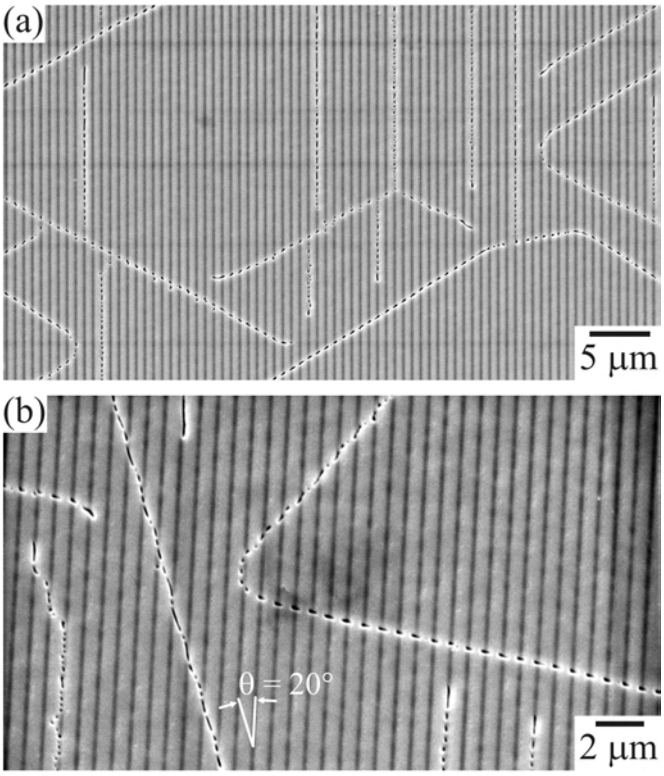

FIGURE 5.16: SEM micrographs showing (a) AOP domain nucleation only at the peaks of light intensity, even when the domain-chains do not preferentially align along these peaks, and (b) the effect of misalignment between the phase mask and the y axes.

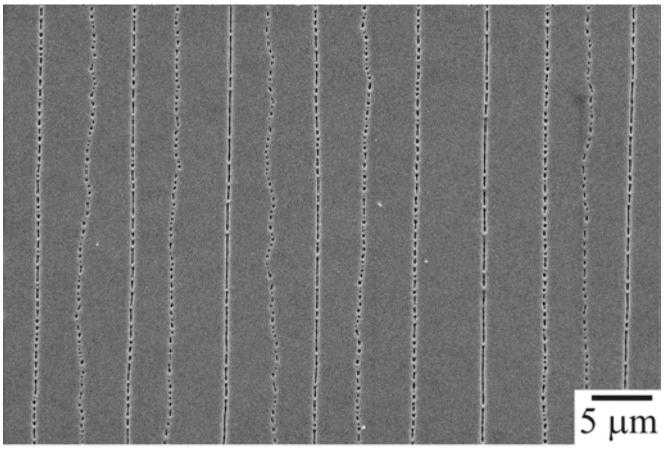

FIGURE 5.17: Aligned AOP domain lines formed without observable ablation, using $\lambda = 266$ nm with an average fluence of ~100 mJ/cm^2.

little or even no visible ablation, as shown in Figure 5.17. Some chains of UV-induced segments appeared very straight and with almost regular periodicity, whereas chains in between exhibited more bending and deviation from a straight line. This may be a result of the same interaction between neighboring lines that prevents line formation along adjacent periods of the phase mask illumination.

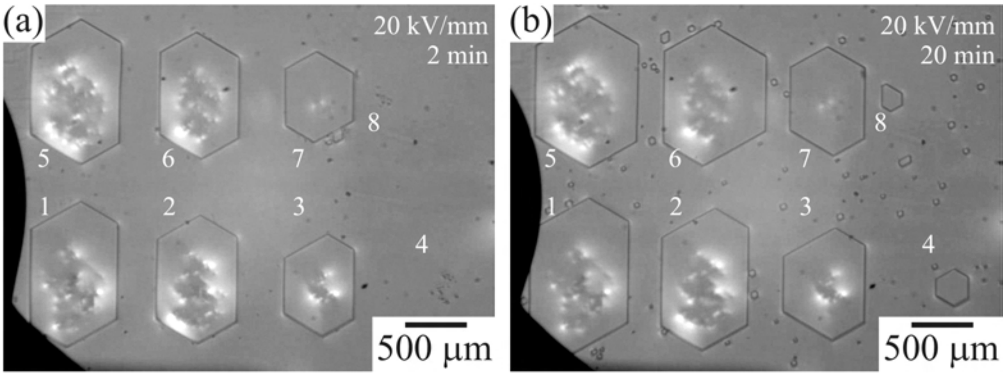

FIGURE 5.18: Polarized optical microscope images of E-field poling of AOP domains formed by $\lambda = 266$ nm unpatterned illumination of the +z face of undoped CLN. Spots 1–4 were exposed to 20 pulses, and 5–8 exposed to 10 pulses. The approximate fluence per pulse of spots 1 and 5 was 700 mJ/cm^2, spots 2 and 6 was 580 mJ/cm^2, spots 3 and 7 was 400 mJ/cm^2, and spots 4 and 8 was 180 mJ/cm^2. The images show the domains formed by 20 kV/mm applied in the poling direction for (a) 2 and (b) 20 minutes.

The effect of illumination via a phase mask was observed by Iain Wellington (University of Southampton) to be dependent upon temperature of the substrate [Wellington07]. Between room temperature and 100°C, no qualitative difference was observed. However, with temperature increasing up to 200°C, the density of the UV-induced lines was observed to decrease significantly, forming with a greater separation than at room temperature. Additionally, the features formed at high temperature were continuous lines, and *not* composed of individual line segments.

5.2.4 Post-Application of E-field

The UV-induced lines have been shown to be surface features, extending only a few microns below the surface. The application of an external electric field may provide a method of pushing these features deeper into the crystal.

An undoped CLN crystal was illuminated by 10–20 pulses of $\lambda = 266$ nm with fluences of 180–700 mJ/cm^2 on the +z face. Following ultrasonic cleaning, an E-field of 20 kV/mm was applied in the poling direction. Domains grew out from and around the illuminated spots, as shown in Figure 5.18 after applying the E-field for (a) 2 minutes and (b) 20 minutes. The area of domain inversion was largest on spots with the largest fluence. Only in the spots with the lowest fluence did the number of pulses make a noticeable difference to the size of the domain inverted region. The duration of the applied field was also most significant for these spots.

The hexagonal domains of Figure 5.18 were bulk domains, extending the entire thickness of the crystal. However, this example has not clarified whether the application of the E-field has caused the UV-induced features to spread and grow, or whether the ablation

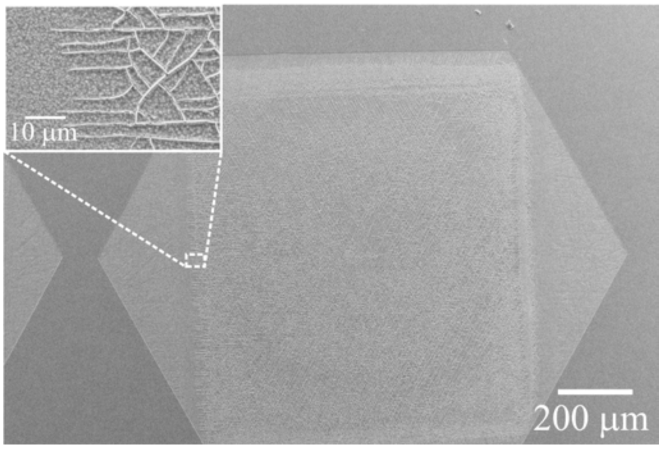

Figure 5.19: Post E-field poling spread a bulk domain preferentially across the UV-exposed regions ($\lambda = 248$ nm). The corner of a large domain is visible on the left side of this SEM image, having grown from a neighboring UV-exposed region. The inset shows a close-up of defects that appear on the +z face of the crystal and in the areas of UV exposure only.

pattern simply induced a local variation in the E-field by structuring of the substrate and thus leading to regular E-field poling, as demonstrated in [Reich98].

A similar exposure using $\lambda = 248$ nm through a rectangular aperture produced UV-induced lines on the +z face. Subsequent application of an E-field near the coercive field produced a bulk hexagonal domain precisely the size of the illumination region, as shown in Figure 5.19. However, upon closer inspection of the +z face, surface defects were visible across the entire UV-exposed region only. The edge of the illuminated region is highlighted in the inset of Figure 5.19, showing the ends of these surface defects. These defects were *not* visible on the −z face.

Applying a smaller voltage for a shorter duration on a crystal with a similar exposure prevented the growth of the domain from spreading over the entire exposure region. This allowed the observation of the domain during growth, as shown in Figure 5.20(a). Here, individual UV-induced lines spread laterally, merging across a large hexagonal section. Throughout the rest of the illumination region, merging was limited to smaller areas at points along the self-organized lines, as shown in (b). The defect lines appeared within the inverted regions, but here can be seen to be extensions of topographical surface defects. These defects are likely a direct result of the violent ablation process, possibly due to cracking of the material at the surface. Upon poling, these damage lines appear to prevent the inversion of the material along it, resulting in the defect lines highlighted in (c). However the hexagonal shapes of the domains indicated that these defects were only on the surface, and can likely be removed by prolonged etch times.

No attempt has been made to optimize this process. However it is clear that UV illumination on the +z face can lead to the spatially-selective E-field poling of bulk domains

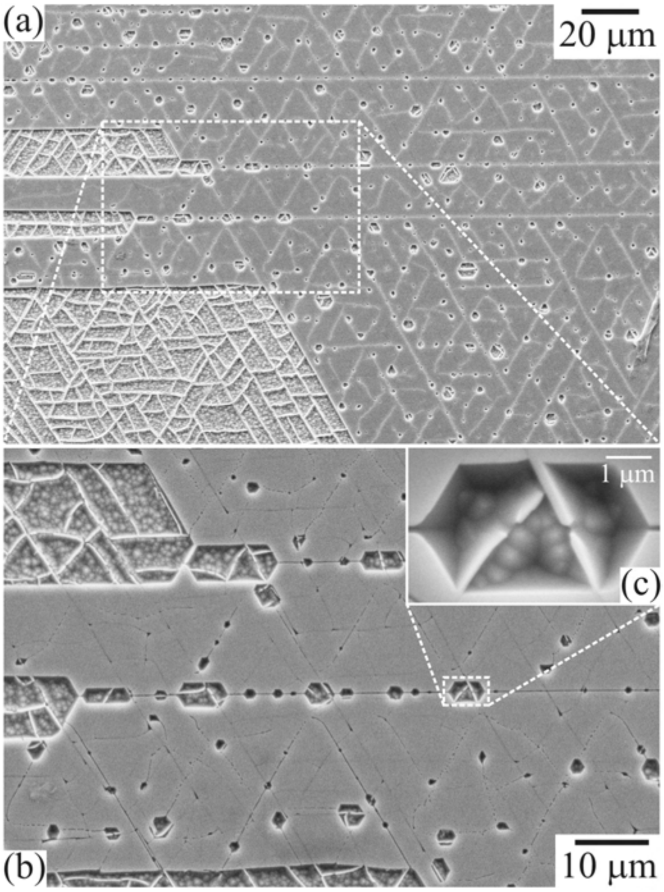

FIGURE 5.20: Post *E*-field poling spread the AOP domains within a UV-exposed region, eventually merging with adjacent domains (a). Points along each AOP domain line spread at different rates (b), and UV-induced surface defects caused incomplete spreading of these domains at the surface (c).

extending to the −z face. If this could be achieved with small feature sizes, the post-application of *E*-field could present a simple method of forming patterned bulk domains.

5.3 Discussion

All of the above experimental results point to the conclusion that the UV-induced surface features on the +z face are in fact *surface domains.* The evidence for the domain-nature of these features includes their selective chemical etching, cross-sectional profiles which appear very similar to surface domains formed by EFP, growth outwards from pre-existing bulk domains, growth strictly along the same directions as EFP domains, amplitude- and phase-contrast in the piezoelectric response measured by SFM, and spreading by post-application of *E*-field. Therefore this process is a demonstration of the all-optical poling (AOP) of LN.

The following sections will detail the kinetics of AOP domain pattern growth and possible mechanisms for the formation of domain inversion via UV illumination.

5.3.1 Kinetics of UV-Induced Domains

AOP domain patterns all display several characteristics which lead to an understanding of the kinetics governing their formation. Nano-domain lines were initiated at domain nucleation sites, which could be UV-induced nucleations or pre-existing domains. The nano-domain lines grew along three directions aligned with the y axes of the crystal. When approaching neighboring domain lines or other surface and bulk domains, lines never joined or crossed, but rather electro-static interaction caused deflection along an alternative growth direction. A line was terminated when no direction existed in which it could maintain a separation greater than this characteristic deflection distance. These pattern characteristics were also observed in light-induced frustrated etching (LIFE) experiments, and their growth has been simulated using the rules above [Scott05]. A similar simulation approach was also employed in [Shur06c] for AOP patterns produced by $\lambda = 308$ nm ns-pulsed light, reproducing the results presented throughout this chapter. These simulations, however, were phenomenological models and required several adjustable parameters, such as nucleation density, deflection distance, and branching probability. Nevertheless, they demonstrated close agreement to experimentally observed patterns.

In all cases, the AOP domain lines appeared to grow outward from starting nucleation sites randomly scattered throughout the illuminated region. In some cases, these nucleation sites were pre-existing hexagonal domains, as shown in Figure 5.7. In most cases, however, these nucleation sites were induced at crystal defects by UV illumination, just as regular EFP initiated at crystal defect sites. These sites may be composed of lattice defects which present a smaller energy barrier to domain inversion, or pre-existing nano-domains. In this scenario, the nucleation site was not visible as a hexagonal domain, but instead was visible only as the convergence of three lines, as shown within the encircled area of Figure 5.4(b).

Growth from these nucleation sites proceeded along the −y directions of the crystal only. Again, this behavior was identical to the growth of hexagonal domains inverted by EFP, except in this case 2D nucleation was dominant over 1D nucleation. Branching, an instance of 2D nucleation, is the growth of a new domain line outward from an existing domain line, which acts as a nucleation site. While not strictly forbidden, typical AOP did not result in branching, although it has been reported using high fluences [Shur06c]. Instead, typical domain lines grew along a single −y direction until they approached other UV-induced lines or other domains.

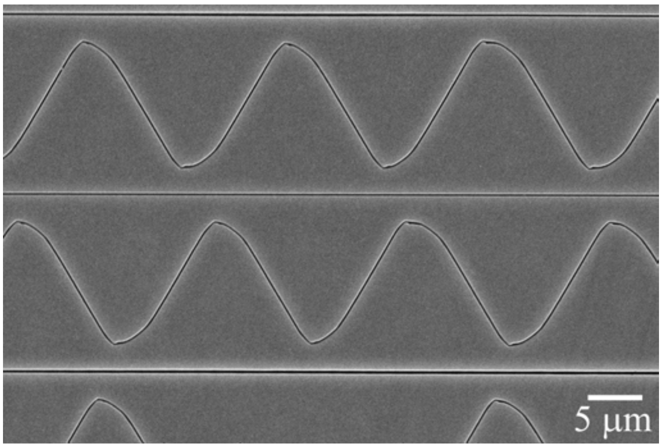

Figure 5.21: SEM micrograph showing the reproducible distances over which the domain lines are deflected. The shape of each bend is also reliably reproduced on a sub-micron scale.

Rather than merging with adjacent domains, nano-domain lines deflected along an alternative path rotated ±120° relative to its original growth direction. This process was repeated very reliably, with a consistent distance between deflections and very similar bend shapes, as shown in detail in Figure 5.21. Using the dye laser operating at λ = 298 nm in undoped CLN, the deflection distance was 1.825±0.11 μm. Using the KrF excimer laser operating at λ = 248 nm in Mg:CLN, the deflection distance was 2.234±0.10 μm. The uncertainties in the measurements were dominated by blurring in the SEM imaging caused by charge accumulation at the edges of the etched trenches, rather than variability in the deflection distance itself. This deflection distance was likely a function of material parameters and the cross-sectional shape of the domain lines.

AOP lines are needle-like domains with angled-walls composed of finite steps of: (1) vertical wall segments parallel to the spontaneous polarization ($\theta = 0°$), and (2) horizontal wall segments perpendicular to the spontaneous polarization ($\theta = 90°$) [Gopalan98]. The horizontal wall segments form head-to-head charged domain walls [Shur00] which are likely the source of the electro-static interaction between the AOP domain lines. Regular bulk domains are composed of only vertical domain walls which are without charge, and hence tend to merge rather than deflect their growth. Deep surface domains also tend to merge because they are dominated by vertical domain walls. As the depth of the surface domain diminishes, however, the averaged domain wall angle θ increases, increasing the proportion of horizontal wall segments and increasing the force of repulsion, as observed with AOP domain lines. These three scenarios are depicted in Figure 5.22. The domain wall angle is inversely related to the domain aspect ratio (depth/width).

The minimum deflection distance also impacted the results of UV illumination through a phase mask. While individual nucleation sites were observed along each high intensity line produced by the phase mask with Λ = 726 nm, neither domain lines nor domain chains formed in adjacent periods. The minimum distance between these domain lines

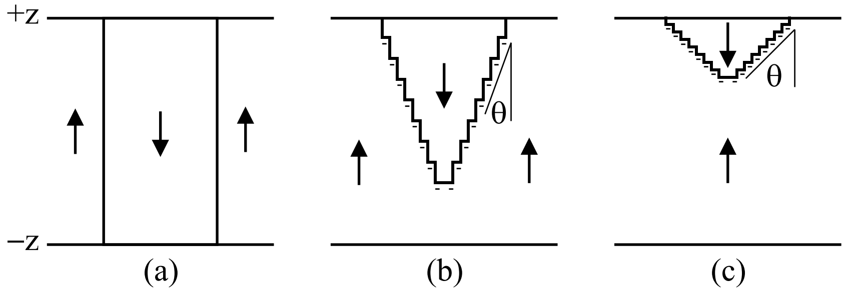

Figure 5.22: Vertical domain walls ($\theta = 0°$) show no charging (a), while increasing θ increases the density of charge on the domain walls (b–c). The negative signs (−) indicate charge compensation at the head-to-head domain interface.

was three periods, or ~2.2 μm. This is in good agreement with the deflection distances measured above, as lines within two periods would be separated by less than the deflection distance observed in self-organized patterns formed by unstructured illumination. Therefore illumination with a period greater than the deflection distance would likely achieve a periodic pattern with domain lines aligned along every adjacent high intensity peak. However, larger periods would also decrease the confinement of the UV-induced domains to the high intensity lines. Periods much greater than the widths of the domain lines would approach the situation of large-area unstructured illumination, resulting in self-organized patterns rather than lines aligned along a single y axis.

Since the deflection distance is believed to be a result of electro-static interaction due to the charge compensation on the head-to-head domain boundaries, a reduction in the spontaneous polarization of the material would be expected to reduce this charge and hence reduce the deflection distance. An increase in crystal temperature is one method of reducing the spontaneous polarization. However, UV illumination with crystal temperatures above 100°C by Iain Wellington (University of Southampton) showed the opposite trend of *increasing* the distance between adjacent domain lines formed via illumination through a phase mask. Currently this effect is unexplained, and is complicated by the temperature range in which LN undergoes a large change in conductivity and several other material properties [Gopalan01].

The AOP process is an instance of non-equilibrium domain reversal conditions. With the incidence of nanosecond-duration UV pulses, the surrounding material heats up rapidly. While heating and cooling does not occur on the short time scale of the pulse, it does occur much faster than the typical switching time used during regular EFP of LN ($\tau_{scr} \simeq 50$ ms) or LT ($\tau_{scr} \simeq 1$ s). As a result, the necessary screening fields were not realized, producing a higher rate of nucleus step generation (2D nucleation) than growth (1D nucleation) [Chernykh05; Shur06b]. In the limit of much greater 2D nucleation than 1D nucleation [$R \gg 1$, as defined in (3.11)], star-like patterns formed and aligned along the y axes, as observed and simulated in [Lobov06]. These patterns appeared identical to the AOP domain lines when viewed at a nucleation point [circled region of Figure 5.4(b)].

From this analysis, the kinetics of AOP domain line growth becomes clear. Starting at a nucleation point, a domain line grows outward along a −y direction by 2D nucleation. The suppression of 1D nucleation prevents the lateral growth of the domain. Therefore the width of the domain remains fixed at the size of nano-scale domain steps which invert simultaneously from 2D nucleation, as observed during hexagonal domain growth by EFP in Figure 3.10. Growth along a single −y axis is preferred to bending or branching due to the greater electro-static self-interaction inherent in these cases. Therefore bending occurs only when the electro-static interaction with a neighboring domain line exceeds the self-interaction of the bend.

The competition between switching time and screening time also impacted the composition of the domain line itself due to the phenomenon of correlated nucleation. Here, the continuous domain lines were broken into colinear line segments, as observed above upon illumination through a phase mask (Section 5.2.3). However, this has also occurred for unpatterned illumination. The formation of these domain chains began at a random nucleation site, depicted in Figure 5.23(a). This initial nucleation induced further nucleation at the distance called the *correlation length*, L_c, as depicted in (b). During this time the initial nucleation site grew along the −y direction. The newly formed correlated nucleation induced another nucleation at a second distance of L_c, as depicted in (c). Previous nucleations also reach a maximum length due to the electro-static interaction between adjacent line segments of the domain chain, separated by a minimum distance, L_s, also depicted in (c). However, L_c and L_s can vary across a crystal, resulting in domain chains which display only quasi-periodicity. When L_c approaches L_s, the correlated nucleation sites are no longer able to grow, forming a chain of small nucleation dots rather than line segments Figure 5.23(d–f).

Experimentally, a range of line segment lengths was observed. Figure 5.24(a) shows correlated nucleation where short line segments construct the self-organized domain lines, corresponding to the case of $L_c > L_s$. Figure 5.24(b), instead, shows correlated nucleation in which domain dots construct the self-organized lines, corresponding to the case of $L_c \simeq L_s$.

One method of controlling the correlation length is by controlling the thickness of the dielectric surface layer. This has been demonstrated by the introduction of an *artificial* dielectric surface layer, increasing the layer thickness and thereby increasing the correlation length [Shur06a]. An alternative method may be to reduce the thickness of the *intrinsic* dielectric surface layer, thereby reducing the correlation length. This is a natural consequence of the AOP process due to the ablation. Therefore, more pulses or higher fluences should remove a greater amount of the intrinsic dielectric surface layer, thus reducing the correlation length. This effect has been observed above where 2 pulses

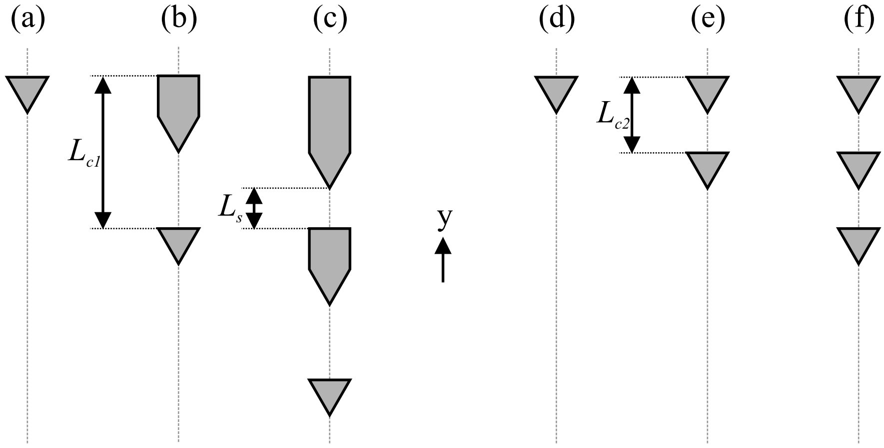

Figure 5.23: The effect of different correlation lengths, $L_{c1} > L_{c2}$, is shown schematically, where a small L_c can inhibit nucleation growth due to the electro-static repulsion between adjacent correlated nucleation sites. Triangles represent initial nucleation, while the pentagons represent growth along the domain line. These shapes are schematic representations only and are not meant to depict actual domain shapes.

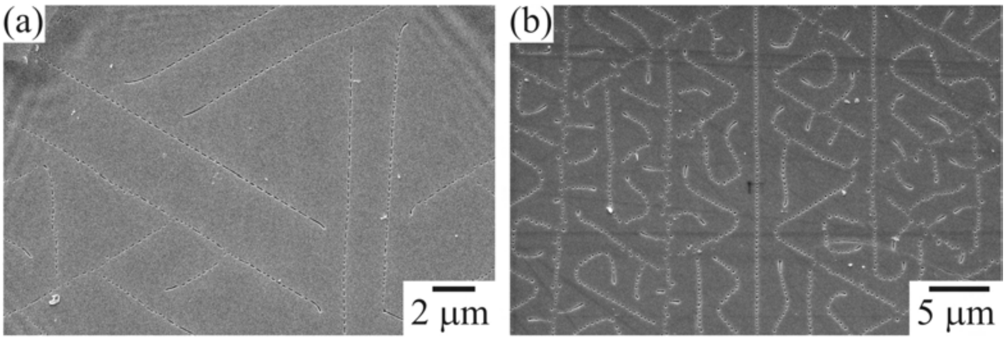

Figure 5.24: Correlated nucleation lines formed from individual (a) line segments or (b) round dots. These undoped CLN samples were illuminated by (a) several pulses of $\lambda = 248$ nm and ~1 J/cm^2, and (b) 100 pulses of $\lambda = 266$ nm and ~1 J/cm^2.

resulted in the line segments of Figure 5.24(a), but 100 pulses resulted in nucleation dots without growth (b).

Crystals from different manufacturers appeared to have different dielectric surface layer thicknesses, which would explain the occurrence of correlated nucleation in some crystals and not in others. In undoped and Mg-doped CLN supplied by Crystal Technology Ltd., AOP predominantly formed *continuous* self-organized domain lines devoid of correlated nucleation. In undoped CLN supplied by Yamaju Ceramics Ltd., however, AOP consistently formed domain chains of correlated nucleation only. The differences in the surfaces of crystals from these suppliers was confirmed by the varying experimental results of UV illumination forming frustrated etching and hydrophilicity.

Mg-doped CLN supplied by Yamaju Ceramics Ltd. provided a further complication, where AOP formed isolated star-like patterns, as shown above in Figure 5.9, rather than the typical intertwined self-organized patterns. This material was of higher quality and had a doping concentration above the ODT, whereas the material supplied by Crystal Technology Ltd. had a higher defect concentration (larger internal field, Table 3.2) and was doped below the ODT. The lower defect density of the Yamaju crystal resulted in the lower nucleation density observed. However this does not explain the short line length growing outward from these nucleations, as other materials exhibited domain lines which appeared limited in length only by the lateral extent of the illumination region and interaction with other lines. It is possible that the velocity of domain growth is much slower in this material, hence producing short lines that are not long enough to interact with the distant neighboring lines. This is supported by observations of EFP, where domain inversion is much smoother and slower in this material as compared to undoped CLN.

5.3.2 Mechanisms of All-Optical Poling

UV illumination was capable of directly forming domain-inverted regions on both polar faces of CLN. On the −z face, these nucleations were shallow surface domains that did not exhibit growth except by increasing the fluence towards the ablation threshold. On the +z face, these nucleations were also shallow surface domains but exhibited preferential growth along the −y directions, forming self-organized patterns. In these complicated light-matter interactions, many forces can contribute to domain reversal.

The incident UV light is absorbed within a shallow depth of the surface. Under some illumination conditions, this can raise the temperature of the crystal at the surface near to the Curie point [Muir06], with several consequences. Firstly, increasing the temperature reduces the coercive field, making domain reversal possible at significantly lower E-fields. Secondly, the pyroelectric effect occurs, wherein the spontaneous polarization reduces with increased temperature, resulting in an over-compensation of charge on the surface. Upon heating, the +z face becomes negatively charged, introducing an E-field that *opposes* domain inversion. Finally, Li out-diffusion is possible at high temperatures, which is well-known to result in domain inversion on the +z face. Secondary ion mass spectrometry (SIMS) measurements have identified UV-ablated material as Li-rich and the underlying UV-modified crystal as Li-deficient [Christensen95]. An important difference in that experiment was the use of a cw scanned beam, where the crystal heating would remain much longer and hence allow for greater diffusion of Li ions than in the case of ns-pulses.

Heating alone appeared insufficient, however, as AOP typically occurred only in the presence of surface ablation. The ablative removal of material causes a reactive ablation force, compressing the crystal below and moving the Li and Nb ions closer to their paraelectric phase positions. Compression reduces the spontaneous polarization and has been shown to induce domain inversion on the +z face of LN [Ohnishi75]. By removing

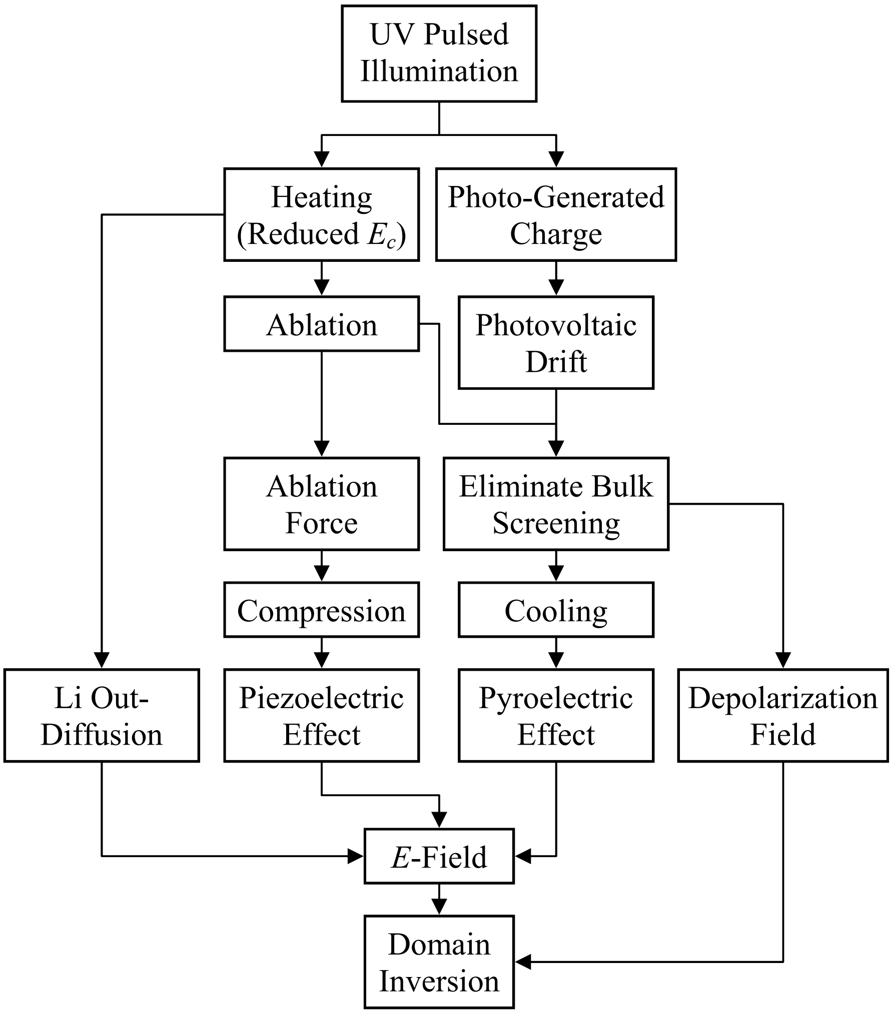

Figure 5.25: Flowchart depicting the possible mechanisms involved in domain inversion by AOP.

the surface layer, the surface compensation charge is also removed, potentially eliminating bulk screening. The remaining uncompensated depolarization field may reach values sufficient to induce domain reversal [Shur06c], which could be a similar effect to the spontaneous backswitching observed under chemical etching [Shur05b]. Additionally, upon cooling of the laser-affected zone at the bottom of the ablated pit, the +z face becomes positively charged due to the lack of surface compensating charge, inducing an E-field in the poling direction, as required. During heat treatment, Nakamura *et al.* observed an increased domain depth by using an increased cooling rate [Nakamura87], indicating that cooling is an important process in thermally-induced domain inversion on the +z face on LN. These UV-induced domain inversion mechanisms are outlined in Figure 5.25.

Exposures by $\lambda = 266$ nm showed the formation of self-organized line patterns even for fluence conditions that did not show any visible ablation under optical microscopy.

However, upon measurement by surface profiler, a surface dip of $\leq$ 100 nm has been detected in the beam centre. One of the reasons this was not visible under microscopy was the Gaussian shape of the beam, resulting in a smooth transition from low intensity to high intensity, and therefore no sharp ablation edges. However, at these low fluences, the surface profiles may represent very modest ablation or other changes to the crystal, whilst still forming AOP domains. λ = 266 nm also produced a higher filling fraction, as compared to 298 nm, due to a higher nucleation rate. This created more domain lines but at the expense of length due to termination upon approach to other lines.

Formation of AOP domain lines was insensitive to a wide range of parameters. The number of pulses incident on the crystal produced very similar results. This is understood due to the ablation and removal of the surface remaining after the previous pulse, thereby creating a new surface for any subsequent domain reversal process. As mentioned above, the number of pulses became important where correlated nucleation occurred and when the ablation depth reduced the thickness of the dielectric surface layer significantly. Varying the pulse fluence produced very similar results when well above the ablation threshold. When using fluences very near the ablation threshold, however, individual nucleations appeared without domain line growth. Similar self-organized domain patterns have also been produced by wavelengths ranging from 248–306 nm. This wavelength range could likely be extended by increasing the pulse fluence for longer wavelengths as the ablation threshold is increased. Longer wavelengths are expected to heat the crystal to a greater depth and may provide a method of forming deeper surface domains.

Ultrashort pulsed light of duration ~130 fs and λ = 800 nm was also used to irradiate the +z face of undoped CLN and Mg:CLN, but failed to produce any similar self-organized surface domains using fluences on both sides of the ablation threshold. The irradiated region did not appear similar to the ns-pulse ablation, with the ultrashort pulses producing relatively little affect on the surrounding crystal. The ultrashort duration of these pulses limited the thermal effects to the crystal, and thereby appeared to prevent the AOP domain formation.

It is interesting to compare domains formed by AOP to domains formed on the +z face of a surface acoustic wave (SAW) device with a patterned inter-digital transducer [Pendergrass87]. The micrographs presented in that article showed etched pits ~0.1 µm wide, and showed evidence of correlated nucleation. In these experiments, domain reversal was attributed to the combined effects of crystal stress and pyroelectric fields, further supporting the proposed mechanisms for the formation of AOP domains.

5.4 Summary

UV illumination has resulted in domain inversion on the +z face of CLN when applying fluences above the ablation threshold. Domains nucleate at defect sites or locations of pre-existing domains, and grow outward along the −y directions, as observed in domains formed by regular EFP. AOP domains are characterized by their strict 2D nucleation, forming 100–300 nm wide domains, extending several microns deep. The domain lines can undergo ordered alignment by periodic illumination via a phase mask, and can be spread laterally and in depth by the subsequent application of an external electric field. Periodic patterning of domains formed by AOP is limited by the electro-static interaction with nearby lines and other domains, and must be countered for small-period patterning. The formation of AOP domains with fluences which produce no ablation would be preferred to eliminate surface damage of a potential device, but to date, AOP domains have been observed primarily in the presence of ablation. An operational regime may exist where illumination by a homogeneous beam profile with a fluence near the ablation threshold will result in a smooth, shallow ablation pit suitable for device operation. Nevertheless, the nano-scale size of these features may prove a desirable property in nano-domain engineering.

Bibliography

[Brown02] P. T. Brown, S. Mailis, I. Zergioti, and R. W. Eason, *Microstructuring of lithium niobate single crystals using pulsed UV laser modification of etching characteristics.* Opt. Mater., 20(2), 125–134 (2002).

[Chernykh05] A. Chernykh, V. Shur, E. Nikolaeva, E. Shishkin, A. Shur, K. Terabe, S. Kurimura, K. Kitamura, and K. Gallo, *Shapes of isolated domains and field induced evolution of regular and random 2D domain structures in* $LiNbO_3$ *and* $LiTaO_3$. Mater. Sci. Eng. B, 120(1-3), 109–113 (2005).

[Chong02] H.-W. Chong, A. Mitchell, J. P. Hayes, and M. W. Austin, *Investigation of KrF excimer laser ablation and induced surface damage on lithium niobate.* Appl. Surf. Sci., 201(1-4), 196–203 (2002).

[Christensen95] F. K. Christensen and M. Mullenborn, *Sub-band-gap laser micromachining of lithium niobate.* Appl. Phys. Lett., 66(21), 2772–2773 (1995).

[Florea02] C. Florea, *Excimer laser treatment of* $LiNbO_3$. In K. K. Wong (editor), Properties of Lithium Niobate, EMIS Datareviews Series, 290–292, INSPEC, London (2002).

[Gopalan98] V. Gopalan and T. E. Mitchell, *Wall velocities, switching times, and the stabilization mechanism of 180° domains in congruent* $LiTaO_3$ *crystals.* J. Appl. Phys., 83(2), 941–954 (1998).

[Gopalan01] V. Gopalan, N. A. Sanford, J. A. Aust, K. Kitamura, and Y. Furukawa, *Crystal growth, characterization, and domain studies in lithium niobate and lithium tantalate ferroelectrics.* In H. S. Nalwa (editor), Ferroelectrics and Dielectrics, volume 4 of *Handbook of Advanced Electronic and Photonic Materials and Devices*, 57–114, Academic Press, San Diego, USA (2001).

[Jungk06] T. Jungk, A. Hoffmann, and E. Soergel, *Quantitative analysis of ferroelectric domain imaging with piezoresponse force microscopy.* Appl. Phys. Lett., 89(16), 163507 (2006).

[Lobov06] A. I. Lobov, V. Y. Shur, I. S. Baturin, E. I. Shishkin, D. K. Kuznetsov, A. G. Shur, M. A. Dolbilov, and K. Gallo, *Field induced evolution of regular and random 2D domain structures and shape of isolated domains in* $LiNbO_3$ *and* $LiTaO_3$. Ferroelectrics, 341(1), 109–116 (2006).

[Morozovska03a] A. N. Morozovska, E. A. Eliseev, and V. V. Obukhovsky, *Light induced micro-domains in ferroelectrics.* Ferroelectrics, 288, 265–275 (2003).

[Morozovska03b] A. N. Morozovska, E. A. Eliseev, V. V. Obukhovsky, and V. V. Lemeshko, *Photomicrodomains in ferroelectrics: formation and light scattering caused by them.* Semiconductor Physics, Quantum Electronics & Optoelectronics, 6(3), 324–332 (2003).

[Muir06] A. C. Muir, G. J. Daniell, C. P. Please, I. T. Wellington, S. Mailis, and R. W. Eason, *Modelling the formation of optical waveguides produced in* $LiNbO_3$ *by laser induced thermal diffusion of lithium ions.* Appl. Phys. A, 83(3), 389–396 (2006).

[Nakamura87] K. Nakamura, H. Ando, and H. Shimizu, *Ferroelectric domain inversion caused in* $LiNbO_3$ *plates by heat treatment.* Appl. Phys. Lett., 50(20), 1413–1414 (1987).

[Ohnishi75] N. Ohnishi and T. Iizuka, *Etching study of microdomains in* $LiNbO_3$ *single crystals.* J. Appl. Phys., 46(3), 1063–1067 (1975).

[Pendergrass87] L. L. Pendergrass, *Ferroelectric microdomain reversal at room temperature in lithium niobate.* J. Appl. Phys., 62(1), 231–236 (1987).

[Reich98] M. Reich, F. Korte, C. Fallnich, H. Welling, and A. Tunnermann, *Electrode geometries for periodic poling of ferroelectric materials.* Opt. Lett., 23(23), 1817–1819 (1998).

[Scott04] J. G. Scott, A. J. Boyland, S. Mailis, C. Grivas, O. Wagner, S. Lagoutte, and R. W. Eason, *Self-ordered sub-micron structures in Fe-doped* $LiNbO_3$ *formed by light-induced frustration of etching.* Appl. Surf. Sci., 230(1-4), 138–150 (2004).

[Scott05] J. G. Scott, Laser-assisted surface and domain microstructuring of lithium niobate. Ph.D. thesis, University of Southampton (2005).

[Shur00] V. Y. Shur, E. L. Rumyantsev, E. V. Nikolaeva, and E. I. Shishkin, *Formation and evolution of charged domain walls in congruent lithium niobate.* Appl. Phys. Lett., 77(22), 3636–3638 (2000).

[Shur05a] V. Y. Shur, *Correlated nucleation and self-organized kinetics of ferroelectric domains.* In J. W. P. Schmelzer (editor), Nucleation theory and applications, 178–214, Wiley (2005).

[Shur05b] V. Y. Shur, A. I. Lobov, A. G. Shur, S. Kurimura, Y. Nomura, K. Terabe, X. Y. Liu, and K. Kitamura, *Rearrangement of ferroelectric domain structure induced by chemical etching.* Appl. Phys. Lett., 87(2), 022905 (2005).

[Shur06a] V. Y. Shur, *Domain engineering in lithium niobate and lithium tantalate: Domain wall motion.* Ferroelectrics, 340(1), 3–16 (2006).

[Shur06b] V. Y. Shur, *Kinetics of ferroelectric domains: Application of general approach to* $LiNbO_3$ *and* $LiTaO_3$. J. Mater. Sci., 41(1), 199–210 (2006).

[Shur06c] V. Y. Shur, D. K. Kuznetsov, A. I. Lobov, E. V. Nikolaeva, M. A. Dolbilov, A. N. Orlov, and V. V. Osipov, *Formation of self-similar surface nano-domain structures in lithium niobate under highly nonequilibrium conditions.* Ferroelectrics, 341(1), 85–93 (2006).

[Sones03] C. L. Sones, Domain engineering techniques and devices in lithium niobate. Ph.D. thesis, University of Southampton (2003).

[Valdivia05a] C. E. Valdivia, C. L. Sones, J. G. Scott, S. Mailis, R. W. Eason, D. A. Scrymgeour, V. Gopalan, and I. Clark, *Nano-scale ultraviolet laser-induced ferroelectric surface domains in lithium niobate.* In Conference on Lasers and Electro-Optics - Europe (invited), OSA, Munich, Germany (2005).

[Valdivia05b] C. E. Valdivia, C. L. Sones, J. G. Scott, S. Mailis, R. W. Eason, D. A. Scrymgeour, V. Gopalan, T. Jungk, E. Soergel, and I. Clark, *Nanoscale surface domain formation on the $+z$ face of lithium niobate by pulsed ultraviolet laser illumination.* Appl. Phys. Lett., 86(2), 022906 (2005).

[Wellington07] I. T. Wellington, C. E. Valdivia, T. J. Sono, C. L. Sones, S. Mailis, and R. W. Eason, *Ordered nano-scale domains in lithium niobate single crystals via phase-mask assisted all-optical poling.* Appl. Surf. Sci., 253(9), 4215–4219 (2007).

Chapter 6

Light-Assisted Poling

The process of EFP provides a reliable, high-quality technique for fabricating controllable periodic domain structures in LN and LT. On the other hand, AOP is a simpler process that has been shown to allow some limited degree of control over tailoring the nanoscale surface domain structure in these materials through illumination by a pulsed laser only. By combining the two approaches, it may be possible to leverage the benefits of each, while minimizing their limitations. A new process, referred to as light-assisted poling (LAP), combines the use of a structured illumination patterning and a uniform electric field to induce a domain pattern in the target material, hoping to achieve this goal of improved ferroelectric domain control.

The LAP process has several potential advantages. Firstly, for periodic domain patterns most often required in QPM devices, interferometry would allow the elimination of the photolithographic mask typically used in EFP for defining the patterned electrode. Therefore, more flexible and less expensive fabrication becomes possible. Secondly, LAP uses a uniform electric field across the whole sample area, eliminating the problem of spatial inhomogeneity caused by the small-scale periodic electrodes used in EFP. The illumination pattern can be tailored to have a high aspect ratio throughout the entire thickness of the material, as opposed to the electric field which is highly concentrated at the edges and corners of the electrodes and quickly becomes uniform below the surface. This advantage has the potential to improve domain depth uniformity, and to extend domain engineering to thicker materials.

This chapter will detail and analyze the results accomplished to date in light-assisted poling using cw and fs-pulsed light in a variety of undoped and doped LN and LT, using focused beams and patterned light. Prior research in this field has been discussed in Section 3.5.

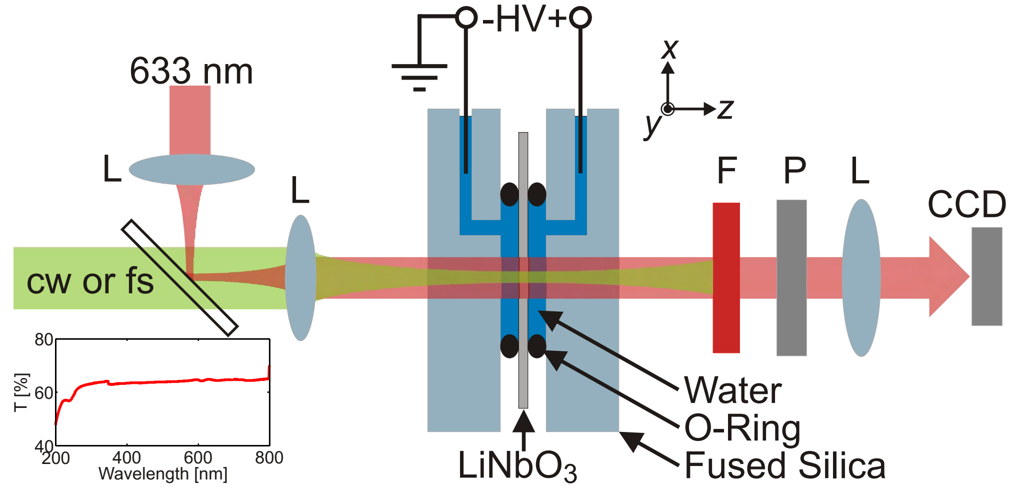

FIGURE 6.1: LAP setup, showing the focusing of the illuminating cw or fs-pulsed beam incident on the −z face of a lithium niobate sample held between water electrodes using transparent fused silica plates. The polarized beam of $\lambda = 633$ nm light is of low intensity and used only for visualization of the poling process via the crossed polarizer and CCD camera. The 3D coordinate system describes the orientation of the target crystal. The inset plots the transmission spectrum of the holder filled with water. (F = red filter; P = polarizer; L = lens; HV = high voltage.) Transparent holder kindly supplied by Professor K. Buse, University of Bonn, Germany.

6.1 Experimental Setup

The experimental setup used for the LAP experiments is shown in its simplest form in Figure 6.1. A transparent holder constructed of UV-grade fused silica surrounds the LN or LT sample, held tightly by insulating silicone O-rings. Holes drilled through the fused silica holder permitted the application of the uniform liquid electrodes (in this case, filtered tap water) onto both faces of the crystal. Both cw and fs-pulsed laser light were focused onto the crystal, in a wavelength range limited only by the transparency of the holder and liquid electrodes, shown in the inset of Figure 6.1. Simultaneous to illumination, high voltage was applied to the +z face of the crystal via the liquid electrodes. In-situ visualization of the poling process was possible via a colinear low-intensity HeNe laser, collimated through the crystal, or a white light lamp. The filter removed the poling laser light from the visualization end of the setup. The crossed polarizer and applied voltage provided stress-induced birefringence and electro-optic refractive index contrast, respectively, at the domain walls, allowing the visualization as the walls formed and grew, as previously discussed in Section 3.1.1.

The first laser system used for the LAP experiments was a cw Ar^+ laser. The individual laser lines used were at wavelengths 457, 488, and 514.5 nm in the blue–green range of the spectrum, well within the transmission region for both LN and LT. The Gaussian beam was spatially filtered and collimated before being focused onto the crystal, providing intensities ranging from W/cm^2 to kW/cm^2.

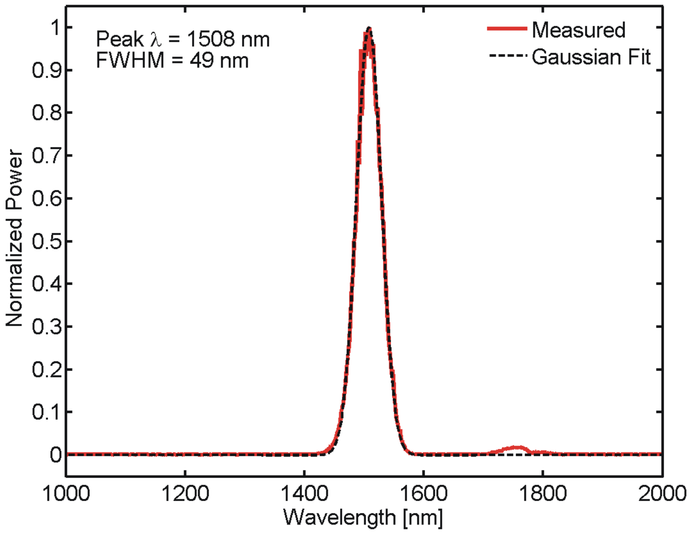

FIGURE 6.2: Spectral measurement of the FAST laser RegA output, tuned near 1500 nm via an OPA.

A similar laser system used for the LAP experiments was a cw frequency-doubled Ar^+ laser (FreD) on loan from Rutherford Appleton Laboratory. This laser provided laser lines of wavelengths 244 and 257 nm, though only the 244 nm line was used in these experiments. The Gaussian beam was focused onto the crystal, providing kW/cm^2 intensities.

The second laser used for the LAP experiments was a Coherent ultrafast laser system in the Femtosecond Applications of Science and Technology (FAST) shared facility at the Optoelectronics Research Centre, providing ~130 fs pulses tunable from the ultraviolet to infrared wavelength regions. The Mira laser is the Ti:sapphire oscillator of the system, utilizing Kerr lens mode-locking. Pumped by a 10 W Verdi laser (λ = 532 nm), the Mira outputs ~nJ energies at a repetition rate of 75 MHz in a wavelength range of 700–980 nm. The Mira seeds two regenerative amplifiers, the RegA and Legend. The RegA, pumped by an 18 W Verdi laser, provides ~μJ energies at a repetition rate of 250 kHz in a wavelength range of 750–850 nm. The Legend, pumped by a 30 W Evolution laser (λ = 527 nm), provides ~mJ energies at a repetition rate of 1 kHz in a wavelength range of 700–900 nm. The RegA and Legend outputs were routed into optical parametric amplifiers (OPA) to generate the tunable wavelength range. This range was further extended by an additional set of second- and third-harmonic modules. An example of a spectral scan of the output from an OPA tuned to near 1500 nm wavelength is shown in Figure 6.2. For the wavelengths used for fs-pulsed LAP, the range 305–383 nm operated at 1 kHz and the range 400–1500 nm operated at 250 kHz.

The properties of these laser sources are summarized in Table 6.1.

TABLE 6.1: Comparison of the properties of the lasers used for light-assisted poling.

Laser:	Ar^+	FreD	Mira	RegA	Legend
Type	cw	cw	pulsed	pulsed	pulsed
Repetition Rate	-	-	75 MHz	250 kHz	1 kHz
Pulse Duration [fs]	-	-	120–140	120–140	120–140
Pulse Energy	-	-	nJ	μJ	mJ
Max Power [W]	3	0.2	1.2	1.2	2.5
Wavelength [nm]	457, 488, 514.5	488	700–980	750–850	700–900
Frequency Conversion [nm]	-	244	350–490	240–700 930–2400	300–2600

6.1.1 Patterned Illumination

Initial LAP experiments used only the unpatterned Gaussian beams from each laser. However, one important advantage of the LAP process is its ability to remove the need for photolithographic patterning by imparting the desired domain pattern via a patterned optical field, as illustrated in Figure 6.3. This patterning of the illuminating laser light was accomplished in several ways.

The simplest and most frequently used method of tailoring the beam was to use a beam expander setup with a negative and positive lens. This Galilean-type expander was used to avoid producing real focal points, preventing break-down in air by the high peak powers. A variable aperture selected a central region of the expanded Gaussian beam to obtain illumination with a more uniform intensity and a more sharply defined boundary. A perfectly uniform beam would be preferred, but as the results have shown, this truncated Gaussian beam was sufficient for reproducible results and was hence used prior to any further patterning of the beam.

The first method for delivering patterned light to the crystal was via mask projection. This technique used a single slit or aluminium absorption mask, imparting its pattern on the light, then projected onto the target crystal to achieve the required degree of magnification,

$$M = -\frac{d_i}{d_o} \tag{6.1}$$

where d_o and d_i are the object and image distances, respectively, shown in Figure 6.4(a). The second method was to use a contact mask placed directly on the surface of the target crystal, shown in Figure 6.4(b), typically using a commercial transmission electron microscope (TEM) grid, commonly available in various sizes of linear and hexagonal patterns. The final method used to pattern the incident light was the illumination of a phase mask, shown in Figure 6.4(c). The phase mask was placed near to the front face of the crystal and resulted in a periodic illumination pattern ideally suited to producing 1D gratings desirable for QPM. A two-dimensionally periodic phase mask could also be

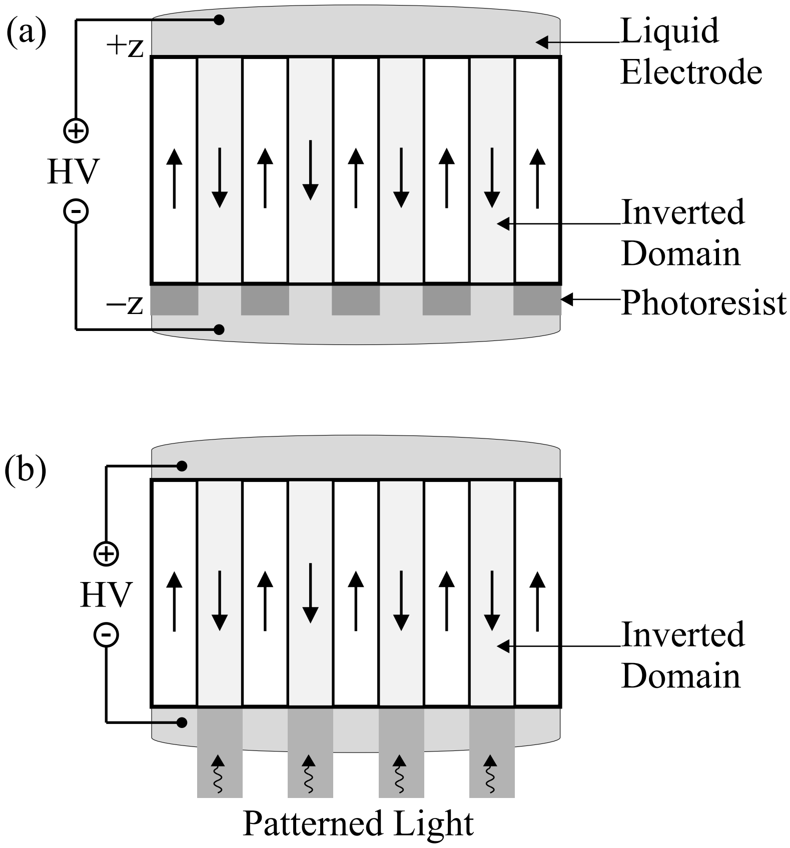

FIGURE 6.3: A comparison of (a) the electric-field periodic poling setup using photolithographically-patterned photoresist defining the electrode on −z face and (b) the light-assisted poling setup using patterned illumination of the −z face with unstructured liquid electrodes.

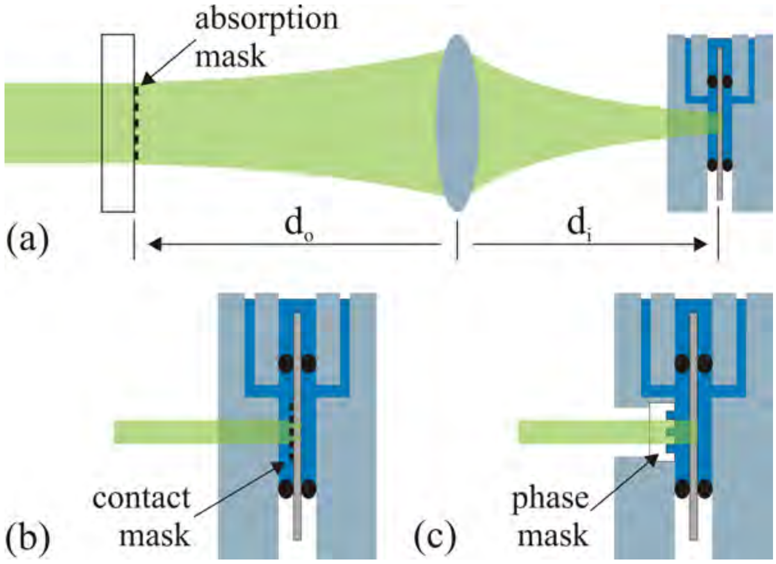

FIGURE 6.4: The methods for patterned illumination during LAP, including (a) absorption mask projection, (b) contact mask illumination, and (c) phase mask illumination.

used in an identical setup for the formation of a 2D nonlinear photonic crystal (NPC), but such a phase mask was not available at this time.

These patterning techniques can also be used in the conventional approach to domain inversion, using the technique of EFP. However, in that case, the patterning is applied to the photolithography of the photoresist layer. An advantage of the LAP process is that these photolithographic steps are eliminated, and patterning is applied directly to the ferroelectric crystal itself.

6.1.2 Results

Illumination using near-infrared, visible, or ultraviolet light from cw or fs-pulsed lasers in conjunction with a simultaneously applied external electric field was capable of forming inverted ferroelectric domains preferentially within the region of illumination in both LN and LT crystals. The following sections discuss the results of the cw and fs-pulsed experiments separately.

6.2 cw LAP

The majority of LAP experiments using cw laser illumination used the visible laser lines of an Ar^+ laser. Additional feasibility studies were conducted using a frequency-doubled Ar^+ laser, providing a UV wavelength of 244 nm, discussed separately in Section 6.2.4. Some of the results from these cw-LAP experiments have been reported in [Sones05; Valdivia05a].

6.2.1 Reduction of the Nucleation Field using cw-LAP

The influence of cw visible light on the nucleation field of various materials was investigated. The materials used were z-cut single crystals, optically polished on both faces. The main crystals explored were undoped CLN, Mg:CLN with doping levels both above and below the ODT, and 1-mol% Mg:SLN. The location of the OH absorption peak was used to determine whether the doping level in the crystal was above the ODT, as discussed in Section 2.2.2.2.

A visible line of an Ar^+ laser was focused to a typical spot radius measuring approximately 45 μm, a compromise allowing sufficiently high intensity while providing a Rayleigh range of approximately 1 cm which is much larger than the thickness of most crystals used (0.5–1 mm). This ensured a relatively uniform spatial distribution across the entire crystal thickness, as compared to other studies where tight focusing resulted in inhomogeneous illumination [Dierolf04]. In the materials under test, the visible wavelengths used ($\lambda = 457$, 488, and 514.5 nm) have very low absorption, $\alpha < 0.005$ mm^{-1}.

Each crystal under investigation was first poled and re-poled typically through five cycles. This cycling determined the dark nucleation field, $E_n(I = 0)$, and for the following LAP experiments also avoided the first poling cycle of the virgin crystal which is well known to have a larger coercive field than all subsequent poling cycles [Brown99]. Therefore the forward and reverse dark nucleation fields, $E_{n,f}(I = 0)$ and $E_{n,r}(I = 0)$, respectively, are determined by averaging several poling cycles beginning with the second cycle, while ramping the electric field at a constant rate of 10 V/mm/s. This cycling obtained a reproducible value that was stable for at least 50 subsequent poling cycles [Sones05].

The light-induced nucleation field, $E_n(I)$, was measured as a function of incident intensity with the beam propagating in the +z direction (i.e. incident on the −z face) while again ramping the electric field at 10 V/mm/s. The minimum electric field resulting in localized domain nucleation was observed optically *in situ* by employing a polarizer crossed relative to the input polarization of the imaging HeNe laser. The value of the electric field was recorded upon observation of a nucleation *pop*, where a nucleation site appeared over a very short time interval, $t \ll 1$ s. Further ramping of the applied voltage, with or without illumination, spread this nucleation point into a larger bulk domain. Averaging over several E-field ramps and illumination at different locations of the crystal provided the nucleation field, $E_n(I)$, at intensity, I. The normalized nucleation field, defined by,

$$E_{n,norm}(I) = \frac{E_n(I)}{E_n(I = 0)} \tag{6.2}$$

is the ratio of the light-induced nucleation field to the dark nucleation field. $E_{n,norm}(I)$ is a convenient figure-of-merit for comparing the relative light-induced effect for different materials because the dark nucleation field can vary by at least two orders of magnitude. The normalized nucleation field is shown in Figure 6.5 as a function of intensity of $\lambda = 514.5$ nm light incident on undoped and Mg-doped LN. In each of these materials, the nucleation field shows a monotonic decrease with increasing laser intensity. At higher intensities, saturation is effectively reached, achieving a maximum reduction defined as,

$$R = 1 - E_{n,norm}(I_{max}) \tag{6.3}$$

The reduction in the nucleation field was most prominent in the Mg-doped congruent and stoichiometric LN crystals doped *above* the ODT. The nucleation field was reduced by up to 91% at high intensities, reaching saturation for $I \gtrsim 2$ kW/cm^2. In the undoped CLN case, a maximum reduction of only ∼31% is achieved. Interestingly, when CLN was doped with Mg *below* the ODT, the reduction of the nucleation field was only slightly greater than the undoped case, resulting in a maximum reduction of ∼41%.

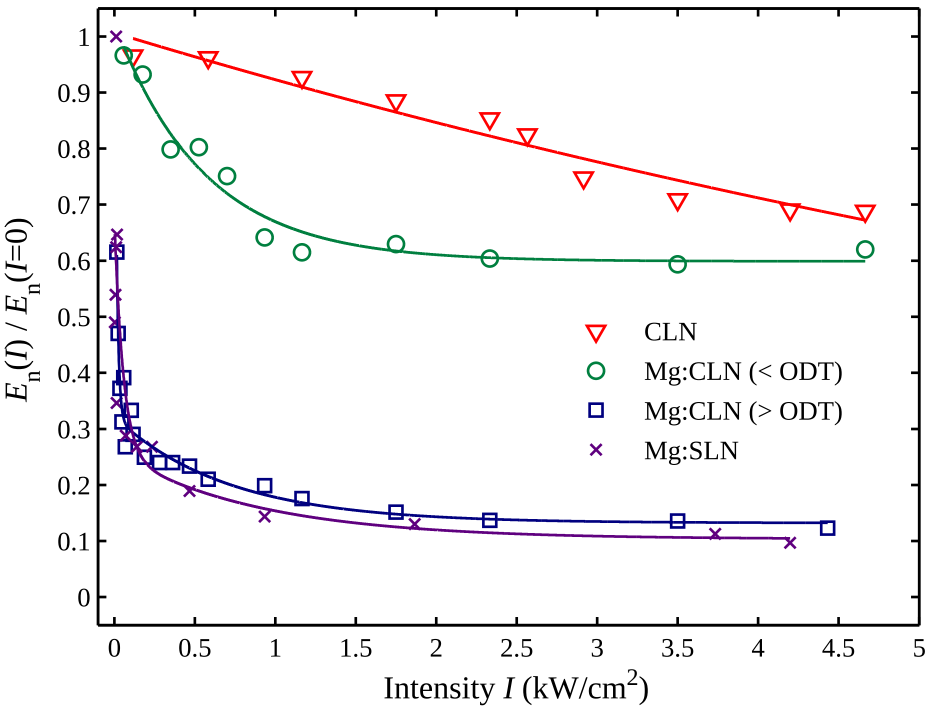

FIGURE 6.5: The normalized nucleation field as a function of incident intensity of $\lambda = 514.5$ nm cw light for undoped CLN, Mg:CLN, and Mg:SLN. The solid lines are least-squares fits to equations of the form $y = c_1 \exp(-x/c_2) + c_3 \exp(-x/c_4) + c_5$.

TABLE 6.2: Electric field required for domain nucleation in different crystals, in the presence and absence of cw light at $\lambda = 514.5$ nm with $I_{max} \simeq 4$ kW/cm^2.

Crystal Type	$E_n(I=0)$ [kV/mm]	$E_n(I_{max})$ [kV/mm]	Reduction [%]
Undoped CLN	20.9	14.3	31
Mg:CLN (< ODT)	5.30	3.15	41
Mg:CLN (> ODT)	6.28	0.78	88
1-mol% Mg:SLN	2.63	0.25	91

The maximum reductions in the nucleation fields using $\lambda = 514.5$ nm and an intensity of $I_{max} = 4$ kW/cm^2 for undoped and doped LN are stated in Table 6.2.

The light-induced nucleation field in these crystals showed little, if any, wavelength dependence from the three visible lines of the Ar$^+$ laser. This is demonstrated for the case of 1-mol% Mg:SLN (doped above the ODT) in Figure 6.6.

The data presented above was measured in the forward poling direction with light incident on the −z face, and both the electric field and light simultaneously applied. A reduction of similar magnitude in the nucleation field has also been observed in the reverse poling direction. For these exposures with uniform illumination across the thickness of the crystal, the effect was also independent of the crystal face that the light was

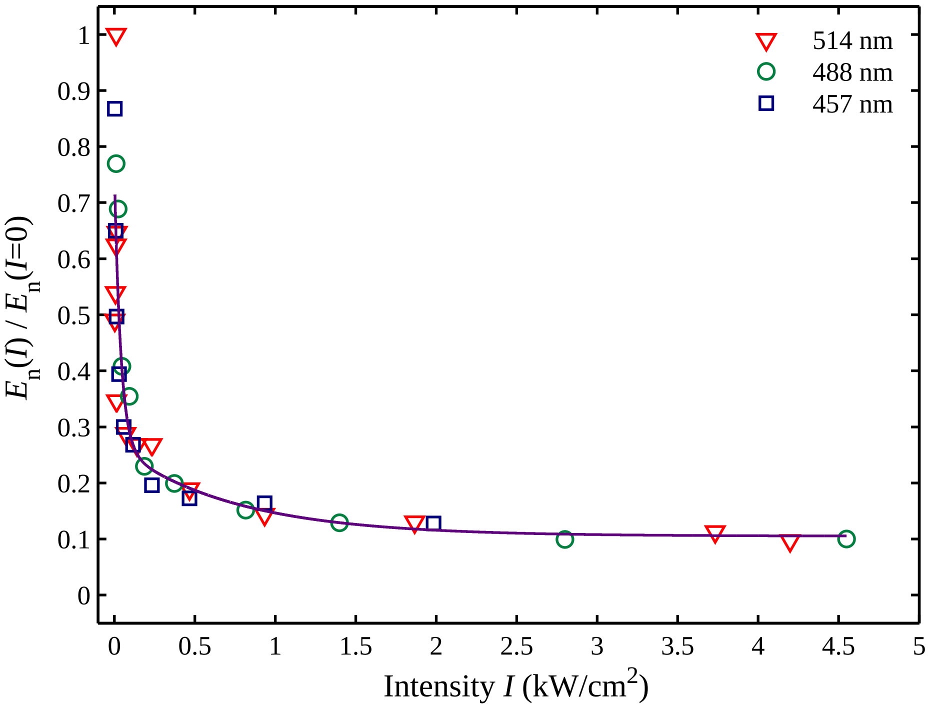

Figure 6.6: The normalized nucleation field as a function of incident intensity of cw light in 1-mol% Mg:SLN using $\lambda = 457$, 488, 514.5 nm. The solid line is the least-squares fit of the data from all wavelengths to an equation of the form $y = c_1 \exp(-x/c_2) + c_3 \exp(-x/c_4) + c_5$.

incident upon. Nonetheless, nucleation always appeared first on the −z face and resulted in a larger inverted domain area as compared to the +z face. Finally, the simultaneous application of both the electric field and laser light was required to observe a reduction in the nucleation field, as any delay between the two resulted in no noticeable effect.

6.2.2 Domain Direct-Write using cw-LAP

This laser-induced reduction of the nucleation field, confined to the area of illumination, provided a simple method of directly writing domain structures into the ferroelectric crystals. A direct-write technique could potentially permit the formation of arbitrary domain patterns without the need of a mask.

To implement this direct-write technique, the laser beam of $\lambda = 514.5$ nm was focused onto the target crystal using various intensities and a constant electric field. Under the conditions of an intensity, $I = 1.2$ kW/cm^2, and an E-field, $E = 4.0$ kV/mm, domain nucleation occurred within ∼1 s in a 5-mol% Mg:CLN sample. Following nucleation within the illuminated region, the crystal was moved manually using a translation stage in steps of approximately 100 µm along the y-axis of the crystal. Repeating this procedure produced a sequence of domain-inverted hexagons several millimetres in length,

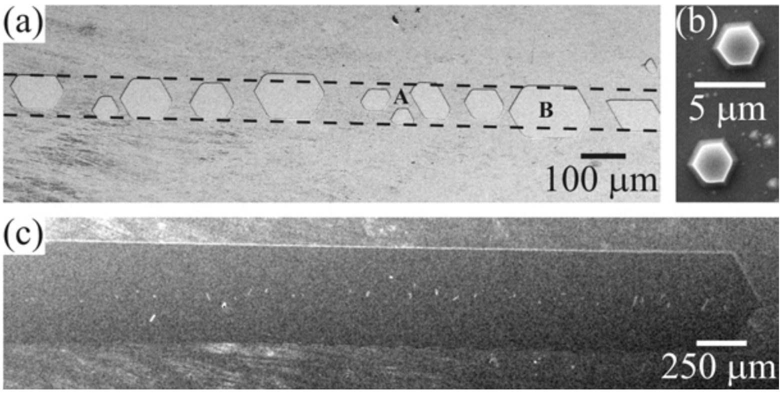

FIGURE 6.7: SEM micrographs of the HF-etched −z face of 5-mol% Mg:CLN in which domain direct-write using cw-LAP formed (a) individual bulk domains by sequential exposure, (b) surface micro-domains induced by a tightly focused beam via a 6.3× objective lens, and (c) a continuously scanned domain line. The dashed lines in (a) indicate the lateral extent of the beam.

shown in Figure 6.7(a) after etching in HF. The dashed lines in this figure represent the $1/e^2$ diameter (~90 µm) of the laser spot. Chemical etching of this sample revealed corresponding domain patterns on both −z and +z faces, indicating the formation of bulk domains extending the entire 0.5-mm thickness of the crystal. The lateral dimensions of these domains vary from 20–120 µm. Their central positions are distributed across the width of the beam as a result of random nucleations within the illuminated region. The region labelled A in Figure 6.7(a) shows one example where three nucleation sites have grown at different positions within the beam and at different rates. The region labelled B in Figure 6.7(a) shows a similar occurrence where the beam has been incident for a prolonged duration, leading to the merger of the individually nucleated sites. Of particular importance is that spreading of the domain occurred inside the beam diameter, and spread outside only with prolonged exposure.

Scanning rather than stepping the beam resulted in a continuously domain-inverted line, as shown in Figure 6.7(c) for a Mg:CLN crystal. The intensity, $I = 2$ kW/cm^2, and high E-field, $E = 4$ kV/mm, contributed to the spreading of the line not only along the translation direction, but also laterally and eventually outside the beam width. In this instance, this led to a line width approaching 500 µm after being exposed to this E-field for a prolonged duration.

To investigate the feasibility of forming domain sizes on the order of micrometres, tighter focus was used via a 6.3× objective lens, providing a spot radius of approximately 20 µm. This beam was capable of producing inverted domains on the −z face of ~2 µm, as shown in Figure 6.7(b). HF differential etching revealed that these were surface domains, and did not extend to the opposite face of the 0.5-mm thick crystal. In this modified setup, however, the short working distance of the lens meant that simultaneous in-situ visualization of the domain kinetics was not possible, and hence further control

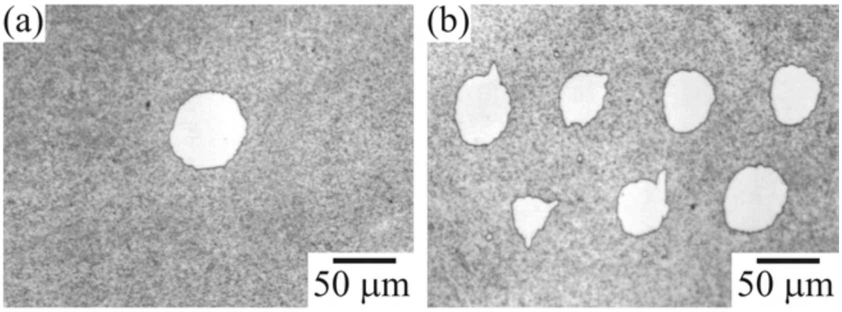

Figure 6.8: cw-LAP patterned illumination using a 400-mesh hexagonal TEM grid on Mg:CLN, showing inverted domains on the −z face using (a) illumination through a single hole (1 s illumination) and (b) sequential illuminations through adjacent holes (∼0.5 s each), using $I = 2$ kW/cm^2 of $\lambda = 514.5$ nm light and $E = 1400$ V/mm.

of these domains proved difficult. Therefore, this domain size does not represent the minimum size achievable, as they have likely grown from their initial sizes at the instant of nucleation. Improving this setup to allow in-situ monitoring should in the future allow for the formation of even smaller domains.

6.2.3 Patterned Illumination using cw-LAP

An alternative to the serial nature of the direct-write technique is illuminating with patterned light which has the potential for large-area patterns inverted at a single time. This can be done in several ways, including projection of a mask pattern, use of a contact mask, and deposition of various materials directly onto the crystal.

A copper TEM grid was used as a simple and inexpensive contact mask for patterned LAP in Mg:CLN, in a setup depicted in Figure 6.4(b). The grids chosen were commercially available hexagonal patterns with a 400-*mesh* (lines per inch) spacing, providing a 2D hexagonal periodicity with $\Lambda = 63.5$ μm. The large spatial period meant that the focused laser beam of the Ar$^+$ laser could illuminate a single open hole of the periodic pattern, thereby allowing individually addressable nucleation spots, as shown in Figure 6.8. Here, domain inverted nucleations were patterned by directly illuminating a single hole in the TEM grid, then sequentially moving the beam to adjacent holes of the mask. A two-dimensional pattern of inverted domains can be easily produced in this manner, potentially allowing tailoring of a NPC on a period-scale for the introduction of intentional crystal defects. A larger beam would allow parallel growth of several domains simultaneously, but would put a lower limit on the number of holes inverted at once, affecting the customizability of the pattern.

Another method of imparting a pattern onto the light incident on the crystal sample is to deposit material directly onto the sample front surface. In effect, this is very similar to the above TEM grid contact mask. However, with deposition, different materials

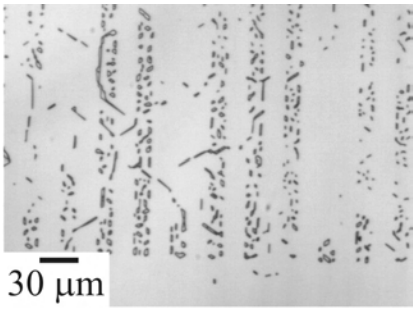

FIGURE 6.9: cw-LAP patterned illumination using a thermally evaporated Al grating with period $\Lambda \simeq 29$ µm on 1-mol% Mg:SLN. The disconnected surface domains outline the location of the Al grating lines prior to their removal.

can be investigated, as well as different thicknesses (i.e. optical densities) and patterns. Aluminium was chosen as an ideal material for its high conductivity ($\sigma \simeq 3.8 \times 10^7$ S/m) and high reflectance ($R \simeq 90\%$ across the visible spectrum). A lift-off technique was used to pattern the Al. On the cleaned crystal, the photoresist was first spun, then the pattern exposed in a mask aligner and developed. A thermal evaporator was used to deposit ~130 nm of Al onto the crystal and photoresist pattern. The crystal was then placed in an acetone bath to achieve the lift-off of the metal on the photoresist, resulting in a negative pattern in the Al. The illumination with $\lambda = 514.5$ nm through a uniform test film showed ~0.02% transmission, achieving the desired high optical density.

The Al-patterned LN crystals were then illuminated by the Ar^+ laser using the LAP technique, with results in a Mg:SLN sample shown in Figure 6.9. Due to the difficulty in the optical visualization of the inverting domain area, over-poling has occurred in this crystal. Originally the $-$z face, this surface has now been almost entirely inverted to the +z face. The remaining disconnected domains outline the original locations of the Al grating lines prior to removal in Al-etchant. Figure 6.9 shows the bottom edge of the periodic pattern, hence the reason no domains are visible at the bottom of this micrograph. To form these disconnected domains, the Al has acted to suppress domain inversion, as less light was incident on the crystal in these areas and thus provided less reduction in the nucleation field. Therefore these micro-domains are of the original orientation of the crystal prior to poling and appear only on the surface. In this way, the process was similar to the formation of domains using the surface poling technique (Section 3.3.3), where over-poling was utilized to invert all but a periodic surface layer as chosen by, in that case, a photoresist layer. The Al, rather than electrically insulating, acted as an *optical insulator*.

LAP is also possible on a crystal with patterned photoresist. Patterning with photoresist would prevent poling of covered areas by inhibiting charge delivery to the surface, while light would induce nucleation elsewhere at a lower voltage than would be required with EFP. However, it proved difficult to optically visualize the domain inversion process due to the edges of the photoresist, resulting in poor control forming only a few short domain lines in selected locations on the crystal, and no truly periodic patterns. Nonetheless, it may be possible to implement this technique with more sophisticated controls and current monitoring.

Patterning via photoresist has an inherent problem that light still impinges upon the crystal below, increasing the conductivity of this area due to the photoconductivity of the material. This conductivity served to allow motion of charge laterally underneath the photoresist, delivering the poling current required in the covered regions. To prevent this from occurring, an opaque photoresist would be preferred. Unfortunately at the time of these experiments, no suitable opaque photoresists were available, some due to high conductivities, high optical transmission, insufficient patterning resolution, or inability to use in an aqueous environment. If a suitable material becomes available, it would have the added benefit of creating modulation in both the optical and electrical properties of poling.

Despite these attempts at using contact masks for patterning the LAP process, they have proved not to be ideal solutions for domain patterning. Firstly, deposition or placement of a contact mask requires processing for each crystal, which are additional undesirable fabrications steps. Secondly, electrode contact with the crystal changes the properties of poling, as noted during investigations of regular EFP using different contact metals or as compared to photoresist-patterned EFP using liquid electrodes [Shur02]. Therefore to eliminate these complications, patterning via mask projection or interference techniques may be preferred. These techniques were further explored using fs-pulsed light in Sections 6.3.3 and 6.3.4.

6.2.4 Ultraviolet cw-LAP

A frequency-doubled Ar^+ laser operating at $\lambda = 244$ nm was used for UV cw-LAP experiments. The intention of these initial exploratory experiments was to determine whether this wavelength would also show an effect on the nucleation of domains in undoped and doped LN materials, and if so, to measure the intensity-dependent nucleation field. While an effect on domain nucleation and spreading was observed, establishing quantitative results was complicated by the qualitatively different poling behavior as compared to the visible cw case.

With UV light illuminating the $-$z face of undoped CLN, preferential domain nucleation did not occur even when the external electric field was ramped very near to the dark nucleation field. However, as the dark nucleation field was reached, general E-field-induced nucleation occurred throughout the crystal (illuminated and non-illuminated regions). At this stage the UV was capable of spreading and merging the nucleated domains, increasing their growth rate. By scanning the beam, a domain inverted region could be painted across the crystal surface. However, the inverted region was not clear as

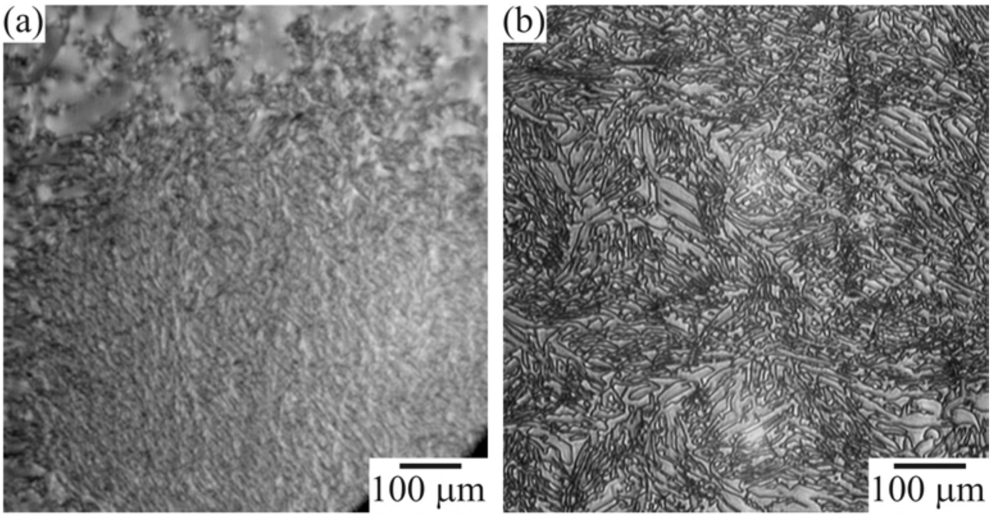

FIGURE 6.10: Optical images of UV cw-LAP in undoped CLN in the forward poling direction (a) immediately after poling, as viewed by the in-situ visualization setup, and (b) a similar area following HF etching of the −z face.

for a typical domain, but rather infiltrated by a random collection of dark patches which seemed to coalesce at the edges of domains and at the boundaries at which domains merged, shown in Figure 6.10(a). It is possible that this was a result of photorefractive damage. However it is important to note that this damage did *not* occur in the absence of domain inversion under these illumination conditions. This damage did, nonetheless, appear throughout the expanding domain while the beam illuminated it; this was true even for expanding areas that had not been directly illuminated by the beam. With the beam off, in contrast, the expanding areas of the domain formed without damage and appeared as clear as a regular EFP domain.

Following this domain inversion process, the crystal was etched in HF for 20 minutes, revealing that this damage was also apparent in the domain orientation on the surface, as shown in Figure 6.10(b). In this optical microscope image of the −z face, many domain-inverted regions are randomly distributed across the surface. However, on the +z face, the entire illuminated region is completely inverted, free of this surface structuring. Therefore this structuring may be related to surface defects which form semi-permanent surface domains that do not invert upon regular E-field poling.

When illuminating the virgin −z face of Mg:CLN, different effects were observed. In the reverse poling direction, localized light-assisted nucleation occurred at $E = 2.4$ kV/mm using $I \simeq 6$ kW/cm^2. However, many scattered nucleation points were spread over a diameter of > 500 μm, as compared to the beam diameter of ∼30 μm. This may have resulted from the high intensity or large electric field, but a similarly sized area of nucleation points were observed for an E-field of just 1.2 kV/mm also. With continued illumination, the nucleation points spread and merged. Unlike the undoped CLN case, the in-situ visualization revealed the formation of a predominantly clear domain without

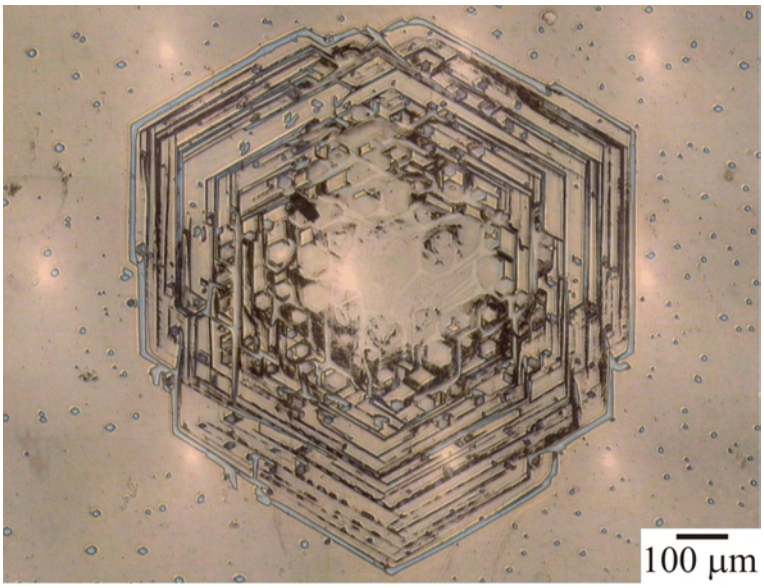

FIGURE 6.11: Optical microscope image of UV cw-LAP of Mg:CLN in the reverse poling direction following HF etching of the $-z$ face. With the beam incident on the crystal, the electric field had been ramped up to $E = 2.4$ kV/mm; subsequently, the entire crystal had been inverted by ramping the voltage above the coercive field.

the same prominent damage. Upon further inspection, however, very dim lines were visible wherever nucleation points had previously merged together. They appeared very similar to imprints of domain walls immediately after jerky wall motion during EFP, but these lines did not gradually disappear as is seen with the wall imprints. After all the nucleation points had merged into a single large domain, the illuminating beam was blocked and unblocked repeatedly. The domain continued to grow without illumination, though at a much slower rate. The same faint lines were visible between the regions inverted with and without illumination. Following this, the voltage was ramped higher to allow the entire crystal to reverse pole. After etching in HF, the resulting domain structure consisted of a sequence of domain-inverted and non-inverted areas, as shown in Figure 6.11. The original nucleation points near the center are still visible, as are the boundaries between regions where the domain grew with and without illumination. Again, this structuring "fixed" surface domains in a permanent orientation.

In the forward poling direction of Mg:CLN, light-assisted nucleation was also possible and appeared first near the center of the beam, shown in Figure 6.12(a–c). However, the growth process of these domains was complicated by the same type of damage first observed above in the undoped CLN case. By continuous exposure to $E = 4$ kV/mm and $I = 6$ kW/cm^2, the domain grew laterally to form a hexagon, but exhibited the same damage induced in the undoped CLN case (c). Blocking the illumination (d), the domain spread at a slower rate, but the inverting region on the outer edges of the domain appeared clear and free from this damage. Illuminating the same spot once again spread the domain at the faster rate, but re-introduced the damage at the newly inverting

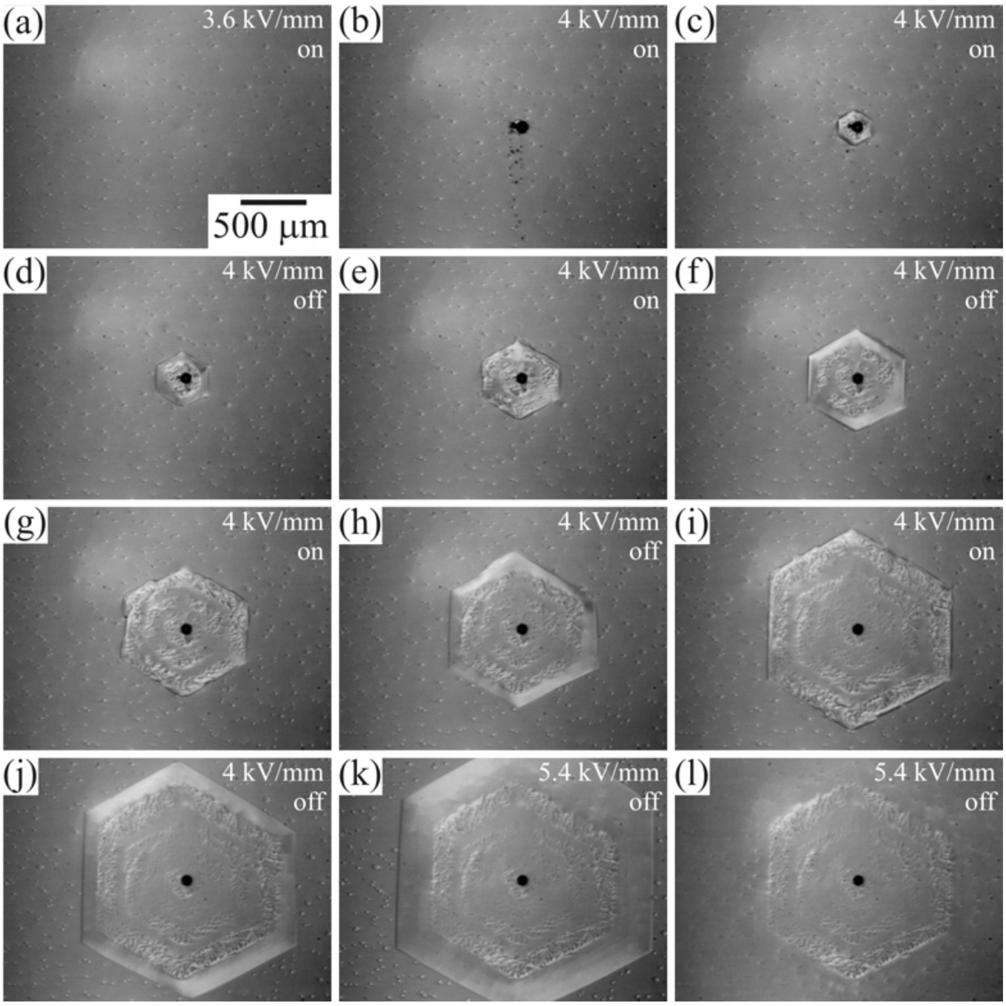

FIGURE 6.12: In-situ visualization of UV cw-LAP of Mg:CLN in the forward poling direction, showing the growth behavior when the incident light $\lambda = 244$ nm of intensity $I = 6$ kW/cm^2 is sequentially blocked (off) and unblocked (on). E-field and the illumination state (on/off) is reported in the top-right corner of each image. The domain spread over the entire crystal to achieve complete poling in (l). The spot diameter was ~30 μm.

boundary without affecting the clear region from the previous step (e). Repeating this several times (f–j) showed that this process was repeatable, always inverting a new clear region when illumination was blocked, and inverting a new damaged region when illumination was unblocked. It is important to note that the same central location was illuminated in each step and was never moved. Therefore, the light incident in the center of the domain affected the growth at the outer edges, well outside the extent of the beam itself, possibly indicating thermal- or photo-induced charge migration to the domain wall. Finally, by ramping to $E = 5.4$ kV/mm with the illumination blocked, the domain expanded to invert the entire crystal without further damage (k–l). Even after complete poling of the crystal, the damaged regions formed during illuminated domain growth remained visible (l).

As these were preliminary experiments into the feasibility and contrasting qualities of using UV light for cw-LAP, only a small set of exposure conditions has been tested. It remains to be determined if other intensity regions and exposure conditions exist such that quality domain inversion without optical damage can occur at a significant reduction in the nucleation field.

6.3 fs-Pulsed LAP

Light-assisted poling using ultrashort pulses of duration 120–140 fs provided a very different regime of operation than in the cw case. Ultrashort pulses provided peak intensities 7–10 orders of magnitude higher than the average intensities. Moving from cw to pulses was also interesting as an analogue to the difference between regular EFP and pulsed-voltage EFP. Finally, the wavelength tunability of the system allowed the testing of a broad spectral range, from 305–1500 nm. The wavelengths for fs-pulsed LAP in the UV (305, 334 nm) and visible (514.5 nm) regions were chosen specifically for comparison to results using cw light, [Wengler05] and Section 6.2, respectively. The success of this technique was therefore applied to a wide variety of patterning techniques and a number of doped LN and LT materials. Some of the results of this section have been reported in [Valdivia05b; Valdivia06a; Valdivia06b; Sones06].

6.3.1 Reduction of the Nucleation Field using fs-LAP

In experiments paralleling those completed using cw-LAP, an intensity-dependent nucleation field using fs-pulsed light was investigated for a host of doped and undoped LN and LT materials. However it was immediately clear that the same procedure was not possible with fs-pulsed light. Results obtained were not consistent from sample to sample, or even from location to location on the same sample. It was quickly realized that the illumination time (or equivalently, number of incident pulses) played a vital role in the nucleation process, which had not been observed in the cw case.

A second very important difference with the fs-pulsed LAP was that light-assisted domains were not always visible using the in-situ visualization setup, which relied on stress-induced birefringence and electro-optic contrast. There are two important reasons for this effect. The first is that the initial domain nucleation induced under fs-pulsed LAP was a shallow surface domain formed under low external electric fields. The shallowness of the domain led to little accumulated contrast from the birefringence at the domain wall. In addition, the relatively low electric fields required for nucleation meant that there was less electro-optic refractive index contrast. It should be noted that domains formed in this way appear clearly with the in-situ visualization setup under most conditions, but when the minimum requirements for domain nucleation were being investigated, this presented complications. To overcome this limitation, it was necessary to use HF chemical etching to reveal whether domain nucleation had occurred. Therefore, unlike the cw case where a smooth ramping of the voltage allowed the in-situ observation of the first instance of domain nucleation, fs-pulsed LAP required exposures at step increments of voltage with later HF etching. This introduced a new uncertainty into the minimum nucleation field, as determined by the voltage step size.

Despite the visualization difficulty due to the illumination-time dependence, it was found that using a suitably slow voltage ramp (of order ∼1 V/mm/s) provided enough time for the nucleated domain to become visible while still allowing a reasonable estimate of the minimum electric field required to induce nucleation. For lower incident intensities where higher electric fields were required for nucleation, this method was more accurate and reproducible, likely due to the greater electro-optic refractive index contrast induced under these conditions. Also, quickly ramping to at least ∼75% of the expected nucleation field did not impact the measurement, and this was particularly useful when high electric fields were required.

This modified voltage ramping method was applied to several different undoped and doped crystals, and summarized in Figure 6.13 using a wavelength of $\lambda = 400$ nm. Again, these results show a highly nonlinear dependence upon intensity, and a rapid decrease in the nucleation field, stabilizing above 10 GW/cm^2 in most cases. However, these curves do not necessarily represent the absolute minimum nucleation field achievable under the intensity and external field conditions. For many of these data points, similar conditions were applied with longer duration or subsequent HF etching to reveal nucleation with either a slightly lower intensity or external electric field. Nonetheless, this data presents general trends and places a useful upper bound on the intensity-dependent nucleation field.

The very different sensitivities to intensity in the tested materials is clearly evident in Figure 6.13. Mg:CLN was most sensitive and also showed the lowest nucleation field, with Mg:SLN achieving similar results. Both undoped CLN and CLT required much larger intensities for domain nucleation and were limited to much higher normalized nucleation fields. Ti-indiffused CLN showed an intermediate sensitivity to wavelength, but achieved a reduction in the nucleation field approaching that of Mg:LN. Interestingly, however, the data fit best to an equation with a single exponential decay rather than the double exponential decay of the other materials.

The minimum nucleation field varied for each material, depending upon the crystal type, dopant, and doping concentration. Relying upon HF etching to determine domain inversion, the minimum nucleation field and the peak intensity used for $\lambda = 400$ nm illumination is summarized in Table 6.3. While the greatest reductions in the nucleation field occurred for Mg-doped LN, not all dopants showed a similar trend. Hf- and high concentrations of Fe-doping had a marginally lower minimum nucleation field than achieved in undoped CLN. But doping CLN with Nd-, Zn-, and low concentrations of Fe,

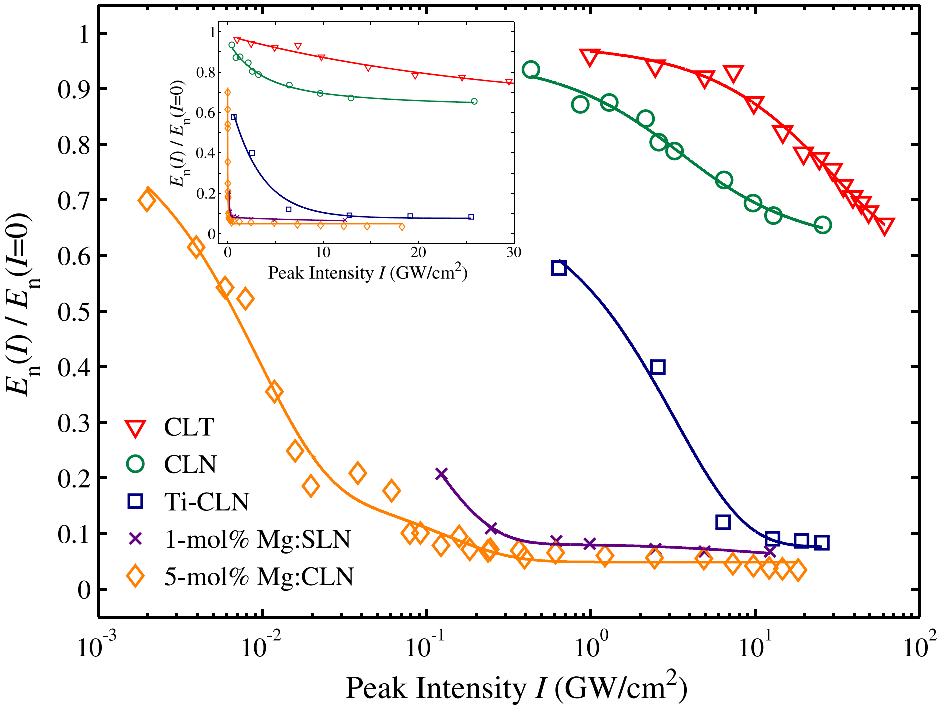

FIGURE 6.13: The normalized nucleation field as a function of incident intensity of fs-pulsed light, $\lambda = 400$ nm, for undoped CLT, undoped CLN, Mg-doped CLN and SLN, and a Ti-indiffused waveguide in CLN. The solid lines are least-squares fits to an equation of the form $y = c_1 \exp(-x/c_2) + c_3 \exp(-x/c_4) + c_5$. The inset presents the same data on a linear scale.

TABLE 6.3: Electric field required for domain nucleation in different crystals, in the presence and absence of fs-pulsed light at $\lambda = 400$ nm. The laser repetition rate was 250 kHz.

Crystal Type	$E_n(I=0)$ [kV/mm]	$E_{n,min}$ [kV/mm]	Intensity, I [GW/cm^2]	Reduction [%]
Undoped CLN	20.806	12.500	15	40
5-mol% Mg:CLN	6.337	0.220	18	97
1-mol% Mg:SLN	2.654	0.172	12	94
5-mol% Hf:CLN	10.984	5.957	24	46
1-mol% Nd:CLN	16.975	15.000	10	12
1-mol% Zn:CLN	19.283	14.340	3.4	26
4-mol% Zn:CLN	10.618	9.510	2.7	10
7-mol% Zn:CLN	7.814	6.003	9.0	23
0.01-mol% Fe:CLN	19.080	15.990	1.4	16
0.1-mol% Fe:CLN	21.350	12.000	2.5	44
Ti-CLN	19.130	1.602	25	92
Undoped CLT	20.405	13.398	61	34
7-mol% Mg:CLT	3.088	2.352	18	24

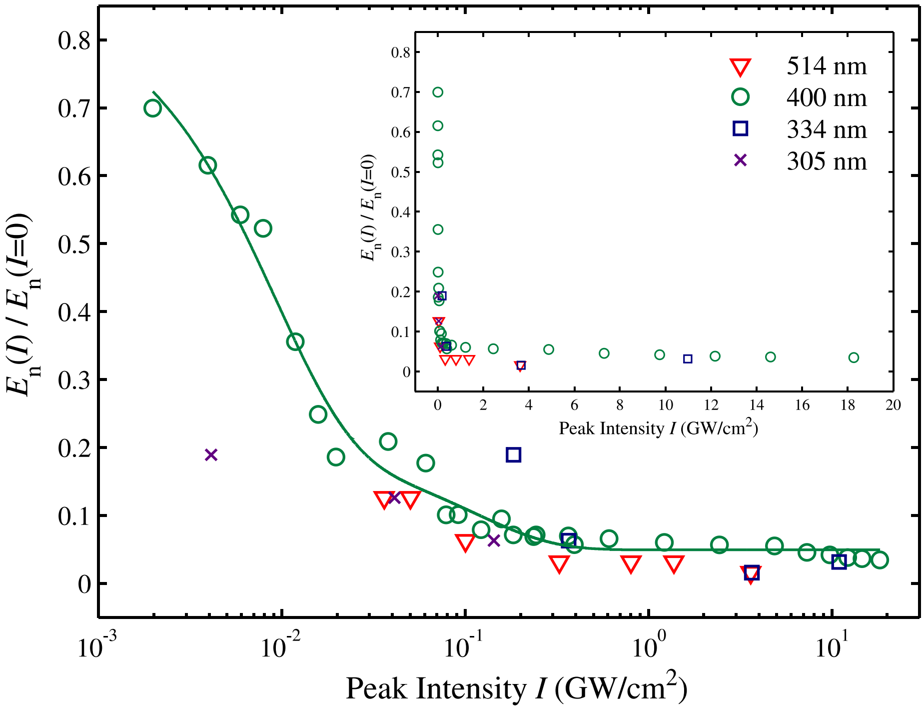

FIGURE 6.14: The normalized nucleation field as a function of incident intensity of fs-pulsed light in 5-mol% Mg:CLN using wavelengths $\lambda = 514.5$, 400, 334, 305 nm. The solid line is a least-squares fit to an equation of the form $y = c_1 \exp(-x/c_2) + c_3 \exp(-x/c_4) + c_5$ for $\lambda = 400$ nm. The inset presents the same data on a linear scale.

or doping CLT with Mg, instead resulted in a *greater* minimum nucleation field. However, in the case of Ti-indiffused waveguide in undoped CLN, the material experienced a much lower minimum nucleation field, approaching that of the Mg:CLN material.

The OPA in the femtosecond laser system was tuned to provide a range of wavelengths from the UV (305 nm) to IR (1500 nm). The nucleation field as a function of intensity for 5-mol% Mg:CLN is plotted for several wavelengths of fs-pulsed light in Figure 6.14 using the modified voltage ramping method. For all these wavelengths, a similar trend is apparent, each attaining significant reductions of the nucleation field. The solid line of the inset is the least-squares fit of the $\lambda = 400$ nm data to an equation of the form $y = c_1 \exp(-x/c_2) + c_3 \exp(-x/c_4) + c_5$. The minimum nucleation field achieved under all wavelengths used in this Mg:CLN material is summarized in Table 6.4, highlighting that for $\lambda = 514.5$ nm, the ultrashort pulses provide nearly an 8-fold advantage over the cw case in the minimum nucleation field achievable. For $\lambda = 800$ nm, the first reported attempt at using IR light for LAP, the reduction achieved was ~81% with a very high power, though still producing a significant result.

A wavelength of $\lambda = 1500$ nm was also used for LAP experiments. However, in the three crystals under test — undoped CLN, 5-mol% Mg:CLN, and 0.01-mol% Fe:CLN — no reduction of the nucleation field was achieved for the intensities up to $I \simeq 30$ GW/cm^2.

Table 6.4: Electric field required for domain nucleation in 5-mol% Mg:CLN in the presence of fs-pulsed light at wavelengths ranging from $\lambda = 305$–800 nm. The repetition rates were 1 kHz for $\lambda = 305$–383 nm and 250 kHz for $\lambda = 400$–800 nm. For comparison, both cw and fs-pulsed values are presented for $\lambda = 514.5$ nm.

Wavelength [nm]	$E_{n,min}$ [kV/mm]	Intensity, I [GW/cm^2]	Reduction [%]
305	0.40	0.14	94
334	0.10	3.6	98
364	0.20	2.2	97
383	0.20	1.0	97
400	0.22	18	97
514.5 (cw)	0.78	$\sim 4\times10^{-6}$ [a]	88
514.5 (fs)	0.10	3.6	98
800	1.20	$\sim$30	81

[a] average intensity

As in the cw case, fs-pulsed LAP induced domain nucleation on the −z face. This was true for both LN and LT, all dopants, and all wavelengths explored, and was independent of whether the light was incident upon the −z or +z face. Therefore, in all experiments the crystal was oriented such that the k-vector of the beam was parallel to the z direction (incident upon the −z face) as shown in Figure 6.1, unless otherwise noted.

6.3.2 Domain Direct-Write using fs-LAP

The phenomenon of fs-pulsed light-induced reduction of the nucleation field can be applied to directly writing domain structures in the surface and bulk of undoped and doped LN and LT. As mentioned in Section 6.3.1, the domain nucleation process has an additional dependence not present in the cw case. As a result, fs-pulsed LAP depends upon the applied electric field, peak intensity, and illumination time. Therefore, any direct-writing of domain structures must take into account an incubation effect that may be present, particularly at low E-field and intensity conditions. Nonetheless, fs-pulsed light provided a very simple and reliable method of engineering a domain structure within the target material.

The majority of experiments conducted made use of $\lambda = 400$ nm light in Mg:CLN. The 400 nm wavelength was produced by an SHG crystal by doubling the fundamental frequency of the laser, thus enabling a larger output and more stable power than provided by the OPA. As evidenced from Section 6.3.1, $\lambda = 400$ nm also showed similar results as the other wavelengths tested, and therefore provided a simple and reliable operating point. Mg:CLN was an ideal material for primary investigations due to its very large intensity-dependent reduction of the nucleation field as well as the ease with which reproducible domain inversion could be formed. Additionally, apart from undoped CLN

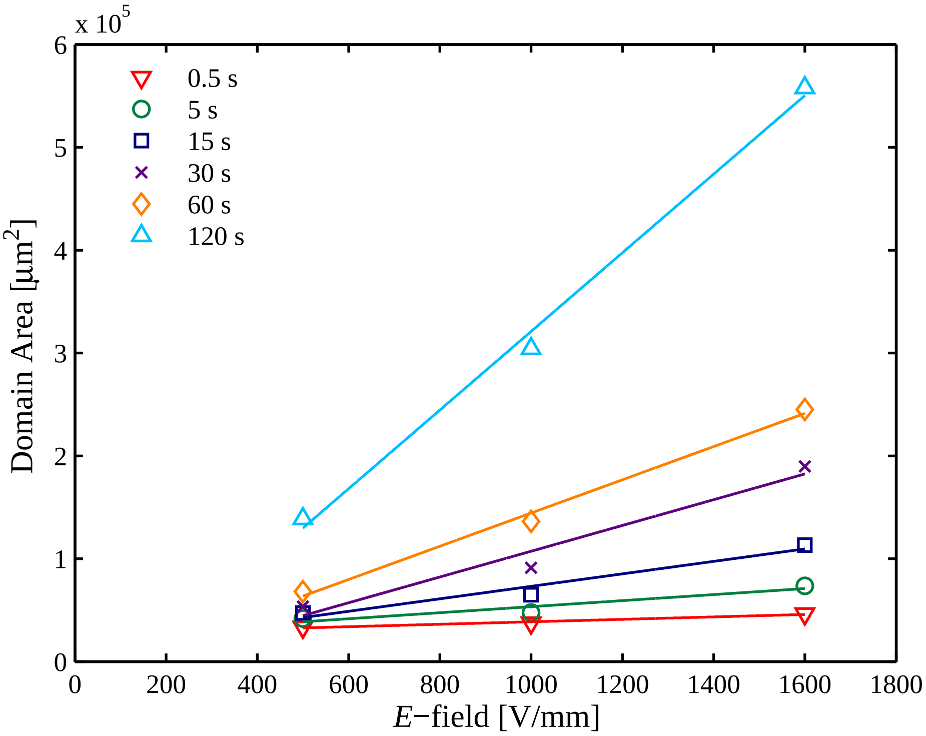

Figure 6.15: Inverted domain area on the −z face of Mg:CLN vs. E-field induced by fs-pulsed LAP for various illumination times and an intensity I = 1.2 GW/cm^2 using λ = 400 nm light. The solid lines are guides for the eye.

and CLT, Mg:CLN is the most studied, reliable, and high-quality material from the LN and LT family commercially available.

The size of the inverted domain area was studied first. By setting the bias voltage applied across the 5-mol% Mg:CLN crystal, then focussing the $\lambda = 400$ nm light onto the −z face, individual domain spots could be written in succession. These inverted domains followed the shape of the illumination pattern, and grew in size following increases in any of the three exposure conditions of E-field, intensity, and illumination time. Following HF etching, these domains were measured via SEM and plotted in Figure 6.15 for various E-fields and exposure times, showing an increasing domain area following both these parameters while illuminating with a constant intensity of I = 1.2 GW/cm^2 and a spot size of $\sim 5\times10^4$ µm^2.

The inverted domain area increased as a function of the illumination time, as shown in Figure 6.16. The curves with intensity of 0.06 and 0.30 GW/cm^2 conform well to a logarithmic fit. However, increasing the intensity by a factor of four to 1.2 GW/cm^2 shows the beginnings of a departure from this logarithmic fit and, for exposures > 20 s, a trend towards a linear increase was observed. For higher intensity and longer exposures, the domain area becomes linearly dependent upon exposure time, as shown in Figure 6.17.

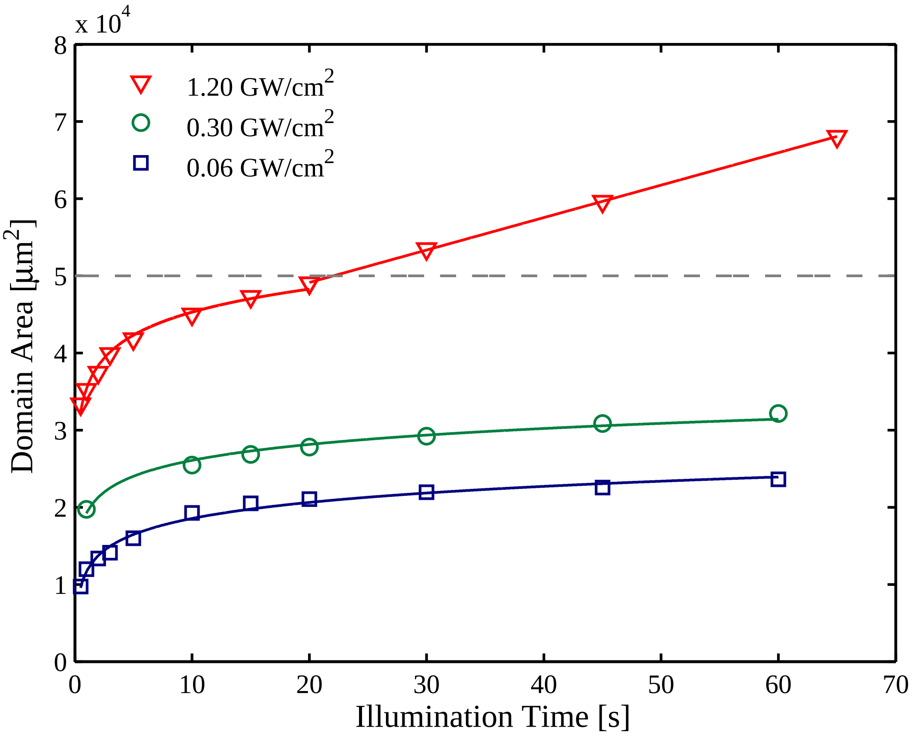

Figure 6.16: Logarithmic fits of inverted domain area on the −z face of Mg:CLN vs. illumination time induced by fs-pulsed LAP for various intensities using $\lambda = 400$ nm light, biased to $E = 0.5$ kV/mm. The solid lines are least-squared fits to an equation of the form $y = c_1 \log_{10}(x) + c_2$ or $y = c_1 x + c_2$. The horizontal dashed line indicates the beam area.

Interestingly, this transition from a logarithmic to linear fit occurs as the inverted domain area approaches the spot area, in this case $\sim 5\times10^4$ µm^2 indicated by the dashed line in Figure 6.16. This means that under the conditions of low exposures, the inverted domain area will only increase slowly with greater exposure time, allowing controlled areas to be inverted. For higher exposures, once the domain has spread beyond the spot size, the domain increases in area more quickly.

This control of the domain growth can be applied to the direct write of domain structures more complicated than simple spots. By translating the beam over the crystal, arbitrary illumination patterns can be written in the crystal, and result in light-assisted domain-inversion patterns. One such example is shown in Figure 6.18, where the manually-controlled beam path spelled out the letters “ORC” in undoped CLN using $\lambda = 400$ nm fs-pulsed light. The structure, limited by the large spot size, was composed of straight and *curved* line segments measuring approximately 120 µm in width. Importantly, the inverted regions formed bulk domains reaching 300 µm from the −z face [Figure 6.18(a)] to the opposite +z face [Figure 6.18(b)], as revealed by HF etching. Additionally, even when viewed on high magnification by the SEM, *curved* domain walls were observed on both faces of the crystal [inset of Figure 6.18(a)]. Straight line segments were also

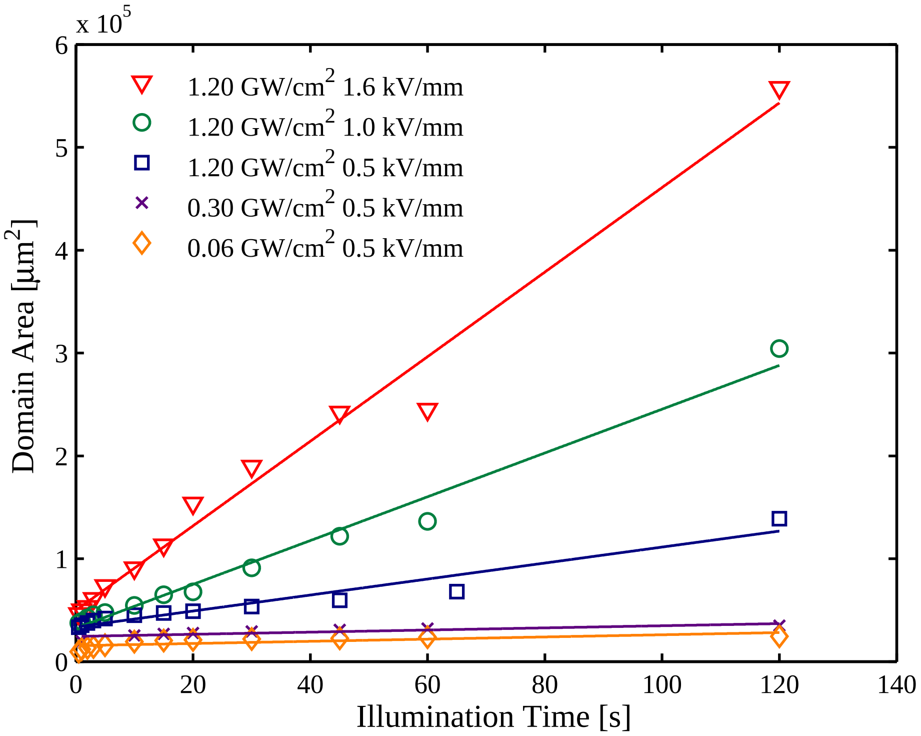

FIGURE 6.17: Inverted domain area on the −z face of Mg:CLN vs. illumination time induced by fs-pulsed LAP for various E-fields and intensities using $\lambda = 400$ nm light. The solid lines are least-squared fits to an equation of the form $y = c_1 x + c_2$.

formed along directions not parallel to any of the x or y axes. Both of these capabilities are potentially very useful in obtaining truly arbitrary domain patterns.

Rounded domain shapes have also been observed using regular EFP, but have been shown to extend no further than ∼10 μm from the −z face of undoped CLN [Jungk05]. On the contrary, the LAP-induced curved and arbitrarily-angled straight domain walls were observed on both the +z and −z faces of the crystal after HF etching. Because of this and the presence of light across the entire crystal, these arbitrary domain shapes are suspected to exist throughout the bulk, although this has not yet been verified.

This direct-write method of domain patterning has also been applied to 5-mol% Mg:CLN with a thickness of 5 mm, a tenfold increase over typical wafer thicknesses. Direct-write via fs-pulsed LAP was also successful in achieving bulk domains in this material, first nucleating at the −z face and extending the entire 5 mm to the opposite +z face. These domains were very large (several hundred micrometres wide), but this was a function of the large beam size and high exposure. Additionally, these bulk domains had internal structures on the +z face, as described further in Section 6.5.4. Under improved focussing and exposure conditions, smaller domains will be possible throughout this large thickness.

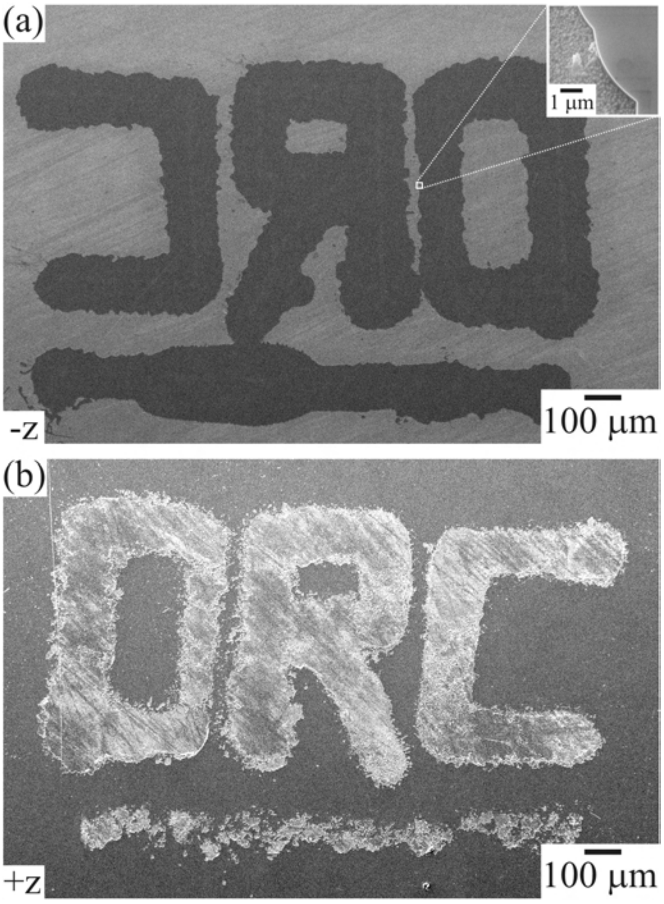

FIGURE 6.18: Domain direct-write using fs-pulsed LAP using $\lambda = 400$ nm in 300-µm thick undoped CLN, showing (a) nucleation on the −z face and (b) extending to the +z face, as revealed by HF etching. An E-field of 16.3 kV/mm and intensity of ∼30 GW/cm^2 were used. The inset of (a) shows a high magnification image of a curved domain wall.

6.3.3 Patterned Illumination via Amplitude Mask using fs-LAP

While direct-write is a useful procedure for obtaining high intensities and for the formation of arbitrary domain patterns, patterning the beam itself prior to illumination of the crystal is preferable for large area inversions, periodic patterns, or well-defined domain edges. This has been achieved by use of a contact mask, mask projection, and phase mask illumination.

As in the cw-LAP case, the simplest contact mask to use was the commercially available 400-mesh copper TEM grid. However, the fs-pulsed case has resulted in greatly enhanced domain formation in comparison, improving upon the control of the domain size and shape. Importantly, nucleation within the irradiation region is not randomly placed as it appeared in the cw case, but rather the inverted region quickly expanded to fill the entire beam pattern. These advantages are clearly observed in Figure 6.19 where $\lambda = 400$ nm light with an intensity of 0.5 GW/cm^2 and an applied E-field of 2 kV/mm exposed a

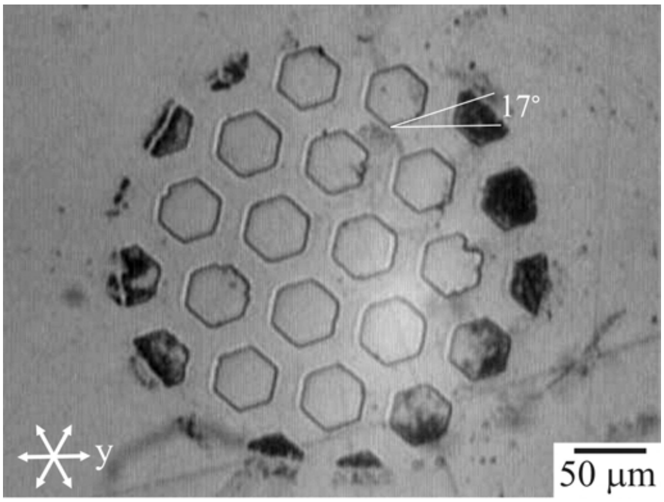

Figure 6.19: Two-dimensional domain patterning via fs-pulsed LAP with illumination through a TEM grid as a contact mask on the −z face. A single illumination of ∼1 s using $\lambda = 400$ nm light with $I = 0.5$ GW/cm^2 and $E = 2$ kV/mm formed all spots simultaneously in this 5-mm thick 5-mol% Mg:CLN. The orientation of the TEM grid was ∼17° away from a y axis of the crystal.

5-mm thick slab of 5-mol% Mg:CLN (Photox Optical Systems Ltd.) for approximately 1 s. The domain shapes closely follow the shapes of the hexagonal holes of the TEM grid despite its 17° rotation relative to a y axis of the crystal. This exhibits a tendency to follow the pattern of the light that is stronger than the natural tendency of domains to follow the y axes of the crystal, as seen in regular EFP. Under these exposure conditions, the inverted hexagons fill almost exactly the 1186 μm^2 area of the TEM grid holes. Some slight variation in the area from hole to hole is a result of the varying intensity due to the truncated Gaussian beam used. It is important to note that these domains do not penetrate to the +z face.

Further exposure through an identical TEM grid yields further lateral growth of the domains. With an intensity of 0.5 GW/cm^2 and E-field of 1.5, 2.0, and 2.4 kV/mm, the inverted domain area follows a logarithmic growth with illumination time, as shown in Figure 6.20, plotting the average size of the domains formed through each hexagonal hole of the grid. Each data point of the 2.4 kV/mm curve corresponds to an image in Figure 6.21(a–h). This figure shows that even for exposure conditions leading to domain growth well beyond the boundary of the mask-induced illumination pattern, the domain walls follow the pattern imparted by the light and are not confined to the hexagonal symmetry of the crystal. (As in the previous image of Figure 6.19, the grid was not aligned to the y axes.) In fact, these domains tend towards a *circular* shape. For an increased exposure of 0.5 GW/cm^2 and 3 kV/mm for 35 s, the nucleated domains from each grid hole merge to form a single large domain inverted region in Figure 6.21(i).

Projection of a patterned beam was accomplished using a positive lens to demagnify an Al mask with a period $\Lambda = 306$ μm by 5–6×. Achieving a ∼57 μm period of illumination

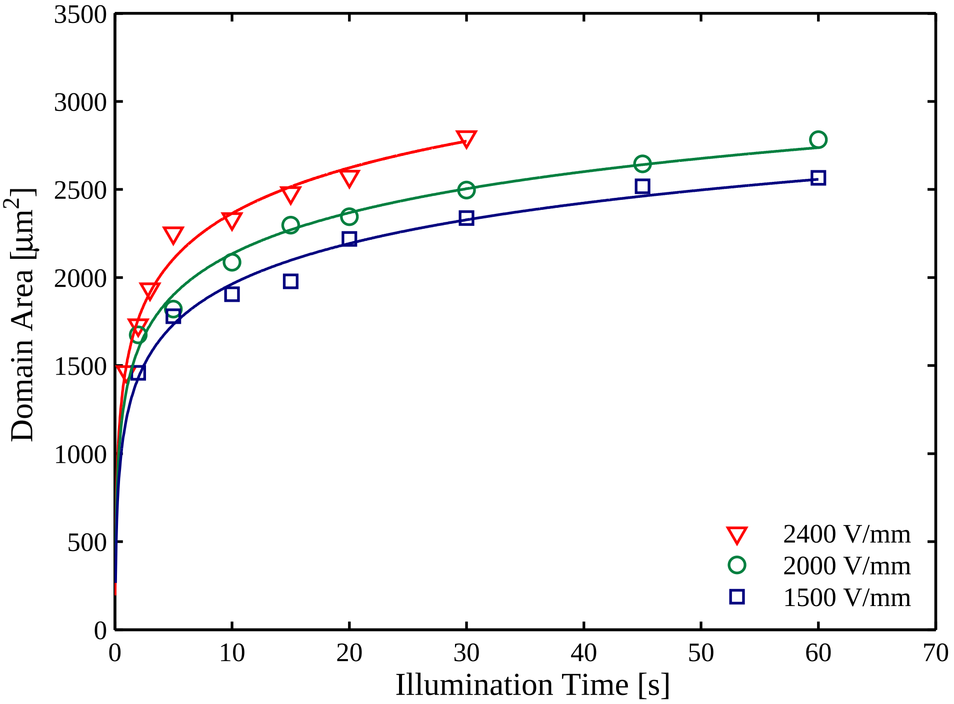

Figure 6.20: fs-pulsed LAP domain growth vs. illumination time, illuminating through a TEM grid contact mask, using $\lambda = 400$ nm light with $I = 0.5$ GW/cm^2 and $E = 1.5$, 2.0, 2.4 kV/mm in Mg:CLN. The solid lines represent least-squared fits to an equation of the form $y = c_1 \log_{10}(x) + c_2$.

on the −z face of the crystal, an $E = 3.6$ kV/mm and illumination of $\lambda = 400$ nm with $I = 0.1$ GW/cm^2 for 10 s resulted in periodic surface domain formation, as shown in Figure 6.22(a). The duty cycle varied from 50–65% due to the varying intensity across the width of the beam and was reproduced in other similar exposures. With a more uniform intensity pattern across the beam, a more uniform duty cycle resulted, as appears in Figure 6.22(b), showing a duty cycle varying from only 55–60% across the width of the beam. However as expected for a truncated Gaussian beam, the largest intensity at the center produced the greatest domain width, reducing towards the edges. In this instance, however, non-ideal focussing yielded a narrow band of illumination in between the primary period, producing a secondary line of domain inversion, highlighted in the inset of Figure 6.22(b).

For the fabrication of useful devices, a period of ∼30 µm or less must be achieved, requiring a demagnification twice that achieved in the above results. A 10× demagnification was used to form such a periodic pattern. However these results were again limited by the visualization setup. All illuminated spots that were clearly visible in-situ were found to have spread laterally and merged with adjacent periods following investigation via HF etching. Several spots which had received less exposure and were not visible in-situ did provide a periodic pattern post-etch, although the duty cycle was poor and

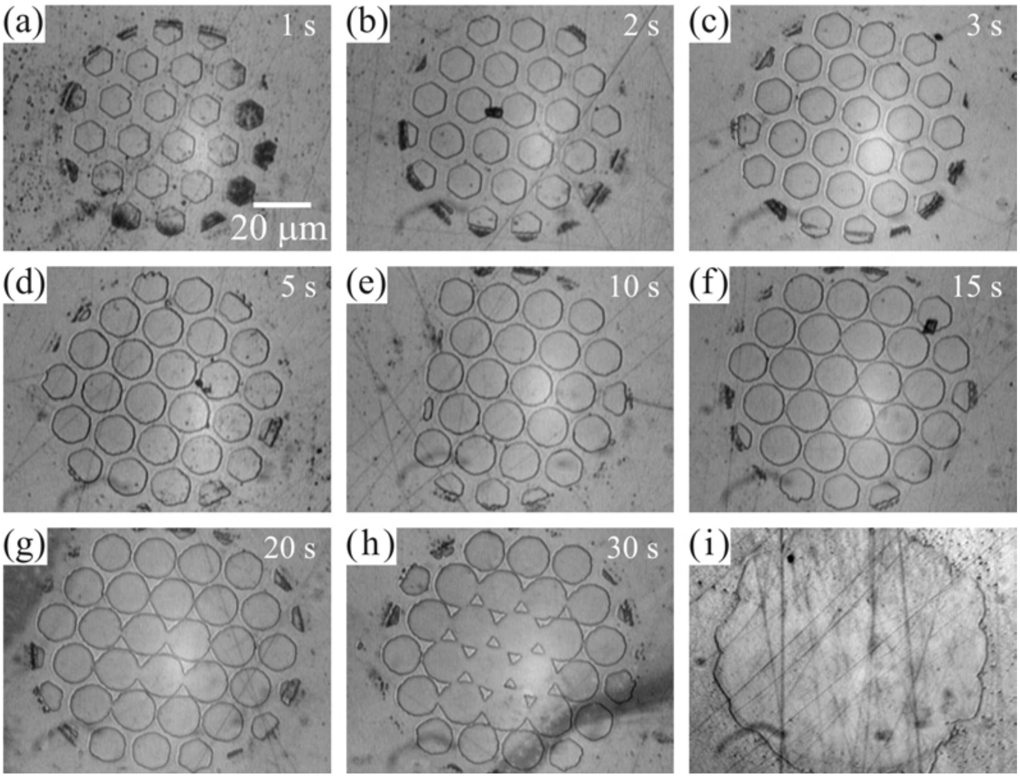

Figure 6.21: Two-dimensional domain patterning via fs-pulsed LAP with illumination through a TEM grid as a contact mask on the −z face. Mg:CLN was exposed to $\lambda = 400$ nm light with $I = 0.5$ GW/cm^2 and $E = 2.4$ kV/mm for 1–30 s (a–h), as indicated at the top of each image. Larger exposure caused merging of all nucleations, as seen in (i), exposed to 0.5 GW/cm^2 and 3 kV/mm for 35 s.

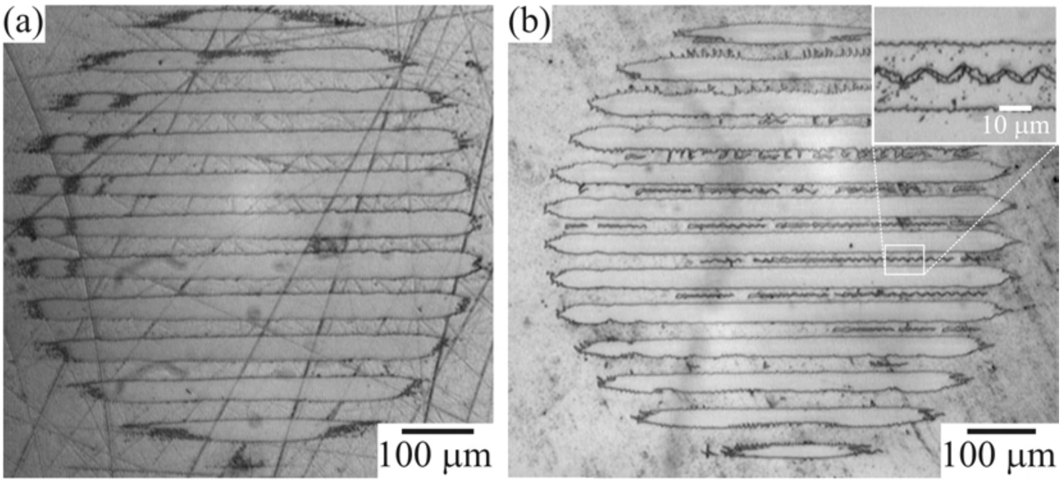

Figure 6.22: Periodic surface-domain patterning via fs-pulsed LAP by mask projection onto the −z face using $\lambda = 400$ nm light. (a) A single illumination of ∼10 s using $I = 0.1$ GW/cm^2 and $E = 3.6$ kV/mm formed all lines simultaneously in this 5-mm thick Mg:CLN. (b) A similar exposure using 0.2 GW/cm^2 and 0.5 kV/mm for 60 s in 0.5-mm thick Mg:CLN.

varied across the spot, merging in several locations. There were several reasons for this difficulty with smaller periods. The first problem was the difficulty in determining the ideal exposure conditions of E-field, intensity, and illumination time when in-situ visualization did not provide feedback. This required that HF etching be used to determine the quality of the poling, or whether poling had occurred at all, thus greatly increasing the feedback cycle from nearly instantaneous to several hours or even days. The second problem was the determination of the conditions for the best imaging. As was evidenced in Figure 6.22(b), when non-ideal imaging occurred on the crystal, non-zero intensity appeared between the desired periodic bands of illumination and thus increased the likelihood of domain spreading and merging. It was also not clear whether the best illumination condition would be to have the sharpest image immediately upon the −z face or at some depth below it, as observed during direct-writing using tight focusing [Dierolf04]. Ideally, the illumination would be uniform throughout the thickness of the crystal, as would be possible for large-diameter two-beam interference, as demonstrated in [Wengler05] using cw UV light from an Ar^+ laser.

6.3.4 Patterned Illumination via Phase Mask using fs-LAP

Another form of patterning via interference is possible using a phase mask placed near the −z face of the crystal. To increase the intensity incident on the phase mask, the truncated Gaussian beam was lightly focused providing a large depth of focus. The target LN crystal was held near the phase mask by the O-rings, as shown in Figure 6.23. The phase mask was oriented such that the grating k-vector was parallel to the x axis of the LN crystal, producing grating intensity lines aligned along the y axis, similar to the photoresist gratings used in the fabrication of PPLN by EFP.

The design of a phase mask for the formation of a QPM LAP domain grating requires knowledge of the dispersion curve of the target material, discussed in Section 2.2.2.2, and the resulting coherence length, discussed in Section 2.1.1. For SHG interactions in Mg:CLN and choosing a fundamental wavelength of $\lambda_{\mathrm{f}} = 800$ nm (which is readily provided by a Ti:sapphire laser), the coherence length was calculated to be $\ell_c = 1312.9$ nm. Therefore, the period of grating required for QPM is $\Lambda_g = 2\ell_c = 2625.8$ nm. For a $+1/-1$ phase mask configuration with normal incidence, the illumination pattern acquires half the period of the phase mask, meaning the phase mask should be designed with $\Lambda_{\mathrm{pm}} = 5251.5$ nm. This period has the added benefit of resulting in phase matching in undoped CLN for $\lambda_{\mathrm{f}} \simeq 813.5$ nm, within the tuning range of a Ti:sapphire laser. The wavelength of operation of the phase mask itself was designed to be $\lambda = 514.5$ nm.

Figure 6.23 also reveals the problem of the aqueous environment in which the phase mask was immersed. Several manufacturers were unable to provide phase masks designed for operation in water, and thus the phase mask used had been optimized for operation in air. Using a scalar approximation, the 0-order of the phase mask can be minimized

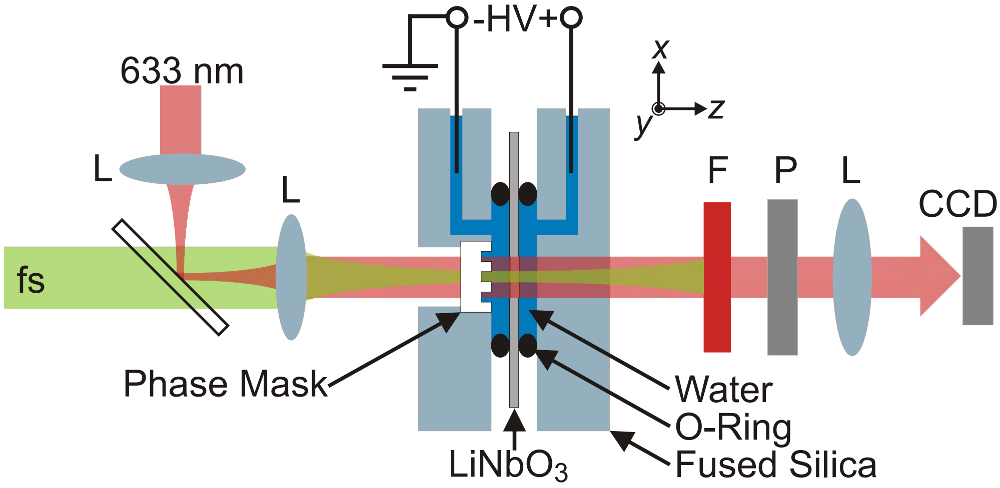

FIGURE 6.23: Patterned LAP setup, showing the fs-pulsed beam incident on a phase mask in front of the −z face of a lithium niobate sample, held between water electrodes using transparent fused silica plates. The polarized beam of $\lambda = 633$ nm light is of low intensity and used only for visualization of the poling process via the crossed polarizer and CCD camera. The 3D coordinate system describes the orientation of the target sample. (F = red filter; L = lens; P = polarizer; HV = high voltage.)

when the groove depth is [Hegedus97],

$$d = \frac{\lambda}{2(n_{\mathrm{pm}} - n_{\mathrm{a}})} \tag{6.4}$$

where n_{pm} and n_{a} are the refractive indices of the phase mask and the ambient materials, respectively, and λ is the design wavelength of the phase mask. Because the groove depth was optimized for $n_{\mathrm{a}} = n_{\mathrm{air}} = 1$, not for n_{water}, the resulting interference pattern is no longer a simple interference of $+/-1$ orders. Instead, there was a very significant 0-order component as well, measured to be ~50% of the incident power in an aqueous environment. In addition to these diffraction orders, higher orders must also be considered due to the wavelength of operation and the design period [Hecht02]:

$$\sin\theta_m = \frac{m\lambda}{\Lambda_g} \qquad \therefore |m| \leq \frac{\Lambda_g}{\lambda} \tag{6.5}$$

where θ_m is the diffraction angle of order m, and Λ_g is the grating period. From this equation, for a period of 5251.5 nm and wavelength of 514.5 nm, 10 diffraction orders are expected from the phase mask, and all were observed.

Due to these disadvantages of the phase mask setup, the ideal periodic diffraction pattern was not realized. The most important result was the production of a diffraction grating with a period equal to the phase mask period, rather than one-half as would be expected for a +1/−1 phase mask configuration. This period resulted from the interference of diffraction orders $m = 0, \pm 1$. However, due to the 0-order, the modulation depth of the diffraction grating changed with distance away from the phase mask [Mills01]. Experimentally this meant that the precise placement of the LN crystal was very important for the reliable fabrication of periodic domains, ideally with a modulation depth of 100% (sinusoidal on/off bands of illumination). A small modulation depth, in contrast, would encourage lateral spreading of the domains so that merging of adjacent periods was more likely.

Despite these issues, periodic domain formation was possible via static illumination of the phase mask by $\lambda = 514.5$ nm light, shown following HF etch in Figure 6.24. In all these typical examples, the period of 5.25 µm was precisely replicated, and the amount of spreading from the spot center to the edges followed the intensity profile of this Gaussian beam. The images have been chosen to show a transition from merging throughout the illumination spot (a) to a separation between all adjacent periods throughout the spot width (f). In general, a reduction of any of the three parameters of E-field, intensity, and illumination time lead to less lateral spreading and more clearly separated domain periods. A more uniform pattern is expected for a more uniform intensity profile, as has been seen in other patterned illumination.

One of the benefits of the use of a phase mask is the ability to scan the beam across the phase mask along the direction of the grating k-vector, greatly extending the number of periods illuminated while maintaining the exposure parameters of E-field and intensity. In this way, the length of the periodic structure is limited only by the length of the phase mask, rather than the size of the beam itself. In this hybrid direct-write/interference technique, the parameter of illumination time is replaced by the *dwell time* of the laser, or equivalently the scan speed. Figure 6.25 shows various regions exposed using this scanning method in 5-mol% Mg:CLN using an intensity and E-field of 0.5 GW/cm^2 and 1200 V/mm, respectively. In (a–b), slow manual scanning caused over-exposure, resulting in merged domains and jagged edges as the domains spread away from the intensity peaks. Under the improved faster manual scanning in (c–d), a high-quality periodically poled grating is formed, exhibiting straight domain walls aligned with the illumination pattern. The inverted/non-inverted duty-cycle of this example is ~25/75. However, precise control of all exposure conditions should allow the formation of the optimal 50/50 duty-cycle. Nonetheless, the 25/75 duty-cycle obtained in these exposures is already optimal for even-ordered QPM [Fejer92], meaning this poled grating would be suitable for our designed SHG interaction.

Prior to chemical etching, these spots were investigated by illumination using a HeNe laser. Despite the absence of surface patterning, diffraction was caused by electro-optic contrast from internal fields [Müller03b] and the charged domain walls of the surface domains. The illuminated spots showed ±1 and ±2 diffraction orders, as depicted in Figure 6.26. Measuring the diffraction angles of the $m = 1$ order allowed the calculation of the diffraction grating period,

$$\Lambda_g = \frac{m\lambda}{\sin\theta} \tag{6.6}$$

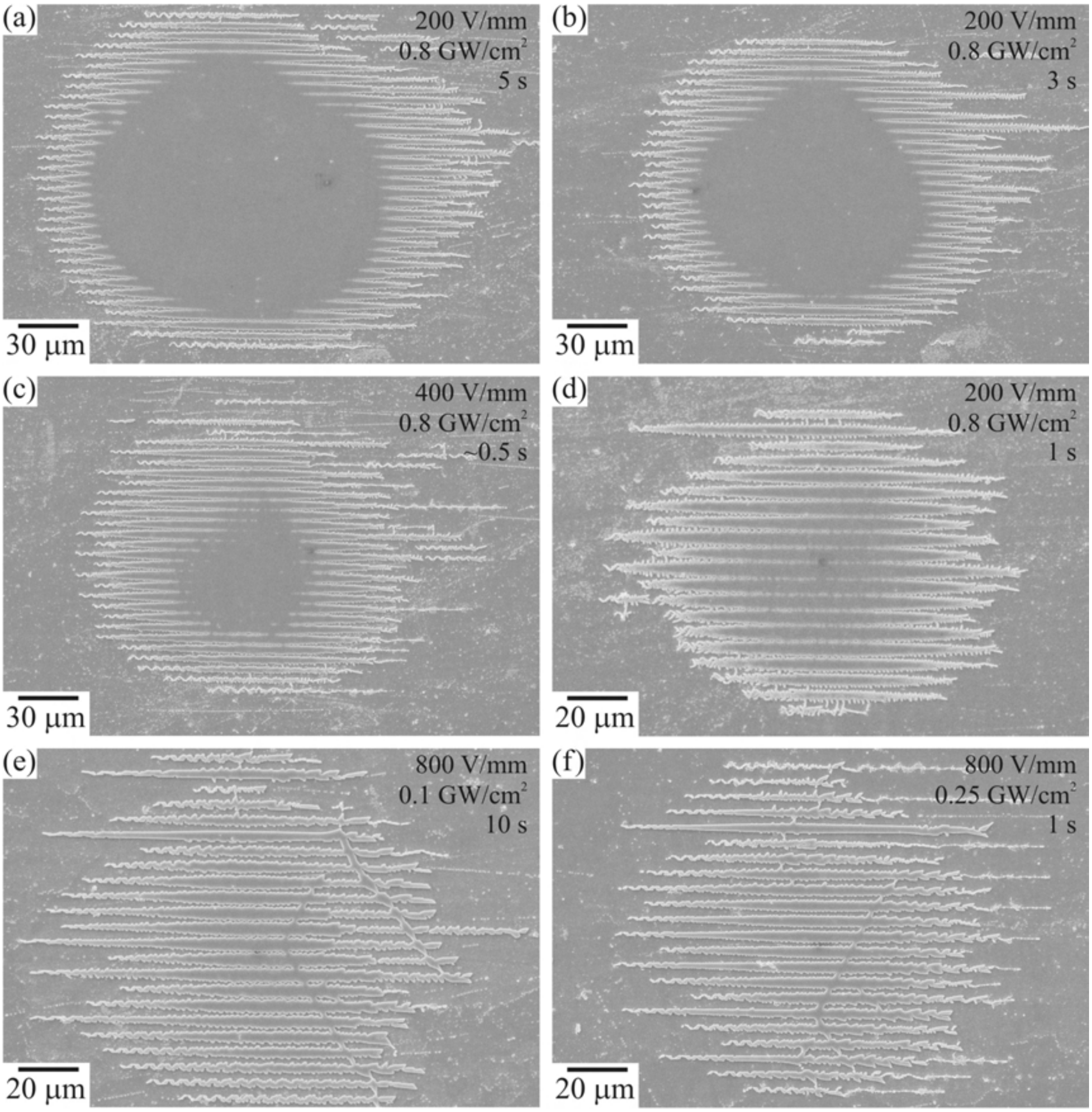

FIGURE 6.24: SEM micrographs of the domain patterns produced in 5-mol% Mg:CLN using phase mask illumination with fs-pulsed light of wavelength $\lambda = 514.5$ nm with an illumination period $\Lambda = 5.25$ μm. The exposure conditions appear at the top-right corner of each image.

where m is the diffraction order, $\lambda = 633$ nm is the wavelength, and θ is the diffraction angle. From this measurement, the diffraction grating period was determined to be 5138 nm. The design period of the phase mask (5251.5 nm) would produce a diffraction angle within 0.15° of the measured angle, well within the measurement accuracy, verifying that the induced pattern in the material closely follows the illumination pattern.

6.3.5 Cross-Sectional Profile of fs-LAP Domains

The depth profile of inverted domains is one of the important parameters governing the formation of useful devices. Ideally, the domain should have vertical walls perpendicular

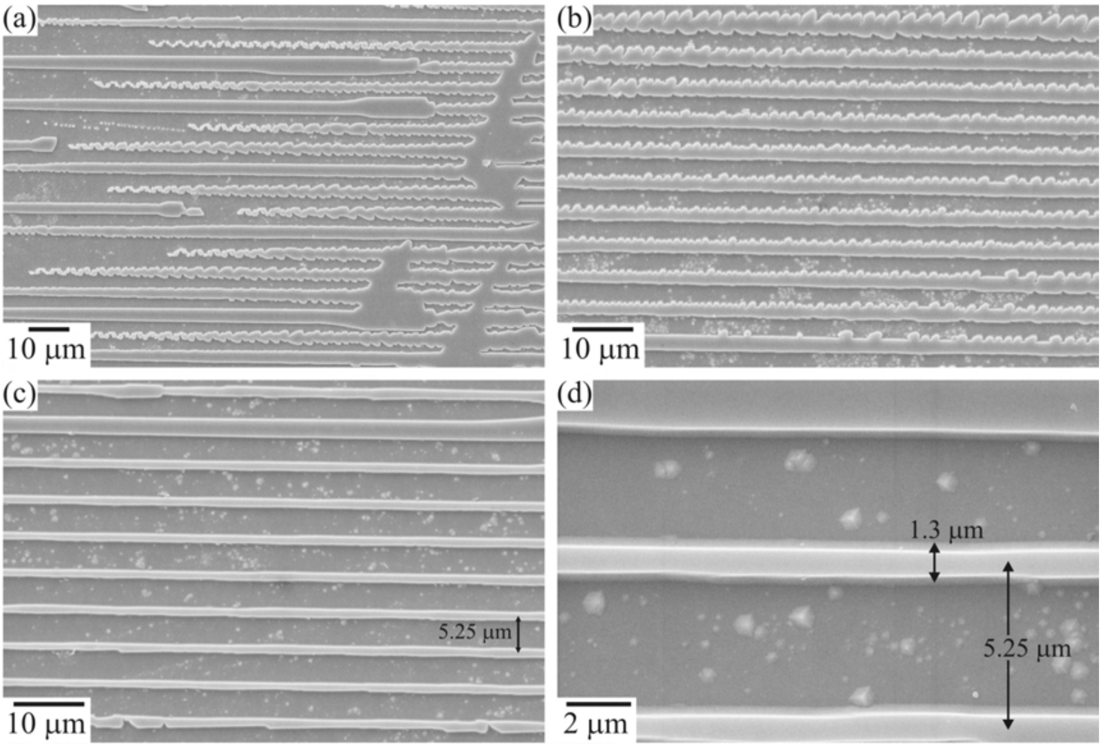

Figure 6.25: SEM micrographs of the domain patterns produced in 5-mol% Mg:CLN using scanned phase mask illumination with fs-pulsed light of wavelength $\lambda = 514.5$ nm with an illumination period $\Lambda = 5.25$ μm. The laser spot was scanned along the x axis of the crystal, with an intensity $I = 0.5$ GW/cm^2 and an electric field $E = 1200$ V/mm. (a–b) Over-exposure leads to merging of adjacent domains and jagged edges. (c–d) Improved exposure conditions with less spreading results in a high-quality periodic grating.

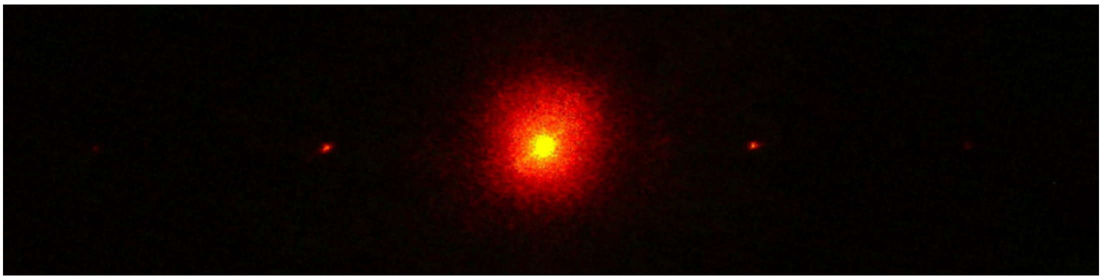

Figure 6.26: Diffraction from an area exposed to fs-pulsed LAP in Mg:CLN prior to chemical etching. The $m = 0$, ±1, ±2 orders are visible using a HeNe laser ($m = \pm2$ are very faint).

to the z face, thus allowing a high aspect ratio and small periods. However, as in EFP domains, a perfectly vertical domain wall is never achieved. By cutting and side-polishing a crystal, the cross-sectional profile of LAP domains can be investigated before and after HF etching.

To investigate the domain profile, LAP domains were formed in 0.5-mm thick 5-mol% Mg:CLN (Yamaju Ceramics Ltd) with an applied electric field, $E = 1000$ V/mm, and an intensity, $I = 1.2$ GW/cm^2, of $\lambda = 400$ nm unpatterned light. The left and right columns of Figure 6.27 show these LAP domains formed with illumination times of 2 s and 45 s, respectively. The optical microscope images of the etched −z faces (a–b) show domains that have extended beyond the boundaries of illumination, indicated by the dotted black lines. Also shown here is that the cross-section taken of these domains was not through the center of the spot, but towards the edge of the illumination. SEM micrographs of the etched y face (c–d) show the cross-sectional profile of these LAP domains, depicting several important features. Firstly, each spot consisted of many needle-like domains penetrating into the bulk, similar to EFP domains. Secondly, the deepest needle-like domains were outside the area of illumination, again depicted by the dotted black lines. These domains grew deeper with longer exposures times, in an approximately logarithmic dependence over the range 1–120 s. However the domain depths within the region of illumination did not have such a dependence, and were mostly within 15–30 µm regardless of the exposure times over that same range.

When the same spots were viewed under a polarized optical microscope prior to any etching of the y face, as shown in Figure 6.27(e–f), a wider and deeper domain profile was revealed. As observed with z-face imaging of domains using a polarized microscope, the "best" imaging of any domain structure was achieved when focused not on the surface, but *below* it. This provided the clearest image of domain shape with the highest resolution. Therefore, the reason for this altered profile by the polarized microscope was due to an accumulated view of the domain throughout the bulk, rather than viewing a slice through it as done with the etched SEM view. However, the views revealed by the SEM cross-section and the polarized microscope both show the same trends of greater growth outside of the region of illumination.

Piezoelectric force microscopy PFM can also reveal y-face cross-sectional profiles of domains formed by conventional EFP in unetched LN due to the piezoelectric coefficient $d_{p(22)}$ [Soergel05]. Although currently unexplained, an additional benefit of this technique is that domain contrast has been recently observed even on the x face of LN [Soergel07], despite the symmetry along this crystalline axis. Therefore, an x-face polished crystal with LAP domains was provided to Dr. Elisabeth Soergel of the University of Bonn who imaged the domain profiles with sub-micron resolution, as shown in Figure 6.28. The PFM background-corrected X-scan was completed in contact mode using a metalized AFM tip with an applied voltage of 10 V$_{\text{pp}}$ with a frequency of ∼38 kHz.

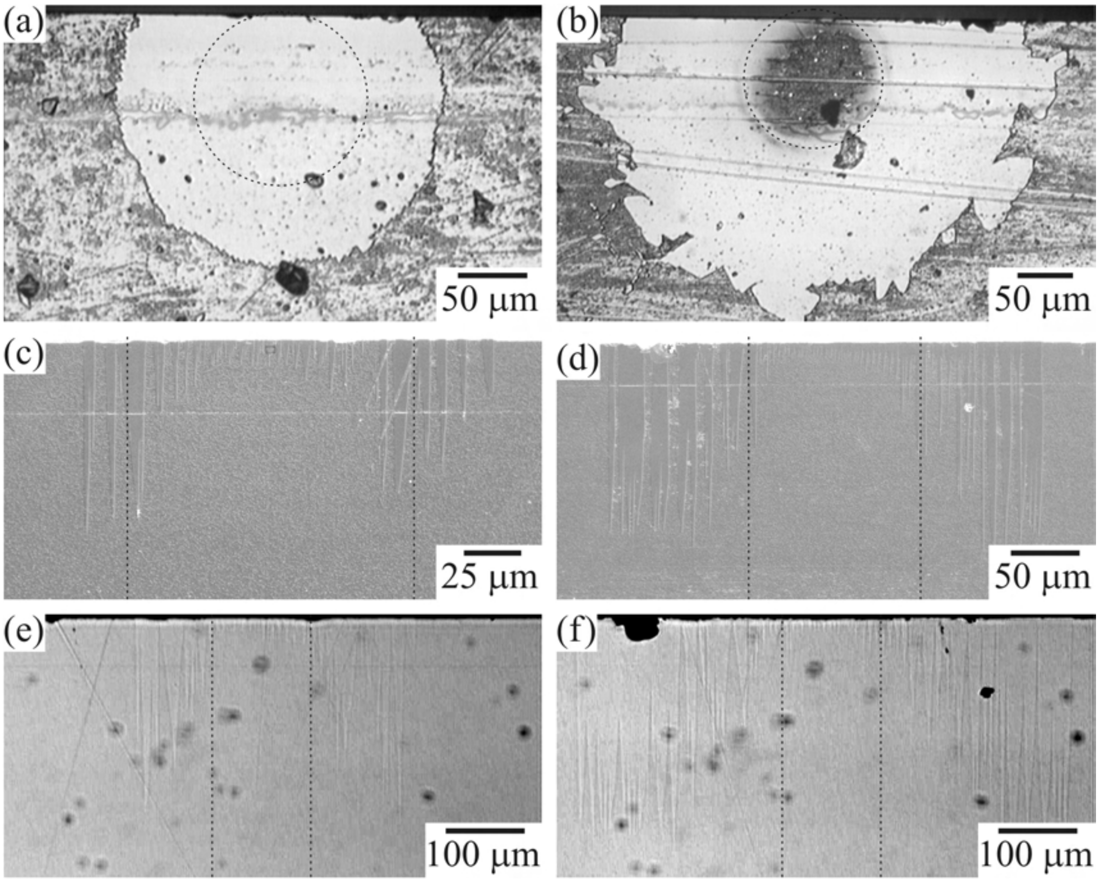

FIGURE 6.27: y face cross-sectional profiles of fs-pulsed LAP domains in Mg:CLN exposed to $E = 1000$ V/mm and $I = 1.2$ GW/cm^2 of $\lambda = 400$ nm light. The left and right columns correspond to spots with exposure times of 2 s and 45 s, respectively. (a–b) Optical microscope images of the etched −z face, (c–d) SEM micrographs of the etched y-face profiles below the −z face, and (e–f) polarized microscope images of the y face prior to chemical etching. The dotted lines enclose the area of illumination.

The needle-like domains observed in the Figure 6.28(a) do not correspond to any topographical features, as confirmed by a simultaneous topography scan of the same region (b).

Currently, the mechanism allowing the imaging of domain profiles on the x face is not understood. The symmetry of the x direction and the fact that domain inversion rotates the crystal about the x axis means that both domain orientations have identical x face surfaces. Therefore for an interaction that is directed only along the x axis, the expectation would be to have no contrast between opposite ferroelectric domains. A possible explanation for this imaging then relies upon the three-dimensional E-field emanating from the tip, possibly interacting with the crystal in-plane, along the y and/or z directions. However it is important to note that Figure 6.28 is not a lateral-force image. Therefore for this explanation to hold it would require that the interaction with the in-plane directions to be coupled to forces along the perpendicular x axis through the non-diagonal terms of the strain tensor.

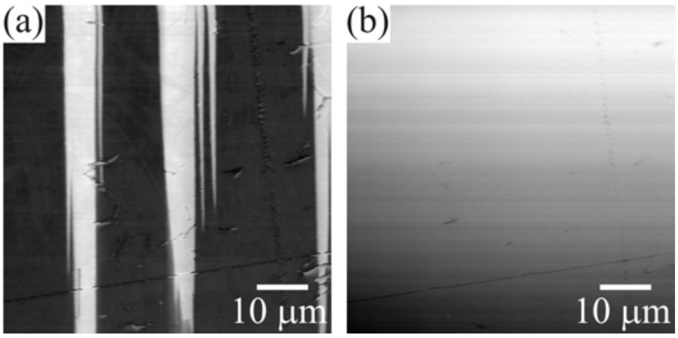

Figure 6.28: PFM (a) X-scan (background-corrected) and (b) topography scan (both imaged simultaneously) of the unetched x-face cross-sectional profile of fs-pulsed LAP domains exposed to E = 3000 V/mm and I = 0.5 GW/cm^2 of λ = 400 nm light for 15 s, showing a region near the −z face of Mg:CLN.

6.4 Latent LAP

The typical light-assisted poling technique requires the simultaneous illumination and application of electric field. Nonetheless, preferential nucleation had also been observed at the location of a previously inverted LAP domain even after the entire crystal had been subsequently uniformly poled through several cycles. This occurred with both cw and fs-pulsed light. However, under the correct conditions it was possible to separate completely these two exposure conditions by permitting the initial illumination of a sample followed after a delay by the application of an electric field. This technique is referred to as latent-light-assisted poling. To date this effect has only been observed using fs-pulsed light, not visible cw light.

The potential advantage of this process is to separate the apparatus used for the illumination and for the application of the electric field. The benefit of this was readily apparent in Section 6.3.4 where placement of the phase mask near the crystal surface located the grating in an aqueous environment, thus altering its periodic pattern and increasing the accuracy requirements upon positioning of the LN crystal. In a latent LAP process, the electrode need not be included during illumination, hence removing the problem completely. This would also eliminate the potential complication of absorption in the electrode material which could result in heating of the crystal, as was intentionally introduced in [Houe95]. The elimination of absorption could be particularly important for LAP processes where UV may be used. Similarly, another benefit could be leveraged in separating the electric field application. The limitation of the use of a transparent electrode would be lifted, permitting the optimization of the ferroelectric capacitor circuit for poling. As discussed in Section 3.3.1, poling characteristics are dependent upon the electrode material. Insulating oils, which are commonly used in EFP, could also be introduced here to reduce the possibility of dielectric breakdown, permit the use of thicker crystals where a greater E-field would be required, and allow the use of a greater amount of surface area which is limited by surface leakage currents near the edges of the crystal.

To investigate the process of latent LAP, several exposures of 0.5-mm thick undoped CLN were made with a sequence as follows. First, a crystal was domain-inverted three times, leaving it with a domain orientation anti-parallel to its virgin state. Second, a truncated Gaussian beam of $\lambda = 400$ nm fs-pulsed light was focused onto the newly-formed +z face of the crystal for an illumination time of 30 s. After a delay of 30 s, the crystal was repositioned and illuminated with identical conditions. This process was repeated a number of times. Following the last illumination and a final 30 s delay, the voltage was ramped up to the desired value over a time of 30 s, whereupon the maximum voltage was maintained for 300 s, then ramped back down to 0 V over a final period of 30 s.

The appearance and growth of domain inversion was observed by varying the intensity of illumination and the applied E-field for a series of spots. Each spot had a varied voltage delay time, defined as the elapsed time from the end of illumination to the start of the voltage ramp. For an intensity $I = 9$ GW/cm^2, the inverted domain area decreased with increasing voltage delay time, as shown in Figure 6.29. Furthermore, larger applied E-fields resulted in more domain growth. For an applied E-field of 8 kV/mm, higher intensities also resulted in larger inverted domain area, as shown in Figure 6.30. The domains formed here represent surface domains only, and hence do not extend to the opposite crystal face. However, under conditions of high exposure (particularly for an E-field with a large value and long application time), other latent-LAP domains have been pushed through to the opposite face of 0.5-mm thick undoped CLN crystal.

Of particular interest from Figure 6.29 is that domain inversion was observed even for an E-field as low as 6 kV/mm, or a reduction of 62% from the dark nucleation field. This was a surprising result as the minimum intensity-dependent nucleation field observed with *simultaneous* illumination showed a reduction of only 40%. Nevertheless, latent LAP formed a sizeable domain even when 6 kV/mm was applied nearly 700 s after illumination. This E-field was also not the limit achievable under the process of latent-LAP, but rather represents the minimum value explored. This fact seems to imply that in undoped CLN the simultaneous presence of the light was actually *inhibiting* domain inversion when these low E-fields were applied. This may also mean that the process used in LAP — setting a voltage bias prior to illumination — may not be the optimal method to use, as illumination of a spot followed immediately by the application of voltage may serve to further reduce the intensity-dependent nucleation field, at least in the case of undoped CLN.

Further measurements of the latent-LAP inverted area extended the voltage delay time up to 10 hours, as shown in Figure 6.31. These curves fit well to a double exponential function of the form $y = c_1 \exp(-x/c_2) + c_3 \exp(-x/c_4) + c_5$, indicating that the effect of

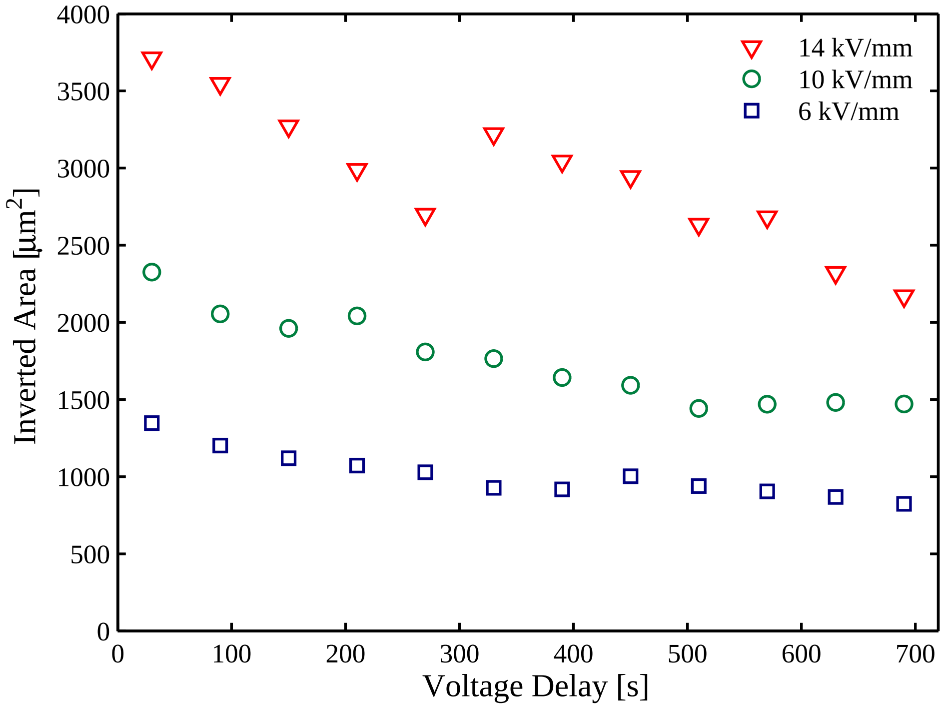

FIGURE 6.29: Inverted domain area vs. voltage delay time for various E-fields using fs-pulsed light of $\lambda = 400$ nm and $I = 9$ GW/cm^2 in undoped CLN.

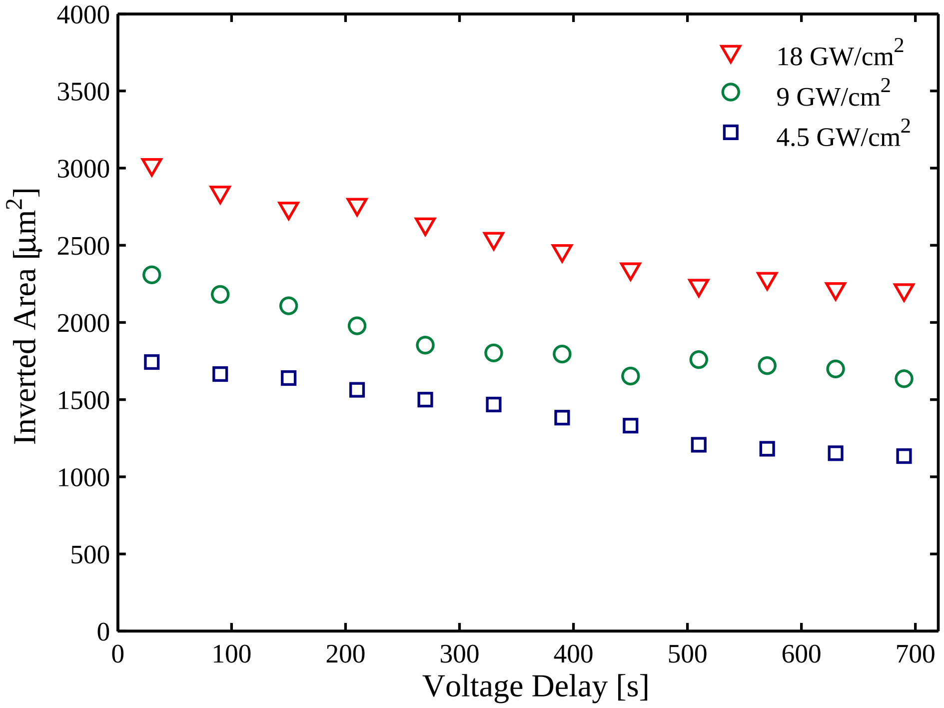

FIGURE 6.30: Inverted domain area vs. voltage delay time for various intensities using fs-pulsed light of $\lambda = 400$ nm with $E = 8$ kV/mm in undoped CLN.

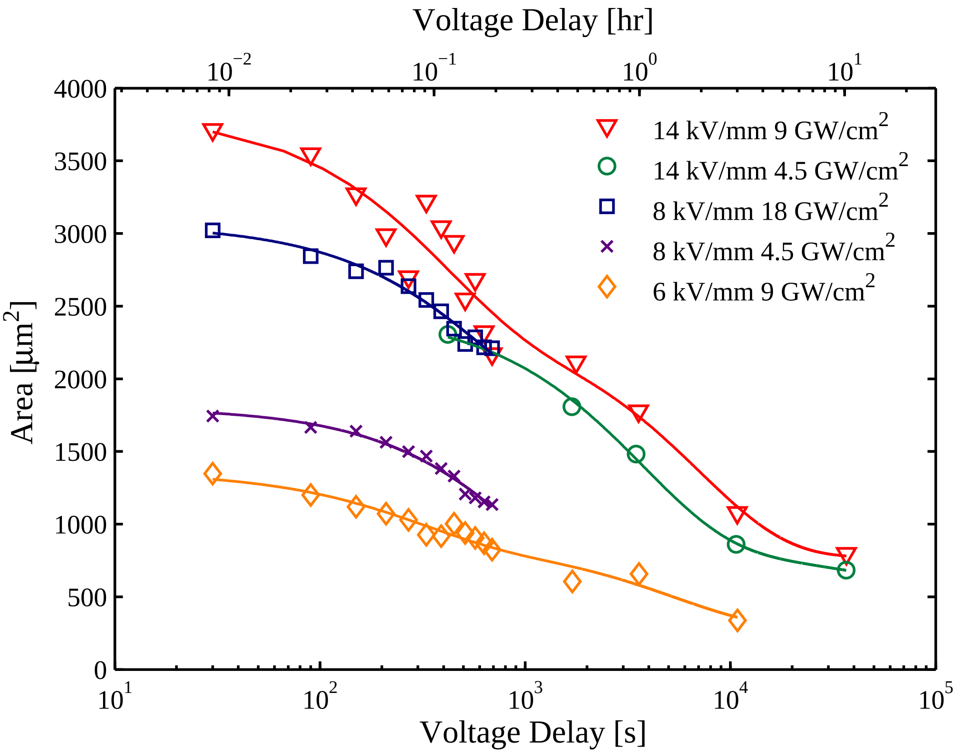

FIGURE 6.31: Inverted domain area vs. voltage delay time for various intensities and E-fields using fs-pulsed light of $\lambda = 400$ nm in undoped CLN. The solid lines represent least-squared fits to an equation of the form $y = c_1 \exp(-x/c_2) + c_3 \exp(-x/c_4) + c_5$.

illumination is based on at least two time-constants. The two curves representing exposures of (8 kV/mm, 4.5 GW/cm^2) and (8 kV/mm, 18 GW/cm^2) contain data up to 700 s and fit well to a single time-constant only, which is of order several hundred seconds. The two curves representing exposures of (6 kV/mm, 9 GW/cm^2) and (14 kV/mm, 9 GW/cm^2) contain data for much longer voltage delays, and therefore clearly exhibit two time-constants of a few hundred seconds and several thousand seconds. The remaining curve of exposure (14 kV/mm, 4.5 GW/cm^2) contains data for long voltage delays only, but seems to follow the shape of the (14 kV/mm, 9 GW/cm^2) curve. To obtain these time-constants more accurately, more data is required for both short and long durations. Averaging over several exposures will also be very important in reducing the variability among the data, as local crystal properties appear to have a noticeable impact on the growth of these domains. Delay times up to a day also resulted in domain inversion, although the exposures used produced disconnected nucleations with limited spreading and merging, and hence were not plotted in Figure 6.31.

As with regular LAP, latent-LAP also formed domains which followed the shape of the illuminating beam and was reproducible between spots and samples. The HF-etched −z face is shown in Figure 6.32, where $I = 9$ GW/cm^2 light formed domains with applied E-fields of (a) 14 kV/mm and (b) 8 kV/mm, after a 570 s voltage delay time. The domain walls of (a) follow crystalline symmetry due to the high E-field applied. However, this

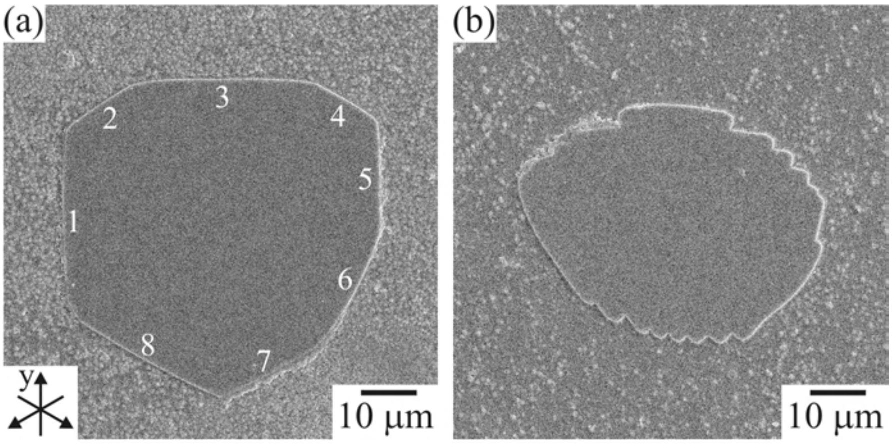

Figure 6.32: Latent-LAP domain shapes induced by $I = 9$ GW/cm^2 of $\lambda = 400$ nm light, followed by applied E-fields of (a) 14 kV/mm and (b) 8 kV/mm after a voltage delay time of 570 s in undoped CLN. Domain walls run parallel to both y and x axes, particularly for the higher applied E-field.

domain was not a regular hexagon as is typical for EFP domains, forming instead an irregular octagon with domain walls parallel to both the y and x axes. The walls labeled 1, 2, 4, 5, 7, 8 are parallel to y axes, while walls labeled 3, 6 are parallel to x axes. The domains walls of (b) also run parallel to both y and x axes, in addition to many more rounded segments, generally following the shape of illumination much more closely due to the lower applied E-field.

All above examples of latent-LAP were in undoped CLN. In similar experiments conducted in 5-mol% Mg:CLN, domain inversion was not observed. A plausible explanation for this is due to the increased dark conductivity caused by the Mg-doping, resulting in a quick return to the crystal state prior to illumination.

6.5 Discussion

Light-assisted poling has been shown to be a process widely applicable to a variety of doped materials and under a wide range of conditions, from wavelengths, intensities, electric fields, and exposure times. The experiments conducted have shown several benefits of using LAP for the formation of both arbitrary and periodically poled structures:

1. The requirement for high voltage equipment, circuit insulation, and safety is all greatly reduced. The lower voltages reduces the likelihood of crystal breakage during poling, and may eliminate the need for an insulating oil bath.
2. The requirement for photolithography is eliminated. Patterned domain structures can be formed directly by patterning the light incident on the crystal, accomplished using amplitude masks, phase masks, or two beam interference. Masks may still

be required for patterning, but the processing steps of each crystal are eliminated, greatly simplifying the fabrication.

3. Direct-write allows the formation of arbitrary domain patterns without the need of masks or photolithography, and the minimum domain size is controlled by the beam size instead of by the features of a mask.
4. Domain engineering is freed from the hexagonal constraints of the domain shapes produced by EFP. Straight domain walls along arbitrary directions and curved domain walls are all possible, as evidenced by high-magnification SEM imaging.

From the results presented above, there are several intuitive trends governing the three main exposure conditions of intensity, electric field, and illumination time. In the direct-write of domain structures, a parameter of *dwell time* (or alternatively, *scanning speed*) replaced the parameter of illumination time. In general, an increase in any or all of these parameters will result in further growth and/or spreading of a domain. With a suitably small applied E-field (determined by the dark nucleation field and dark poling properties of the material), exposed regions grew to a maximum size governed by the beam size and exposure conditions, and thereafter appeared to grow no further. According to the plot of Figure 6.16, the domains continued to expand, but followed a logarithmic profile with illumination time. Under low exposure conditions, surface domains formed with depths that were suitable for waveguiding applications. Pushing surface domains through to the +z face may be possible in a controlled manner by increasing an exposure parameter, or by later pulsed-E-field poling. Under higher exposure conditions, bulk domains extending throughout the thickness of the crystal were also possible. However, hexagonal domain shapes were reasserted particularly when using a high E-field, with a rule-of-thumb transition point near ~1 kV for 0.5-mm thick Mg:CLN.

Important characteristics of LAP are the influence of doping, comparison of cw to fs-pulsed effects, influence of wavelength, kinetics of domain growth, mechanisms of domain nucleation and growth, and possible applications. These topics are discussed in the following sections.

6.5.1 Influence of Doping on Light-Assisted Poling

The dopant type and concentration had a profound effect upon LAP results. This was most evident in Mg:LN where both cw and fs-pulsed experiments yielded a much greater reduction in the nucleation field than undoped CLN. Outlined in Table 6.2, the reduction of nucleation field for cw light of $\lambda = 514.5$ nm increased nearly 3-fold from 31% in undoped CLN to 88% with the introduction of 5-mol% Mg-doping. The results of fs-pulsed light at $\lambda = 400$ nm, outlined in Table 6.3, similarly showed an increase from 40% reduction of the nucleation field in undoped CLN to 97% with the introduction of 5-mol% Mg-doping. In both cases, a similar reduction was observed in Mg:SLN.

In the materials discussed above, all doping concentrations were above the ODT. Below the ODT, however, the light-induced reduction of the nucleation field showed intermediate values closer to the undoped CLN case, shown above in Figure 6.5. A similar observation was made for several Mg concentrations below the ODT using UV cw-LAP [Wengler05]. In this thesis, Mg:CLN ($<$ ODT) refers to 5.5-mol% CLN from Crystal Technology Ltd., where the 5.5-mol% specified the concentration of the MgO in the melt. As verified by OH-absorption measurements (Table 2.3), the amount of Mg incorporated into the crystal was below the ODT. As a result, the reduction of the nucleation field is not much greater than for undoped CLN, and follows an exponential trend with a single decay-constant. For the data of Figure 6.13, the plot labelled “5-mol% Mg:CLN” actually refers to two crystals: 5-mol% CLN from Yamaju Ceramics Ltd. and 4.9-mol% CLN from Crystal Technology Ltd., both doped *above* the ODT as verified by their OH-absorption spectra. This latter crystal from Crystal Technology was a newer material where the fabrication process had been improved to increase the incorporation of the Mg into the crystal. Both these CLN materials doped above the ODT showed identical $E_n(I)$ responses and therefore the data has been plotted together in a single curve, following an exponential trend with two decay-constants. The behavior of these materials implies that the mechanism behind the enhancement in LAP of Mg:CLN must also rely on the change in the crystal at threshold, as discussed in Section 6.5.5. Additionally, the quality of the material with a doping concentration less than the ODT was likely very poor with a high defect density, as evidenced by the relatively large internal field compared to other Mg-doped materials (Table 3.2). If these include additional $\mathrm{Nb_{Li}}$ anti-site defects then even higher concentrations of Mg dopant would be required to achieve the ODT than in standard undoped CLN.

This large reduction of the nucleation field in Mg:CLN was also expected in materials incorporating other photoresistant dopants such as Zn and Hf. However, using fs-pulsed LAP the intensity-dependent nucleation field was reduced by up to only 26% in 1-, 4-, 7-mol% Zn-doped congruent lithium niobate (Zn:CLN) and only 46% in 5-mol% Hf:CLN (Table 6.3). Additionally, the inverted regions in Zn:CLN tended to follow the crystalline hexagonal symmetries similar to regular EFP. It was immediately evident from Table 2.3 that none of these materials showed a shift in the OH-absorption band, contrary to expectations for the 7-mol% Zn:CLN and 5-mol% Hf:CLN with doping levels at or above their respective ODT. As observed in one of the Mg-doped materials, this may have been a result of a lower concentration of dopant incorporating into the crystal from the melt than expected. Compared to Mg:CLN, both Zn:CLN and Hf:CLN are experimental materials not offered commercially as a stock item. The Zn:CLN was supplied by Photox Optical System Ltd. and was custom fabricated. The Hf:CLN was supplied by Edvard Kokanyan, a researcher at the National Academy of Sciences in Armenia. This Hf:CLN material contained many defects throughout the crystal where nucleation initiated on each poling cycle during uniform EFP. The high defect concentration was confirmed by the internal field — the largest measured in any of the studied materials (Table 3.2).

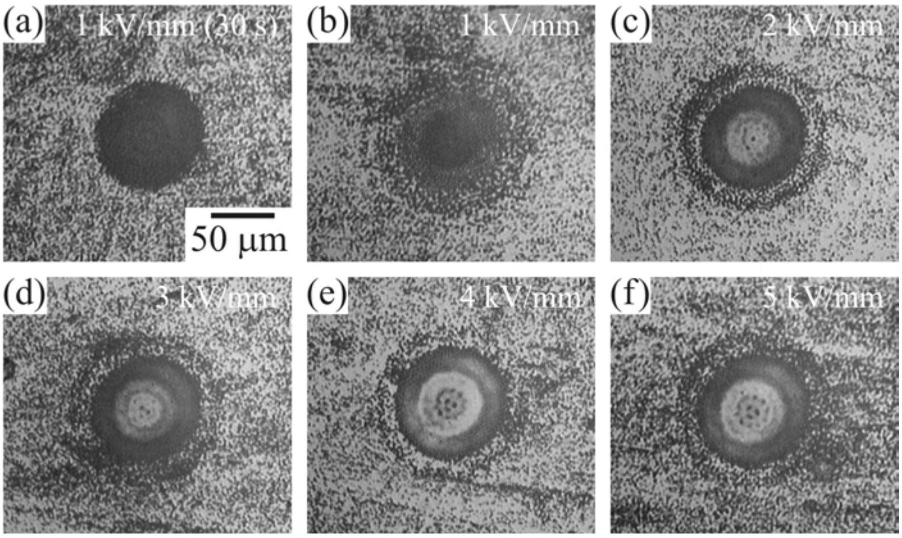

Figure 6.33: Frustrated etching induced by fs-pulsed LAP in 7-mol% Zn:CLN using $\lambda = 400$ nm light with $I = 10$ GW/cm^2 for 90 s, with the applied E-field indicated in each image. The spot imaged in (a) underwent an exposure of only 30 s. A similar exposure with $E = 6$ kV/mm formed a hexagonal domain. The scale is identical in each image.

LAP of Zn:CLN showed an additional effect when applying voltages below the nucleation field, causing frustrated etching as depicted in Figure 6.33 after an HF etch of 20 minutes. Here, low electric fields resulted in a dense packing of frustrated etch hillocks within the beam spot (a). As the electric field was increased, (b)–(f), the frustrated etch region extended further outwards while an expanding central region showed an increased smoothness after etching. This effect may be an E-field-controlled *enhanced etching* similar to the phenomenon observed in Section 4.2.2. These frustrated etching features were not observed in LN or LT with any other dopant.

Fe:CLN was also found to result in a relatively small reduction of the nucleation field, with a modest 12% reduction with 0.01-mol% doping, which is actually less than the 40% reduction in undoped CLN. With increased doping up to 0.1-mol%, the LAP effect was restored to 44% reduction, very similar to the undoped CLN case. It should be noted that the reason for the very different doping concentrations of Fe as compared to Mg, Zn, or Hf is that Fe introduces a broad absorption band in the visible region, such that 0.01-mol% doping appeared tinted, while 0.1-mol% was brownish. Doping with 1-mol% Fe or more is comparatively rare for most applications because even moderate doping concentrations provide significant increases in photorefractivity.

In addition to the change in nucleation field, Fe-doping in these concentrations appears to reduce the quality of domain inversion using fs-pulsed LAP with $\lambda = 400$ nm. Instead of forming domain structures defined closely by the intensity pattern as observed in Mg:CLN, inverted domains in Fe:CLN were often composed of several separate nucleation clumps within the beam width or oddly-shaped structures unrelated to the beam shape and varying between different spots. Clearly the nucleation process was not controlled as strongly by the light intensity in these materials as it was in Mg:CLN, and instead the local properties of the material dominate the behavior of nucleation.

Doping LN with optically active Nd ions was also found to exhibit a small reduction of the nucleation field by LAP of a mere 12%, which was much less than in undoped CLN when using $\lambda = 400$ nm fs-pulsed light. When utilizing a wavelength $\lambda = 813.5$ nm within the optical absorption band of this dopant, no preferential domain inversion was observed. With high intensity, a photorefractive effect was visible, but the light was not capable of spreading or merging pre-existing domains formed by EFP even when biased near the coercive field.

In CLT, as compared to CLN, higher intensities were required to achieve similar reductions in the nucleation field using fs-pulsed LAP, achieving a 34% reduction at maximum, although this may not have been saturated. Additionally, the domains formed did not always follow the intensity pattern, and appeared to depend strongly upon the local properties of the material. As with LN, doping LT with Mg was expected to enhance the effect of LAP and therefore two doping concentrations were sourced from Yamaju Ceramics Ltd. The first material, 1-mol% Mg-doped congruent lithium tantalate (Mg:CLT), was not suitable for experimentation because of problems with regular EFP. During each poling cycle, forward poling was successful but was characterized by domain spreading along all directions rather than the prefered crystalline directions [Figure 6.34(a)]. During reverse poling, electrical breakdown occurred for all crystals tested. In the second material, 7-mol% Mg:CLT, electrical poling was successful [Figure 6.34(b–c)] but had the same nucleation points in both the forward (b) and reverse (c) poling directions, indicating that the same large defects influenced nucleation on both faces of the crystal. LAP achieved a maximum reduction of the nucleation field of only 24% which was lower than the undoped case. From Table 2.3, neither of these materials showed a significant shift in their OH-absorption bands, implying that even the 7-mol% material had incorporated a concentration below the ODT into the crystal structure. Therefore these results are inconclusive in determining whether Mg-doping will have a similar effect in CLT as it does in CLN due to the poor quality of materials.

Despite the fact that indiffusion is a very different process from doping of the melt during crystal growth, the indiffusion of Ti into CLN was also investigated. The introduction of Ti showed a reduction of the nucleation field of up to 92% using fs-pulsed LAP, which brings this material close to the performance of Mg:CLN. The indiffusion of Ti in the crystal has very different behavior than Mg-doping, however. The substitution of the Ti^{4+} on the Nb^{5+} sites causes an effective negative charge, reducing Fe^{3+} to Fe^{2+} ions [Glass80]. This increases the susceptibility to optical damage [Fejer86] despite an increased photoconductivity [Schmidt80]. Therefore, a more likely candidate material for a practical device would be Ti-indiffused Mg:CLN, where the drawbacks of Ti are

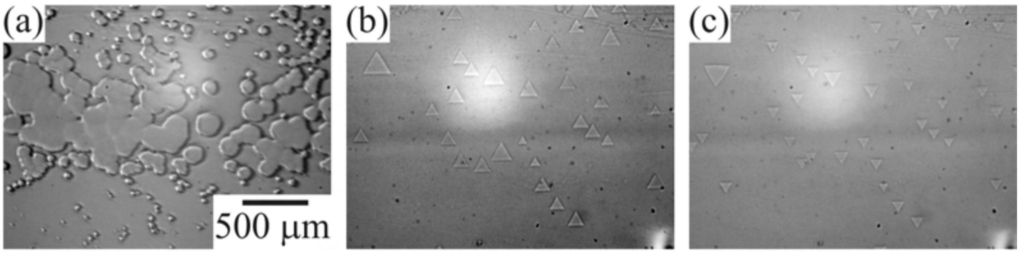

FIGURE 6.34: Domain spreading in (a) 1-mol% and (b–c) 7-mol% Mg:CLT supplied by Yamaju Ceramics Ltd. Nucleation of the material doped with 7-mol% MgO occurred at the same positions for both (b) forward and (c) reverse poling. The domain triangles are flipped vertically due to the inversion of the y axis during poling. The three images are shown on the same scale.

decreased [Fejer86] and the reduction of the nucleation field would also be expected to at least match that of bulk Mg:CLN.

Using LAP instead of EFP provides an advantage in the processing of this material. Due to the high temperature required for Ti-indiffusion, the +z face may suffer from an undesirable domain-inverted layer formed by Li out-diffusion. This causes problems for EFP which often uses patterned electrodes on the +z face where the material properties have been changed. LAP, on the other hand, nucleates preferentially on the −z face, completely avoiding the Li out-diffused layer on the opposite face, and has been shown easily to invert domains after Ti-indiffusion.

The success of LAP domain inversion in Ti-indiffused material indicates that a device based on a Ti-indiffused waveguide should be possible. For instance, phase-mask patterned LAP becomes a possibility for simple fabrication of QPM PPLN gratings in waveguiding devices.

Due to the fact that many of these doped materials were experimental in nature, improvements in their growth (resulting in reduced defect density and more reliable dopant incorporation) may yield much improved LAP behavior.

6.5.2 Comparison of cw and fs-pulsed LAP

There are very significant differences in the behavior of LAP using cw and fs-pulsed light. Table 6.5 summarizes the differences between the cw and fs-pulsed LAP processes discussed below.

Domains formed by cw-LAP nucleated suddenly in a “pop” and were clearly visible by electro-optic contrast and stress-induced birefringence when using crossed polarizers. However, domains formed by fs-pulsed LAP were not visualized upon nucleation until they were allowed to grow by additional exposure. This lack of visibility was only partially due to the lower electro-optic contrast caused by the relatively small E-field,

Table 6.5: Comparison of cw and fs-pulsed LAP.

Property	cw LAP	fs-pulsed LAP
Illumination	continuous wave	∼130 fs, 1 or 250 kHz
Intensity [W/cm^2]	10^0–10^3	10^6–10^{11}
Wavelengths [nm]	457, 488, 514.5	305, 334, 364, 383, 400, 514.5, 800
Max. $E_n(I)$ Reduction	91%	98%
Nucleation	"pops"	slowly becomes visible
In-situ Visibility	yes	not visible for low exposures
Nucleation Location	anywhere within spot	follows illumination shape & size
Nucleation Density	low	high
Nucleation Shape	hexagonal, arbitrary	arbitrary angles, curves
Domain Size	large	small, periodic

and may also have been a result of a lower stress-induced birefringence [Dierolf04]. In these cases, HF etching was necessary to determine when nucleation had occurred.

With cw LAP, large domains were simple to nucleate and grow in undoped and Mg-doped CLN, but have not been achieved in CLT. Light-assisted nucleation did not necessarily occur at the centre of the beam, but often at several random locations within the beam radius. These often hexagonal nucleation points then expanded and merged throughout the illuminated region. Scanning the beam formed domain lines that expanded outside of the beam width due to the high applied voltage and the slow scanning speed required to allow the nucleation points to merge. This led to the 500-μm wide domain line formed by scanning, as shown in Figure 6.7(c). Due to the randomness of the nucleation, low nucleation density, relatively slow spreading, and tendency to form hexagonal domains, this expansion outside of the illuminated regions may be an inherent problem in direct-write approaches using cw light. However, as evidenced by Figure 6.8, arbitrary shapes are possible with high intensity and low applied E-field. Hexagonal domains are more likely to occur when using a focused Gaussian beam which encourages lateral spreading, as opposed to when a patterned beam with sharper edges in the intensity pattern is employed.

Many of the limitations discussed above were overcome by using fs-pulsed LAP where ∼130 fs pulses provided average intensities of similar magnitude to the cw light, but peak intensities 7–10 orders of magnitude higher. Inducing nucleation in both CLN and CLT materials was possible, forming both large and small domains, and periodic structures with a period of 5.25 μm. Nucleation closely followed the shape of illumination and quickly spread over the entire beam spot, as discussed below in Section 6.5.4. The domain-inverted region spread across the entire illumination area quickly enough to prevent spreading outside of the beam width, forming useful direct-write structures controlled by the scan speed. A lower nucleation field, particularly in Mg:CLN, also permitted the use of lower voltages for which the domain wall velocity is reduced in dark regions [Gopalan98], further limiting domain spreading outside of the beam spot. Additionally, domain walls were not limited to the hexagonal symmetry of the crystal, permitting straight line segments along directions not parallel to any of the x or y axes, as well as curved walls. Finally the large reduction of the nucleation field permitted domain nucleation at voltages as small as 50 V applied across a 500-µm thick Mg:CLN crystal, removing the need for high voltage equipment.

One important difference between the above cw and fs-pulsed LAP experiments is the incident intensity. In contrast, the high intensities provided by a diffraction-limited spot of cw visible light in [Dierolf04] produced direct-write domain lines with jagged walls that followed the illumination pattern and were not visible by a polarized microscope due to little stress. These were very similar in appearance to the high peak intensity fs-pulsed LAP domains that closely follow the shape of the illuminated region, perhaps indicating that the high intensity was required to avoid hexagonal shapes. Additionally, low exposures of fs-pulsed LAP produced domains which are not visible by a polarizing microscope. In the diffraction-limited cw experiments, on the other hand, the position of nucleation was reported to be “near” the beam [Dierolf04], but not precisely determined by it, unlike the fs-pulsed LAP results.

A final inherent difference in fs-pulsed LAP is the nature of applying brief pulses of light to a crystal instead of a continuous stream of photons. This difference may have a suitable analogy with the difference between pulsed-voltage and conventional non-pulsed EFP, the implications of which are discussed below in Section 6.5.4.

6.5.3 Influence of Wavelength on Light-Assisted Poling

In cw-LAP, no wavelength dependence was measured across the visible wavelengths used from an Ar^+ laser (457, 488, 514.5 nm). All wavelengths resulted in the same reduction in the nucleation field in Mg:CLN, as shown in Figure 6.6. No other differences across these wavelengths were observed, each allowing the nucleation, growth, and spreading of domains without observable damage to the domain or the surrounding material. Due to these similarities across wavelengths, the 514.5 nm laser line was typically employed because it provided the greatest output power from the laser.

The results presented above using visible cw-LAP can be directly compared with results published by our collaborators at the University of Bonn, where large-area UV cw exposures of undoped and Mg-doped CLN demonstrated similar nucleation field trends for the wavelengths of 334 nm and 305 nm [Wengler05]. The most important similarity was the requirement for Mg-doping above the ODT to achieve the maximum reduction in the nucleation field. However, these reductions were much less than those produced by visible light, reaching a maximum of only ∼50%. It is noteworthy that these UV intensities reached only ∼100 mW/cm^2, significantly below the intensities used for visible illumination. Nonetheless, the UV results demonstrate a clear saturation for the maximum intensities used and therefore no significant reduction would be expected for higher intensities.

Recently, cw light-assisted domain inversion was demonstrated using $\lambda = 647$ nm red light from a Kr-ion laser [Li07]. In that study, 647-nm light produced a maximum reduction in the nucleation field that was approximately half of the reduction by 514-nm light, and reached saturation at nearly twice the intensity. The wavelength dependence from 351–799 nm cw light was also explored, showing an exponential decrease in the maximum reduction of the nucleation field with increasing wavelength [Zhi07]. Therefore, the wavelength used across the near-UV and visible regions is an important factor for the light-assisted nucleation field, with higher photon energies achieving a greater reduction with lower intensity.

Preliminary investigations into cw UV light of $\lambda = 244$ nm, outlined in Section 6.2.4, did not result in controlled direct-write structures, but rather required electric fields very near the dark nucleation field and produced damage. This damage appeared visually similar to artifacts left behind by tiny nucleation points whenever a domain structure was maintained for a long duration during dark EFP, as depicted in Figure 6.12. Here, the UV-induced damage regions are densely populated with bright and dark regions. Outside the UV-affected region, randomly distributed crystal defects caused nucleation sites to form (a–k). After being held many minutes in this domain state, the applied E-field was ramped to the coercive field and the UV-induced hexagonal domain spread across the entire crystal, leaving behind similar bright and dark spots where the nucleation points had been located (l). Whereas these former nucleation points of regular EFP largely disappear over time, the UV-induced damage remained much longer. It was likely that in both instances charge accumulated at defects in the material causing a refractive index contrast via the electro-optic effect, which then slowly dissipated after poling by charge migration. The important difference between the EFP and UV-induced defects, and also between the visible and UV wavelength regimes, is that the latter provides photons with energy exceeding the bandgap of LN, thus potentially redistributing a greater amount of charge into defect traps.

Both the in-situ optical microscope and HF etched views of this UV-induced damage are visually very similar to the observations made of charged domain walls [Shur00]. In that instance, indium tin oxide, $Sn:In_2O_3$ (ITO) electrodes had been used to nucleate domains on the +z face but were unable to grow completely through to the −z face due to the intrinsic dielectric layer. The result was a needle-like domain pattern that was visible under optical microscopy due to the electro-optic refractive index contrast of the charged domain walls. It was noted in those experiments as well that these domains appeared "fixed" and were not removed upon the application of a reversed electric field, but rather additional charged needle-like domains were created.

An additional characteristic of UV cw-LAP in Mg:CLN is that the poling direction (either forward or reverse) strongly influences the results. This may simply be due to the strong absorption of $\lambda = 244$ nm which guarantees that the incident light affects the incident face of the crystal only. This requires verification by repeating the same experiments in both forward and reverse poling directions with the light incident on the virgin +z face instead of the −z face.

In fs-pulsed LAP, a much broader wavelength range has been explored due to the tunability of the ultrashort-pulse laser system, ranging from the UV (305–383 nm) to visible (400 & 514.5 nm) to IR (800 & 1500 nm). The repetition rates of 1 and 250 kHz were available for UV and visible–IR wavelengths, respectively. Across the UV and visible regions, similar reductions in the nucleation field were achieved, reaching a maximum of $> 98\%$ reduction in Mg:CLN using $\lambda = 334$ and 514.5 nm. For some wavelengths, the accuracy of the minimum nucleation field was limited by the number of experiments conducted due to a limited availability of the laser, and therefore some data points merely reflect the lowest E-field attempted. Therefore, all wavelengths used in the UV–visible range showed similar reductions and are likely capable of achieving a similar maximum reduction under optimal conditions of intensity and illumination time.

Powers used to form domains were vastly different in the different wavelength regimes, as suggested by Table 6.4. In the UV range, as little as 100 nW was capable of nucleating domains using $\lambda = 305$ nm. In the visible range, this increased to 10–100 μW. In the infrared with $\lambda = 800$ nm, 200–300 mW were used. However, for $\lambda = 1500$ nm IR light, powers up to 23 mW were insufficient for domain nucleation or spreading at any applied voltage in undoped, 5-mol% Mg-doped, or 0.01-mol% Fe-doped CLN.

6.5.4 Kinetics of Light-Assisted Poling

In many ways, the nucleation and growth of domains induced by cw-LAP are similar to these processes in regular EFP domains. Firstly, the intensity-dependent nucleation field is repeatable and sharply defined at a constant voltage ramp rate. Secondly, nucleation points within the illuminated region appear with a sudden "pop". Finally, these nucleated domains typically (but not always) follow the hexagonal symmetry of the crystal, and expand laterally in the same manner as EFP domains. Therefore the kinetics of domain growth by cw-LAP are very similar to the EFP case.

In contrast, fs-pulsed LAP demonstrated many different features than readily viewed in regular EFP. In fact, many features of domain growth via this technique showed characteristics following other extreme switching conditions of AOP (Chapter 5) and non-equilibrium poling (Section 3.4.3).

Domains formed by fs-pulsed LAP under moderate to high exposure conditions, as discussed mainly above, form completely connected inverted regions across the entire

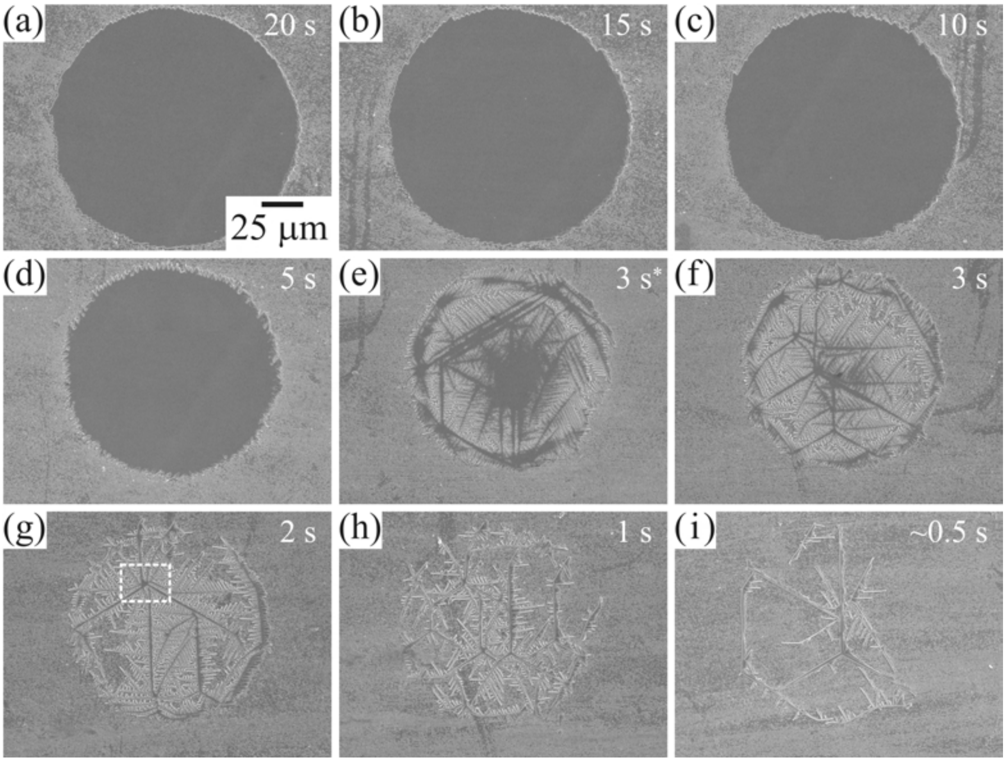

FIGURE 6.35: Etched domain profile on the −z face of Mg:CLN formed by fs-pulsed LAP using an E-field bias of $E = 500$ V/mm and illumination by $\lambda = 400$ nm with $I = 0.06$ GW/cm^2 and illumination times of 20–0.5 s as indicated in each image. The inverted region in (e) has been formed using a 50% larger intensity of 0.09 GW/cm^2 and is shown as an intermediate growth point between (d) and (f). The scale is identical in each image.

beam spot. However, as suggested in Figure 6.25 for example, the edges of these domains do not always follow straight lines. This was caused by their growth characteristics, which could be investigated more conveniently in the low exposure regime. To this end, a low intensity 0.06 GW/cm^2 of $\lambda = 400$ nm light was focused onto a Mg:CLN crystal biased with $E = 500$ V/mm. Figure 6.35 shows the illuminated regions after HF etching for 20 minutes. The illumination time of each spot was varied, with (a) t = 20 s, (b) 15 s, (c) 10 s, (d) 5 s, (e) 3 s (0.09 GW/cm^2), (f) 3 s, (g) 2 s, (h) 1 s, (i) ~0.5 s. The spot in (e) employed a 50% higher intensity than all other spots to demonstrate an additional growth stage between (d) and (f).

This sequence of images shows the growth dynamics of the domains with time. In Figure 6.35(a), a large circular domain-inverted region was observed, as expected. Reducing the exposure time from 20 s to 5 s (a–d) decreased the diameter of the domain and made the edges more jagged, but otherwise left the appearance of the domain unchanged. Further reductions in the exposure time (e–i), however, revealed a very different structure within the outer boundaries of the illuminated spot. With a 3 s exposure (e,f), large parts of the inverted interior of the spot segmented into connected lines of domains running along both the y and x axes. Shorter exposures (g–i) resulted in greater separation

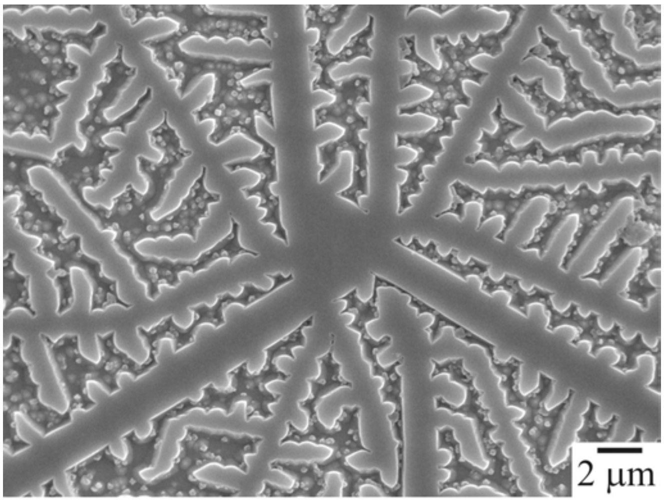

Figure 6.36: Branching of fs-pulsed LAP domains during growth on the −z face of Mg:CLN, showing a magnified view of the boxed region of Figure 6.35(g).

and a smaller density of these features. The boxed region of Figure 6.35(g) is shown in greater detail in Figure 6.36, highlighting the merging and branching inherent in these structures.

Therefore, fs-pulsed LAP induced nucleation in random locations throughout the illuminated area, likely correlated to defects in the crystal and to the hot-spots within the beam. These nucleations rapidly grew along the y and x axes, with a greater number of lines following the y axes. Longer illumination led to an increased branching density and more domain line growth. Still longer illumination resulted in the eventual merging of these domain branches in the most dense areas, eventually leading to merging across the entire illumination region, forming the uniformly inverted domain expected for moderate to high exposure conditions.

A similar initial nucleation occurred in undoped CLN while quickly scanning a beam with an intensity ∼4 GW/cm^2 of $\lambda = 400$ nm light with a bias of 18 kV/mm, as shown in Figure 6.37. The main difference as compared to previous examples in Mg:CLN, which used very different intensity and applied E-field, is the lack of branching observed. In this case, a rapid scan speed resulted in domain lines qualitatively similar to AOP domains induced by ns-pulsed UV light. However, unlike AOP domains, these lines aligned with all three x axes as well as the three y axes. The regions with a higher density of domain lines correspond to slower scanning speeds (hence longer dwell time). In areas where the beam was held briefly without motion, merging throughout the illuminated area was observed, as seen in the two merged regions, labeled **A** and **B**, toward the right side of Figure 6.37. Only these two regions were clearly visible via the in-situ optical monitoring during fabrication. Multiple passes of the beam over similar areas were also able to form a solid line of domain inversion. Therefore, repeated exposure acts cumulatively to spread existing nucleation lines. Similar AOP-like domain lines were observed between

Figure 6.37: Self-organized lines following the fs-pulsed LAP scanning of $\lambda = 400$ nm light of $I \simeq 4$ GW/cm^2, with $E = 18$ kV/mm bias in undoped CLN. Shown is a single continuous line of exposure where the right side of the top image connects to the left side of the bottom image.

the high-intensity peaks of the periodic illumination grating formed by mask projection, as shown in the inset of Figure 6.22(b).

Subsequent to the merging of domain branches, the inverted domain area followed a logarithmic growth pattern with increasing exposure time, as shown in Figure 6.16. This logarithmic dependency held until the size of the inverted area was approximately equal to the illumination spot area. Above this size, the domain area grew linearly with time. This marked a very important transition point, where previously the domain walls grew in the presence of light (i.e. LAP) and subsequently the domain walls grew in the absence of light (i.e. EFP). However, as reported in [Gopalan98], the sideways wall velocity in regular EFP follows the relation,

$$v_s^{\mathrm{EFP}} = v_{s,o} \exp\left[-\frac{\alpha_s}{E - E_{int}}\right] \tag{6.7}$$

where $v_{s,o}$ and α_s are constants, E is the applied E-field, and E_{int} is the internal field. During EFP under the observed E-fields, wall velocity is constant, hence the motion of the wall is linear with time. However, to obtain an *area* that is linear with time t, this requires the velocity to be changing,

$$v_s^{\mathrm{LAP}} \propto t^{-1/2} \tag{6.8}$$

A component of the local E-field is due to the light-induced charge redistribution caused by illumination, and this decreases as the walls moves further away from the illuminated region according to the $1/r^2$ relation of Coulomb's law. This does not entirely account for the relation of (6.8), but it does imply a slowing of the wall velocity away from the illumination region, as observed.

Domain growth must also be considered in the depth direction; i.e. along the z axis.

It was previously noted that for all conditions, LAP domains nucleated on the −z face. Subsequent growth was capable of pushing these domains from the −z face to the +z face, providing similar etch profiles on each surface, as shown in Figure 6.18 for example. However, forming these bulk domains via LAP was not always straight-forward.

Biasing a 0.5-mm thick Mg:CLN crystal at 0.6 kV/mm, a $\lambda = 400$ nm exposure of $I = 0.6$ GW/cm^2 for a few seconds yielded very little penetration of the domain to the +z face, as shown in Figure 6.38(a–b). Under these conditions only a few points along the outer edge of the beam reached the +z face, which may be due to a greater build-up of photo-induced charge near the boundary of the illuminated region. Increasing the E-field bias to 1.1 kV/mm induced similar domain inversion patterns even when the intensity was reduced to 0.02 GW/cm^2, as viewed by in-situ optical monitoring. However, for these domains formed under LAP at higher E-fields, a later application of a greater E-field, ∼4 kV/mm, in the absence of illumination forced lateral spreading of the domain outside the beam spot, shown in Figure 6.38(c). Because the depth wall velocity v_d^{EFP} follows a similar relation to (6.7) using EFP, the increased E-field bias was also expected to cause a greater penetration to the +z face. Indeed, under these conditions a much greater penetration of the domain to the +z face resulted in a domain-inverted ring, as shown in Figure 6.38(d). Interestingly, the central area which had been previously illuminated remained in the original domain orientation, indicating a reduction in the rate of depth penetration within the illumination region.

Applying LAP to 1-mol% Zn:CLN provided additional insight into the growth in the depth direction, though the low quality of the material meant that results were not always consistent between spots of identical exposure. Nonetheless, the exposures of Figure 6.39 present a general trend. With a lower voltage, a short illumination time formed hexagonal etched regions on both the −z and +z faces (a). Increasing the illumination time formed a larger hexagon, but also showed a greater unetched area within the hexagon on the +z face (b). Increasing the applied E-field from 16 kV/mm to 17 kV/mm and increasing the illumination time further enlarged the outer dimensions of the hexagon, but also decreased the inverted area within it on the +z face (c–d). Furthermore, the ring of inversion along the boundary of the hexagon was broken into segments, divided by thin lines of the original domain orientation running along the y axes. A possible explanation for this is the *re-poling* of the newly-formed −z face by LAP-induced nucleation, where the low intensity at the edges of the beam formed the domain fingers dividing the outer ring. However in the center of the spot shown in (c) where the intensity would be greatest, re-poling was not observed, indicating that another mechanism may also be involved. For instance, the re-poling of the inverted region competes with the opposite process of the domain growing across the bulk from the original −z face.

To attempt to resolve whether re-poling of the newly-formed −z face was indeed a process involved in these domain patterns, 5-mm thick Mg:CLN was illuminated by $\lambda = 400$ nm

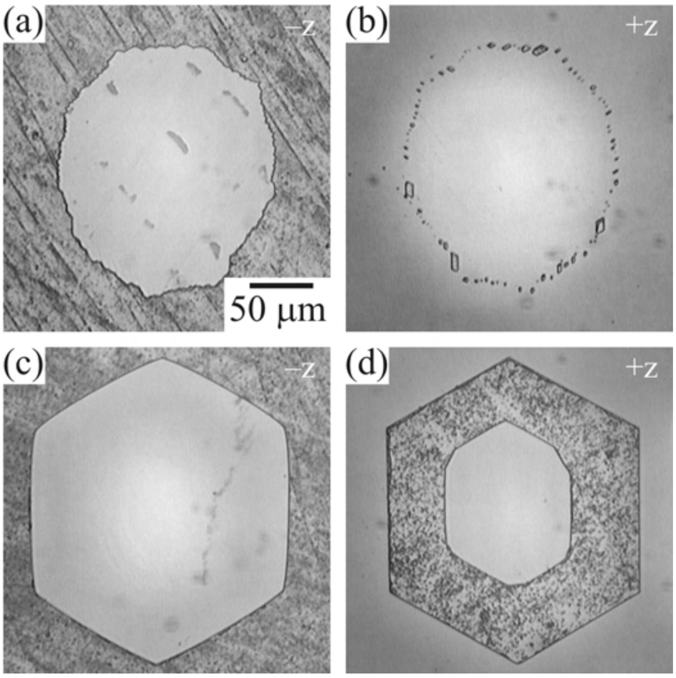

Figure 6.38: Etched domain profiles on the −z and +z faces of Mg:CLN formed by fs-pulsed LAP using $\lambda = 400$ nm light. A 0.6 kV/mm bias and 0.6 GW/cm^2 illumination formed an inversion pattern following the illumination pattern on the −z face (a) with only a small area of penetration to the +z face at the edges of the beam (b). With 1.1 kV/mm and 0.02 GW/cm^2, a similar domain formed, but with a subsequent dark voltage ramp to ∼4 kV/mm, a larger hexagon grew on the −z face (c) which penetrated to the +z face except within the center of the previously illuminated region (d). The scale is identical in each image.

light of $I = 0.3$ GW/cm^2, directly writing an inverted-domain line by scanning the beam over the −z face. Biasing the crystal with $E = 2$ kV/mm, two passes of the beam over the same line formed a surface domain following the pattern of illumination on the −z face, as shown in Figure 6.40(a). Increasing the E-field to 3 kV/mm and using eight passes of the beam over the same line formed a hexagonal etched area on the −z face that expanded to a width greater than the beam diameter. The etched pattern on the +z face, in contrast, showed the same outer dimensions of this hexagon, but the inner region of the line where the beam had passed was left in the original domain orientation. Figure 6.40(b) shows the start of this line where the hexagonal shape capped the end of the illuminated line. On the eighth and final pass, the beam was allowed to move beyond the end of the hexagonal domain on the opposite tip of the line. As depicted in Figure 6.40(c), this one final pass of the beam prevented the capping of the line with a hexagonal inverted region.

From these images, the following observations were made. Throughout the length of the illuminated line, an etched hexagonal shape formed on both the −z and +z faces. However because the crystal was transparent at this wavelength, the beam illuminated both sides of the crystal. By first pushing the domain through to the +z face, either the

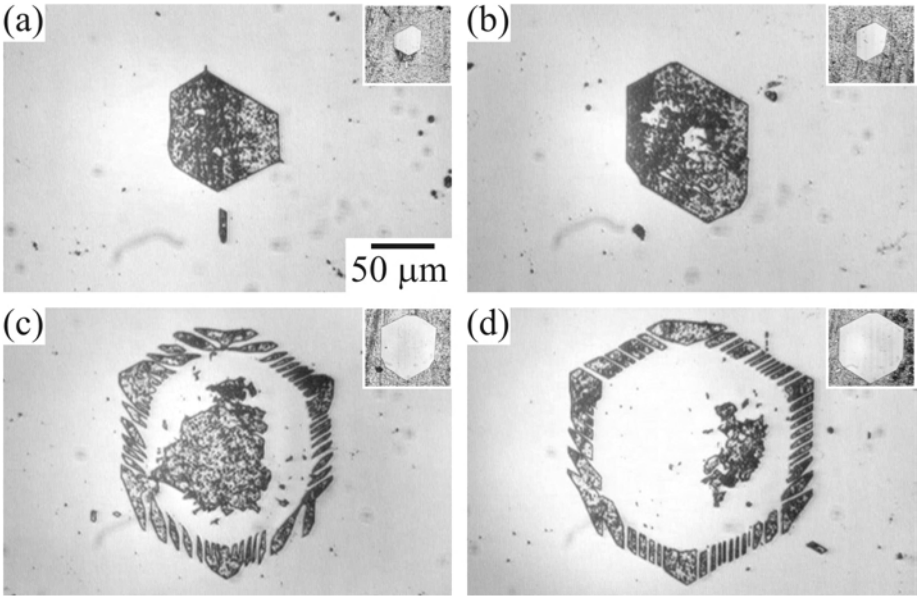

Figure 6.39: Etched domain profiles on the +z face of Zn:CLN formed by fs-pulsed LAP using $\lambda = 400$ nm light. (a–b) Lower voltage and short exposure times form hexagonal etched regions on both faces. (c–d) A higher voltage and longer duration yields spreading outside of the illuminated area and penetration of the domain to the +z face primarily outside the beam. The corresponding −z face view of each image is shown in the inset. The scale is identical in each image.

beam then caused nucleation on the newly-formed −z face, re-inverting the orientation back to the original +z face, or a diminished growth rate in the region of illumination prevented the domain from reaching the +z face. This was observed only in the central region of the hexagon where the beam was located. Furthermore, when the final pass of the beam moved beyond the boundary of the domain that had formed from the previous seven passes, the beam also re-inverted the end cap of the hexagon. Had this final pass not moved beyond the end of the hexagon, both ends would have appeared similar to Figure 6.40(b). Therefore, re-poling of the opposite z face must play a significant role, as suspected from the previous etch profiles of Figure 6.39.

This issue of re-poling may be avoided in the future by adjusting the exposure conditions. Firstly, using tighter focus onto the −z face could reduce the intensity on the opposite crystal face and thereby increase its nucleation field. With a suitably low applied electric field E, nucleation could thus be limited to the front face only. Additionally, using exposure conditions where the domain did not expand laterally beyond the region of illumination prevented re-inversion on the opposite face, as clearly demonstrated by the “ORC” domain pattern of Figure 6.18. The conditions that were successful in this instance were high intensity coupled with a smaller ratio $E/E_n(I = 0)$.

The y face cross-sectional profiles of LAP domains have also revealed that the depth profile varies across the inverted region. As shown in Figure 6.27, areas that have expanded beyond the illuminated region grow in depth at a faster rate than the area within the

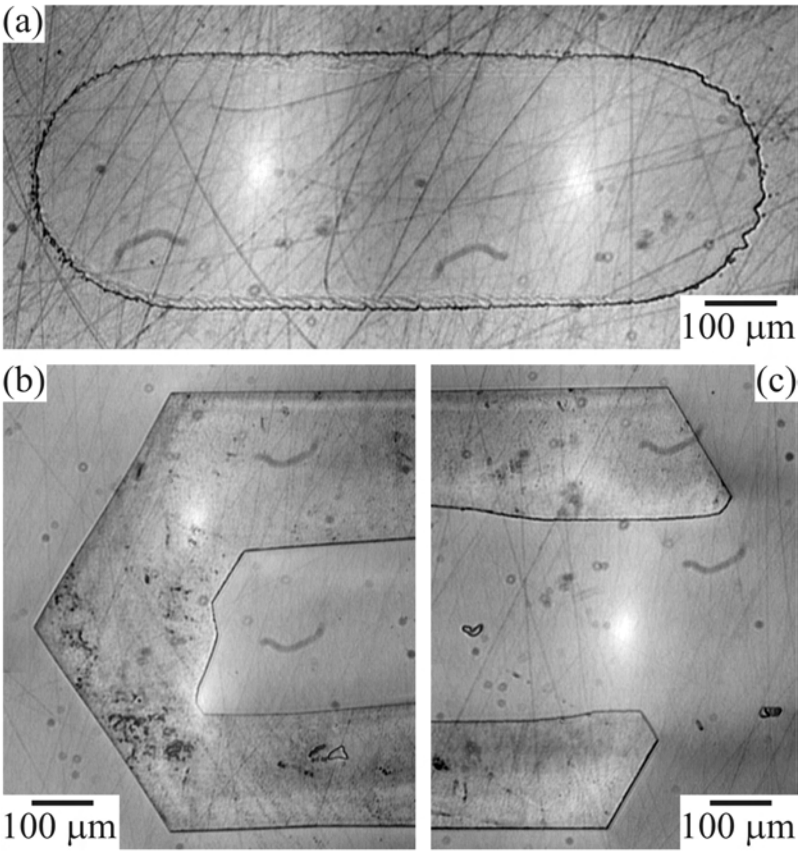

Figure 6.40: Re-poling of the +z face in 5-mm thick Mg:CLN induced by LAP using $I = 0.3$ GW/cm^2 of $\lambda = 400$ nm light. (a) Two passes of the beam with $E = 2$ kV/mm formed a surface domain on the −z face. Eight passes with 3 kV/mm pushed the domain to the +z face, but resulted in re-poling (b) in the center of the line and (c) where the beam moved beyond the edge of the hexagon on the final pass.

beam when using an E-field of 1 kV/mm in Mg:CLN. For E-fields significantly below this, domains would be expected to conform more closely to the pattern of illumination, with higher intensities and longer exposure pushing the domain deeper within the beam. At this time, there are no y face cross-sectional profiles to support this hypothesis, but the +z face etch profiles do corroborate this supposition.

Therefore, there are two processes at work governing the depth profile and the resulting +z face etch profile. Firstly, the rate of depth penetration outside of the region of illumination is faster when using moderate to high E-fields. Secondly, the beam may re-pole the newly-formed −z face soon after inversion. Together, these processes can explain the etch patterns seen on the y face and +z faces.

Finally, as mentioned above in Section 6.5.2, the pulsed nature of fs-pulsed LAP may have a suitable analogy in the difference between pulsed-voltage and conventional non-pulsed EFP. Pulsed-voltage poling first nucleates a domain and subsequent pulses push the domain deeper towards the opposite face. In pulsed-LAP it is also possible that these short-duration high-intensity light pulses first nucleate a surface domain, then subsequently push the domain deeper and simultaneously spread it to fill the illumination pattern. Here, however, the voltage bias remains constant and instead the local nucleation field, modulated by each light pulse, is reduced below the applied E-field. The depth profile of these domains has not yet been verified to follow this trend, but the sideways growth has been observed above in Figure 6.35.

6.5.5 Mechanisms of Light-Assisted Poling

The mechanisms of light-assisted poling are currently not well understood. Several contributing possibilities have been proposed, but all are qualitative and may be applicable in certain circumstances only. A new proposal based on the experiments of Section 6.2 and outlined in [Sones05] involves the reduction of the pinning strength of defect centres.

Early LAP experiments were carried out with UV wavelengths. Using the UV lines of an Ar^+ laser, Müller *et al.* speculated that reduction in the observed coercive field may be due to absorption-induced temperature increase by $\lambda = 351$ nm or the photo-generation of crystal defects creating additional nucleation points by $\lambda = 334$ nm [Müller03a]. However, no evidence was provided for either of these hypotheses. Wengler *et al.* extended these experiments to $\lambda = 305$ nm, where strong absorption induced a diminishing intensity across the crystal thickness, resulting in a varying photoconductivity ($\sigma_{ph} \propto I$), and by Ohm's Law provided a depth-varying E-field rather than the uniform E-field of a regular parallel plate capacitor [Wengler05]. Therefore, this model proposed that the coercive field was not modified, but rather the local E-field governed the poling behavior.

LAP with visible light was first explored by Dierolf and Sandmann using a diffraction-limited spot of $\lambda = 488$ nm [Dierolf04]. By micro-Raman measurements, they determined that any change in the crystal temperature due to the focused light was $< 10°$C even with these large intensities, and were insufficient to account for the observed reduction in the coercive field. The present cw-LAP experiments used similar powers but much greater spot sizes, and therefore even less temperature change was expected. At the same time, reduction in the coercive field of only 75% was induced by an increase in the temperature to 250°C in Mg:CLN [Ishizuki03] and undoped LT [Battle00]. Nonetheless, Dierolf and Sandmann proposed that a pyroelectric effect induced by cooling behind a scanned beam could add to the applied E-field. In the present experiments, however, preferential nucleation is obtained in the continued presence of light as well as during scanning, and therefore cooling was not a possible mechanism. In the case of $\lambda = 244$ nm cw-LAP, however, strong absorption and the localized heating of a small volume likely contributed to the minor reduction of the nucleation field measured for this wavelength.

Dierolf and Sandmann also proposed a light-induced coercive field reduction caused by inhomogeneous illumination along the z axis [Dierolf04]. Photoionization of defects was believed to have created a space charge field near the −z face that added to the applied E-field in the direction required for domain inversion. However, in the present cw-LAP experiments, tight focusing onto the −z face was not required to invert domains, and in most cases relatively homogeneous intensity was present across the 0.5-mm thick crystals.

Recently, the reduction in the nucleation field for near-UV to near-IR light was attributed to light-induced defects in [Li07; Zhi07], in agreement with [Müller03a]. The persistence of these defects lead to preferential inversion at these sites on subsequent poling cycles even in the absence of further illumination, as observed herein. However, the nature of these proposed defects has not been investigated.

A new possible explanation of light-induced reduction of the nucleation field involving the reduction of pinning strength in defect centres was first proposed in [Sones05] in relation to the work presented in Section 6.2. Domain growth under low E-fields is dominated by domain pinning [Kim01]. The amount of domain pinning is strongly dependent upon stoichiometry, and hence pinning is directly proportional to the defect density. The defects involved are likely the $\mathrm{Nb_{Li}}$ anti-site and $\mathrm{V_{Li}}$ defect clusters which present an energy barrier for the crossing of a domain wall, hence its action as a pinning site [Kim01]. However, domain wall movement and bowing between pinning defects has been observed in undoped CLN under E-fields an order of magnitude lower than the coercive field [Yang99]. Therefore it is proposed that light may cause a reduction in the pinning strength of these defects, allowing domain wall movement at a lower E-field. Under this model, microscopic domains nucleate at surface defect sites as observed in regular EFP. Illumination, however, reduces the ability of the pinning centres to inhibit domain growth.

In Mg:CLN, doping concentrations above the ODT lead to nearly complete replacement of the $\mathrm{Nb_{Li}}$ with $\mathrm{Mg_{Li}}$. This material is well-known to have a reduced coercive field (Table 3.2) and a smooth and slower domain wall velocity [Nakamura02], implying a higher concentration of pinning centres, each with a lower pinning strength. This material also shows a sudden increase in the effect of light on its nucleation field, implying that the pinning centres have a greater sensitivity to light. The high density of pinning centres results in the ability of light to nucleate domains in arbitrary positions with arbitrary shapes, as the expanding domain wall becomes pinned on the nearest centre outside of illumination.

Wengler *et al.* have also proposed this model of recharging pinning defects to explain their observed reduction of the coercive field of UV wavelengths in undoped and Mg-doped CLN [Wengler05]. In these experiments, a Mg concentration greater than the ODT also achieved the greatest reduction of the coercive field, attributing this to Mg replacing the $\mathrm{Nb_{Li}}$ anti-site defects.

The creation and migration of charge carriers may also be an important mechanism underlying LAP. Firstly, the walls of LAP domains formed by moderate to high exposures remained visible under crossed polarizers even with no applied voltage. By passing the same beam over the inverted domain while the voltage remained zero, the irradiated domain walls became much less visible, just as uniform irradiation "erases" a photorefractive grating [Ohmori75]. The etch profile remained unchanged by this pass of the beam at 0 V, however, indicating that the redistributed charge did not impact the domain after formation. Furthermore, if the crystal underwent a complete poling cycle, the tendency for nucleation to occur on the previous LAP domain location was reduced. Secondly, cross-sectional profiles of LAP domains showed the greatest depth at the edges of illumination where photo-induced charge carriers migrated and accumulated. Thirdly, UV cw-LAP caused optical damage at the domain boundary even when this had expanded far beyond the illuminating beam, indicating that photo-induced charge may have been encouraged to migrate to the edge of the inverted region. Fourthly, latent-LAP was only possible in undoped CLN which has a much lower conductivity than Mg:CLN. This implied that in Mg:CLN, photo-induced charge redistributed faster than the delay times under test, preventing the latent poling effect under these conditions. Finally, light-induced space charge provided surface-charge compensation, contributing to the stabilization of the new domain.

6.5.6 Applications of Light-Assisted Poling

The benefits of LAP can be leveraged for several different applications. These include periodically poled structures in both waveguiding and thick bulk geometries.

Nonlinear interactions in waveguiding devices are beneficial for their strong confinement, counteracting diffraction and maintaining a high intensity over long distances. Domain inversion using LAP has been demonstrated in Ti-indiffused planar waveguides in Section 6.3.1, forming inverted domains with E-fields significantly below the intensity-dependent nucleation field in regular undoped CLN. The cross-sectional profiles of LAP domains in the region of illumination have been shown to be greater than 10 μm deep even for low exposures, which is significantly larger than the depth required for a single-mode waveguide in LN at visible and infrared wavelengths. Furthermore, periodic poling of Mg:CLN has been possible using illumination through a phase mask, producing optically periodically-poled lithium niobate (OPPLN). Combining these results could potentially lead to simple fabrication of small-period QPM structures for second harmonic wavelength generation down to the ultraviolet region. If these techniques could be straight-forwardly applied to CLT, UV generation would be particularly useful due to the reduced absorption in this region.

A simple extension of this periodic poling is to take advantage of the arbitrary domain shape and two-dimensional patterning capability. Demonstrations of poling via amplitude masks have already shown that the resulting domains can be made to conform to the shapes of the mask in two-dimensional patterns. Therefore the restriction of hexagonal symmetry can be lifted from the design of two-dimensional nonlinear photonic crystal (NPC) for improved performance.

A more difficult goal would be the further reduction of the one-dimensional period such that backward-wave generation becomes possible. Light-induced domains by AOP have been demonstrated down to ∼100 nm, indicating that domains of the size required for this application are in fact possible. As of yet, LAP domains have not been demonstrated on this size scale, but suitable illumination conditions to achieve these results have also never been attempted.

Devices relying on electro-optic functionality would also benefit from LAP fabrication, such as electro-optically controlled Bragg grating or two-dimensional photonic crystal. There has been much recent progress in the development of near-stoichiometric materials with very low coercive fields, however a permanently low coercive field would severely limit the magnitude of the E-field that could be applied without causing the domain structure to be compromised [Tian05]. Additionally, an extremely low E_c results in an unstable domain structure. Therefore the advantage of LAP fabrication is the ability to use materials with intrinsically high coercive fields, and to dynamically lower the nucleation field during fabrication only. This processing results in domain structures that are stable upon the application of external fields below this much larger intrinsic (dark) coercive field. However, this research also implies that caution must be taken for high intensity operation of electro-optic domain-engineered devices, as the propagating light may have an undesired impact on the domain structure. This is particularly important in Mg:CLN, although it could also influence the operation of devices in undoped CLN when applying high external fields.

In contrast to the planar geometries of waveguiding devices, bulk domain formation is also a possibility. Traditionally, a limitation of E-field poling has been in the thickness of the material over which it was possible to invert domains. Recently, studies have been made of materials with larger thicknesses to allow for a large aperture nonlinear interaction, using 3-mm [Grisard01; Ishizuki03] and 5-mm [Ishizuki05a; Ishizuki05b] thick crystals. However, these examples of thick PPLN all suffer from a duty cycle that varies significantly across the crystal thickness. Nevertheless, a large aperture device would allow higher power applications by permitting larger powers with intensities small enough that they will not result in optical damage. In [Ishizuki03], researchers used high temperatures of 250°C to reduce the coercive field by 75%. The advantage of LAP is the comparatively large reduction in the nucleation field, making conditions sufficient for fabrication at room temperature and with insulation by air only. To date, domains 5-mm thick have been formed but with much larger dimensions than the ∼30 µm period useful in OPO operation, for example. Therefore much work in determining the optimal exposure conditions for such high-aspect-ratio gratings remains to be completed.

Finally, a potentially very useful application of the LAP process is not to nucleate domains but rather to spread pre-existing domains in a process called *light-assisted domain trimming*, analogous to the laser trimming common in electronic integrated circuits. For domain engineered devices formed via *any* poling technique, errors in domain nucleation, spreading, or merging could all be corrected via directed illumination under a low–moderate E-field. Additionally, performance of a domain grating could be tuned for maximum efficiency by making small adjustments to the duty cycle. For nonlinear interactions of long wavelengths that do not impact the poling characteristic (i.e. IR), this tuning may also be possible with simultaneous *in situ* observation of the nonlinear interaction. These trimming functions could be very beneficial in improving the performance and yield of domain engineered materials.

LAP trimming of domain gratings could also introduce new functionality into a PPLN crystal or other domain engineered material. For instance, by transversely-patterning the EFP electrode, a transversely-varying interaction length was formed in a PPLN, creating a top-hat beam profile in the second-harmonic beam [Imeshev98]. Alternatively, a regular (transversely-uniform) PPLN (or NPC) could be fabricated by EFP, then later trimmed using LAP to introduce a transversely-varying grating length or duty cycle to achieve the same result. In 1D or 2D electro-optic photonic crystals, direct-write LAP could also introduce defects into the crystal structure for new functionality, such as defect modes and optical resonances.

6.6 Summary

Light-assisted poling has been investigated using cw and, for the first time, fs-pulsed light, achieving a reduction in the nucleation field by up to 90% and 98%, respectively, in Mg:LN doped above the ODT. Although Mg:LN appeared to be an ideal material for LAP domain engineering, LAP has also been demonstrated for a wide variety of doped LN and LT. Other photoresistant dopants, such as Zn and Hf, were expected to result in similar benefits to the LAP process, but due at least in part to poor material quality, did not show such enhancements. Nonetheless, LAP has been successful using a wide range of wavelengths from UV to IR, including 457–514.5 nm using cw and 305–800 nm using fs-pulsed light. Many of the limitations of cw-LAP were overcome by the use of fs-pulsed light. While cw lasers are currently much cheaper and often more readily available than fs-pulsed lasers, the development of new laser systems, such as fs-pulsed fibre lasers, is expected to reduce this issue in the future.

The localized nature of the reduction in the nucleation field permitted patterned domain engineering. Direct-write techniques and patterned illumination directly resulted in corresponding domain patterns. Contact masks and mask projection allowed the inversion of periodic domain structures in a single uniform illumination of the mask. Furthermore, illumination via a phase mask formed optically periodically poled gratings with $\Lambda = 5.25$ μm, limited in size only by the availability of the mask period, providing a reliable method of forming precise, small-period domain-engineered materials.

The latent-LAP process allowed the separation of both illumination and voltage steps, potentially simplifying the fabrication of domain engineered materials. This allows independent optimization of the setup for each step, and could enable the use of wavelengths that would be absorbed or the use of high intensities that could damage the electrode material.

Bibliography

[Battle00] C. C. Battle, S. Kim, V. Gopalan, K. Barkocy, M. C. Gupta, Q. X. Jia, and T. E. Mitchell, *Ferroelectric domain reversal in congruent $LiTaO_3$ crystals at elevated temperatures*. Appl. Phys. Lett., 76(17), 2436–2438 (2000).

[Brown99] P. T. Brown, G. W. Ross, R. W. Eason, and A. R. Pogosyan, *Control of domain structures in lithium tantalate using interferometric optical patterning*. Optics Comm., 163(4-6), 310–316 (1999).

[Dierolf04] V. Dierolf and C. Sandmann, *Direct-write method for domain inversion patterns in $LiNbO_3$*. Appl. Phys. Lett., 84(20), 3987–3989 (2004).

[Fejer86] M. M. Fejer, M. J. F. Digonnet, and R. L. Byer, *Generation of 22 mW of 532-nm radiation by frequency doubling in Ti:MgO:$LiNbO_3$ waveguides*. Opt. Lett., 11(4), 230–232 (1986).

[Fejer92] M. M. Fejer, G. A. Magel, D. H. Jundt, and R. L. Byer, *Quasi-phase-matched second harmonic generation: Tuning and tolerances*. IEEE J. Quant. Electron., 28(11), 2631–2654 (1992).

[Glass80] A. M. Glass, I. P. Kaminow, A. A. Ballman, and D. H. Olson, *Absorption loss and photorefractive-index changes in Ti:$LiNbO_3$ crystals and waveguides*. Appl. Opt., 19(2), 276–281 (1980).

[Gopalan98] V. Gopalan and T. E. Mitchell, *Wall velocities, switching times, and the stabilization mechanism of 180° domains in congruent $LiTaO_3$ crystals*. J. Appl. Phys., 83(2), 941–954 (1998).

[Grisard01] A. Grisard, E. Lallier, K. Polgar, and A. Peter, *3 mm-thick periodically poled lithium niobate*. In Conference on Lasers and Electro-Optics, Technical Digest. Summaries of papers presented at the Conference on Lasers and Electro-Optics. Postconference Technical Digest (IEEE Cat. No.01CH37170), 291, OSA, Baltimore, USA (2001).

[Hecht02] E. Hecht, Optics. Addison Wesley, 4 edition (2002).

[Hegedus97] Z. S. Hegedus, *Contact printing of Bragg gratings in optical fibers: rigorous diffraction analysis*. Appl. Opt., 36(1), 247–252 (1997).

[Houe95] M. Houe and P. D. Townsend, *Thermal polarization reversal of lithium niobate.* Appl. Phys. Lett., 66(20), 2667–2669 (1995).

[Imeshev98] G. Imeshev, M. Proctor, and M. M. Fejer, *Lateral patterning of nonlinear frequency conversion with transversely varying quasi-phase-matching gratings.* Opt. Lett., 23(9), 673–675 (1998).

[Ishizuki03] H. Ishizuki, I. Shoji, and T. Taira, *Periodical poling characteristics of congruent MgO:*$LiNbO_3$ *crystals at elevated temperature.* Appl. Phys. Lett., 82(23), 4062–4064 (2003).

[Ishizuki05a] H. Ishizuki and T. Taira, *Fabrication and characterization of 5-mm-thick periodically poled MgO:*$LiNbO_3$ *device.* In Conference on Lasers and Electro-Optics, 2108–2110, OSA, Baltimore, USA (2005).

[Ishizuki05b] H. Ishizuki and T. Taira, *High-energy quasi-phase-matched optical parametric oscillation in a periodically poled MgO:*$LiNbO_3$ *device with a 5 mm X 5 mm aperture.* Opt. Lett., 30(21), 2918–2920 (2005).

[Jungk05] T. Jungk and E. Soergel, *Depth-resolved analysis of ferroelectric domain structures in bulk* $LiNbO_3$ *crystals by scanning force microscopy.* Appl. Phys. Lett., 86(24), 242901 (2005).

[Kim01] S. Kim, V. Gopalan, K. Kitamura, and Y. Furukawa, *Domain reversal and nonstoichiometry in lithium tantalate.* J. Appl. Phys., 90(6), 2949–2963 (2001).

[Li07] D.-S. Li, D.-A. Liu, Y.-N. Zhi, W.-J. Qu, L.-R. Liu, and J. Zhang, *Red laser-induced domain inversion in MgO-doped lithium niobate crystals.* Chin. Phys. Lett., 24(4), 971–974 (2007).

[Mills01] J. D. Mills, An investigation of phase-mask diffraction patterns and fibre Bragg gratings with scanning near-field optical microscopy. Ph.D. thesis, University of Southampton (2001).

[Müller03a] M. Müller, E. Soergel, and K. Buse, *Influence of ultraviolet illumination on the poling characteristics of lithium niobate crystals.* Appl. Phys. Lett., 83(9), 1824–6 (2003).

[Müller03b] M. Müller, E. Soergel, and K. Buse, *Visualization of ferroelectric domains with coherent light.* Opt. Lett., 28(24), 2515–2517 (2003).

[Nakamura02] K. Nakamura, J. Kurz, K. Parameswaran, and M. M. Fejer, *Periodic poling of magnesium-oxide-doped lithium niobate.* J. Appl. Phys., 91(7), 4528–4534 (2002).

[Ohmori75] Y. Ohmori, Y. Yasojima, and Y. Inuishi, *Photoconduction, thermally stimulated luminescence, and optical damage in single crystal of* $LiNbO_3$. Jpn. J. Appl. Phys., 14(9), 1291–1300 (1975).

[Schmidt80] R. V. Schmidt, P. S. Cross, and A. M. Glass, *Optically induced crosstalk in* $LiNbO_3$ *waveguide switches.* J. Appl. Phys., 51(1), 90–93 (1980).

[Shur00] V. Y. Shur, E. L. Rumyantsev, E. V. Nikolaeva, and E. I. Shishkin, *Formation and evolution of charged domain walls in congruent lithium niobate.* Appl. Phys. Lett., 77(22), 3636–3638 (2000).

[Shur02] V. Y. Shur, E. L. Rumyantsev, E. V. Nikolaeva, E. I. Shishkin, R. B. Batchko, M. M. Fejer, R. L. Byer, and I. Mnushkina, *Domain kinetics in congruent and stoichiometric lithium niobate.* Ferroelectrics, 269, 189–194 (2002).

[Soergel05] E. Soergel, *Visualization of ferroelectric domains in bulk single crystals.* Appl. Phys. B, 81(6), 729–751 (2005).

[Soergel07] E. Soergel, *Personal communication* (2007).

[Sones05] C. L. Sones, M. C. Wengler, C. E. Valdivia, S. Mailis, R. W. Eason, and K. Buse, *Light-induced order-of-magnitude decrease in the electric field for domain nucleation in MgO-doped lithium niobate crystals.* Appl. Phys. Lett., 86(21), 212901 (2005).

[Sones06] C. L. Sones, C. E. Valdivia, S. Mailis, and R. W. Eason, *Ultra-short light-pulse assisted electric field domain engineering of lithium niobate.* In Photonics 2006, Hyderabad, India (2006).

[Tian05] L. Tian and V. Gopalan, *Comparison of domain reversal and electro-optic properties of congruent and stoichiometric lithium tantalate.* In Integrated Optics: Devices, Materials, and Technologies IX, volume 5728, 278–282, SPIE, San Jose, CA, USA (2005).

[Valdivia05a] C. E. Valdivia, C. L. Sones, S. Mailis, R. W. Eason, M. C. Wengler, and K. Buse, *Visible-light-induced tenfold reduction of the electric field required for ferroelectric domain nucleation in MgO-doped lithium niobate.* In Conference on Lasers and Electro-Optics, CMW4, OSA, Baltimore, USA (2005).

[Valdivia05b] C. E. Valdivia, C. L. Sones, S. Mailis, J. D. Mills, and R. W. Eason, *Ultrashort-pulse optically-assisted domain engineering in lithium niobate.* In International Symposium on Micro- and Nano-Scale Domain Structuring in Ferroelectrics (ISDS), Ekaterinburg, Russia (2005).

[Valdivia06a] C. E. Valdivia, C. L. Sones, S. Mailis, and R. W. Eason, *Ultrashort-pulse light-assisted periodic poling of lithium niobate and lithium tantalate.* In Conference on Lasers and Electro-Optics, CMB2, OSA, Long Beach, USA (2006).

[Valdivia06b] C. E. Valdivia, C. L. Sones, S. Mailis, J. D. Mills, and R. W. Eason, *Ultrashort-pulse optically-assisted domain engineering in lithium niobate.* Ferroelectrics, 340, 75–82 (2006).

[Wengler05] M. C. Wengler, U. Heinemeyer, E. Soergel, and K. Buse, *Ultraviolet light-assisted domain inversion in magnesium-doped lithium niobate crystals.* J. Appl. Phys., 98(6), 064104 (2005).

[Yang99] T. J. Yang, V. Gopalan, P. J. Swart, and U. Mohideen, *Direct observation of pinning and bowing of a single ferroelectric domain wall.* Phys. Rev. Lett., 82(20), 4106–4109 (1999).

[Zhi07] Y. Zhi, D. Liu, W. Qu, Z. Luan, and L. Liu, *Wavelength dependence of light-induced domain nucleation in MgO-doped congruent* $LiNbO_3$ *crystal.* Appl. Phys. Lett., 90(4), 042904 (2007).

Chapter 7

Conclusions and Future Research

Ferroelectric domain engineering has enabled the fabrication of a host of efficient nonlinear optical devices, demonstrating quasi-phase-matched nonlinear interactions and a variety of other functions. In LN, one of the most widely used and researched nonlinear materials, device operation has been limited by the inability to form inverted domains reliably below sizes of several microns using conventional EFP. In this research, the methods of all-optical poling and light-assisted poling were employed to fabricate inverted domains. Additionally, two latent optical poling techniques have been used, where an E-field was applied after UV pulsed illumination to spread the nano-domains, or an E-field was applied after a set delay time following fs-pulsed visible illumination. The objective of the investigations into these poling techniques was to further the understanding of the kinetics and light-material interaction in the domain inversion process, and to demonstrate feasible domain engineering techniques for bulk and waveguiding devices.

7.1 UV-Light-Induced Surface Modification

UV illumination of the $-$z face of lithium niobate has previously been shown to produce etch frustrated regions which were assumed to be the result of light-induced surface charge. However, illumination with unpatterned and periodically patterned UV light has demonstrated two distinct sets of results. Fluences well below the ablation threshold formed isolated etch-*frustrated* dots. Increasing the fluence towards the ablation threshold formed connected etch-*resistant* regions. These features have been imaged and erased by scanning with an SFM. These results indicate that etch frustration is due to the formation of UV-induced shallow surface domains which are encouraged to spread and merge upon the increase of the incident fluence.

Further research into the process of UV-induced surface modification will benefit from the recent improvements in the understanding of the nature of the PFM signals. Use of the background subtraction technique will enable improved imaging, permitting the investigation of the minimum feature size of the etch-resistant dots. Lateral spreading and merging can be measured as a function of fluence. Furthermore, the relative depth of these features may be indirectly measured by the amplitude of PFM deflection or by the time required to re-invert an area. The depth of the shallow surface layer of domain inversion is expected to vary for the fluence and wavelength used. Additionally, an E-field applied after illumination may show further depth penetration.

While several applications would benefit from pushing these domains deeper to waveguide depths, minimizing the domain depth could also have a practical application. For instance, several types of devices utilize domain inversion and preferential etching for device microstructuring (ex. [Sones02]). However, instead of photolithographically patterning and subsequent poling of the crystal, a thin domain inversion layer could be formed on the $-$z face in a single simple step. This has the added benefit of maintaining the same domain orientation throughout the crystal which might be attractive for some applications. In the fabrication of a multi-step device, a UV-induced shallow domain surface layer could be created in areas of a device in which HF etching must be prevented in a subsequent fabrication steps. These surface layer modifications would of course be most useful in bulk devices or in other devices in which the top layer has a small influence on device operation.

7.2 All-Optical Poling

All-optical poling of lithium niobate was achieved by UV illumination of the +z face, forming self-organized nano-domain lines strictly oriented along the y axes. These lines grew out from a starting nucleation point along the $-$y directions only, and were deflected away from other lines and domains via electro-static interaction at distances of $\sim$2 µm. Illumination via a phase mask allowed the ordered alignment of these features along a single y axis, although the periodicity was limited by this interaction distance. PFM allowed the non-destructive visualization of these nano-domains in both amplitude and phase response, although the limited depths and nano-scale dimensions reduced the contrast of anti-parallel domains. The application of an E-field after illumination spread the nano-domains laterally and in depth.

Further research could investigate the effect of exposure conditions on the domain depth, as revealed by y-face cross-sections. In addition to the lasers already employed for the illumination of the +z face, other lasers will also allow a study of the role of absorption depth by varying the wavelength. Utilizing several different lasers may also allow a study of the effect of pulse duration on the formation of AOP domains. There is no evidence to suggest that ns-pulses are ideal, although fs-pulses were not successful in the fluence range tested. However, pulse durations of picoseconds to microseconds drastically differ in the effects of heating and strongly influences ablation. Pulse-train bursts, containing a sequence of many pulses packed closely in time, has also been shown to improve ablation quality by accumulating heat in the surrounding material [Marjoribanks01], and may have a strong impact on the formation of AOP domains. Finally, fluence may also impact the domain depth. Therefore many exposure parameters can be controlled to alter the conditions under which the AOP domain lines form, which may prove to change other properties than simply the depth profiles.

Illumination in presence of an E-field oriented in the poling direction could be an alternative route to pushing domains deeper into the crystal. The externally applied E-field may have a secondary effect of altering the kinetics of domain growth, possibly increasing the nucleation density or rate of 1D nucleation. The formation of surface domains with a greater depth may also have the added benefit of reducing the interaction length, reducing the minimum distance between adjacent domain lines.

Reliable control over AOP domain growth may be achieved by a systematic study of the post-application of an E-field following irradiation. Surface domains may be forced deeper by short-duration E-fields, and spread laterally through longer and larger E-fields. A compromise between domain width and depth may need to be made if growth in the depth and lateral dimensions occurs simultaneously. This may not pose a problem, as the depth sufficient for waveguiding structures will most likely prove accessible since the as-formed depth is already $\sim$2 μm. Spreading laterally in a controlled manner may allow the engineering of the duty cycle of a periodic structure. However, producing uniform spreading across the entire length of the UV-induced line may present a great technical challenge.

In the experiments already conducted on post-application of E-field to AOP domains, the etch profiles on the +z face were heavily influenced by surface defects. These defects may be reduced by use of lower fluences closer to the ablation threshold. However, the defect problem could be ignored entirely for optical interactions away from the +z surface. For instance, if sufficiently small domains can be pushed through to the $-$z face, this would allow either waveguiding interactions at the $-$z face or bulk optical interactions.

Finally, illumination of other types of crystals could also provide insight into the formation mechanisms of AOP domains. Initial unpatterned exposures of y-cut CLN, for instance, has induced several isolated rectangular domains aligned along the z axis. Controlling this periodically would present a useful geometry for waveguiding QPM devices. Other materials such as SLN and LT could also be explored.

7.3 Light-Assisted Poling

Light-assisted poling of LN and LT was achieved by simultaneously applying an E-field and an optical field of wavelengths ranging from near-UV to near-IR. Using either cw or fs-pulsed light, the nucleation field reduced with increased intensity. LAP was most effective in Mg-doped materials in which cw and fs-pulsed light reached a 90% and 98% reduction in the nucleation field, respectively. This domain engineering technique allowed domain formation via direct-writing or mask patterning, and permitted arbitrary domain shapes free from the crystalline symmetry constraints on both polar faces. Periodic poling over small areas has been demonstrated with a period of 5.25 μm by illumination though phase mask.

Latent-LAP, wherein a crystal is illuminated by fs-pulsed light and then subjected to an electric field after a set delay, has also caused domain inversion. The size of the inverted region was dependent upon both the time delay and applied voltage for the exposures tested. Latent-LAP was successful in undoped CLN but not in Mg:CLN, where it is believed that the higher conductivity allowed the redistribution of photo-generated charge in a time scale shorter than the delays used. Furthermore, latent-LAP was not possible using cw light in either material.

Many directions of future research remain for LAP, and all would benefit from several improvements in the setup and monitoring. Firstly, an improved and higher resolution in-situ optical monitoring setup would be highly beneficial for the visualization of microscopic features during micro-domain growth. For example, phase contrast has been successfully used in a LAP process recently [Zhi07]. Secondly, the E-field application time should be controlled to prevent further unintentional domain growth after illumination. An ideal implementation of this would be the use of millisecond-duration voltage pulses, as used in pulsed EFP. This would allow for the simultaneous application of pulsed E-field and pulsed optical field, which may lead to tighter control of domain spreading and depth growth. Thirdly, large area domain inversion, such as in periodic poling, would greatly benefit from control and monitoring of the poling current. In the present experiments this had not been implemented due to the microscopic nucleations of interest, and the correspondingly minute poling current. In high-quality domain engineering, these improvements will be vital to the fabrication reliability and performance of devices.

The depth profiles must be controlled for useful domain engineering. Increasing either intensity or exposure time is expected to increase the domain depth, but requires systematic study. This domain growth with increasing time (number of pulses) will determine if the analogy between pulsed-voltage EFP and pulsed-light LAP is accurate. The use of lower E-fields is also expected to reduce the domain spreading outside of the beam area, and thereby ensure that the maximum depth is achieved *within* the illuminated region.

Domain profiles are also affected by crystal temperature, as discussed in [Kurimura05], where a lower temperature during pulsed EFP resulted in higher aspect ratio (lower sidewall angle). However, this occurred at the expense of a reduced nucleation density, forming segmented domain lines rather than continuous periodic lines. LAP increases the nucleation density at room temperature, and therefore may counteract the effects of lower temperature, achieving higher aspect ratios within high-quality gratings.

Micron-scale periodic domain patterning has been achieved by illumination through a phase mask. The period realized in these experiments was limited only by the phase mask in use. Smaller period phase masks may allow PPLN with sub-micron periodicities. Alternatively, two-beam interference may allow for simpler control of the period. This has been demonstrated using UV light [Wengler05], although the low intensities available limited the nucleation density and hence quality of the grating. Higher intensity, particularly available using fs-pulsed light, is expected to improve these results. Another method of patterning the domain structure is through the deposition of a material on the crystal surface. The use of an opaque insulating material might improve domain patterning by simultaneously insulating the material both electrically and optically. The uniformity of domain inversion under all these patterning techniques would improve by the use of a top-hat beam profile.

Finally, the LAP process can be explored in new materials. Firstly, higher quality LN with dopant concentrations above the ODT incorporated into the crystal are crucial for an analysis of its effect on LAP and for device performance. Additionally, other types of crystals, such as KTP, could be explored. Finally, LAP has been successful in Ti-indiffused waveguides, but could also be extended to Zn or proton-exchanged waveguides for QPM devices. Initial attempts of LAP, and indeed regular EFP, in proton-exchanged waveguides have proved very sensitive to the fabrication conditions of the waveguide itself.

7.4 Summary

The research included in this thesis has investigated the influence of light on domain inversion in LN and LT materials. Pulsed UV illumination without applied E-fields have formed surface domains on both polar faces of LN. Simultaneous application of an E-field and an optical field, using both cw and fs-pulsed light, has shown significant reductions in the nucleation field, providing simple methods of optically patterning the domain structure. These investigations have increased the understanding of the kinetics of domain inversion, particularly under the influence of light, and demonstrated routes to high-quality fabrication of domain engineered materials. Future research will be directed towards the demonstration of a functional frequency-conversion device using these light-induced domain inversion techniques.

Bibliography

[Kurimura05] S. Kurimura, *Micro- and nano-scale domain structuring in ferroelectrics, Round table discussion.* In International Symposium on Micro- and Nano-Scale Domain Structuring in Ferroelectrics (ISDS), Ekaterinburg, Russia (2005).

[Marjoribanks01] R. S. Marjoribanks, Y. Kerachian, P. R. Herman, and S. Camacho-Lopez, *Pulsetrain 'burst' machining: Ultrafast-laser microprocessing at ultrahigh (>100 MHz) pulse-rates.* In Conference on Lasers and Electro-Optics, 575–576, OSA, Baltimore, USA (2001).

[Sones02] C. Sones, S. Mailis, V. Apostolopoulos, I. E. Barry, C. Gawith, P. G. R. Smith, and R. W. Eason, *Fabrication of piezoelectric micro-cantilevers in domain-engineered $LiNbO_3$ single crystals.* J. Micromech. Microeng., 12(1), 53–57 (2002).

[Wengler05] M. C. Wengler, U. Heinemeyer, E. Soergel, and K. Buse, *Ultraviolet light-assisted domain inversion in magnesium-doped lithium niobate crystals.* J. Appl. Phys., 98(6), 064104 (2005).

[Zhi07] Y. Zhi, D. Liu, W. Qu, Z. Luan, and L. Liu, *Wavelength dependence of light-induced domain nucleation in MgO-doped congruent $LiNbO_3$ crystal.* Appl. Phys. Lett., 90(4), 042904 (2007).

Appendix A

Publications and Presentations

A.1 Journal Papers

1. I. T. Wellington, C. E. Valdivia, T. J. Sono, C. L. Sones, S. Mailis, R. W. Eason. Ordered nano-scale domains in lithium niobate single crystals via phase-mask assisted all-optical poling. Appl. Surf. Sci., 253(9), 4215-4219 (2007).
2. C. E. Valdivia, C. L. Sones, S. Mailis, J. D. Mills, and R. W. Eason. Ultrashort-pulse optically-assisted domain engineering in lithium niobate. Ferroelectrics, 340, 75-82 (2006).
3. C. E. Valdivia, C. L. Sones, J. G. Scott, S. Mailis, R. W. Eason, D. A. Scrymgeour, V. Gopalan, T. Jungk, E. Soergel, and I. Clark. Nanoscale surface domain formation on the +z face of lithium niobate by pulsed ultraviolet laser illumination. Appl. Phys. Lett., 86(2), 022906 (2005).
4. C. L. Sones, M. C. Wengler, C. E. Valdivia, S. Mailis, R. W. Eason, and K. Buse. Light-induced order-of-magnitude decrease in the electric field for domain nucleation in MgO-doped lithium niobate crystals. Appl. Phys. Lett., 86(21), 212901 (2005).
5. C. L. Sones, C. E. Valdivia, J. G. Scott, S. Mailis, R. W. Eason, D. A. Scrymgeour, V. Gopalan, T. Jungk, and E. Soergel. Ultraviolet laser-induced sub-micron periodic domain formation in congruent undoped lithium niobate crystals. Appl. Phys. B., 80(3), 341-344 (2005).

A.2 Conference Presentations

1. C. E. Valdivia, C. L. Sones, S. Mailis, and R. W. Eason. Ultrashort-pulse light-assisted periodic poling of lithium niobate and lithium tantalate. In Conference on Lasers and Electro-Optics, OSA, Long Beach, USA (2006).
2. C. E. Valdivia, C. L. Sones, S. Mailis, J. D. Mills, and R. W. Eason. Ultrashort-pulse optically-assisted domain engineering in lithium niobate. In International Symposium on Micro- and Nano-Scale Domain Structuring in Ferroelectrics (ISDS'05), Ekaterinburg, Russia (2005).
3. C. E. Valdivia, C. L. Sones, J. G. Scott, S. Mailis, R. W. Eason, D. A. Scrymgeour, V. Gopalan, and I. Clark. Nano-scale ultraviolet laser-induced ferroelectric surface domains in lithium niobate. In Conference on Lasers and Electro-Optics - Europe (invited), OSA, Munich, Germany (2005).
4. C. E. Valdivia, C. L. Sones, S. Mailis, R. W. Eason, M. C. Wengler, and K. Buse. Visible-light-induced tenfold reduction of the electric field required for ferroelectric domain nucleation in MgO-doped lithium niobate. In Conference on Lasers and Electro-Optics, OSA, Baltimore, USA (2005).

A.3 Other Publications

1. S. Mailis, C. E. Valdivia, C. L. Sones, A. C. Muir, R. W. Eason. Latent laser-assisted domain inversion in congruent lithium niobate. In Conference on Lasers and Electro-Optics - Europe 2007.
2. T. Jungk, A. Hoffman, E. Soergel, S. Mailis, A. C. Muir, I. T. Wellington, C. E. Valdivia, C. L. Sones, R. W. Eason. UV laser-induced ferroelectric domain structures investigated by piezoresponse force microscopy. In Conference on Lasers and Electro-Optics - Europe 2007.
3. T. J. Sono, J. G. Scott, C. L. Sones, C. E. Valdivia, S. Mailis, R. W. Eason, J. G. Frey, and L. Danos. Reflection second harmonic generation on a z-cut congruent lithium niobate crystal. Phys. Rev. B, 74(20), 205424 (2006).
4. C. L. Sones, C. E. Valdivia, S. Mailis, R. W. Eason. Ultra-short light-pulse assisted electric field domain engineering of lithium niobate. In Photonics 2006, Hyderabad, India (2006).
5. R. W. Eason, S. Mailis, C. L. Sones, A. J. Boyland, A. C. Muir, T. J. Sono, J. G. Scott, C. E. Valdivia, and I. T. Wellington. Progress in Ferroelectric Domain Engineering at the Micro/Nanoscale. In Electroceramic Materials and Applications, Ceramic Transactions, Ed. R. W. Schwartz, Wiley, 196, 93-108 (2006).

6. S. Mailis, C. L. Sones, C. E. Valdivia, I. T. Wellington, A. C. Muir, J. G. Scott, and R. W. Eason. UV radiation-induced surface wetting changes in lithium niobate single crystals. In Conference on Lasers and Electro-Optics - Europe, OSA, Munich, Germany (2005).
7. C. L. Sones, I. T. Wellington, C. E. Valdivia, S. Mailis, R. W. Eason. Light-induced domain engineering in ferroelectrics: A route to sub-micron poling. Council for the Central Laboratory of the Research Councils (CCLRC), Rutherford Appleton Laboratory, Central Laser Facility Annual Report 2005-2006, 182-184 (2006).
8. C. L. Sones, C. E. Valdivia, J. G. Scott, S. Mailis, R. W. Eason, D. A. Scrymgeour, V. Gopalan, T. Jungk, E. Soergel, and I. P. Clark. Light-induced domain engineering in ferroelectrics. Council for the Central Laboratory of the Research Councils (CCLRC), Rutherford Appleton Laboratory, Central Laser Facility Annual Report 2004-2005, 185-187 (2005).

A.4 Other Presentations

1. C. E. Valdivia, C. L. Sones, S. Mailis, I. T. Wellington, R. W. Eason. Domain engineering with a light touch (poster presentation). In Optoelectronics Research Centre Colloquium, University of Southampton (2006).
2. C. E. Valdivia, C. L. Sones, S. Mailis, J. G. Scott, R. W. Eason. Domain engineering with a light touch (oral presentation). In Optoelectronics Research Centre Colloquium, University of Southampton (2005).
3. C. E. Valdivia, C. L. Sones, J. G. Scott, S. Mailis, I. T. Wellington, T. J. Sono, R. W. Eason. Domain engineering with a light touch (oral presentation). Professor Karsten Buse group meeting, University of Bonn (2005).

Appendix B

Prints of Publications